UNIVERSITÀ
DI SIENA
1240

Dipartimento di Biotecnologie Mediche

Dottorato in Biotecnologie Mediche

38° Ciclo

Coordinatore: Prof. Francesco Iannelli

Beyond single-agent therapy: synergistic drug combinations and HSPG-Binding compounds as innovative strategies against SARS-CoV-2 variants

Candidato/a

Camilla Biba

Università degli studi di Siena

Firma digitale del/della candidato/a

Firmato digitalmente da:
CAMILLA BIBA
Luogo: Siena

Supervisore

Ilaria Vicenti

Università degli studi di Siena

Co-supervisore/i

Maurizio Zazzi

Università degli studi di Siena

Anno accademico di conseguimento del titolo di Dottore di ricerca

2024/2025

Index

My PhD activities 1

1. Introduction 3

1.1 General overview and epidemiology 3

1.2 SARS-CoV-2 genome organization and life cycle 4

1.2.1 Genome organization 4

1.2.3 Sars-CoV-2 life cycle 6

1.3 SARS-CoV-2 Transmission 9

1.4 Clinical manifestations and pathogenesis 10

1.5 SARS-CoV-2 Persistence and Long-COVID 13

1.6 SARS-CoV-2 evolution 16

1.7 Current measure to counteract COVID-19: monoclonal antibodies, vaccines and antivirals. 20

1.7.1 Monoclonal Antibodies 20

Evolution of Monoclonal Antibody Therapy during the COVID-19 Pandemic 21

1.7.2 Antiviral drugs 23

1.7.3 SARS-CoV-2 vaccines 25

1.8 New strategies against SARS-CoV-2 27

1.8.1 Host-targeted antivirals (HTAs) 27

1.8.2 Compounds targeting Heparan Sulfates 29

1.8.3 Synergistic strategies to inhibit SARS-CoV-2 Infection 31

2. AIMS 33

3. Methods 34

3.1 In Vitro Combinatorial Activity 34

In vitro experiments 34

Cell Line used for the assays 34

Cytotoxicity Assay 35

Viral stocks 36

Viral Titration Assay 36

Antiviral Activity Assay 37

Dose-Effect Relationships with Compound Combinations 37

Statistical Analysis 38

3.2 LB-1 activity 38

In vitro experiments 38
Cell lines 39
Viral stocks 39
Viral Titration Assay 39
Cytotoxicity assay 40
4 Results 42
4.1 Combinatorial effect 42
4.1 LB-1 47
5. CONCLUSIONS 51
6. REFERENCES 54
7. PUBLISHED PAPERS 62

My PhD activities

During my enrollment in the Doctoral School of Medical Biotechnologies at the University of Siena, I actively participated in the Laboratory of Microbiology and Virology, contributing to multiple research projects focused on antiviral drug discovery. My research gave me the possibility to explore a variety of viral pathogens, including Severe Acute Respiratory Syndrome Coronavirus 2 (SARS-CoV-2), West Nile Virus (WNV), Dengue Virus (DENV), Zika Virus (ZIKV), Human Immunodeficiency Virus-1 (HIV-1) and Influenza virus. Beside the two projects that will be discussed deeply in this doctoral thesis, I was involved in several research collaborations that allowed me to test novel compounds and assess mechanisms of viral replication and resistance. In particular, I have worked with Professor Manini and Professor Montomoli of the Department of Molecular and Developmental Medicine (University of Siena) studying the unusual epidemiological pattern of the 2021/2022 influenza season in Italy, which did not reach the usual peak probably because of the COVID-19 containment measures such as social distancing, remote working, use of face masks (Milano et al.,2024). In another project, I actively collaborated with Professor Messina of Department of Molecular and Developmental Medicine, in an investigation on the effects of violet-blue light (VBL) on the infectivity and structural integrity of SARS-CoV-2 compared to influenza A and B viruses. We demonstrated that SARS-CoV-2 is markedly more susceptible to VBL, proposing as mechanism of viral inactivation the oxidative damage to the lipid envelope instead of direct RNA degradation. This finding highlighted the vulnerability of SARS-CoV-2 to light-based disinfection approaches and gives us a better understanding of the molecular mechanism behind its susceptibility (Amodeo et al.,2025). I have also worked with Professor Campiani (Department of Biotechnology, Chemistry and Pharmacy, University of Siena) in the characterization of novel covalent peptidomimetic inhibitors targeting the SARS-CoV-2 main protease (Mpro), a key enzyme for viral replication. Through structure–activity relationship analyses, molecular docking, and X-ray crystallography, we identified compounds with promising antiviral activity, offering valuable information to guide the development of next-generation Mpro inhibitors (Rossi et al.2025). I have contributed to proteomic analyses in collaboration with Professor Luca Bini's laboratory on newly synthetized compounds targeting WNV and DENV viruses, and I investigated the role of PARP12 and ADP-ribosylation in viral infections in collaboration with CNR Naples.

Furthermore, I was involved in the evaluation of neutralizing antibody responses in people living with HIV after receiving a third dose of the BNT162b2 mRNA vaccine, in collaboration with the laboratory of Professor Parisi (Department of Molecular Medicine, University of Padova). Using live-virus neutralization assays, we found that while all participants showed detectable responses against the ancestral B.1 lineage six months post-vaccination, their neutralizing titers against the Omicron BA.5 variant were significantly lower, underscoring the impact of viral evolution on vaccine-induced immunity (Vicenti et al., 2023). Continuing in the field of HIV-1 research, we evaluated the *in vitro* susceptibility of multidrug-resistant HIV-1 strains to doravirine and islatravir, as well as their combinatorial activity. Despite complex resistance profiles, the two drugs showed mainly additive and sometimes synergistic effects, although their activity decreased in the presence of multiple resistance-associated mutations, particularly M184V/I (Giammarino et al., 2025)

Finally, I evaluated different next-generation sequencing (NGS) methodologies for HIV-1 genotypic resistance testing, comparing the performances of an in-house amplicon-based protocol to a commercial NGS kit. Both methods detected additional resistance mutations compared to Sanger sequencing, but the in-house protocol showed better genome coverage (Biba et al., 2024). Ultimately, during the last 7 months of my PhD, I worked at the Emory National Primate Research Center (USA), exploring molecular mechanisms underlying AIDS pathogenesis through sequencing of natural and non-natural SIV hosts belonging to the same genus of Cercopithecus. Throughout these experiences, I acquired a broad range of technical skills, including proficiency in cell cultures (VERO-E6, A549, CACO-2, HUH-7), ability to work in Biosafety Level 3 laboratories, ELISA and Cell Titer-Glo assays, Illumina sequencing, nucleic acid extraction, and isolation of CD4+ T-cells from whole blood. These activities provided me with a solid foundation in antiviral research, virology, and advanced laboratory techniques, combining both in vitro experimentation and genomic analysis.

1. Introduction

1.1 General overview and epidemiology

Human coronaviruses (HCoVs) form a subgroup within the *Coronaviridae* family and are associated with a wide range of respiratory infections, from mild illnesses such as the common cold to more severe conditions like bronchiolitis and pneumonia. The Coronaviridae family is taxonomically categorized into two subfamilies: Coronavirinae and Torovirinae. Viruses belonging to the Torovirinae subfamily are morphologically distinct from those in the Coronavirinae, primarily due to their helical, toroid-shaped nucleocapsid structure (Lamer & Haagmans, 2022). Within Coronavirinae, four genera are recognized: Alphacoronavirus, Betacoronavirus, Gammacoronavirus, and Deltacoronavirus. Alphacoronaviruses and Betacoronaviruses infect only mammals, while Gammacoronaviruses and Deltacoronaviruses have a broader host range, including both avian and mammalian species (Mahdy Mohamed et al., 2020). A defining feature of coronaviruses is their ability to cross species barriers, a process facilitated by the presence of diverse animal reservoirs that support viral replication and maintenance. Since the early 2000s, multiple HCoVs have been linked to major global outbreaks of severe respiratory disease. The first significant event occurred in November 2002 in Foshan, China, with the emergence of severe acute respiratory syndrome coronavirus (SARS-CoV), which spread internationally in 2003 and had an estimated case fatality rate of 10%. In June 2012, Middle East respiratory syndrome coronavirus (MERS-CoV) was identified in Jeddah, Saudi Arabia, and drew global attention due to its higher fatality rate (around 37%). Most recently, in December 2019, a novel coronavirus later named SARS-CoV-2 appeared in Wuhan, China. Closely related to SARS-CoV, this virus initiated the COVID-19 pandemic: the most widespread and impactful coronavirus outbreak to date (Kirtipal et al., 2020). Sequencing of SARS-CoV-2 genomes revealed a close relationship (approximately 88% genome identity) with two bat-derived strains, bat-SL-CoVZXC21 and bat-SL-CoVZC45, which had been isolated from bats in Zhoushan, China, in 2015 and 2017, respectively (Lu et al., 2020). In addition, SARS-CoV shares only 79% genome identity with SARS-CoV-2, while MERS-CoV shares about 50% (Sallard et al., 2021). The initial SARS-CoV-2 genome (strain Wuhan-Hu-1), released on January 10, 2020, did not phylogenetically cluster with any known bat coronavirus, suggesting that recombination may have played a role in its emergence. Later genomic analyses identified RaTG13, a coronavirus detected in a *Rhinolophus affinis* bat from Yunnan Province in 2013, as

its closest known relative (Boni et al., 2020). Furthermore, comparative genomic studies suggest that the SARS-CoV-2 genome present a mosaic structure shaped by multiple recombination events involving a SARS-CoV-2-like ancestor, RaTG13, and coronaviruses identified in pangolins from Guangdong Province (Singh & Yi, 2021).

The spread of SARS-CoV-2 has caused disease and numerous fatalities across the world. At the time of writing, WHO reported 7,099,375 deaths since the beginning of the pandemic and 5,184 hospitalizations in the last 28 days (last access August 2025). Aside from the sudden pandemic (which caused massive socio-economic difficulties worldwide), SARS-CoV-2 has also been associated with prolonged illness such as long COVID, again contributing to the effects on world health.

1.2 SARS-CoV-2 genome organization and life cycle

1.2.1 Genome organization

The genome of SARS-CoV-2 is a single-stranded positive-sense RNA of approximately 30 kilobases in length with a 5' cap structure and a 3'-poly-A tail. It consists of 14 functional open reading frames (ORFs), including two noncoding regions at both ends. The ORFs leads to a total of 29 viral proteins: 16 non-structural proteins NSPs, 4 structural proteins and 9 accessory protein (Yao et al., 2020, Bai et al., 2022). After viral entry, the SARS-CoV-2 RNA genome is directly translated, leading to two polyproteins from two large open reading frames: ORF1a and ORF1b (*Figure 1*). The programmed frameshift at the 3' end of ORF1a lead to the production of pp1a and pp1ab. These polyproteins are required for the replication-transcription complex (RTC) assembly and are processed into the 16 NSPs by two viral cysteine proteases: NSP3 (papain-like protease, PL_{pro}) and NSP5 (main protease, M_{pro}). Some of the most crucial non-structural proteins in the SARS-CoV-2 life cycle include the RNA-dependent RNA polymerase (RdRp) NSP12, the viral helicase NSP13, and the NSP14, with 3'–5' exonuclease (ExoN) proofreading activity. This proofreading activity is a unique feature of RNA viruses and plays a central role in coronavirus evolution and cross-species transmission potential. Indeed, ExoN error correction reduces the SARS-CoV-2 genome's mutation rate compared to other RNA viruses and facilitates genetic recombination, as demonstrated in vitro using NSP14 knockout viral models (Gribble et al., 2021).

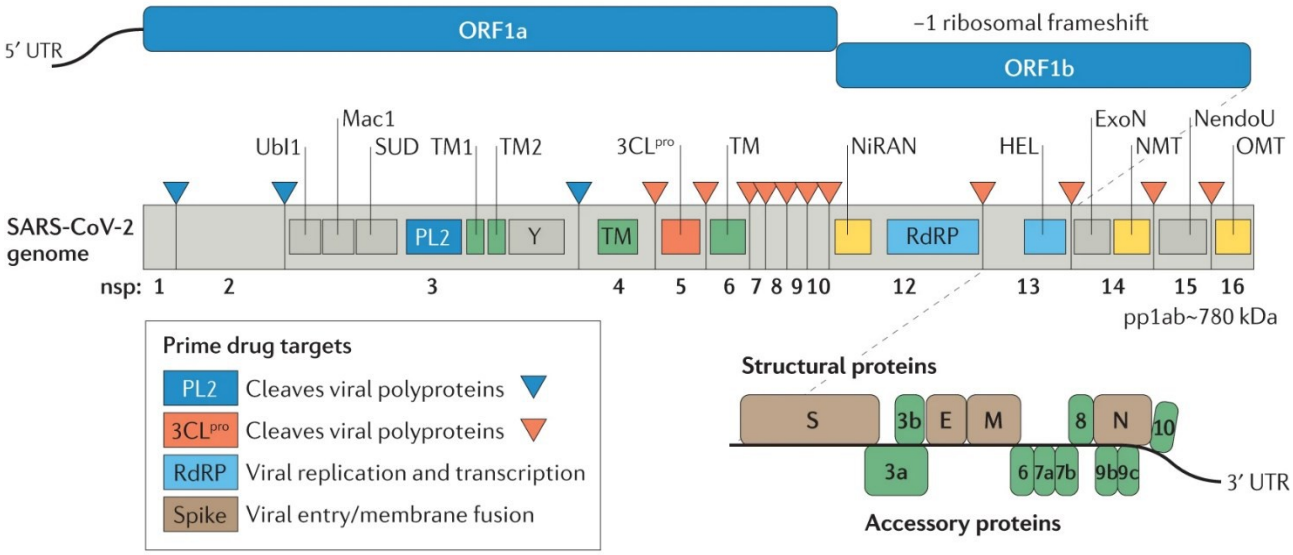

Figure 1 SARS-CoV-2 genome (Yang et al., 2021)

At the 3' end of the SARS-CoV-2 genome there are four ORFs encoding the major structural proteins: nucleocapsid (N), spike (S), membrane (M), and envelope (E). These structural proteins contribute to virion assembly as well as immune evasiveness. (Yang et al.,2021; Naqvi et al., 2020; Hoffman et al., 2020, V'kovski et al., 2020). Among the structural proteins, the spike (S) glycoprotein is essential for viral entry mediating both attachment to the host cell membrane and membrane fusion. The spike glycoprotein is a homotrimer and its replication units are present within the viral envelope, conferring the crown-like (corona) appearance to SARS-CoV-2. After viral maturation within infected cells, the S protein is cleaved by host furin or furin-like convertases within the Golgi apparatus into two subunits, S1 and S2, which remain non-covalently associated (Jackson et al., 2022). The S1 subunit contains the receptor-binding domain (RBD, residues 306–534), which interacts with host cell surface receptors and dictates viral tropism and pathogenicity. The transmembrane S2 subunit contains the fusion peptide, which induces viral and cellular membrane fusion. (Naqvi et al., 2020; Qing et al., 2020; Jackson et al., 2022).

One of the unique features of SARS-CoV-2 is the polybasic cleavage site (PRRAR) at the S1/S2 boundary, with a proline residue. This site is not present in closely related betacoronaviruses (Coutard et al., 2020) and has been demonstrated to enhance viral infectivity. Pre-cleavage of the spike protein can enable extended cell tropism and zoonotic transmission and enhance the transmissibility of the virus (Neerukonda et al., 2020; V'kovski et al., 2020).

The envelope (E) protein is another structural protein involved in viral morphogenesis, pathogenesis, assembly, and budding. It is a viroporin that forms ion channels, creating protein-lipid pores involved in ion transport. (Bianchi et al., 2020).

The M protein, which has three transmembrane domains, also interacts with the E, N, and S proteins playing a key role in virion shaping. It is the most highly expressed structural coronavirus protein during viral replication and has a critical role in virus assembly (Naqvi et al., 2020).

The N protein is present alongside the viral RNA genome inside the nucleocapsid. It helps in encapsidating the RNA into the ribonucleocapsid and has interactions with the viral genome and other viral proteins, including NSP3 and M, during assembly. The N protein of SARS-CoV-2 is preserved and shares approximately 90% sequence identity with that of SARS-CoV (Naqvi et al., 2020).

Several accessory genes, such as ORF3a, ORF3b, ORF6, ORF7a, ORF7b, ORF8b, ORF9b, and ORF14 encodes for 9 accessory protein, which are located between the structural genes. These proteins are involved in the regulation of viral infection, although they may not be incorporated in the virion, except for ORF3a and ORF7a (Yang et al.2021; Bai et al., 2021).

1.2.3 Sars-CoV-2 life cycle

The SARS-CoV-2 spike protein's receptor-binding domain (RBD) binds with high affinity to angiotensin-converting enzyme 2 (ACE2) *(Figure 2)*, a transmembrane glycoprotein that is expressed at high levels in various species, including humans, ferrets, cats, and bats, as well as in several organs such as the lungs, heart, intestines, and kidneys (Andersen et al., 2020; Neerukonda et al., 2020; Hoffmann et al., 2020).

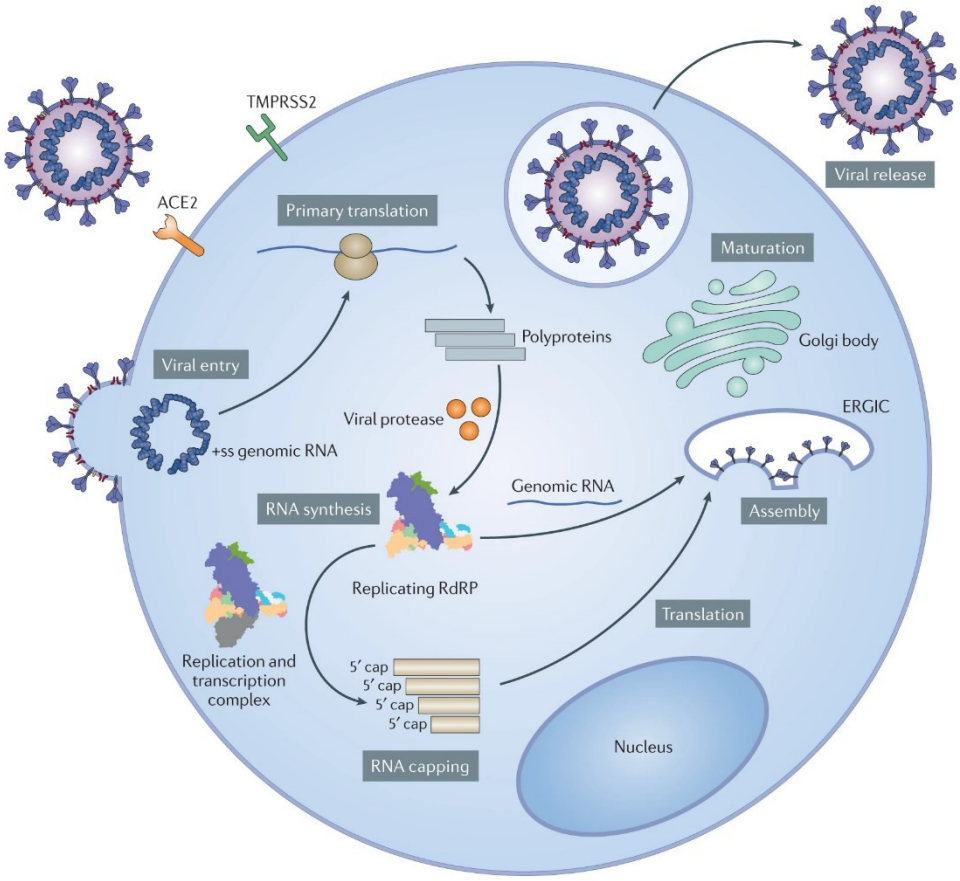

Figure 2 SARS-CoV-2 life cycle adapted by Yang et al., 2021

As mentioned above *(1.2 Sars-CoV-2 genome organization)* both spike monomers presents two functional regions: the largely exposed S1 subunit (residues 1–686), which is primarily involved in receptor binding, and the partially covered S2 subunit (residues 687–1,273), which facilitates membrane fusion (Walls et al., 2020). The RBD in the S1 region undergoes a conformational change, alternating between the closed/down and the open/up states *(Figure 3)*.

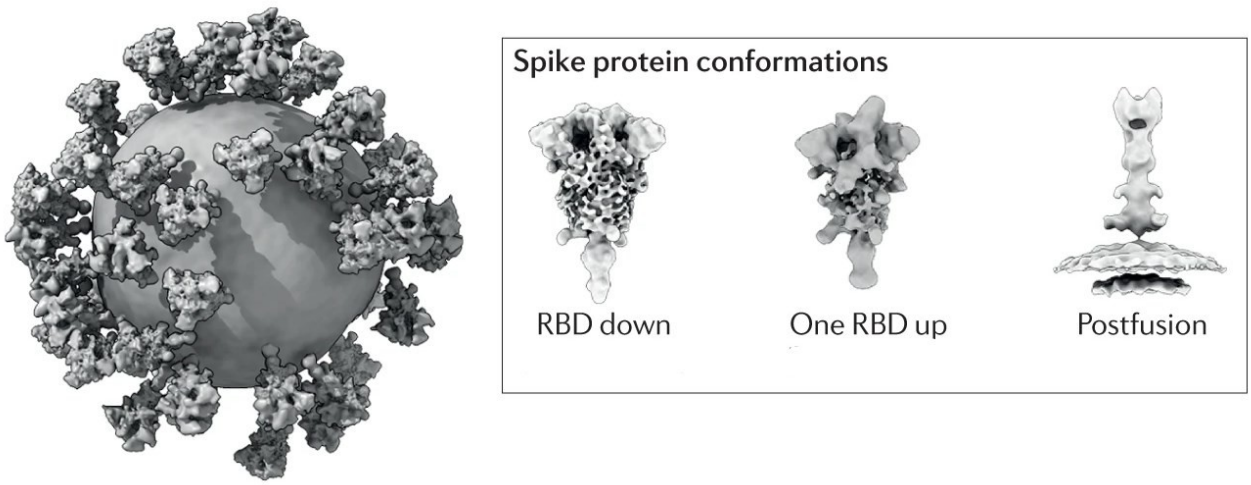

Figure 3 Close/down vs open/up states, adapted from Yang et al., 2021

In its open conformation, the RBD binds to ACE2, the crucial first step for viral entry into host cells (Wrapp et al., 2020; Lan et al., 2020). Residues 438–506 define the receptor-binding motif (RBM), the portion of the spike that directly bind ACE2, while the remaining residues constitutes the RBD core. Within the S1 subunit, two domains located downstream of the RBD are referred as the S1 carboxy-terminal domains (CTDs).

Upon binding with the ACE2 receptor, the spike protein undergoes proteolytic activation, a prerequisite for membrane fusion. This cleavage is facilitated by a host serine protease, TMPRSS2, that is localized on epithelial cell surfaces, particularly in the respiratory tract. TMPRSS2-facilitated cleavage is a critical step in the viral life cycle (Hoffmann et al., 2020; V'kovski et al., 2020). However, in the absence of TMPRSS2-expressing cells, SARS-CoV-2 can use an alternative entry mechanism. After binding to ACE2, the virus can enter host cells by clathrin-mediated endocytosis, where activation is facilitated by cathepsins in endosomal vesicles (Bayati et al., 2021). Following cell entry, the viral RNA genome is released in the cytoplasm and translated. The NSPs assemble into the RTC, which generates negative-strand RNA intermediates that serve as templates for the production of positive-sense genomic and sub-genomic RNAs. This process is facilitated by the NSP-driven remodeling of the rough endoplasmic reticulum (ER) membrane into specialized replication compartments. Subsequently, sub-genomic RNAs are used for the synthesis of structural proteins, which are integrated into the ER and secreted through the secretory route to the ER-Golgi intermediate compartment. There, the newly synthesized viral genome is encapsulated with the nucleocapsid (N) protein and, together with the other structural proteins, are encapsulated into mature virions which are transported to the cell surface in vesicles and released into extracellular space by exocytosis (Hoffmann et al., 2020; V'kovski et al., 2020; Jackson et al., 2020; Tebha et al., 2024).

1.3 SARS-CoV-2 Transmission

The respiratory route has been established as the most significant and efficient mode of SARS-CoV-2 transmission, with the pathogen being spread on respiratory droplets or aerosols emitted by an infected subject and inhaled by people in proximity. While early in the pandemic there was concern about fomite transmission, such as disease transmission indirectly through contaminated surfaces, current evidence indicates that this route plays only a minimal role in SARS-CoV-2 spread. Although SARS-CoV-2 can remain viable for several hours on surfaces under laboratory conditions, recovery of replication-competent virus from real-word environments is rare and occurs only at very low levels. For this reason, aerosol transmission, particularly in the close range, is now globally accepted as the primary route of SARS-CoV-2. The risk is greatest with short-range aerosols since they contain a higher concentration of viral particles, and, moreover, aerosol concentrations dissipate rapidly for long distances (*Figure 4*),

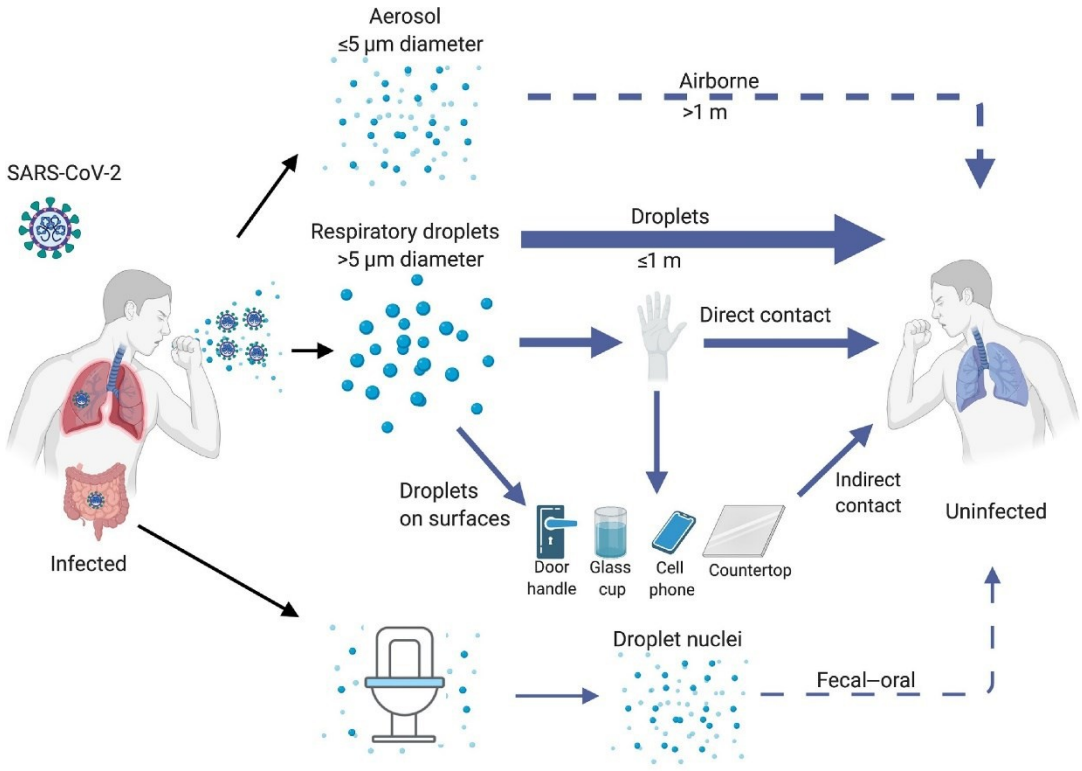

Figure 4 Mechanisms of SARS-CoV-2 Transmission (Harrison et al., 2020)

which results in decreased transmission. Notably, in hospitals, there have been some well-documented cases that have confirmed human-to-human transmission over distances that exceed 1.8 meters. Indeed, transmission events at larger ranges are more likely to happen in poorly ventilated rooms or where air flow patterns carry contaminated air from the infected patient to others (Meyerowitz et al., 2022). Other transmission routes such as sexual, fecal–oral, and bloodborne have been suggested but they are not yet documented. Mother-to-child

vertical transmission of SARS-CoV-2 appears to be rare. While some studies have reported SARS-CoV-2-specific IgM antibodies in neonates, the results must be interpreted cautiously because the IgM test is subject to false positives, especially in the context of systemic inflammation. In addition, certain neonates have also been detected positive by polymerase chain reaction (PCR) at birth, increasing the probability of exposure in the perinatal period. Infrequent case reports have also revealed SARS-CoV-2 placental infection, providing further, even if limited, evidence of possible in utero transmission. In addition, viral RNA has also been detected in breast milk, although so far, no cases of SARS-CoV-2 transmission to infants from breastfeeding have been established (Meyerowitz et al., 2021).

1.4 Clinical manifestations and pathogenesis

Patients with COVID-19 may experience a wide spectrum of symptoms, ranging from none or flu-like illness to severe complications such as acute respiratory distress syndrome (ARDS). Indeed, COVID-19 can be classified as mild, moderate, or severe depending on disease severity. Symptoms onsets occur 2-14 days (*Figure 5*) after SARS-CoV-2 infection, averaging approximately 5 days. The acute phase of COVID-19 usually lasts until 2-3 weeks from the beginning of symptoms (Rana et al., 2021). Severity of COVID-19 can be characterized by several factors: the viral load, genetic factors, existence of underlying diseases, age, sex, use of immunosuppressants, and immunity. Comorbidities such as cardiovascular disease, kidney damage, liver dysfunction, diabetes, Parkinson's disease, and cancer can be associated with a poor prognosis.

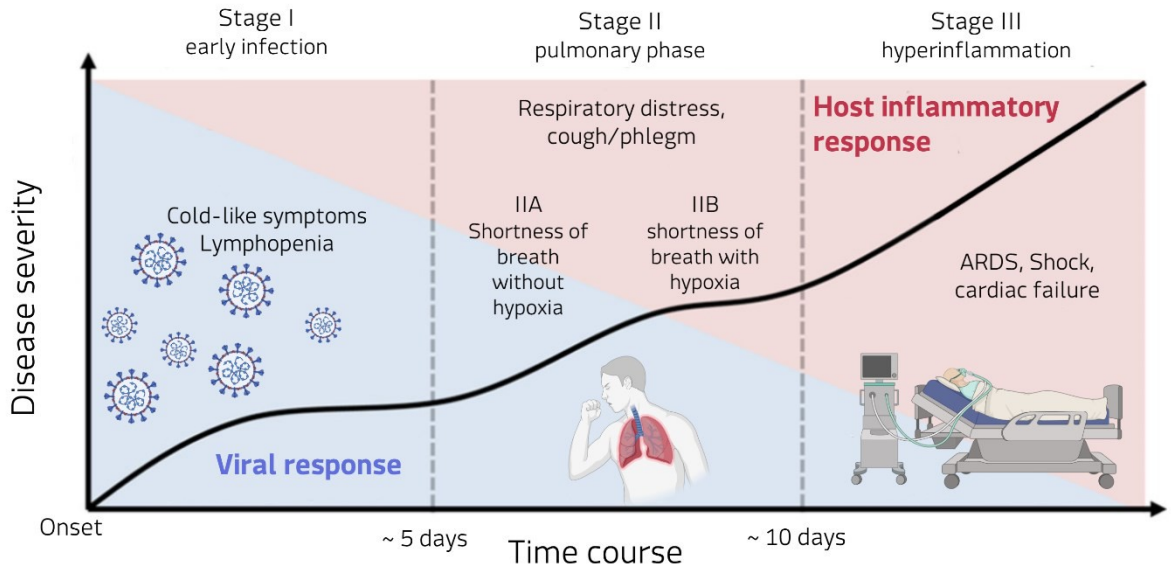

Figure 5 Disease progression, created in https://BioRender.com

Generally, mild COVID-19 is characterized mainly by myalgia, cough and mild fever. Patients with the moderate form of the disease may exhibit mild pneumonia, whereas typical symptoms of severe COVID-19 are severe pneumonia and hypoxemia, leading to complications such as ARDS, systemic inflammatory response syndrome, multiorgan failure and/or shock (Rana et al., 2021; Xie et al., 2023). SARS-CoV-2 can infect monocytes, macrophages, dendritic cells, and lymphocytes which play an important role in the development of cytokine storms. In COVID-19 a massive release of cytokines (prevalently IL-6) causes an increase in the leukocyte's recruitment to multiple body organs, especially in the lung, leading to ARDS. This life-threatening lung condition reduces the oxygen efflux from the alveoli to the blood leading to the use of mechanical ventilators (Machhi et al., 2020). Consequently, the most common causes of death are ARDS, severe viral pneumonia, and multiple organ failure (Xie et al., 2023). Notably, the severity of pulmonary manifestations can be influenced by several factors. Elderly individuals appear to exhibit higher ACE2 expressions in the lungs. Moreover, ACE2 expression is elevated in adipose tissue, making obesity, frequently associated with comorbidities such as hypertension and diabetes, an important risk factor (Xie et al., 2023).

COVID-19 infection can also be characterized by extrapulmonary manifestations *(Figure 6),* including cardiovascular disease, gastrointestinal disease, nervous system disorders, skin and eye conditions.

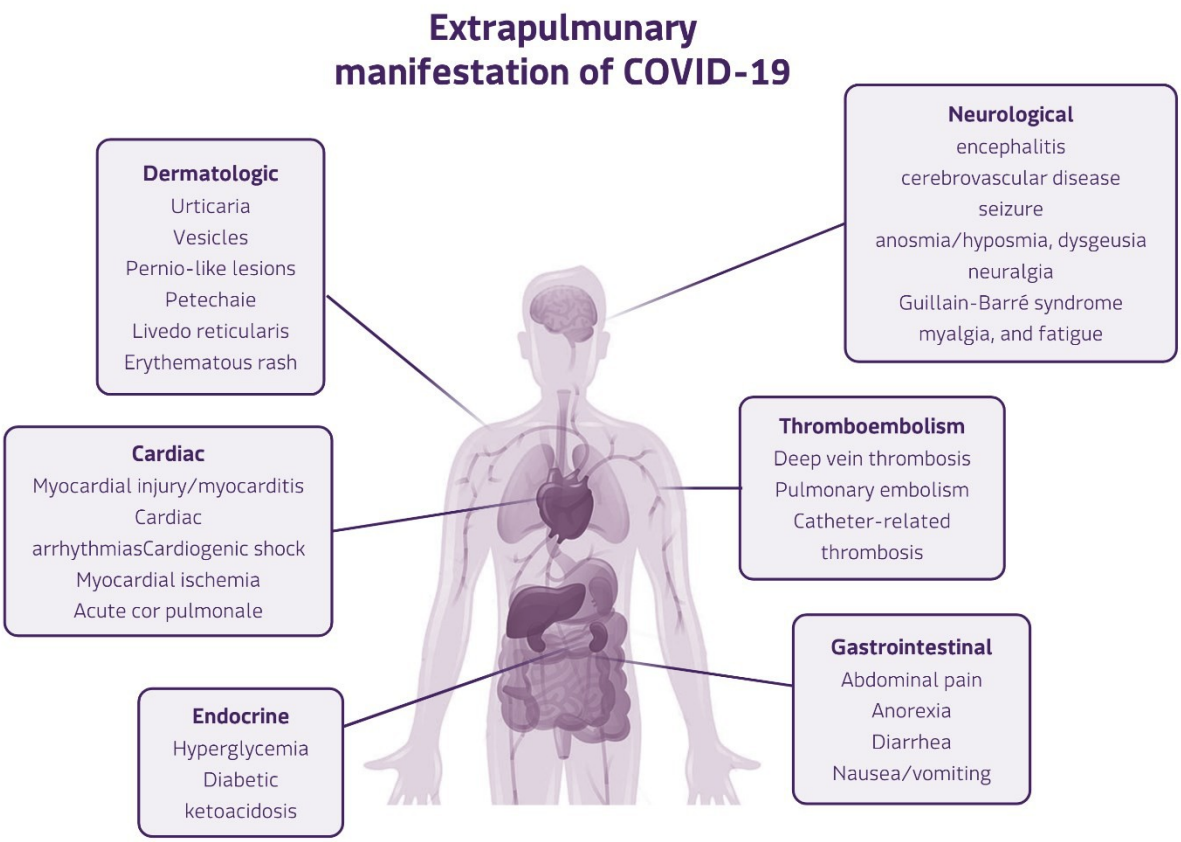

Figura 6 Extrapulmunary manifestation of COVID-19, created in https://BioRender.com

Cardiovascular involvement in COVID-19 can arise through two main mechanisms that lead to cardiac manifestations: the direct effect of SARS-CoV-2 on ACE-2 receptor in cardiac tissue, and the cytokine storm that can cause heart failure. In the first mechanism, the virus can bind ACE-2 receptors on cardiomyocytes, leading to the degeneration of heart system or to inflammatory storms. This may result in arrhythmia, hypertension, palpitation, myocardial damage, and heart failure (Xie et al., 2023). Regarding the nervous system, ACE-2 receptors are highly expressed both in the central nervous system (CNS) and in the peripheral nervous system (PNS). SARS-CoV-2 can infect neurons and glial cells, such as astrocyte and microglia, triggering the innate immune response. Neurological manifestations of SARS-CoV-2 infection have been classified into three groups:

1) CNS involvement (headache, altered consciousness, encephalitis, cerebrovascular disease, seizures, and ataxia);
2) peripheral nervous system involvement (anosmia/hyposmia, dysgeusia, visual alterations, neuralgia, and Guillain-Barré syndrome);
3) musculoskeletal involvement myalgia, and fatigue (Cárdenas et al, 2022).

In the digestive tract, recent studies suggest that SARS-CoV-2 could cause gastroenteritis by replicating it in human enterocytes. The direct effect of SARS-CoV-2 viral overload on esophageal epithelial cells and ACE-2 receptors in the mucous layer of the stomach and small intestines can lead to gastrointestinal (GI) manifestations such as diarrhea, vomiting, nausea, and abdominal pain. (Durairajan et al., 2023; Xie et al., 2022). Furthermore, the detection of SARS-CoV-2 RNA in feces provides additional evidence that the virus may replicate within the epithelial cells of the GI tract. SARS-CoV-2 infection also affects the permeability of the intestinal membrane, resulting in enterocyte dysfunction. Consequently, patients often display elevated levels of calprotectin, a biomarker released by neutrophils during gastrointestinal inflammation, along with increased serum IL-6 levels. (Durairajan et al., 2023).

Skin manifestations in COVID-19 patients primarily include rash and erythema, which are more frequently seen in mild and moderate patients and may precede respiratory symptoms. SARS-CoV-2 can also reach the eyes either through direct contact with infected secretions or via the bloodstream, binding to ACE2 receptors found on the conjunctiva and cornea, leading, in some patients, to eye redness, foreign body sensation, or conjunctivitis (Xie et al., 2022).

1.5 SARS-CoV-2 Persistence and Long-COVID

In addition to the acute clinical syndrome of COVID-19, SARS-CoV-2 can lead to a chronic condition called long-COVID, which consists of persistent and often debilitating symptoms lasting for 3 months or more after acute infection. Although the term long COVID was adopted by public health bodies in USA, WHO uses the term post-COVID condition (PCC), and the UK National Institute for Health and Clinical Excellence uses ongoing symptomatic COVID-19 and

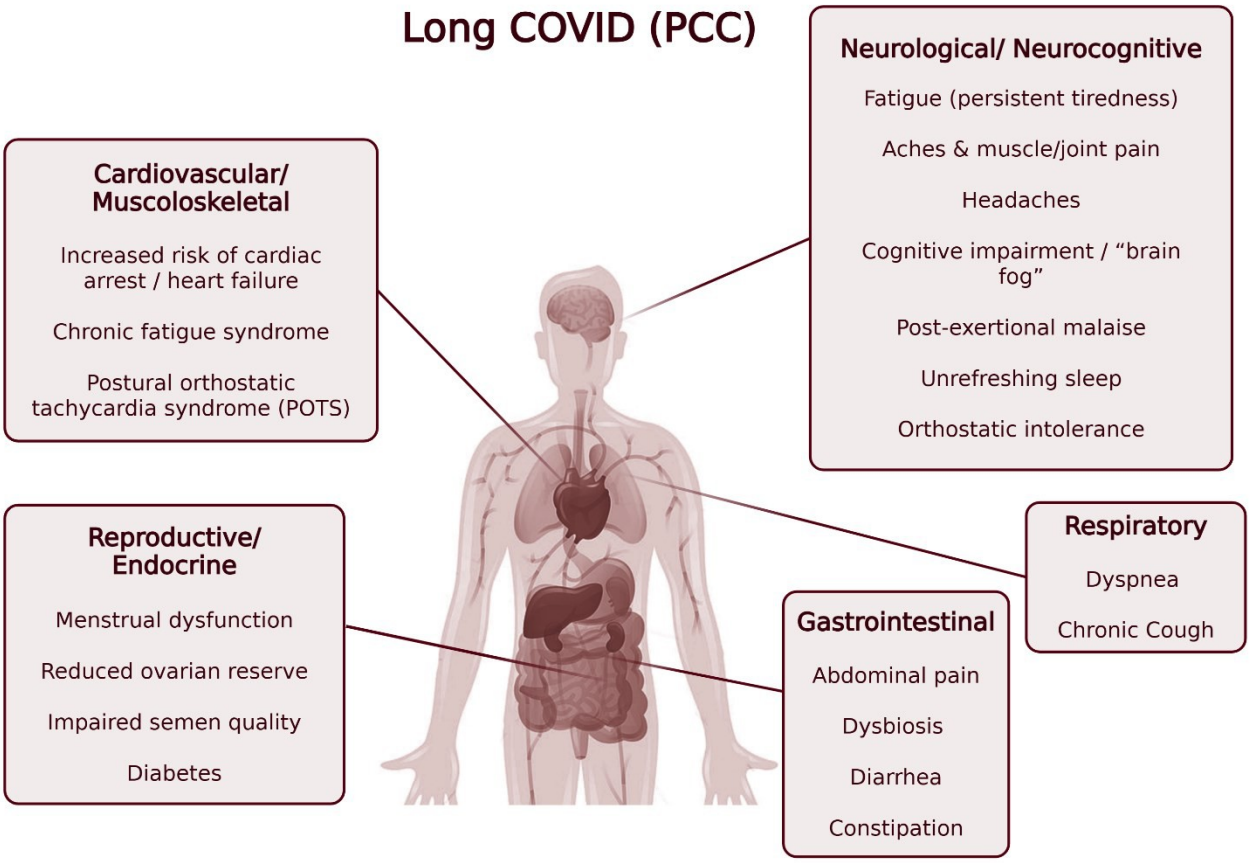

Figure 7. Long COVID manifestations, created in https://BioRender.com

post-COVID-19 syndrome (Greenhalgh et al.,2024). Epidemiological studies indicate that 6 in 100 COVID-19 patients develop PCC, with most of the evidence coming from individuals infected during the first two years of the pandemic (www.who.int). The main manifestations of PCC are fatigue, aches and muscle pain or joints, feeling breathless, headaches, difficulty in thinking or concentrating and alterations in taste. These symptoms range from mild to severe and can affect the capacity to work and perform daily activities. In addition, PCC has been associated with a wide range of systemic presentations (*Figure 7*), including the cardiovascular system (increased risk of cardiac arrest and heart failure), endocrinal system (diabetes), musculoskeletal system (chronic fatigue syndrome and postural orthostatic tachycardia syndrome, POTS). Neurocognitive dysfunction closely resembles myalgic encephalomyelitis/chronic fatigue syndrome (ME/CFS), and is characterized by persistent fatigue, post-exertional malaise, unrefreshing sleep, cognitive impairment ("brain fog"), and orthostatic intolerance for at least six months. PCC has been also linked to immune dysregulation (reduced NK cell activity, T-cell exhaustion), vascular dysfunctions and viral reactivation (EBV, HHV-6/7and CMV). Additional associated conditions include mast cell activation syndrome, connective tissue disorders, and endometriosis. There are also reported

reproductive abnormalities as menstrual dysfunction, reduced ovarian reserve, and impaired semen quality in males. Respiratory symptoms, such as chronic cough and dyspnea, are associated with airway epithelial damage, whereas gastrointestinal manifestations may present as nausea, constipation, abdominal pain, and dysbiosis particularly with reduced abundance of butyrate-producing bacteria (www.who.int; Zaidi & Dehgani-Mobaraki, 2024). While numerous biological mechanisms are under consideration, increasing evidence suggests that SARS-CoV-2 persistence contributes to PCC through the formation of tissue-based viral reservoirs which sustain inflammation, impair immune responses, and disrupt cellular function, even though infection was initially expected to be transient in immuno-competent patients. In support of this, single- or double-stranded viral RNA or proteins have been detected weeks after the acute infection in multiple tissues such as the gut, or in host cells such as platelets and megakaryocytes. Immune responses, suggesting persistent viral antigen stimulation, have also been described. Some reports have detected SARS-CoV-2 proteins in plasma up to 14 months after infection, indicating the release from tissue reservoirs into circulation (Proal et al., 2024). Moreover, autopsy studies have found viral RNA or protein in tissues such as the brain, nerves, and eyes, months after the infection onset. Evidence suggests that reservoir formation could begin during acute infection and could be influenced by both host and viral factors, with immune system failure to completely eliminate the virus being one of the main causes of reservoir persistence. Additionally, higher initial viral loads, extended viral shedding, and severe acute illness have all been associated with subsequent PCC (Stein et al., 2022; Lu et al., 2024). As shown in *Figure 8*, once established, the viral reservoir can be maintained by several mechanisms: viral RNA may persist without producing new virions, may be translated to elicit immune responses, or may replicate slowly or sporadically, infecting additional cells leading to the fluctuating symptoms of long COVID. Antivirals offer a direct approach to target the viral reservoir by inhibiting specific steps in the replication cycle and preventing the generation of new virions. Agents like nirmatrelvir–ritonavir and remdesivir are being studied in long-COVID trials. Monoclonal antibodies (mAbs) are also promising, as they not only neutralize replicating viruses but can also mediate elimination of viral proteins (Proal et al., 2024).

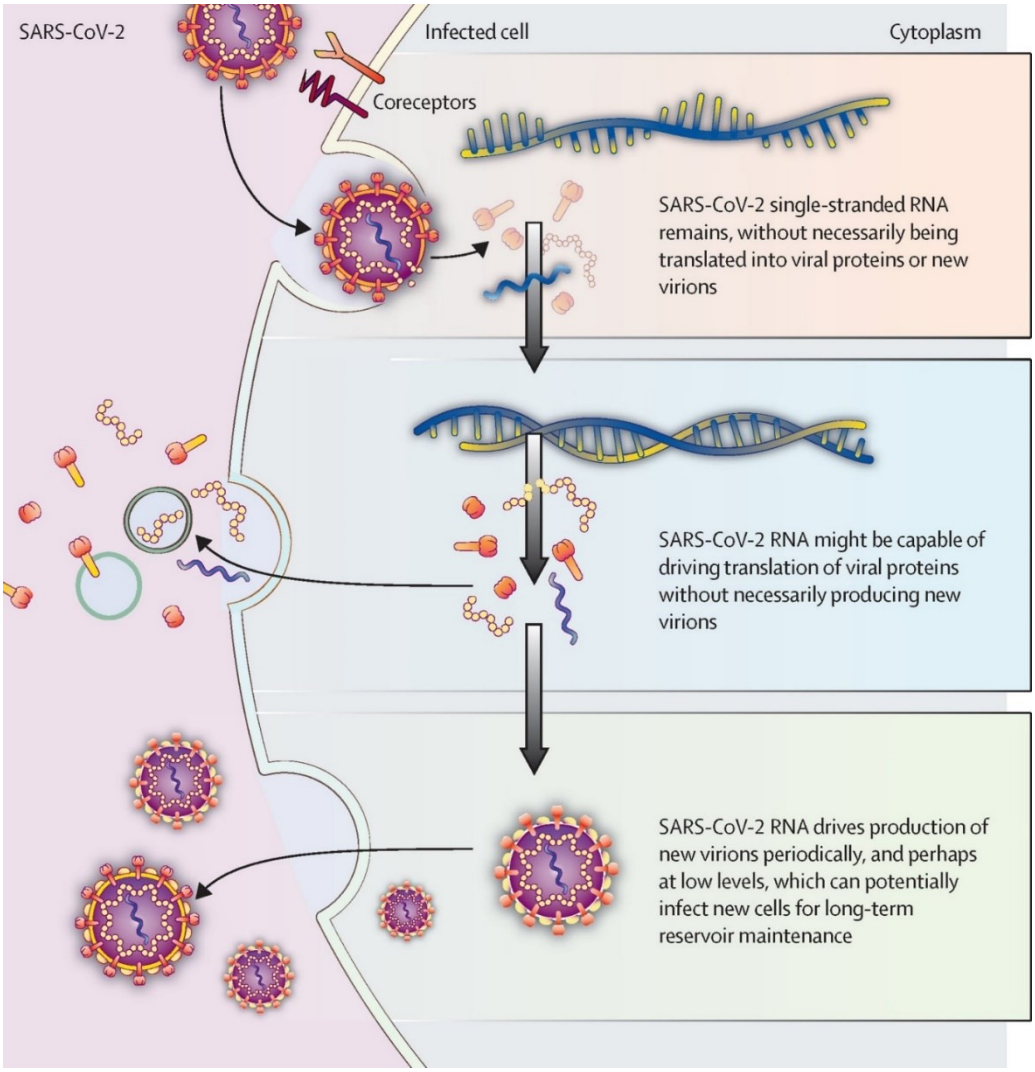

Figure 8. SARS-CoV-2 reservoir in long COVID (Proal et al., 2024)

1.6 SARS-CoV-2 evolution

During replication in host cells, viruses accumulate mutations at a high rate, which may provide evolutionary advantages under selective pressures such as antiviral drugs, immune responses, or increased transmissibility (Tao et al., 2021). In SARS-CoV-2, the combination of a broad host range, recombination capacity, and widespread circulation has further promoted the emergence of new variants, many of which carry adaptive mutations in the spike protein (Vega et al., 2022). Consequently, since the beginning of the pandemic, the virus's mutational ability was linked to an increased global public health risk, leading to the definition of a variant as a viral genome with one or more non-synonymous mutations in the spike region as compared to the Wuhan-Hu-1 reference ancestral genome. Indeed, the emergence of variants at the end of 2020 prompted the WHO to adopt Greek letters to classify them into Variants of Interest (VOIs) and Variants of Concern (VOCs), aiming to prioritize global surveillance and research

(www.who.int). Greek letters have been conserved for VOCs until March 2023, while VOIs have been designated by validated scientific nomenclature such as Nextstrain and Pango (e.g., XBB.1.5/23A for the latest VOI). Additionally, the Variant Under Monitoring (VUM) category was introduced to identify variants with genetic changes suspected to affect viral characteristics and with preliminary evidence of a growth advantage over other circulating variants (ww.who.int). Current VUMs and VOI are listed in *tables 1 and 2*. Although SARS-CoV-2 continues to evolve in multiple variants, it is known to have a lower mutation rate compared to most other RNA viruses (Tao et al., 2021). This feature is mainly due to its large genome and to the presence of proofreading exonuclease ExoN, which removes mis-incorporated nucleotides during transcription, thereby limiting replication errors. Indeed, coronavirus exonucleases have

Pango lineage	Next strain clade	Genetic features	Earliest documented samples	Date of designation and risk assessments
JN.1*	24A	BA.2.86 + S:L455S	25-08-2023	18-12-2023 JN.1 Initial Risk Evaluation 18 December 2023 JN.1 Updated Risk Evaluation 9 February 2024 JN.1 Updated Risk Evaluation 15 April 2024

*Table 1. Currently circulating variants of interest (VOIs) (as of 2 December 2024) * Excludes JN.1 sublineages listed as VUMs. Adapted from www.who.int*

been shown to decrease replication errors by 15–20-fold in vitro, providing a mutation rate approximately 10-fold lower than the influenza virus in vivo (Tao et al., 2021).

Pango lineage	Next strain clade	Genetic features	Earliest documented samples	Date of designation and risk assessments
KP.3.1.1	24E	KP.3 + S:S31-	27-03-2024	19-07-2024
XEC	24F	JN.1 + S:T22N, S:F59S, S:F456L, S:Q493E, S:V1104L	26-06-2024	24-09-2024 XEC Initial Risk Evaluation 09 December 2024
LP.8.1	25A	JN1 + S:S31-, S:F186L, S:R190S, S:R346T, S:V445R, S:F456L, S:Q493E, S:K1086R, S:V1104L	01-07-2024	24-01-2025 LP.8.1 Initial Risk Evaluation 03 February 2025
NB.1.8.1	25B	JN1 + S:T22N, S:F59S, S:G184S,S:A435S, S:F456L, S:T478I, S:Q493E	22-01-2025	23-05-2025 NB.1.8.1 Initial Risk Evaluation 23 May 2025
XFG	25C	JN1 + S:T22N, S:S31P, S:K182R, S:R190S, S:R346T, S:K444R, S:V445R, S:F456L, S:N487D, S:Q493E, S:T572I	27-01-2025	25-06-2025 XFG Initial Risk Evaluation 25 June 2025

Table 2. Currently circulating variants under monitoring (VUMs) (as of 4 september 2025). Adapted from www.who.int

Despite this proofreading capability, SARS-CoV-2 still evolves into multiple variants because ExoN's activity, by decreasing the error rate, is able to increase the propensity of viral recombination when variant with different mutations infect the same host (Gribble et al., 2021; Tao et al., 2021). Moreover, there are several additional mechanisms that contribute to the accumulation of mutations: (i) RNA editing by host APOBEC and ADAR enzymes (Tao et al., 2021), (ii) insertions and deletions evading ExoN proofreading, and (iii) the extremely large pandemic population size and prolonged duration of the pandemic (Tao et al., 2020; Saramago et al., 2021; www.who.int). Together, these processes drive SARS-CoV-2 antigenic drift,

particularly in viral regions recognized by the immune system, such as the spike-encoding region, thereby contributing to the failure to establish long-term immunity after infections.

The first major Spike protein mutation, D614G, was detected in January 2020. This substitution likely emerged to stabilize the protein, possibly linked to the acquisition of the novel furin-cleavage site. Indeed, both the furin-cleavage site and the D614G mutation were conserved throughout the pandemic, demonstrating their critical role in transmission and infectivity (Chen et al., 2025). After nearly two years of viral evolution, the first Omicron variant emerged at the end of 2021, exhibiting increased transmissibility and immune evasion compared to the Delta variant, becoming the fifth and last so called global VOC. During 2022, Omicron B.1.1.529 evolved in a plethora of sublineages, from BA.1 to BA.5, as well as recombinant lineages such as the XBB, which then dominated the first half of 2023. Afterwards, toward the end of 2023, JN.1 (BA.2.86.1.1), derived from BA.2.86, became the dominant strain. This lineage gained an unprecedented number of mutations: it has more than 70 additional mutations in the spike protein compared to Wuhan-Hu-1 strain. In 2024 new lineages including KP.3, LB.1, and KP.3.1.1 emerged, with KP.3.1.1 spreading mostly starting from September 2024, being classified as VUM. While most variants increased receptor-binding affinity via mutation in the RBD, JN.1 showed reduced ACE2 affinity compared to BA.2.86, likely due to the L455S amino acid substitution. Interestingly, the Q493E mutation of KP.3 alone decreased ACE2 binding affinity, but, when combined with L455S and F456L substitutions, ACE2 affinity was restored to high levels (Chen et al., 2025). These observations highlight the adaptive strategy of the most recent SARS-CoV-2 Omicron variants: balancing reduced receptor binding to evade antibodies neutralization with 'compensatory' mutations that restore or enhance binding affinity. In addition to the modulation of the receptor affinity, mutations in the spike protein can alter viral fusogenicity, another key determinant of infectivity. Earlier Omicron subvariants such as BA.1 and BA.2 could not form cell syncytia and appeared to rely more on endocytosis to enter host cells, possibly due to an altered furin cleavage site. In line with this, the JN.1 subvariant shows reduced pathogenicity in animal models and lower disease severity in humans (Chen et al., 2025). As SARS-CoV-2 continues to evolve under selective pressures, new variants with advantageous mutations in the N-terminal domain (NTD) have emerged; for example, KP.3.1.1 and XEC recently became dominant, carrying unique NTD changes such as Ser31del, Thr22Asn, and Phe59Ser. JN.1 sublineages such as LP.8.1 are now replacing them due to growth advantages. Particularly, the emergence of KP.3.1.1 and XEC compromised ACE2

binding strength affecting their fitness but enhancing their immune evasion ability. In contrast, LP.8.1 was able to preserve ACE2 binding as KP.3, while obtaining immune evasion capabilities

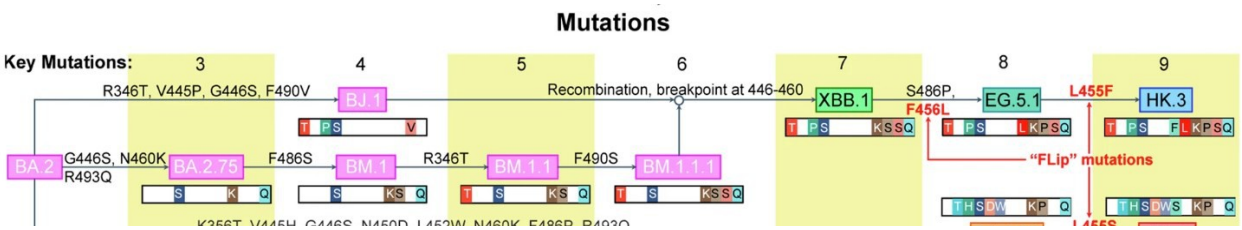

Figure 9 SARS-CoV-2 variants and main mutations (Liu et al., 2025)

similarly to XEC. These characteristics highlight the trade-off between immune evasion and ACE2 binding strength, demonstrating the importance of monitoring the currently circulating LP.8.1 variant *(Figure 9)* (Liu et al.,2025). Overall, the first omicron variant that appeared in 2021 and its progeny are characterized by high immune escape ability, reduced pathogenicity, and elevated transmissibility. The continuous re-emergence of lineages such as BA.2.86, JN.1, KP.3.1.1, and LP.8.1 emphasize the adaptive nature of the virus, further supporting the need for global surveillance of SARS-CoV-2 spread and evolution (Liu et al., 2024; Kaku et al,2024).

1.7 Current measure to counteract COVID-19: monoclonal antibodies, vaccines and antivirals.

Since its emergence in 2020, COVID-19 has prompted extensive research and the development of multiple therapeutic options and vaccines. However, their efficacy has been challenged by ongoing viral evolution, leaving the optimal treatment and protection strategies for high-risk patients uncertain.

1.7.1 Monoclonal Antibodies

Monoclonal antibodies (mAbs) are recombinant proteins that can be obtained from B cells of convalescent patients or from humanized mice exposed to SARS-CoV-2 antigens. These antibodies exert their activity by neutralizing the virus and preventing its entry into host cells (Taylor et al., 2021, www.ema.europa.eu). During the first 2 years of the pandemic, FDA (Food and Drug Administration) authorized emergency use of multiple mAbs such as bamlanivimab, etesevimab, casirivimab, imdevimab, sotrovimab, tixagevimab, and cilgavimab. However, since the emergence of Omicron variant, none of them have been effective for hospitalized people with COVID-19 due to the high number of mutations in the spike protein, and consequently their emergency use authorization has been progressively revoked (Focosi et al., 2024, Iketani et al., 2022). Indeed, the main issue with mAbs against SARS-CoV-2 is that

ongoing mutations acquisition in the Spike glycoprotein leads to immune evasion, resulting in their reduced efficacy. Administering more than one mAb together was an initially promising strategy; however, this approach quickly became ineffective with the advent of Delta VOC and remained ineffective against subsequent Omicron VOCs (Focosi et al., 2024). As a result, all SARS-CoV-2 mAbs have had their authorizations withdrawn.

Evolution of Monoclonal Antibody Therapy during the COVID-19 Pandemic

Two of the first produced mAbs were casirivimab and imdevimab, which were obtained from humanized mice and convalescent patients. They were designed to target different regions of the SARS-CoV-2 spike protein simultaneously, providing enhanced resistance over individual antibodies. Initial in vitro studies and clinical use were successful for treatment and post-exposure prophylaxis until the emergence of the BA.1 (Omicron) variant: some mutations of the spike protein, S371L and Q493R for casirivimab and S371L, N440K, and G446S for imdevimab, made the combination ineffective. Subsequent Omicron sublineages, such as BA.2 and BA.4/5, had preserved or even boosted these resistance mutations, which ultimately led to the withdrawal of the approval of the antibodies (Iketani et al., 2024).

This also occurred with bamlanivimab and etesevimab, which were obtained from convalescent patients. Both were originally approved for treatment and post-exposure prophylaxis, but these antibodies lost efficacy against BA.1 due to the E484A and Q493R mutations for bamlanivimab, and S371L, K417N, Q493R, N501Y, and N856K for etesevimab. For this reason, similarly to casirivimab/imdevimab the authorization was revoked (Iketani et al., 2024).

Sotrovimab, isolated from a SARS-CoV-infected patient in 2003, was an exception in that, as it initially retained a partially activity against BA.1. However, resistance emerged in BA.2 with the S371F mutation. This reduction in effectiveness led to the revocation of its emergency use authorization, despite vivo testing suggesting that there may be some residual antiviral effect remaining, possibly due to immune effector mechanisms or reduced pathogenicity of Omicron (Iketani et al., 2024).

Tixagevimab and cilgavimab were initially effective for treatment and prophylaxis. Both antibodies were active until the emergence of BA.1, that acquired resistance-conferring mutations (S371L, E484A, Q493R for tixagevimab; G446S for cilgavimab). There was a partial recovery with BA.2 and BA.4/5 due to residual potency of cilgavimab, whereas tixagevimab was

inactive. Despite that, with the following sublineages BQ and XBB, there was the acquisition of further resistance mutations (R346T, K444T, V445P), leading to loss of efficacy of the combination (Iketani et al., 2024).

Bebtelovimab initially exhibited broad activity against all presently circulating SARS-CoV-2 variants, such as Omicron sublineages through BA.4/5, with modest reductions against BA.2.75. However, the later emergence of BQ and XBB sublineages made the antibody completely ineffective due to K444T and V445P mutations. The other monoclonal antibodies such as regdanvimab and amubarvimab/romlusevimab followed the same route, as they were all ineffective against BA.1 variant (Iketani et al., 2024).

Summing up, while mAbs initially presented a powerful tool against COVID-19, the rapid evolution of SARS-CoV-2, particularly with the emergence of Omicron and its sublineages, has introduced worldwide resistance, leading to the revocation of many authorizations (Iketani et al., 2024).

Despite that, most recently, the European Union's Committee for Medicinal Products for Human Use (CHMP) gave to Sipavibart, a new generation mAb designed to overcome this challenge, a positive opinion (Keam et al., 2025). Sipavibart has demonstrated broader neutralizing activity against historical as well as numerous recent SARS-CoV-2 variants, including XBB.1.5, XBB.1.16, XBB.2.3, and BA.2.86. On 20th January 2025, this mAb was approved in the EU for pre-exposure prophylaxis of COVID-19 in adults and adolescents aged ≥12 years and weighing ≥40 kg who are immunocompromised due to underlying medical conditions or immunosuppressive therapy (Keam et al., 2025). However, based on *in vitro* studies, Sipavibart is not active against JN.1 sublineages KP.1.1, LB.1, and KP.3.3, all of which carry the F456L mutation (Keam et al., 2025). Other RBD escape mutations, including T415I and K458E, were also associated with reduced susceptibility in vitro (Keam et al., 2025). In view of this, EMA (European Medicines Agency) advises healthcare professionals to check the current epidemiological situation in their region and avoid usage of Sipavibart when variants carrying the F456L mutation are prevalent (www.ema.europa.eu).

1.7.2 Antiviral drugs

Since the beginning of the pandemic, several new or repurposed therapeutics have been developed against SARS-CoV-2, targeting different steps of viral cycle, such as blocking viral entry or inhibiting viral replication. It is crucial that antivirals are administered during the early stage of infection, before the onset of cytokine storm, since immune hyperactivation induced by uncontrolled viral replication cannot be mitigated by them (Chavda et al., 2022). Currently the EMA and the Italian Medicines Agency (AIFA) list remdesivir (RDV) and nirmatrelvir/ritonavir (NRM/RTV) as the direct-acting antivirals (DAAs) approved for the treatment of COVID-19 (www.aifa.gov.it; www.ema.europa.eu). The U.S. Food and Drug Administration (FDA) has also approved molnupiravir (MNP) for the treatment of adults with mild-to-moderate COVID-19 who are at high risk of severe COVID-19 progression, including hospitalization or death (www.fda.gov). However, EMA refused the authorization of MNP in the European Union, as the Committee for Medicinal Products for Human Use (CHMP) concluded that clinical benefit was not convincingly demonstrated in adults at risk of severe COVID-19 and that the overall risk-benefit balance could not be established (ww.ema.europa.eu).

Molnupiravir

MNP is an orally administered prodrug (EIDD-28/MK4882) and its active form is a nucleoside analog β-d-N^4-hydroxycytidine (NHC, or EIDD-1931). It was originally developed at Emory University for the treatment of alphaviruses infections (such as Venezuelan equine encephalitis virus), but it is effective against a wide range of viruses such as influenza viruses and coronaviruses. MNP is converted into its active metabolite NHC, which acts as a pyrimidine analog for the RdRp, resulting in lethal mutagenesis for the virus (Focosi et al., 2024).

Remdesivir

RDV is an inhibitor of viral RNA polymerase (ww.ema.europa.eu). It is a repurposed drug, previously approved for the treatment of Ebola Virus infection, influenza viruses and multiple coronaviruses (Vicenti et al.,2021). It interferes with the production of viral RNA by targeting the viral RdRp, causing the early termination of the new RNA chain elongation. RDV itself is an inactive prodrug that must be metabolized within cells to produce remdesivir-triphosphate, the active metabolite, which is an adenosine analogue. As is well known, the ability of SARS-CoV-2 to rapidly mutate represents a major challenge for antiviral therapies. However, RDV appears to have a relatively high barrier to resistance, remaining active *in vitro* against all major SARS-

CoV-2 sublineages and VOCs (Focosi et al., 2024). RDV is approved for use in adults and children from 4 weeks of age and weighing at least 3 kg, who present pneumonia and/or are at increased risk of developing severe COVID-19. The drug is administered as a once-daily intravenous infusion:

- In patients with pneumonia requiring supplemental oxygen, the recommended treatment duration is at least 5 days, and up to a maximum of 10 days.
- In patients who do not require supplemental oxygen, therapy should be initiated within 7 days of symptom onset and continued for 3 days (ww.ema.europa.eu).

The most common adverse reactions to RDM are increased blood levels of liver enzymes and nausea. For this reason, current guidance recommends discontinuation of therapy if transaminases levels exceed 10 times the upper limit of normal, especially if accompanied by clinical symptoms of liver inflammation (Focosi et al., 2024; ww.ema.europa.eu).

Nirmatrelvir/Ritonavir

NRM is an inhibitor of the SARS-CoV-2 main protease (M_{pro}), also known as 3C-like protease ($3CL_{pro}$), a chymotrypsin-like cysteine protease essential for viral replication. To enhance its pharmacokinetics, NRM is co-administered with RTV, an inhibitor of CYP3A4 hat reduces NRM metabolism and, consequently, extends its plasma half-life (Focosi et al., 2024; ww.ema.europa.eu). Since the emergence of Omicron sublineages, SARS-CoV-2 M_{pro} has been subjected to mutations such as P132H. Importantly, these changes have not affected the catalytic site, and NRM/RTV has retained in vitro and in vivo efficacy against a broad range of Omicron sublineages including BA.1, BA.1.1, BA.2, BA.2.12.1, BA.4, BA.5, BA.2.75, BQ.1.1, and XBB. The most common side effects of NRM/RTV are dysgeusia, diarrhea, headache and vomiting. One of the major issues with this combination are drug/drug interactions: RTV can increase blood levels of many medications that are catabolized by CYP3A4 (anticoagulants, anticonvulsants, immunosuppressants, cyclosporine A). Moreover, co-administration with CYP34A inducers may reduce NRM or RTV plasma concentration, impairing their efficacy (Focosi et al., 2024). NRM/RTV is administered orally twice daily for 5 days. It should be initiated as soon as possible after diagnosis and within 5 days of symptom onset of (ww.ema.europa.eu). It is important to highlight that the administration of NRM/RTV has been associated with events of virological rebound (also reported for MNP), causing an increased potential of virus transmission and the reappearance of symptoms. A mechanism that is

thought to cause the virus rebound is the attenuation of the specific antibody and T-cell response caused by early NRM/RTV treatment (Focosi et al., 2024; ww.ema.europa.eu).

1.7.3 SARS-CoV-2 vaccines

Vaccines remain a cornerstone in the control of the COVID-19 pandemic, and enormous efforts have been dedicated to the development of anti-SARS-CoV-2 vaccines design to elicit robust antibody responses capable of blocking and neutralizing the virus. According to the WHO statistics, since the first COVID-19 vaccine was deployed on 22 July 2020, more than 13,64 billion vaccine doses has been administered worldwide (www.who.net, last access August 2025).

SARS-CoV-2 vaccine platforms can be broadly categorized into viral component-based and whole virus-based approaches. The first one includes protein subunits, virus-like particles, DNA-based vaccines, RNA-based vaccines, and both non-replicating and replicating viral vectors. Whole-virus-based vaccines, in contrast, include inactivated and live-attenuated vaccines. In this context, recombinant vaccines, containing only selected antigenic structures of the virus, have emerged as particularly advantageous. They reduce the risks associated with live-attenuated vaccines, while providing strong efficacy and safety profiles. Their role in decreasing the global burden of COVID-19 and other viral diseases has been highly promising, as confirmed by ongoing clinical and real words studies. Since the pandemic began, the vaccine landscape has evolved through distinct generational phases:

- First-generation vaccines (2020–2021): mRNA vaccines (e.g., BNT162b2, mRNA-1273) and adenoviral vector vaccines (e.g., ChAdOx1 nCoV-19, Ad26.COV2.S) formed the cornerstone of initial global immunization campaigns.
- Second-generation vaccines (2022–2023): protein subunit vaccines (e.g., NVX-CoV2373) were introduced, alongside bivalent mRNA boosters adapted to early Omicron lineages (BA.1, BA.4/BA.5).
- Third-generation vaccines (2023–2025): updated monovalent boosters targeting more recent variants of concern, including XBB.1.5 and JN.1, were deployed to restore protection against evolving strains.

A number of recombinant vaccine candidates have entered clinical trials, with some of them completing phase III studies and receiving regulatory approval from medical agencies for broader use (Yadav et al., 2023). Currently, five COVID-19 vaccines are authorized by EMA: the

protein subunit vaccines Bimervax and Nuvaxovid and the mRNA-based vaccines Comirnaty, Kostaive and Spikevax (ww.ema.europa.eu). Evaluating the duration of vaccine-induced protection against SARS-CoV-2 is particularly challenging due to the continuous emergence of immune-evading variants. During the pandemic, vaccination schedules were adapted according to infection peaks and the occurrence of reinfections caused by novel variants. Booster doses, essential to prevent waning immunity, are generally recommended for individuals at higher risk of reduced vaccine efficacy, such as immunocompromised patients (Chavda et al., 2022; Trilla et al.,2025). In most countries, vaccination strategies have evolved from the initial goal of universal vaccination to a more targeted approach, focusing on high-risk groups, who typically receive one or two booster doses per year. High-risk groups include:

- Individuals aged ≥60 years
- Patients with moderate or severe immunosuppression
- Patients with comorbidities or chronic diseases
- Pregnant women
- Resident of long-term care facilities
- Health care workers (HCWs) and long-term facility workers.

While this approach aims to maximize protection for vulnerable populations and adapt to the changing epidemiological landscape, an emerging concern is the decline in COVID-19 vaccination coverage. This trend may be attributed to several factors, including the perception of COVID-19 as a less severe disease and the reduced enforcement of vaccination recommendations by health authorities and healthcare professionals. Indeed, the percentage of the population receiving booster doses with updated vaccines has decreased with each successive season. In this context, it is crucial to adapt control and prevention strategies to the needs of vulnerable populations. This involves designing targeted vaccination programs and ensuring the allocation of adequate resources and funding for their effective implementation. For the 2024–2025 COVID-19 vaccination campaign, the WHO, EMA, and FDA have issued recommendations, highlighting the use of updated monovalent vaccines, containing antigens from the Omicron JN.1 or KP.2 variants, which are expected to provide enhanced protection compared to previous bivalent formulations (Trilla et al., 2025).

1.8 New strategies against SARS-CoV-2

1.8.1 Host-targeted antivirals (HTAs)

Recently, host-targeting antivirals (HTAs) have been investigated as a novel strategy for the treatment of viral infections. This class of antivirals is particularly interesting because, unlike DAAs that target viral proteins or factors, they act on host cell pathways. Moreover, since numerous viruses rely on similar host pathways, HTAs could offer a particularly promising broad-spectrum antiviral effect (He et al., 2024; Zheng et al., 2022). Although viruses may develop resistance to HTAs by adapting their replication to use alternative host pathways, HTAs still have a higher genetic barrier compared to DAAs, as mutations conferring resistance in host cell genes are extremely rare and usually limited to germline variations or tumor cells. In addition, HTAs and DAAs can be combined to simultaneously target both viral components and

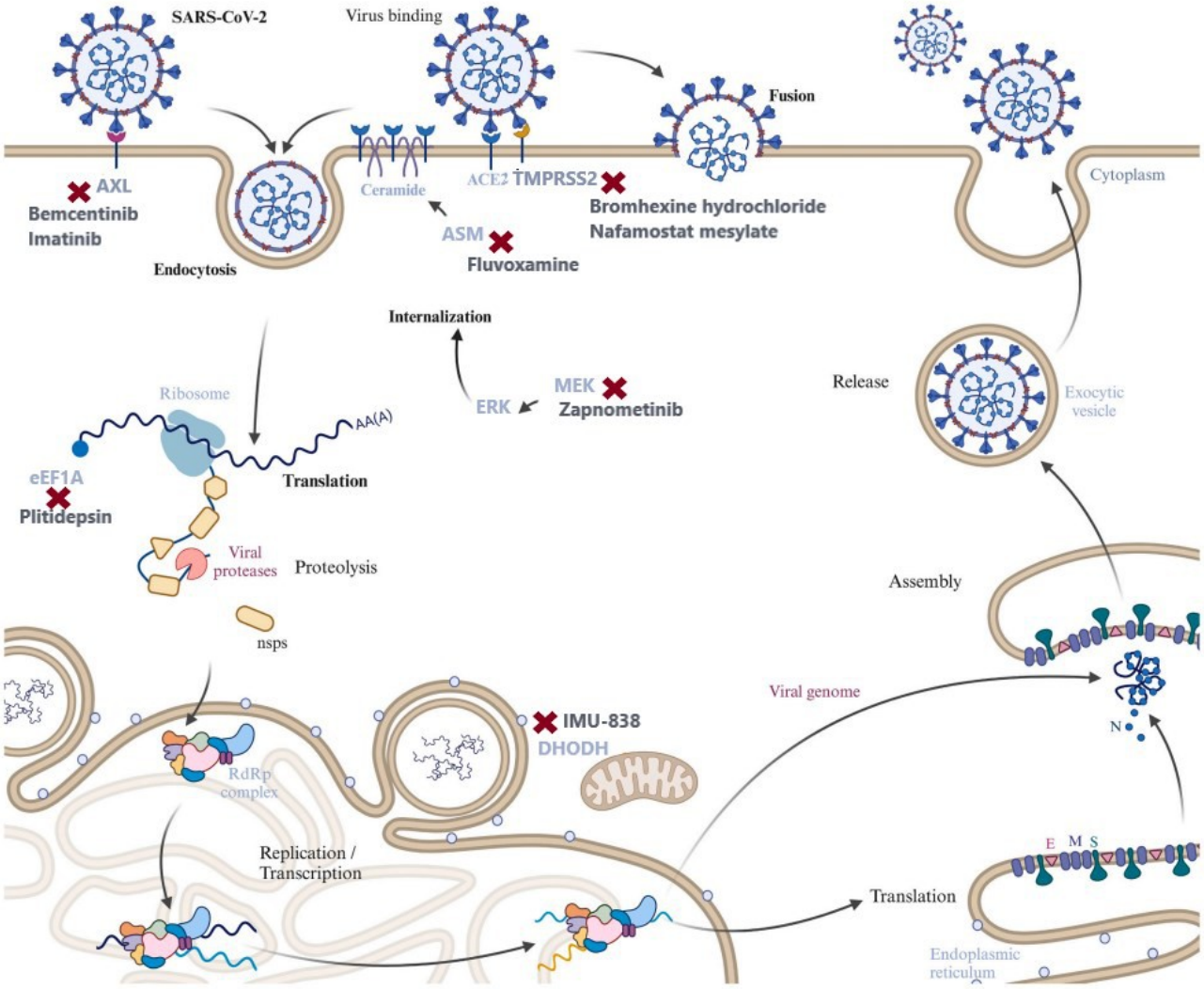

Figure 9 Mode of action of host-targeted small molecule inhibitors against SARS-CoV-2 in clinical trials.

host factors, thereby enhancing antiviral activity and increasing the barrier to resistance.

However, despite their high genetic barrier and potential combinatorial activity with DAAs, HTAs may still present some limitations that should be considered, including cytotoxicity, off-target effects, and regulatory barriers (Schreiber et al., 2024). Even so, given that is a recent area of research, several HTAs are currently being developed or repurposed for a better understanding of their effects. Here, we will discuss some examples of HTAs and their mechanisms of action.

Imatinib and Bemcentinib are both AXL kinase inhibitors able to prevent viral entry, as SARS-CoV2 can avoid canonical ACE2 pathway by using the AXL receptor as an alternative route. In particular, Imatinib could be an interesting option as it is a repurposed drug previously used in myeloid leukemia, and its toxicity and safety profile is already well documented (Wang et al., 2021).

Bromhexine hydrochloride is another repurposed drug, traditionally used as a mucolytic agent with a well-established safety profile. Beyond its classical mechanism of action, it can also inhibit TMPRSS2, which, as previously described, is crucial for viral entry. Another TMPRSS2 inhibitor is Nafamostat Mesylate, although clinical results regarding this drug have been inconsistent (Schreiber et al., 2024).

Continuing with the idea of adapting existing drugs against SARS-CoV-2 infection, another agent is Fluvoxamine, a selective serotonin reuptake Inhibitor (SSRI). It has demonstrated antiviral activity by altering the acid sphingomyelinase/ceramide pathway, which promotes the formation of ceramide-rich membrane domains required for viral docking and entry, thereby blocking viral uptake. Fluvoxamine is an attractive candidate also because it is inexpensive, widely available, and safe for long-term use (Carpinteiro et al., 2021; Hashimoto, 2023).

While the previous examples focused on drugs targeting viral entry, HTAs can also interfere with host metabolic and translational mechanisms critical for viral replication. IMU-838 is a selective human dihydroorotate dehydrogenase (DHODH) inhibitor, which interferes with pyrimidine biosynthesis, thereby possibly blocking viral genome replication (Hahn et al., 2020). Similarly, Plitidepsin, an inhibitor of the eukaryotic translation factor eEF1A involved in protein biogenesis, has demonstrated strong antiviral activity in preclinical models by inhibiting viral polyprotein translation (Schreiber et al., 2024; White et al., 2021). Finally, in line with these strategies, Probenecid and Zapnometinib have also shown antiviral activity against SARS-CoV-2. Probenecid, traditionally used to treat gout, has demonstrated antiviral effects, although its precise mechanism remains unclear. Zapnometinib, an inhibitor of MEK1/MEK2, is able to

prevent viral entry and replication, as the MEK1/2 pathway appears to be involved in the formation of infectious viral particles. Moreover, it can also suppress the hyperinflammatory response observed in severe COVID-19 (Schreiber et al., 2024).

In summary, HTAs such as Bemcentinib, Bromhexine, Fluvoxamine, Imatinib, IMU-838, Nafamostat mesylate, Plitidepsin, Probenecid, and Zapnometinib illustrate the wide range of host pathways (*Figure 9*) that can be targeted to inhibit SARS-CoV-2. The majority of these molecules have shown promising results in preclinical studies and early clinical trials. However, in the absence of large-scale, randomized phase 2 and 3 trials, it is not yet possible to draw firm conclusions about their therapeutic potential. While early reports are encouraging, the overall evidence remains limited, highlighting the urgent need for robust studies to determine the clinical efficacy of these HTAs in the treatment of COVID-19.

1.8.2 Compounds targeting Heparan Sulfates

Heparan sulfate proteoglycans (HSPGs) are abundantly expressed on epithelial cells, where they participate in cell adhesion and signaling processes. Importantly, HSPGs can act as co-

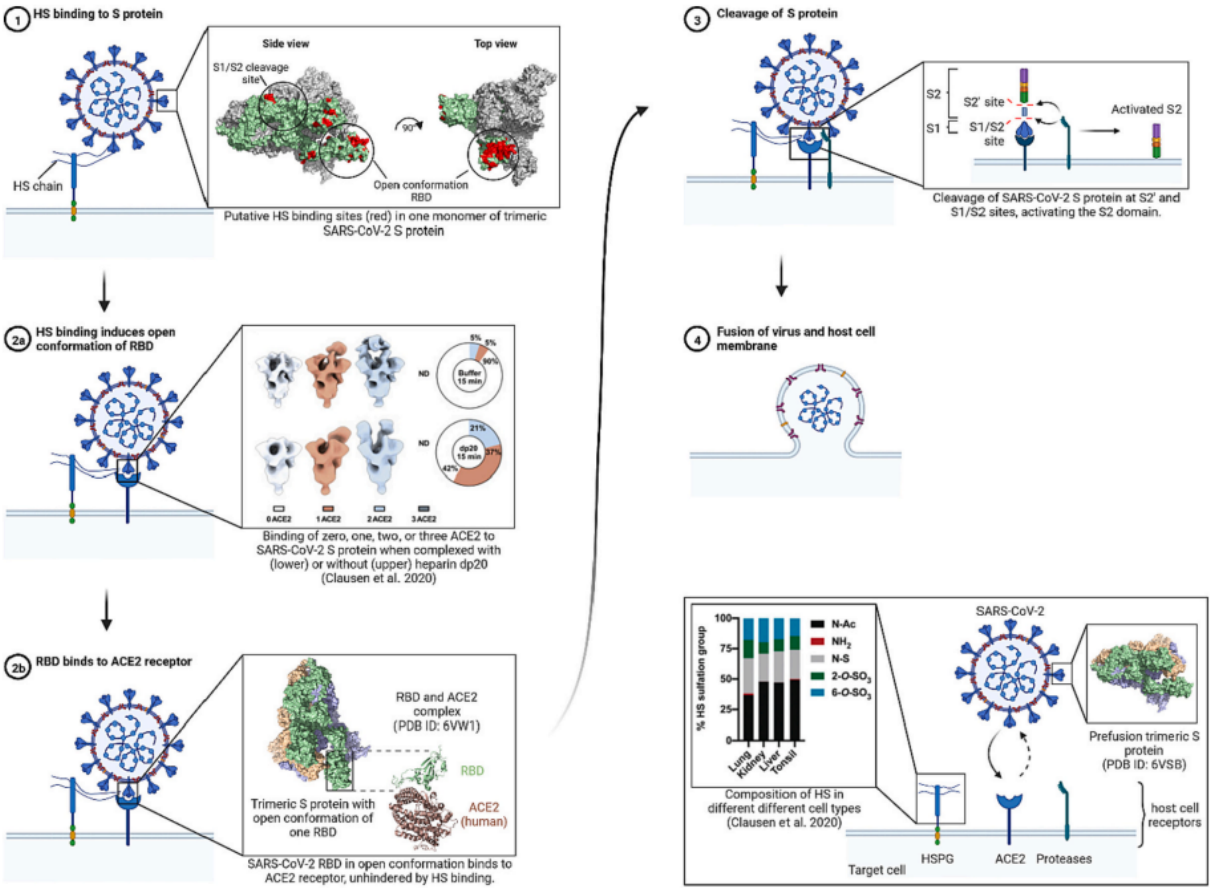

Figure 10. The diverse role of heparan sulfate and other GAGs in SARS-CoV-2 infections and therapeutics Friederike Eilts

receptors for SARS-CoV-2 entry (*Figure 10*). The negatively charged heparan sulfate (HS) chains of HSPGs electrostatically interact with basic amino acids on viral surface proteins, promoting virion clustering on the cell membrane and facilitating subsequent interaction with the ACE2 receptor (*Figure 10*). Mutations present in Omicron variants, such as Q493R, Q498R, and Y505H in BA.1/BA.2, and Q498R and Y505H in BA.4/BA.5, replace uncharged residues with basic ones, likely enhancing binding affinity to HS. Notably, the Omicron receptor-binding domain (RBD) is also characterized by a unique hairpin loop (residues 369–379) and an increased positive electrostatic potential which, together with an expanded ACE2-binding interface, may further modulate heparin-binding affinity compared to wild-type (WT) and Delta SARS-CoV-2 (Gelbach et al., 2022). In this context, several studies using surface plasmon resonance (SPR) have confirmed direct binding between HS and the SARS-CoV-2 spike protein. Moreover, heparin, a highly sulfated analog of HS, has been shown to inhibit SARS-CoV-2 infection by masking basic residues within the receptor-binding domain (RBD) and the multifunctional S1/S2 region, thereby preventing viral attachment and entry (Eilts et al., 2023; Paiardi et al., 2022). The use of heparin or other HSPG-related compounds may therefore represent a promising therapeutic strategy, exploiting the virus's affinity for HS to counteract viral entry itself. Indeed, heparin and its derivatives can bind to the spike protein, preventing the virus from attaching to HS on host cells. Additionally, they inhibit viral entry by physically blocking the furin cleavage site and preventing the spike protein from adopting the 'open' conformation required for ACE2 binding. Beyond their antiviral activity, heparin and related compounds, also possess anticoagulant and anti-inflammatory properties, which are highly relevant to COVID-19 pathophysiology, particularly in the context of thrombosis and hyperinflammation (*Figure 11*).

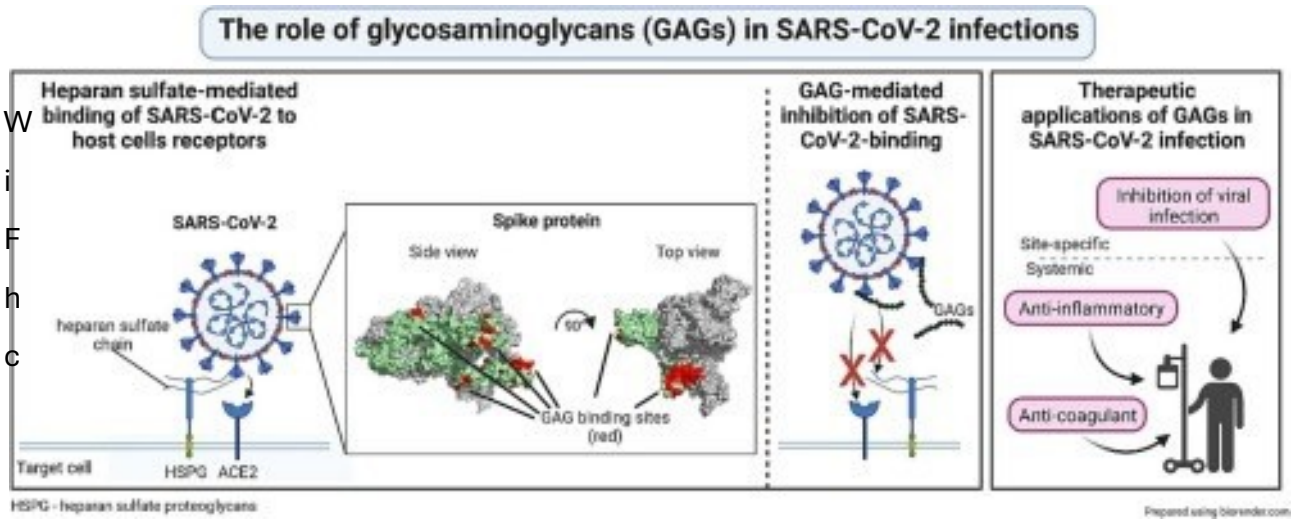

Figure 11 The diverse role of heparan sulfate and other GAGs in SARS-CoV-2 infections and therapeutics Friederike Eilts

1.8.3 Synergistic strategies to inhibit SARS-CoV-2 Infection

Although the World Health Organization declared the end of the COVID-19 emergency in May 2023, SARS-CoV-2 continues to circulate endemically and remains a major cause of severe illness among high-risk groups (Semenzato et al., 2022; Turtle et al., 2023). In this context, antiviral strategies remain a critical area of investigation and combinations of antiviral regimens represent an attractive approach, as they may have several advantages:

- Enhanced efficacy: the use of a synergistic strategy with compounds acting at different stages of the viral life cycle, allows for lower drug dosages.
- Prevention of resistance: as demonstrated in HIV and HCV treatment, combination therapy limits the evolution of drug-resistant viral mutants.

The prevention of resistance is particularly relevant for SARS-CoV-2, as virus evolution in immunocompromised patients, who may experience prolonged viral loads, can lead to the emergence of VOCs. While combination of antiviral treatments has proven to be effective for other chronic RNA viruses, there is currently no approved combination treatment against SARS-CoV-2 (Wagoner et al., 2022). DAAs may not completely prevent progression to severe disease, and their clinical use is limited by drug–drug interactions (e.g., NRM) and less practical administration routes (e.g., RDV) (Del Borgo et al.,2023). For instance, cotreatment with host-targeting antivirals (HTAs), such as TMPRSS2 inhibitors (camostat, nafamostat, avoralstat), and MNP, demonstrated strong synergistic inhibition of SARS-CoV-2 replication in lung epithelial cells, with activity against Beta and Delta variants. Similarly, MNP combinations with brequinar (inhibitor of pyrimidine synthesis) or with NRM/r, showed synergistic activity compared to monotherapy, as these regimens target distinct stages of the viral life cycle (entry and replication, respectively), enhancing efficacy and limiting viral evolution and resistance (Wagoner et al., 2022). Clinical data also support these findings: a study by Mikulska et al., 2023 showed that among 22 highly immunocompromised patients with chronic/relapsing SARS-CoV-2 infection, combination therapy showed promising outcomes. Eighteen patients (82%) received a full triple therapy: two antivirals (RDV and NRM/r in 17 cases and RDV with MNP in 1) plus monoclonal antibodies (tixagevimab/cilgavimab in 15 patients and sotrovimab in 3). The remaining four patients (18%) were treated with double antiviral therapy (remdesivir and nirmatrelvir/r in 3 cases and remdesivir and molnupiravir in 1). Viral sequencing was possible for 18 patients, revealing one Delta variant, while the rest belongs to different Omicron

subvariants. Overall, treatment was associated with an early virological response as well as a combined virological and clinical response by day 30 after initiation (Mikulska et al., 2023). As is widely known, immunocompromised patients are at particularly high risk of severe and persistent SARS-CoV-2 infection due to impaired humoral responses. A prospective cohort study (Calderón-Parra et al., 2024) comparing monotherapy with combination therapy (SOT plus RDV in 39 patients or NRM/r in 4 patients), showed that combined treatment significantly reduced the risk of COVID-19 progression, especially in patients with low anti-S IgG titers. Among 43 patients receiving combination therapy, no cases of progression were observed, whereas all 12 cases of disease worsening occurred in the monotherapy group. These findings provide strong evidence that synergistic regimens combining DAAs and mAbs can improve outcomes in high-risk populations, even against circulating Omicron variants, further supporting the rationale for combination therapy in vulnerable patients (Calderón-Parra et al., 2024). In conclusion, the use of antivirals with distinct viral targets, (i.e., RDV, NRM/r, MNP) or HTAs (i.e., camostat, nafamostat), and mAbs such as SOT in synergistic combinations is a promising strategy. Such regimens may be especially beneficial for immunocompromised patients, helping to prevent antiviral resistance and improving clinical outcomes. Further studies, including animal models and clinical case series, are encouraged to optimize combination therapy protocols in patients with protracted infections.

2. AIMS

The continuous emergence of SARS-CoV-2 variants might affect transmission rates, disease progression, vaccine development, and the effectiveness of current therapeutics. At the same time, long COVID has been recognized as a chronic condition of significant concern within the scientific and medical community, with no approved treatments. Increasing evidence indicates that SARS-CoV-2 can persist for months or even years, contributing to long COVID symptoms and sequelae. This scenario highlights the urgent need for clinical trials targeting chronic viral infections. In this context, novel therapeutic approaches are being explored. Among these, heparan sulfate-targeting agents and combination therapies exploiting synergistic antiviral mechanisms, may be critical for preventing or mitigating long COVID.

The aim of this thesis was to investigate new strategies to counteract SARS-CoV-2 infection. Specifically, we evaluated the therapeutic efficacy of an HSPG-binding tetrapeptide (LB-1) in preventing viral entry using a live virus cell-based assays against Omicron BA.1 and BA.5 variants. In parallel, we assessed the cooperative activities of pairwise drug combinations in vitro using a VERO E6 cell-based assay, infecting cells with either the ancestral B.1 strain or the highly divergent BQ.1.1 variant. Within this system, pairwise combinations of authorized DAAs were tested, including nirmatrelvir (NRM), remdesivir (RDV), and the active metabolite of molnupiravir (EIDD-1931). Furthermore, the effectiveness of RDV in combination with four monoclonal antibodies (sotrovimab, bebtelovimab, cilgavimab, and tixagevimab) was evaluated against the susceptible B.1 strain. Collectively, these experiments aimed to assess the therapeutic potential of an HSPG-binding tetrapeptide, and synergistic drug combinations as strategies against both early and emerging SARS-CoV-2 variants.

3. Methods

3.1 In Vitro Combinatorial Activity

In vitro experiments

In this study, we tested the combinatorial *in vitro* activity of antiviral drugs Remdesivir (RDV; MCE®), Nirmatrelvir (NMR; MCE®) and EIDD-1931, the active form of Molnupinavir (MNP; MCE®) and biosimilar mAbs bebtelovimab (BEB; ref. PXTA1750-100), sotrovimab (SOT; ref. PXTA1637-100), tixagevimab (TIX; ref. PXTA1032-100) and cilgavimab (CIL; ref. PXTA1033-100), supplied by ProteoGenix SAS (Schiltigheim, France). Antivirals were resuspended in 100% DMSO at the stock concentration of 20 mM for RDV and 10 mM for NRM and EIDD-1931 and the biosimilar mAbs in phosphate-buffered saline PBS. P-glycoprotein (P-gp) inhibitor (CP-100356 hydrochloride,CE®) was used in the experiments to increase the uptake of the drugs by inhibiting P-gp, a protein of the cell membrane which can pumps antivirals out of the cell, which is abundantly expressed on VERO E6 cell lines used in this thesis (Zhu et al.,2022; Fiaschi et al., 2022). CP-100356 was resuspended in 100% DMSO at a concentration of 10 mM as well.

Half-maximal cytotoxic drug concentration (CC_{50}) of the compounds was determined by CellTiter-Glo 2.0 Luminescent Cell Viability Assay (Promega) according to the manufacturer's protocol as explained in paragraph *2.2. Cytotoxicity Assay*. Once determined the CC_{50}, a not-toxic dose was chosen for each compound and used as starting drug concentration in the subsequent antiviral assays.

Cell Line used for the assays

VERO E6 (ATCC® CRL 1586TM), an adherent cell line derived from the kidney of the African green monkey, was used to titrate the viral stocks and to test the antiviral activity of the combined compounds. VERO E6 cells were propagated in DMEM High Glucose (Euroclone) supplemented with 10% Fetal Bovine Serum (FBS, Euroclone) and 1% of Streptomycin/Penicillin (PS) (Euroclone) and passaged at the 70-90% confluence. The same medium, containing 1% of FBS instead of 10% (infection medium), was used in all experiments requiring viral infection. Cells were incubated in a humified incubator at 37°C with 5% of CO_2 concentration. Uninfected cell cultures were handled in a BSL2 laboratory, whereas all the infection experiments were performed in a BSL3 containment.

Cytotoxicity Assay

Cytotoxicity assays were performed to assess the cell toxicity of each antiviral compound and to determine the non-toxic concentration to be used as a starting point for the subsequent antiviral experiments. To determine cell viability, the CellTiter-Glo 2.0 Luminescent Cell Viability Assay (Promega, G9241) was used, according to the manufacturer's instruction. This highly sensitive method measures the ATP produced by viable cells. The amount of ATP

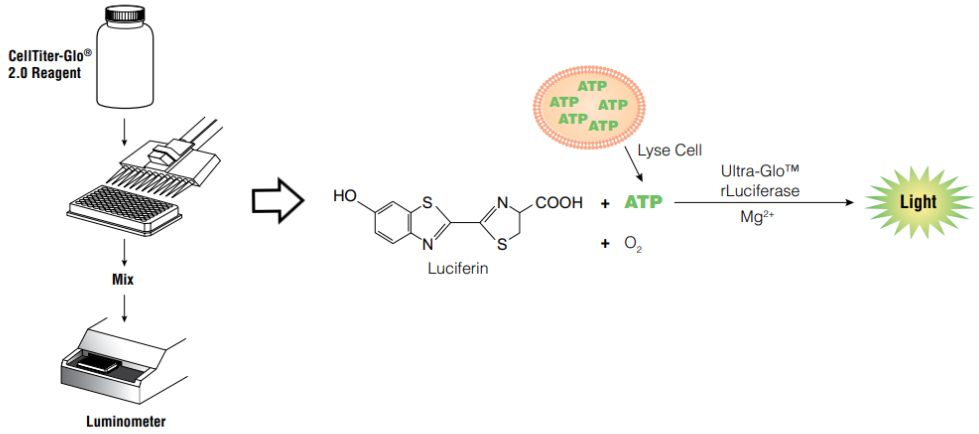

Figure 12 CellTiter-Glo 2.0

produced is proportional to the cell viability: in non-toxic conditions, cells are viable and in an active metabolic state, expressing high levels of ATP (*Figure 12*).

The cytotoxicity of CP-100356 was first assessed to select the concentration that had 90–100% cell viability. Following determination of the optimal CP-100356 concentration (0.5 µM), cytotoxicity of RDV, MNP, NRM, BEB, SOT, TIX, CIL with or without CP-100356 was explored. In addition, cytotoxicity of compound combinations was assessed.

In brief, 6,000 Vero E6 cells/well were seeded in tissue-treated 96-well plates and incubated at 37 °C and 5% CO_2 for 24 h. Compounds were serially 4-fold diluted in duplicates at 6x the selected working concentrations. For combination assays, 30 µL of one compound dilution was mixed with 30 µL of another, followed by the addition of 60 µL of CP-100356 (6× stock) resulting in a final concentration of 1.5 x for CP-100356 and the compounds. The mixtures were then added to the cells and incubated for 1 h at 37 °C in 5% CO_2. After incubation, 60 µL of fresh medium was added to each wells to mimic the virus addition step in the antiviral assay and to adjust all compounds, including CP-100356, to a final concentration of 1x. Cells were then

incubated for 72 h at 37 °C in 5% CO_2. Cytotoxicity was then measured by the CellTiter-Glo® 2.0 Luminescent Cell Viability Assay (Promega, Madison, WI, USA) following the manufacturer's instructions. Each plate had mock control (negative control, cells only), a DMSO control curve, and a toxicity control (100% DMSO). Luminescence was measured using the GloMax® Discover Multimode Microplate Reader (Promega), and data were plotted using GraphPad Prism software version 9.0 (La Jolla, CA, USA).

The half-maximal cytotoxic concentration (CC_{50}) and 90% cell viability corresponding concentration (CC_{10}) were calculated by non-linear regression analysis of dose–response curves from the ECanything function in GraphPad Prism. The CC_{10} values were subsequently used as the starting concentrations for the antiviral activity assays.

Viral stocks

The SARS-CoV-2 stocks used for the experiments included the wild type B.1 (EPI_ISL_2472896) and the Omicron BQ.1.1 (EPI_ISL_17257516) variant, kindly provided by the Department of Biomedical and Clinical Sciences Luigi Sacco, University of Milan, Italy.

Viral Titration Assay

Before performing *in vitro* experiments, the viral stocks were titrated in VERO E6 cell line to determine the tissue culture infectious doses for milliliter ($TCID_{50}$/ml), which is defined as the dilution of viral stock required to infect 50% of a given cell culture (Lei et al., 2020). The optimal incubation time (72h) and the experimental conditions (e.g. cell confluence) were previously set up in propagation experiments (Vicenti et al., 2021), and were maintained in titration, live virus neutralization and phenotypic assays.

To perform the titration, six replicates of 5-fold serial dilution of each viral stock were made and transferred into a 96-well plate containing 6,000 pre-seeded VERO E6 cells per well and incubated for 72h at 37°C supplemented with 5% CO_2. In each plate a mock control (uninfected cells) was included to normalize the results. The cell viability and consequently the $TCID_{50}$ was determined by CellTiter-Glo 2.0 Luminescent Cell Viability Assay (Promega) using the instrument GloMax® Discover Multimode Microplate Reader (Promega).

Antiviral Activity Assay

The combination of various DAA drugs (NRM/EIDD-1931, NRM/RDV, and RDV/EIDD-1931) was evaluated against the B.1 and BQ.1.1 variants. In addition, RDV was tested in combination with four mAbs (RDV/SOT, RDV/BEB, RDV/CIL, RDV/TIX), since their parenteral route of administration makes them clinically compatible. These mAb/antiviral combinations could be tested only against the prototype strain B.1, since none of the mAbs selected were found to be active against the variant BQ.1.1.

To generate the dual-drug matrices, six 4-fold serial dilutions of the first drug were mixed with six 4-fold serial dilutions of the second drug in 96-well plates, resulting in 36 distinct conditions in a two-dimensional matrix. For the combination treatments, CP-100356 was also included, and the compounds mixtures were incubated for 1 h at 37 °C on pre-seeded, semiconfluent VERO E6 cells, and subsequently infected with B.1 or BQ.1.1 viral stocks at a MOI of 0.005.

For the mAb/antiviral combinations, B.1 viral stocks were pre-incubated at 37 °C for 1 h with serial dilutions of the mAbs and then used at 0.005 MOI to infect VERO E6 cells pretreated with serial dilutions of the DAAs. In both experimental setups, infected cultures were incubated for 72 h at 37 °C with 5% CO_2, and then cell viability was determined through the CellTiter-Glo 2.0 assay as described above. Each plate included four independent dose–response curves of the compounds, a mock-infected control, and an infection control without antivirals for normalization. All experiments were independently performed in duplicate.

Dose-Effect Relationships with Compound Combinations

Data from the antiviral activity of compound combinations were analyzed using the SynergyFinder 3.0 web platform (https://synergyfinder.fimm.fi/). Drug–drug interactions were quantified using the Zero Interaction Potency (ZIP) model, which estimates synergy by analyzing shifts in the potency of dose–response curves between single agents and their combinations. The ZIP approach integrates features of the Loewe additivity and Bliss independence models, providing a comprehensive framework for interpreting interaction patterns in high-throughput drug screening (Yadav et al., 2015). Briefly, the Loewe model assumes that two drugs act as if they were the same, while the Bliss model calculates the expected combined effect independently from each other. For each drug pair, SynergyFinder reports a global Synergy Score (SS), which represents the percent change in response to drug interactions compared with the effects of the individual compounds. For example, a synergy score of 20 corresponds

to a 20% increase in activity above the predicted additive effect. Results are visualized through two- and three-dimensional synergy maps, where synergistic areas appear in red and antagonistic regions in green. According to the platform's thresholds, interactions are classified as antagonistic (SS ≤ −10), additive (−10 < SS < 10), or synergistic (SS ≥ 10) (Ianevski et al., 2022). Additionally, the software includes a "weighted synergy" analysis, which emphasizes synergy observed at lower concentration ranges that are more relevant for minimizing toxicity and favoring clinical applicability. To validate the computational analysis, drug concentrations consistently identified as synergistic (SS > 10) were selected for confirmatory assays. In these experiments, Compound 1 was tested at three fixed concentrations (its IC_{50} and two successive two-fold dilutions), combined with six four-fold serial dilutions of Compound 2. The IC_{50} values of Compound 2 in the presence of Compound 1 were then compared with the IC_{50} of Compound 2 alone, and fold-shifts were calculated as IC_{50} [Compound 2 alone] / IC_{50} [Compound 1 + Compound 2].

Statistical Analysis

Since statistical comparison between summary or weighted synergy scores (SS) from different combinations of compounds were not provided in SynergyFinder 3.0, additional analyses were performed. Because the summary SS is the mean of all individual SS values derived from calculation for every tested concentration pair, combinatorial effects overall of the three DAA pairs and three RDV/mAb groups were compared by Kruskal–Wallis test with subsequent Mann–Whitney post hoc pairwise tests. SS values generated by the same concentrations of DAA/DAA that were tested against B.1 and BQ.1.1 viral variants were compared using the Wilcoxon signed-rank test. All statistical calculations were made with IBM SPSS Statistics 20 (IBM Corp., Armonk, NY, USA) and p-values were regarded as two-sided.

3.2 LB-1 activity

In vitro experiments

In this study, we investigated the in vitro activity of an HSPG-binding tetrapeptide (LB-1), resuspended in physiological solution at a stock concentration of 2 mM.

Cell lines

Two cell lines were used for viral titration and antiviral activity assays: Vero E6 (previously described), an adherent kidney cell line derived from the African green monkey, and the human intestinal epithelial Caco-2 (ATCC HTB-37) cell line.

Vero E6 cells were maintained in high-glucose DMEM (Euroclone) supplemented with 10% fetal bovine serum (FBS) and 1% penicillin/streptomycin (P/S) (Euroclone) and passaged at 70–90% confluence. Caco-2 cells were propagated in EMEM (Sigma Aldrich) supplemented with 10% FBS (Euroclone), 1% P/S (Euroclone), and 2mM glutamine (Euroclone). For all infection experiments, the corresponding culture medium was used with FBS reduced to 1% (infection medium).

Cells were incubated at 37 °C in a humidified atmosphere containing 5% CO_2. Uninfected cell cultures were handled under BSL-2 conditions, whereas all viral infection experiments were carried out in a BSL-3 facility.

Viral stocks

The SARS-CoV-2 stocks used for the experiments included the Omicron BA.1 (EPI_ISL_6777160), BA.5 (EPI_ISL_14513768) and Delta (EPI_ISL_6943992) SARS-CoV-2 variant. Viral stocks were expanded into VERO E6 cells and titrated as described in the next chapter.

Viral Titration Assay

Viral stocks were titrated in Vero E6 and Caco-2 cell lines before performing the in vitro tests, to achieve $TCID_{50}$/mL. Six replicates of a five-fold serial dilution of each viral stock were prepared and the added to 96-well plates containing 13,000 pre-seeded Caco-2 cells per well. Fifty microliters of each viral dilution were incubated with the cells for 1 h, after which the viral supernatant was removed and replaced with 200 µL of fresh EMEM. Plates were then incubated at 37 °C with 5% CO_2 for 24 h. A mock control was included on each plate to normalize the result. After 24 h, 50 µL of supernatant from each well was transferred to 96-well plates containing 6,000 pre-seeded Vero E6 cells per well, followed by the addition of 150 µL of fresh medium. After additional 24 h incubation, viral titers were determined by ELISA for SARS-CoV-2 nucleocapsid protein. Briefly, cells were fixed with formaldehyde 10% (Carlo Erba) for 20 min, washed with PBS 1X, and permeabilized with 1% Triton X-100 (Carlo Erba) for 20 min. After washing, the cell monolayer was incubated with a monoclonal mouse antibody (clone

AP201054; Novus Bio) followed by a polyclonal HRP-conjugated anti-mouse IgG secondary antibody (Novus Bio, NB7570). Absorbance was measured after a 10 min incubation with TMB substrate (Sigma Aldrich) at 450 nm (OD450) using the absorbance module of the GloMax Discover Multimode Microplate Reader (Promega).

Cytotoxicity assay

Cytotoxicity assay was performed to determine the toxicity of the antiviral drug LB-1 and to identify the non-toxic concentration to be used as the starting point for subsequent experiments. Concentrations maintaining 90–100% cell viability were selected. Briefly, 13,000 Caco-2 cells per well were seeded onto tissue-treated 96-well plates and incubated at 37 °C with 5% CO_2 for 24 h. Two-fold serial dilutions of LB-1 and of the saline solution in which it was resuspended were subsequently added to Caco-2 cells. Simultaneously, 6,000 Vero E6 cells per well were seeded in 96-well tissue-treated plates and incubated under the same condition. After 24 h, 50 µL of LB-1 dilutions were added to the Vero E6 cells, followed by 150 µL of DMEM containing 1% FBS. Plates were incubated for an additional 24 h, and the half-maximal cytotoxic concentration (CC_{50}) of LB-1 was determined using the CellTiter-Glo® 2.0 Luminescent Cell Viability Assay (Promega). Each plate included a mock control, a vehicle control curve (physiological solution in which LB-1 is resuspended), and a toxicity control (100% DMSO). Luminescence was measured with the GloMax® Discover Multimode Microplate Reader (Promega, Madison, WI, USA), and results were analyzed using GraphPad Prism software version 9.0 (La Jolla, CA, USA). CC_{50} and the concentration corresponding to 90% cell viability (CC_{10}) were calculated by non-linear regression analysis of the dose–response curves using the ECanything function in GraphPad Prism. The CC_{10} value was subsequently used in the antiviral activity assay.

Antiviral Activity Assay

The day before infection, 13,000 Caco-2 cells per well were seeded into 96-well adhesion plates to reach approximately 70% confluence on the day of infection. To assess the antiviral activity of LB-1, two-fold serial dilutions were set, starting from the maximum non-toxic concentration (2 mM) and incubated on the cells for 1 h. A fixed amount of live SARS-CoV-2 BA.5, BA.1, and Delta strains (MOI = 0.01) were then added and incubated at 37 °C for 1 h. After incubation, the virus–compound mixture was removed, and the wells were replenished with fresh medium containing the corresponding LB-1 dilutions.

The same day of the experiment, 6,000 Vero E6 cells per well were pre-seeded. After 24h, 50 µL of supernatant from infected Caco-2 cultures was transferred to pre-seeded Vero E6, followed by the addition of 150 µL of DMEM supplemented with 1% FBS.

ELISA targeting the SARS-CoV-2 nucleocapsid protein was performed to determine the half-maximal inhibitory concentration (IC_{50}) of LB-1. Each assay included a mock control, virus control, and two reference inhibitors with known IC_{50} values: RDV and previously tested human immune serum.

Flow cytometry

Flow cytometry experiments were performed using 2×10^5 cells per well, plated in U-bottom 96-well plates (ThermoFisher). All reagents used for incubation and staining were resuspended in phosphate-buffered saline (PBS, Sigma-Aldrich) supplemented with 5 mM Ethylenediaminetetraacetic acid (EDTA) and 1% Bovine serum albumin (BSA, Sigma-Aldrich) to maintain cells in suspension and minimize aggregation or nonspecific binding. To determine the binding activity of the LB-1 peptide, cells were incubated for 30 minutes with different molar concentrations of the biotinylated peptide, either in the absence or presence of heparin and subsequently stained with streptavidin-FITC. In additional experiments, cells were treated with heparinase I (0.03 IU/mL, Sigma-Aldrich) at 37 °C for 1 hour prior to LB-1 peptide staining. Flow cytometric analysis was performed using a Guava flow cytometer (Millipore) by acquiring 10,000 events per sample, and data were analyzed with FCS Express 6 software.

4 Results

4.1 Combinatorial effect

To investigate the drugs' combinatorial effects, we first tested the three DAAs (EIDD-1931, RDV, NRM) individually, determining their IC_{50} values against B.1/BQ.1.1, which were 2.40 ± 0.40/1.59 ± 0.44, 0.06 ± 0.03/0.03 ± 0.01 and 0.10 ± 0.03/0.10 ± 0.01 μM, respectively. The same experiments were conducted with mAbs (CIL, TIX, BEB and SOT) which resulted active only against the B.1 variant, with IC_{90} values of 0.20 ± 0.13, 0.07 ± 0.04, 0.03 ± 0.01, 0.81 ± 0.32 μg/mL, respectively. In *table 3* all the IC_{50}, CC_{50}, and CC_{10} values are reported.

	CC_{50} μM Mean ± SD	CC_{10} μM Mean ± SD	IC_{50} μM vs. B.1 Mean ± SD	IC_{90} μM vs. B.1 Mean ± SD	IC_{50} μM vs. BQ.1.1 Mean ± SD	IC_{90} μM vs. BQ.1.1 Mean ± SD
NRM	40.7 ± 4.0	2.9 ± 0.2	0.1 ± 0.03	0.2 ± 0.1	0.1 ± 0.01	0.2 ± 0.01
EIDD-1931	43.3 ± 6.0	3.1 ± 0.4	2.4 ± 0.4	2.5 ± 0.1	1.6 ± 0.4	1.8 ± 0.7
RDV	17.2 ± 0.2	4.2 ± 0.6	0.06 ± 0.03	0.2 ± 0.05	0.03 ± 0.01	0.1 ± 0.01
	CC_{50} ng/mL Mean ± SD	CC_{10} ng/mL Mean ± SD	IC_{50} ng/mL vs. B.1 Mean ± SD	IC_{90} ng/mL vs. B.1 Mean ± SD	IC_{50} μM vs. BQ.1.1 Mean ± SD	IC_{90} μM vs. BQ.1.1 Mean ± SD
SOT	>2400	>2400	813 ± 324	1718 ± 594	NA	NA
BEB	>60	>60	33 ± 7	89 ± 9	NA	NA
CIL	>360	>360	204 ±1354	1385 ± 862	NA	NA
TIX	>360	>360	68 ± 41	305 ± 71	NA	NA

Table 3 Cytotoxicity and anti-SARS-CoV-2 activity of nirmatrelvir (NRM), EIDD-1931 (the active form of molnupiravir), remdesivir (RDV), sotrovimab (SOT), bebtelovimab (BEB), cilgavimab (CIL) and tixagevimab (TIX) in VERO-E6 cells. Antivirals were tested against the Wild Type B.1 strain and the BQ.1.1 Omicron variant. CC_{50}: half-maximal toxic drug concentration; CC_{10}: drug concentration causing 10% cells cytotoxicity; IC_{50}: half-maximal inhibitor drug concentration; IC_{90}: drug concentration inhibiting 90% of viral replication; SD: Standard Deviation; NA: Not Active.

At the next stage, we tested NRM/EIDD-1931, NRM/RDV and RDV/EIDD-1931 combos against the wild type B.1 and BQ.1.1 strains, while all mAbs were tested in combination with RDV, which is the only injectable DAA, against the wild type B.1. The analysis of the DAA/DAA or RDV/mAbs combos were performed with SynergyFinder 3.0 software, applying the ZIP multiple synergy algorithm. This algorithm combines Bliss and Loewe reference models giving back summary of SS and weighted SS metrics, making an average of all the dose combination measurements and at the clinically relevant lower dose windows. In *Figure 13*, is shown an example of the output generated by analyzing the 36-cell matrix obtained with NRM/RDV combo against B.1 SARS-CoV-2 strain.

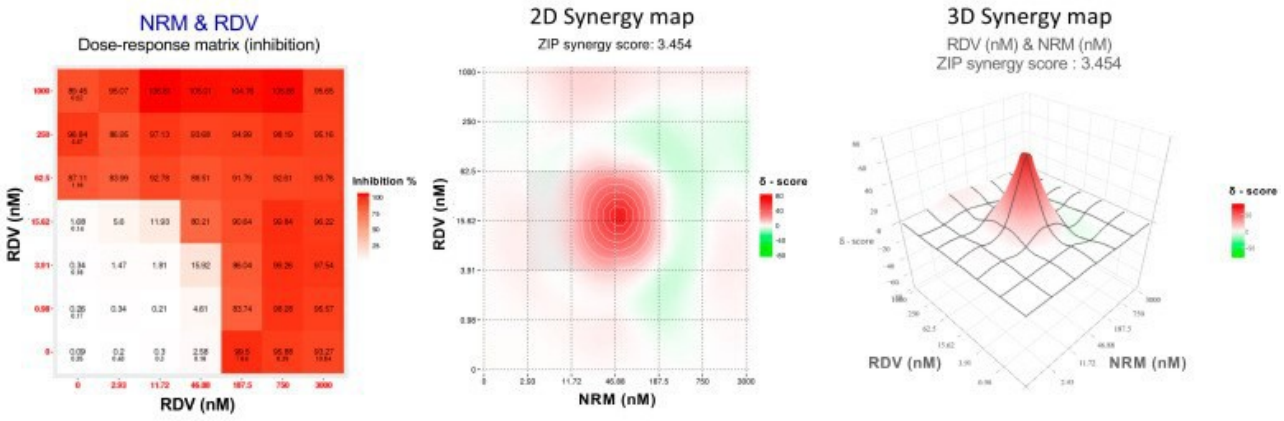

Figure 13 Dose–response matrix, two-dimensional (2D) and three-dimensional (3D) synergy maps generated using SynergyFinder 3.0 by applying the ZIP model on the Nirmatrelvir (NRM)/Remdesivir (RDV) combination tested against the ancestral B.1 SARS-CoV-2 strain.

The weighted SS for all the DAA combinations indicated additivity against B.1 (2.1 ± 0.4 for NRM/EIDD-1931, 1.9 ± 1.4 for NRM/RDV and 0.9 ± 0.7 for RDV/EIDD-1931) and BQ.1.1 (0.0 ± 0.7 for NRM/EIDD-1931, 2.1 ± 2.1 for NRM/RDV and 1.7 ± 2.5 for RDV/EIDD-1931). Additivity was also observed for all RDV/mAb combos against B.1 (6.1 ± 2.9 for RDV/SOT, 4.2 ± 3.3 for RDV/BEB, 0.8 ± 0.1 for RDV/CIL and 2.6 ± 2.7 for RDV/TIX). The more comprehensive summary score metric confirmed additivity for all the combinations tested. Summary and weighted SS are indicated in *Table 4*, while the 2-D Synergy plots generated by each experiment are shown in *Figure 13,* both showing an overall additive effect. However, analyzing more in details specific

	Summary SS vs. B.1 Mean ± SD	Weighted SS vs. B.1 Mean ± SD	Summary SS vs. BQ.1.1 Mean ± SD	Weighted SS vs. BQ.1.1 Mean ± SD
NRM/EIDD-1931	−3.1 ± 3.1	2.1 ± 0.4	−2.7 ± 1.3	0.0 ± 0.7
RDV/EIDD-1931	0.4 ± 6.2	0.9 ± 0.7	2.6 ± 6.5	1.7 ± 2.5
NRM/RDV	2.0 ± 2.0	1.9 ± 1.4	−0.2 ± 3.7	2.1 ± 2.1
RDV/SOT	8.8 ± 10.3	6.1 ± 2.9	NP	NP
RDV/BEB	5.7 ± 2.6	4.2 ± 3.3	NP	NP
RDV/TIX	0.6 ± 6.4	2.6 ± 2.7	NP	NP
RDV/CIL	−2.0 ± 0.5	0.8 ± 0.1	NP	NP

Table 4 Summary synergy scores (SS) and weighted SS of all the tested antiviral combinations generated using the Synergy Finder 3.0 online software (https://synergyfinder.fimm.fi/ accessed on 12 October 2023). The antiviral pairwise combinations of nirmatrelvir (NRM), EIDD-1931 (the active form of molnupiravir), and remdesivir (RDV) were tested against the ancestral B.1 and the Omicron BQ.1.1 SARS-CoV-2 variant. The combinations of RDV with each of the four monoclonal antibodies (mAb), including sotrovimab (SOT), bebtelovimab (BEB), cilgavimab (CIL), and tixagevimab (TIX), were tested only against the ancestral B.1 SARS-CoV-2 variant. NP: Not performed

drug combo concentration, particularly the ones below IC_{90} of individual drugs, we found a synergistic effect as represented in *Table 4*.

The highest SS were obtained among different RDV/mAb combinations, particularly with SOT, BEB, and TIX (*Table 4*). These results were also confirmed by the highest overall summary and weighted SS. Globally, in DAA combinations, just some specific concentrations pair showed synergy. Among them, NRM/RDV showed the highest SS, compared to all the other combos that showed a weak synergy. Kruskal-Wallis analysis revealed significant differences ($p < 0.001$) when we compared SS values obtained with the DAA/DAA and DAA/mAb combinations against

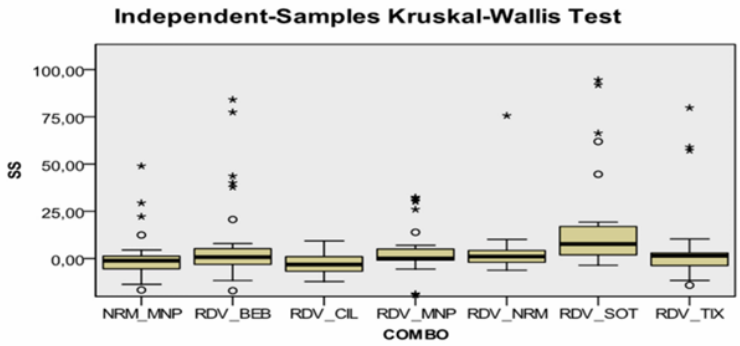

Total N	252
Test Statistic	48,797
Degrees of Freedom	6
Asymptotic Sig. (2-sided test)	,000

Figure 14 Overall combinatorial effects of the three DAA pairs as well as those of the three RDV/mAb groups were compared by the Kruskal-Wallis test followed by Mann Whitney pairwise comparisons between groups. Statistical analysis was performed by IBM SPSS Statistics, version 20 (IBM Corp., Armonk, NY, USA)

B.1 virus. Particularly, post-hoc pairwise analysis detected significant synergy for RDV/SOT compared with the other mAb combos (RDV/BEB, $p = 0.006$; RDV/CIL, $p < 0.001$; RDV/TIX, $p = 0.006$) and DAA/DAA combos (NRM/EIDD-1931, $p < 0.001$; NRM/RDV, $p = 0.010$; RDV/EIDD-1931, $p = 0.004$).

However, for most dual combinations, the weighted synergy scores that indicated synergistic effects were often rare outliers within the overall distribution of data points (*Figure 14*). SS values remained significantly higher for the RDV/SOT combo when comparing only the four DAA/mAb combinations ($p < 0.001$ compared with RDV/CIL and $p = 0.002$ compared with RDV/BEB and RDV/TIX).

In the subset of DAA/DAA combinations, the same number of synergistic cases were observed for both B.1 and BQ.1.1 viruses (8 each). Additionally, the synergy scores (SS) did not differ significantly between the two variants at matched drug concentrations ($p = 0.153$).

Synergy Score Stratum	Drug Combination	Concentrations [a]	Viral Variant
>50	RDV/NRM	0.02/0.05	B.1 and BQ1.1
	RDV/SOT	0.04/8.8	B.1
		0.04/35.2	
		0.04/140.6	
	RDV/BEB	0.04/0.6	B.1
		0.04/2.2	
		0.04/8.9	
	RDV/TIX	0.04/2.2	B.1
		0.04/8.8	
30–50	NRM/EIDD-1931	0.05/0.75	B.1
		0.05/1.50	B.1 and BQ.1.1
	RDV/SOT	0.01/562.5	B.1
		0.04/562.5	B.1
	RDV/TIX	0.04/35	B.1
10–29.9	NRM/EIDD-1931	0.003/0.07	B.1
		0.01/0.08	B.1
		0.05/0.09	B.1
	RDV/EIDD-1931	0.02/1.5	B.1 and BQ.1.1
		0.03/0.75	BQ.1.1
	RDV/NRM	0.02/0.05	B.1
		0.004/0.05	B.1 and BQ.1.1
		0.006/0.05	BQ.1.1
		0.02/0.03	BQ.1.1
		0.02/0.01	BQ.1.1
	RDV/BEB	0.01/8.9	B.1
	RDV/TIX	0.01/35	B.1

Table 5 Concentrations of pairwise drug combinations below each drug IC_{10} and showing synergism in the SynergyFinder 3.0 matrix, stratified by synergy score values (10–29.9, 30–50, and above 50)

To validate this data, the IC_{50} synergistic potency shift was measured in an antiviral in vitro assay where cells were treated with three fixed drug concentrations of the first compound plus scalar concentrations of the second compound. To achieve this, NRM and RDV were selected as fixed drug as they showed repeatedly synergy at the concentration of 0.05 and 0.02 µM, respectively (*Table 5*). The results show that the IC_{50} of NRM with the addition of RDV 0.06 µM and 0.03 µM was reduced by 33- and 8-fold against B.1 and by >140- and 14-fold against BQ.1.1,

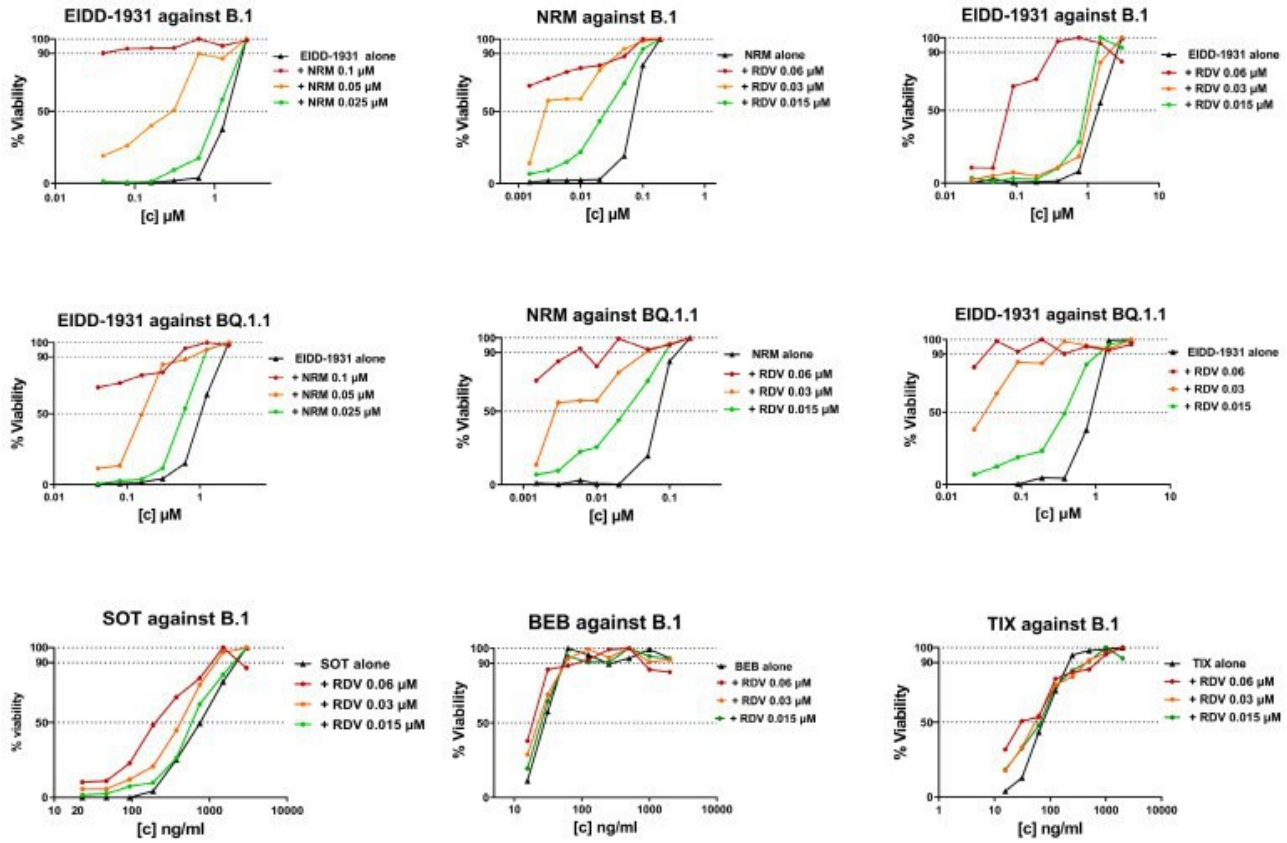

Figure 15. IC_{50} synergistic potency shift experiments in B.1 or BQ.1.1 virus infected VERO E6 cells treated with three fixed drug concentrations of Compound 1 (as indicated in the graph title) plus scalar concentrations of Compound 2 (as indicated in the in the legend). The three concentrations of Compound 1 were chosen as the IC_{50} of Compound 1 alone, plus two 2-fold dilutions. The scalar concentration of Compound 2 is the same as that used in the SynergyFinder 3.0 matrix. The concentration of Compound 2 on the x-axis is expressed as micromolar for DAA and as ng/mL for mAb, while the y-axis shows the percentage of cell viability. DAA/DAA combinations were tested against the ancestral B.1 SARS-CoV-2 strain and the BQ.1.1 Omicron variant, while RDV/mAb combinations were tested only against the ancestral B.1 SARS-CoV-2 strain. Graphs were generated using GraphPad PRISM software version 9 (La Jolla, CA, USA).

respectively (*Figure 15, table 6*).

Against B.1			
EIDD-1931 IC_{50} Fold Reduction	NRM 0.1 µM	NRM 0.05 µM	NRM 0.025 µM
	88	11	1
	RDV 0.06 µM	RDV 0.03 µM	RDV 0.015 µM
	>26	26	2
NRM IC_{50} Fold Reduction	RDV 0.06 µM	RDV 0.03 µM	RDV 0.015 µM
	33	8	1
SOT IC_{50} Fold Reduction	RDV 0.06 µM	RDV 0.03 µM	RDV 0.015 µM
	4	2	2
BEB IC_{50} Fold Reduction	RDV 0.06 µM	RDV 0.03 µM	RDV 0.015 µM
	2	1	1
TIX IC_{50} Fold Reduction	RDV 0.06 µM	RDV 0.03 µM	RDV 0.015 µM
	3	2	1
Against BQ.1.1			
EIDD-1931 IC_{50} Fold Reduction	NRM 0.1 µM	NRM 0.05 µM	NRM 0.025 µM
	28	7	2
	RDV 0.06 µM	RDV 0.03 µM	RDV 0.015 µM
	>30	30	3
NRM IC_{50} Fold Reduction	RDV 0.06 µM	RDV 0.03 µM	RDV 0.015 µM
	140	14	2

Table 6. IC_{50} synergistic potency shift was measured in infected VERO E6 cells treated with 3 fixed drug concentrations of Compound 1 plus scalar dilution of Compound 2, for each combination. Fold shift values in Compound 2 IC_{50} were calculated as: IC_{50} [Compound 2 alone] / IC_{50} [Compound 1 + Compound 2]. DAA were tested against wild type B.1 SARS-COV-2 strain and BQ.1.1 variant while mAb/RDV combinations only against wild type B.1 SARS-COV-2 strain.

A synergistic potency shift in EIDD-1931 IC_{50} was also induced by the addition of NRM at 0.1 µM and 0.05 µM against B.1 (88- and 11-fold, respectively) and against BQ.1.1 (28- and 7-fold, respectively) and by the addition of RDV at 0.06 µM and 0.03 µM against B.1 (>26- and 26-fold, respectively) and against BQ.1.1 (>30- and 30-fold, respectively). Regarding fixed RDV concentration/mAb combo, lower synergistic potency shifts were observed. Indeed, addition of RDV 0.06 µM reduced SOT, BEB, and TIX IC_{50} by 4-, 2- and 3-fold, respectively, while the addition of RDV 0.03 µM reduced SOT and TIX IC_{50} by 2-fold and did not affect BEB IC_{50}. Finally, at the lowest concentration tested (0.015 µM) RDV induced a 2-fold reduction only in SOT IC_{50}. In conclusion, these results suggest a synergistic interaction within DAA/DAA combinations, even if a cooperative effect was observed between RDV/SOT.

4.1 LB-1

LB-1 in vitro activity

The antiviral activity of LB-1 was evaluated against different SARS-CoV-2 VOC, specifically BA.1, BA.5, and Delta. Assays were performed starting from the CC_{10} value of the compound (2mM),

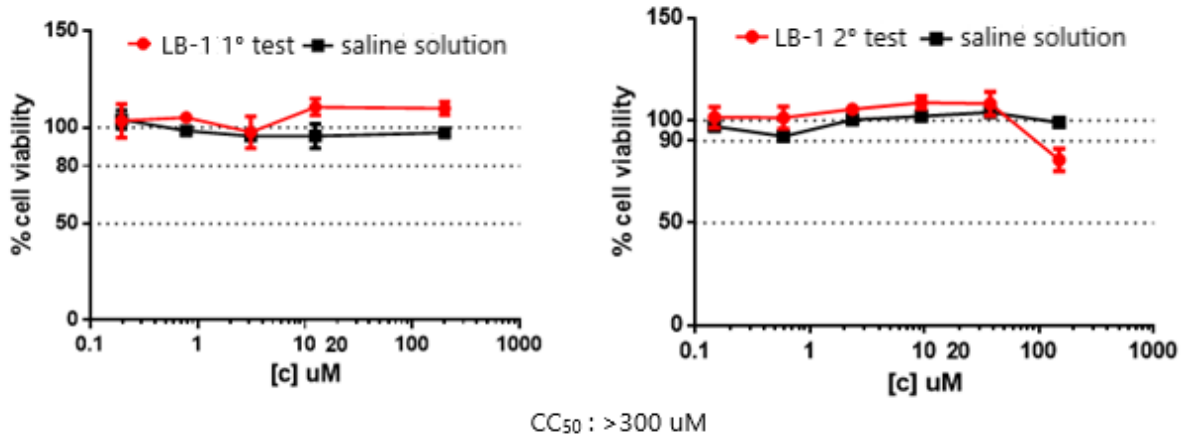

Figure 16 LB-1 cytotoxicity assay

previously determined by cytotoxicity assays *(Figure 16)* to identify a concentration that is non-toxic yet suitable for infection studies. Under these conditions, LB-1 inhibited the BA.1 and BA.5 sublineages of Omicron with IC_{50} of 21.5 ± 2.8 µM and 19.5 ± 1.7 µM, respectively, corresponding to a selectivity index (SI) of > 13.95 and >15.38. In contrast, the compound showed no detectable inhibition of the Delta variant, reflecting a variant-specific difference in viral entry mechanisms (*Figure 17*).

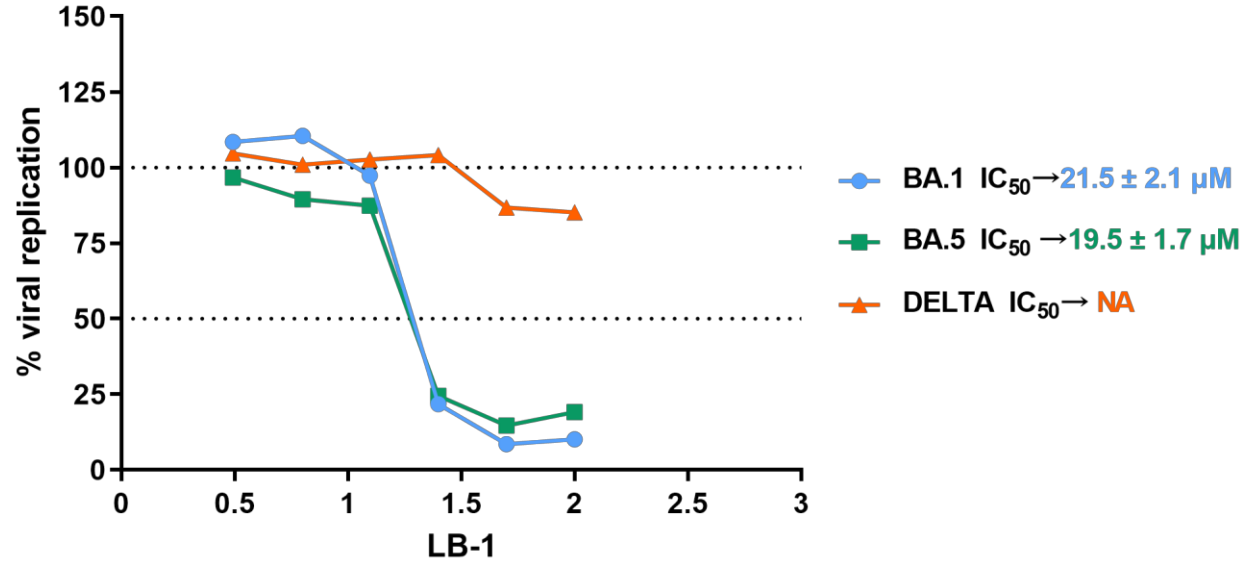

Figure 17. Antiviral activity of LB-1 against Omicron sublineages (BA.1, BA.5) and Delta SARS-CoV-2

LB-1 Flow-Cytometry

The binding of the LB-1 peptide to Caco-2 cells (*Figure 18A, B*) and its inhibition by heparin (*Figure 18C, D*) were assessed using flow cytometric. As shown, LB-1 bounds Caco-2 cells in a dose-dependent manner, and this binding was effectively blocked by heparin. To further

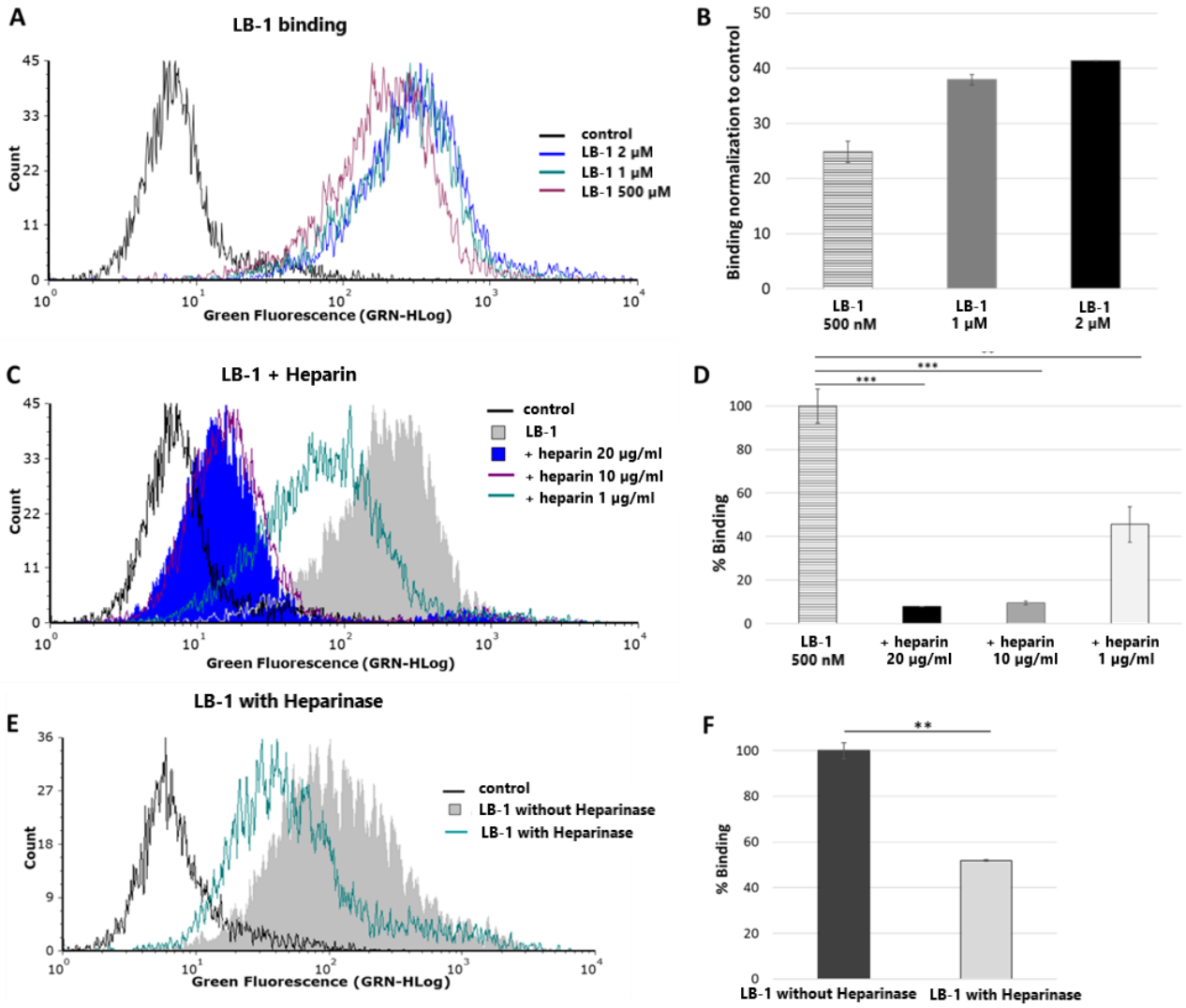

*Figure 28 Binding of LB-1 peptide to human Caco-2 cells analyzed by flow cytometry assay. A-B) Binding of LB-1, C-D) inhibition of LB-1 binding by heparin, E-F) binding of LB-1 on Caco-2 cells treated with heparinase I. *** p<0.001, ** p<0.01 calculated using one-way ANOVA with Dunnett's multiple comparisons test compared to control (D), calculated using two-tailed unpaired t-tests (F) with GraphPad PRISM version software 10*

confirm the specificity of LB-1 for heparan sulfate proteoglycans (HSPGs), Caco-2 cells were treated with heparinase I to remove the heparan sulfate chains of proteoglycans (Figure 17E, F). As observed in the figure, LB-1 binding to heparinase-treated cells was significantly reduced. Caco-2 cells were infected with SARS-CoV-2 Omicron BA.5 at an MOI of 0.05 in the presence

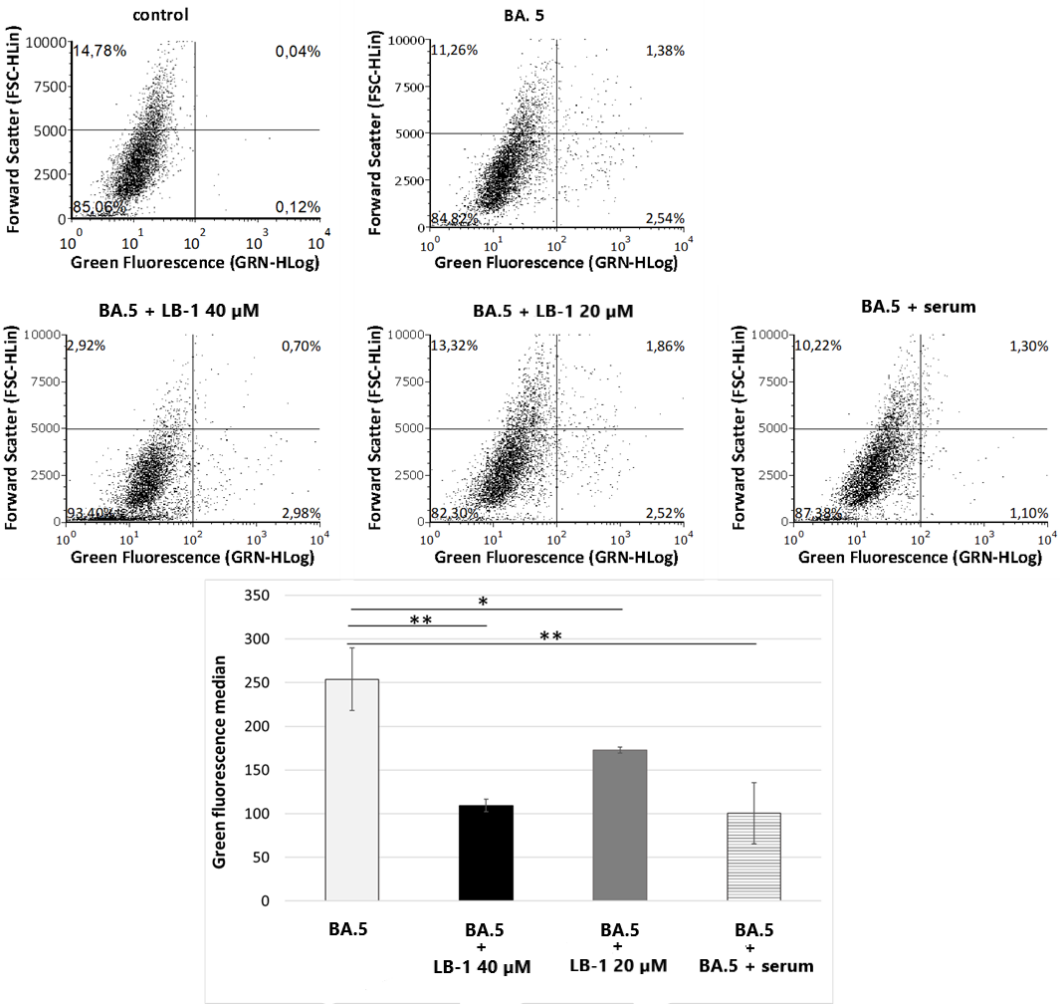

*Figure 19. Antiviral activity of NT4 peptide on SARS-CoV-2 strain BA.5 in the Caco-2 cell line analyzed by flow cytometry. ** p<0.01, * p<0.05 calculated using one-way ANOVA with Dunnett's multiple comparisons test versus control with GraphPad PRISM version 10 software*

of the LB-1 peptide at two concentrations (40 and 20 µM). After infection, the expression of the viral nucleocapsid (N) protein was evaluated by flow cytometry using a commercial monoclonal antibody specifically targeting this viral antigen (*Figure 19*). This approach allowed monitoring of viral entry and replication in host cells under different treatment conditions. To further assess the reproducibility of the assay and better characterize the inhibitory effect of LB-1, results from peptide-treated cells were directly compared with those obtained using human serum containing neutralizing antibodies specific for the same viral strain. As shown in *Figure 18*, Omicron BA.5 variant infection of Caco-2 cells was markedly reduced in the presence of LB-1 in a clear dose-dependent manner. Specifically, cells treated with the highest tested concentration of LB-1 (40 µM) displayed a significant reduction in fluorescence signal of the viral N protein, while cells treated with 20 µM showed a moderate but still significant decrease. These findings indicate that LB-1 exerts a measurable inhibitory effect on SARS-CoV-2 infection *in vitro*, supporting its potential as an antiviral agent.

5. CONCLUSIONS

The continuous evolution of SARS-CoV-2 and the persistent challenges posed by COVID-19 and long-COVID have highlighted the limitations of relying exclusively on currently approved DAAs. As we have seen throughout the pandemic, the ability of the virus to acquire mutations leads to immune evasion and therapeutic acquired resistance. For this reason, there is the need of innovative approaches that can maintain efficacy against emerging variants while providing enhanced protection for vulnerable populations. This thesis has addressed these challenges by investigating two promising approaches: the synergistic combination of existing antiviral drugs and the development of host-targeting compounds that interfere with viral entry mechanisms. The investigation of drug combinations revealed evidence that synergistic interactions between approved antivirals can enhance therapeutic efficacy. While our analysis of NRM, RMD, and EIDD-1931 combinations showed predominantly additive effects when evaluated across the entire concentration range, the identification of specific synergistic concentration provided crucial insights into optimal dosing strategies. The fact that the potency of NRM could be enhanced by up to 140-fold when combined with RMD against the highly divergent BQ.1.1 variant represents a particularly significant finding. This result suggests that combination therapy could be useful to reduce drug dosages while maintaining or even improving antiviral efficacy, potentially addressing concerns about drug toxicity and tolerability that have limited the clinical utility and usage of these antivirals. Moreover, the maintenance of synergistic effects against both the ancestral B.1 strain and the immune-evading BQ.1.1 variant is particularly encouraging from a clinical perspective as it may provide a more robust therapeutic approach that is less susceptible to viral evolution. Our findings are supported also by recent clinical observations from immunocompromised patients (Mikulska et al., 2023; Calderón-Parra et al., 2024), where combination therapies have shown promising outcomes in cases of persistent viral infection, supporting the significance of our in vitro findings.

Our exploration of RMD combined with mAbs revealed slightly different results, with additive to mild synergistic effects observed against the susceptible B.1 strain. While the synergy was generally lower than that observed with DAAs combinations, the cooperative activity between RMD and SOT was noteworthy. In addition, as this is an *in vitro* study, it doesn't consider the potential immune effector mechanisms of SOT, supporting a possible positive effect of this combination in the clinical practice in high-risk patients.

Regarding the HTAs, the investigation of the heparan sulfate proteoglycan-binding tetrapeptide LB-1 represents a different approach of antiviral intervention, as it targets the host cell machinery rather than viral components. The compound's selective activity against Omicron sublineages BA.1 and BA.5, with IC_{50} values in the low micromolar range, represents a proof-of-concept for host-targeting strategies that could complement existing direct-acting antivirals. The specificity of LB-1 activity against Omicron variants likely reflects the unique mutations in these strains that have enhanced their affinity for glycosaminoglycans. Mutations such as Q493R, Q498R, and Y505H, which substitute uncharged residues with basic ones, have altered the electrostatic properties of the spike protein, creating new opportunities for therapeutic intervention. Flow cytometry studies confirmed that LB-1 binds to host cells in a dose-dependent manner and that the binding can be competitively inhibited by heparin, supporting the proposed mechanism of action whereby the peptide competes with cellular heparan sulfate for viral binding sites.

As mentioned before, the demonstration of synergistic drug interactions provides a scientific foundation for combination therapy protocols that could be rapidly implemented in clinical practice, particularly for immuno-compromised patients who remain at high risk for severe COVID-19. The ability to achieve enhanced antiviral effects at lower drug concentrations could address some of the tolerability issues that have limited the broader adoption of certain antivirals, potentially expanding their utility to populations who might otherwise be unable to tolerate full therapeutic doses.

The host-targeting approach of LB-1 offers a complementary strategy that could be particularly valuable in prophylactic settings or as part of combination regimens. The potential for local delivery through intranasal sprays or inhalation could maximize antiviral effects while minimizing systemic exposure, addressing safety concerns that often arise with novel therapeutic agents. Moreover, the targeting of host cellular machinery rather than viral proteins provides a higher genetic barrier to resistance development, as viruses cannot readily mutate host cell components.

However, several important limitations must be acknowledged in interpreting these results. All experiments were conducted using *in vitro* cell culture systems, which, while providing valuable mechanistic insights, have not yet been tested *in vivo* and we don’t know the effect on the complex pathophysiology of SARS-CoV-2 infection in humans and mices. The role of the

immune system in viral clearance, in tissue-specific expression patterns of target receptors, and the influence of comorbid conditions on drug efficacy remain to be evaluated. Additionally, our study could be extended to further investigate the effect on other viral variants, understanding betterer their evolutionary pattern.

Looking forward, the strategies investigated in this PhD thesis represent important additions to the evolving arsenal of COVID-19 therapeutics. The synergistic combination approach of already approved drugs offers the possibility of a rapid clinical application, as their individual safety has already been tested. This could provide rapid benefits for high-risk patients while serving as a bridge to more advanced therapeutic approaches.

The host-targeting strategy, while requiring longer development timelines, offers the promise of more durable therapeutic effects that are less susceptible to viral evolution, for this reason continuing our tests using LB-1 in combination with previously approved DAAs could be a promising approach. In addition, while antivirals may lose their efficacy as the virus evolves through the development of resistance mechanisms, the combination of multiple therapeutic approaches that target different steps of the viral life cycle offers the prospect of maintaining clinical benefit across viral variants and patient populations. The work presented in this thesis provides a foundation for this comprehensive approach, demonstrating both the scientific feasibility and clinical potential of these innovative therapeutic strategies.

The goal of this research is to contribute to a more comprehensive and resilient therapeutic framework for managing SARS-CoV-2 infections. While antivirals used alone may lose efficacy as the virus evolves and acquires resistance, the combination of multiple therapeutics targeting different steps of the viral life cycle offer the prospect of maintaining clinical benefit across viral variants and patient populations. These findings support the potential of integrated antiviral strategies to provide broader and more durable protection, particularly for vulnerable populations, and lay the groundwork for future translational research.

6. REFERENCES

1. A. Gupta, Y. Gonzalez-Rojas, E. Juarez, M.C. Casal, J. Moya, D.R. Falci, E. Sarkis, J. Solis, H. Zheng, N. Scott, A.L. Cathcart, C.M. Hebner, J. Sager, E. Mogalian, C. Tipple, A. Peppercorn, E. Alexander, P.S. Pang, A. Free, C. Brinson, M. Aldinger, A.E. Shapiro, for the C.-I. Investigators, Early Covid-19 Treatment With SARS-CoV-2 Neutralizing Antibody Sotrovimab, MedRxiv. (2021) 2021.05.27.21257096. 10.1101/2021.05.27.21257096.
2. Andersen, K.G., Rambaut, A., Lipkin, W.I. et al. The proximal origin of SARS-CoV-2. Nat Med **26,** 450–452 (2020). https://doi.org/10.1038/s41591-020-0820-9.
3. Bai C, Zhong Q, Gao GF. Overview of SARS-CoV-2 genome-encoded proteins. Sci China Life Sci. 2022 Feb;65(2):280-294. doi: 10.1007/s11427-021-1964-4. Epub 2021 Aug 10. PMID: 34387838; PMCID: PMC8362648.
4. Bayati, A., Kumar, R., Francis, V., & McPherson, P. S. (2021). SARS-CoV-2 infects cells after viral entry via clathrin-mediated endocytosis. Journal of Biological Chemistry, 296.
5. Bianchi, M., Benvenuto, D., Giovanetti, M., Angeletti, S., Ciccozzi, M., Pascarella, S., 2020. Sars-CoV-2 Envelope and Membrane Proteins: Structural Differences Linked to Virus Characteristics? Biomed Res. Int. https://doi.org/10.1155/2020/4389089
6. Boni MF, Lemey P, Jiang X, Lam TT, Perry BW, Castoe TA, Rambaut A, Robertson DL. Evolutionary origins of the SARS-CoV-2 sarbecovirus lineage responsible for the COVID-19 pandemic. Nat Microbiol. 2020 Nov;5(11):1408-1417. doi: 10.1038/s41564-020-0771-4. Epub 2020 Jul 28. PMID: 32724171.
7. Calderón-Parra J, Gutiérrez-Villanueva A, Ronda-Roca G, Jimenez MLM, de la Torre H, Ródenas-Baquero M, Paniura-Pinedo M, Lozano-Llano C, Pintos-Pascual I, Fernández-Cruz A, Ramos-Martínez A, Muñez-Rubio E. Efficacy and safety of antiviral plus anti-spike monoclonal antibody combination therapy vs. monotherapy for high-risk immunocompromised patients with mild-to-moderate SARS-CoV2 infection during the Omicron era: A prospective cohort study. Int J Antimicrob Agents. 2024 Mar;63(3):107095. doi: 10.1016/j.ijantimicag.2024.107095. Epub 2024 Jan 18. PMID: 38244814.
8. Cárdenas G, Fragoso G, Sciutto E. Neuroinflammation in Severe Acute Respiratory Syndrome Coronavirus-2 (SARS-CoV-2) infection: Pathogenesis and clinical manifestations. Curr Opin Pharmacol. 2022 Apr;63:102181. doi: 10.1016/j.coph.2021.12.008. Epub 2021 Dec 31. PMID: 35074661; PMCID: PMC8782621.
9. Chavda VP, Kapadia C, Soni S, Prajapati R, Chauhan SC, Yallapu MM, Apostolopoulos V. A global picture: therapeutic perspectives for COVID-19. Immunotherapy. 2022 Apr;14(5):351-371. doi: 10.2217/imt-2021- 0168. Epub 2022 Feb 21. PMID: 35187954; PMCID: PMC8884157.
10. Chen B, Farzan M, Choe H. SARS-CoV-2 spike protein: structure, viral entry and variants. Nat Rev Microbiol. 2025 Jul;23(7):455-468. doi: 10.1038/s41579-025-01185-8. Epub 2025 May 6. PMID: 40328900.
11. Cho J, Shin Y, Yang JS, Kim JW, Kim KC, Lee JY. Evaluation of antiviral drugs against newly emerged SARS-CoV-2 Omicron subvariants. Antiviral Res. 2023 Jun;214:105609. doi: 10.1016/j.antiviral.2023.105609. Epub 2023 Apr 20. PMID: 37086978; PMCID: PMC10118056.

12. Coutard B, Valle C, de Lamballerie X, Canard B, Seidah NG, Decroly E. The spike glycoprotein of the new coronavirus 2019-nCoV contains a furin-like cleavage site absent in CoV of the same clade. Antiviral Res. 2020 Apr;176:104742. doi: 10.1016/j.antiviral.2020.104742. Epub 2020 Feb 10. PMID: 32057769; PMCID: PMC7114094
13. Deeks ED. Casirivimab/Imdevimab: First Approval. Drugs. 2021 Nov;81(17):2047-2055. doi: 10.1007/s40265-021-01620-z. PMID: 34716907; PMCID: PMC8556815.
14. Del Borgo C, Garattini S, Bortignon C, Carraro A, Di Trento D, Gasperin A, Grimaldi A, De Maria SG, Corazza S, Tieghi T, Belvisi V, Kertusha B, De Masi M, D'Onofrio O, Bagaglini G, Bonanni G, Zuccalà P, Fabietti P, Tortellini E, Guardiani M, Spagnoli A, Marocco R, Alunni Fegatelli D, Lichtner M, Latina Covid-Group. Effectiveness, Tolerability and Prescribing Choice of Antiviral Molecules Molnupiravir, Remdesivir and Nirmatrelvir/r: A Real-World Comparison in the First Ten Months of Use. Viruses. 2023 Apr 21;15(4):1025. doi: 10.3390/v15041025. PMID: 37113006; PMCID: PMC10145588.
15. Durairajan SSK, Singh AK, Saravanan UB, Namachivayam M, Radhakrishnan M, Huang JD, Dhodapkar R, Zhang H. Gastrointestinal Manifestations of SARS-CoV-2: Transmission, Pathogenesis, Immunomodulation, Microflora Dysbiosis, and Clinical Implications. Viruses. 2023 May 24;15(6):1231. doi: 10.3390/v15061231. PMID: 37376531; PMCID: PMC10304713.
16. Eilts F, Bauer S, Fraser K, Dordick JS, Wolff MW, Linhardt RJ, Zhang F. The diverse role of heparan sulfate and other GAGs in SARS-CoV-2 infections and therapeutics. Carbohydr Polym. 2023 Jan 1;299:120167. doi: 10.1016/j.carbpol.2022.120167. Epub 2022 Sep 28. PMID: 36876764; PMCID: PMC9516881.
17. Flores-Vega VR, Monroy-Molina JV, Jiménez-Hernández LE, Torres AG, Santos-Preciado JI, Rosales-Reyes R. SARS-CoV-2: Evolution and Emergence of New Viral Variants. Viruses. 2022 Mar 22;14(4):653. doi: 10.3390/v14040653. PMID: 35458383; PMCID: PMC9025907.
18. Focosi D, Franchini M, Maggi F, Shoham S. COVID-19 therapeutics. Clin Microbiol Rev. 2024 Jun 13;37(2):e0011923. doi: 10.1128/cmr.00119-23. Epub 2024 May 21. PMID: 38771027; PMCID: PMC11237566.
19. Gelbach AL, Zhang F, Kwon SJ, Bates JT, Farmer AP, Dordick JS, Wang C, Linhardt RJ. Interactions between heparin and SARS-CoV-2 spike glycoprotein RBD from omicron and other variants. Front Mol Biosci. 2022 Aug 15;9:912887. doi: 10.3389/fmolb.2022.912887. PMID: 36046608; PMCID: PMC9420978.
20. Greenhalgh T, Sivan M, Perlowski A, Nikolich JŽ. Long COVID: a clinical update. Lancet. 2024 Aug 17;404(10453):707-724. doi: 10.1016/S0140-6736(24)01136-X. Epub 2024 Jul 31. PMID: 39096925.
21. Gribble, J., Stevens, L. J., Agostini, M. L., Anderson-Daniels, J., Chappell, J. D., Lu, X., & Denison, M. R. (2021). The coronavirus proofreading exoribonuclease mediates extensive viral recombination. PLoS pathogens, 17(1), e1009226.
22. Harrison AG, Lin T, Wang P. Mechanisms of SARS-CoV-2 Transmission and Pathogenesis. Trends Immunol. 2020 Dec;41(12):1100-1115. doi: 10.1016/j.it.2020.10.004. Epub 2020 Oct 14. PMID: 33132005; PMCID: PMC7556779.
23. Hoffmann M, Kleine-Weber H, Schroeder S, Krüger N, Herrler T, Erichsen S, Schiergens TS, Herrler G, Wu NH, Nitsche A, Müller MA, Drosten C, Pöhlmann S. SARS-CoV-2 Cell Entry Depends on ACE2 and TMPRSS2 and Is Blocked by a Clinically Proven Protease Inhibitor. Cell. 2020 Apr 16;181(2):271-280.e8. doi: 10.1016/j.cell.2020.02.052. Epub 2020 Mar 5. PMID: 32142651; PMCID: PMC7102627.

24. Iketani S, Liu L, Guo Y, Liu L, Chan JF, Huang Y, Wang M, Luo Y, Yu J, Chu H, Chik KK, Yuen TT, Yin MT, Sobieszczyk ME, Huang Y, Yuen KY, Wang HH, Sheng Z, Ho DD. Antibody evasion properties of SARS-CoV-2 Omicron sublineages. Nature. 2022 Apr;604(7906):553-556. doi: 10.1038/s41586-022-04594-4. Epub 2022 Mar 3. PMID: 35240676; PMCID: PMC9021018.
25. Jackson CB, Farzan M, Chen B, Choe H. Mechanisms of SARS-CoV-2 entry into cells. Nat Rev Mol Cell Biol. 2022 Jan;23(1):3-20. doi: 10.1038/s41580-021-00418-x. Epub 2021 Oct 5. PMID: 34611326; PMCID: PMC8491763
26. Kaku Y, Okumura K, Padilla-Blanco M, Kosugi Y, Uriu K, Hinay AA Jr, Chen L, Plianchaisuk A, Kobiyama K, Ishii KJ; Genotype to Phenotype Japan (G2P-Japan) Consortium; Zahradnik J, Ito J, Sato K. Virological characteristics of the SARS-CoV-2 JN.1 variant. Lancet Infect Dis. 2024 Feb;24(2):e82. doi: 10.1016/S1473-3099(23)00813-7. Epub 2024 Jan 3. PMID: 38184005.
27. Kirtipal N, Bharadwaj S, Kang SG. From SARS to SARS-CoV-2, insights on structure, pathogenicity and immunity aspects of pandemic human coronaviruses. Infect Genet Evol. 2020 Nov;85:104502. doi: 10.1016/j.meegid.2020.104502. Epub 2020 Aug 13. PMID: 32798769; PMCID: PMC7425554.
28. Lamers MM, Haagmans BL. SARS-CoV-2 pathogenesis. Nat Rev Microbiol. 2022 May;20(5):270-284. doi: 10.1038/s41579-022-00713-0. Epub 2022 Mar 30. PMID: 35354968.Mahdy, M. A., Younis, W., & Ewaida, Z. (2020). An overview of SARS-CoV-2 and animal infection. Frontiers in veterinary science, 7, 1084.
29. Lan, J., Ge, J., Yu, J. et al. Structure of the SARS-CoV-2 spike receptor-binding domain bound to the ACE2 receptor. Nature **581,** 215–220 (2020).
30. Liu J, Yu Y, Yang S, Jian F, Song W, Yu L, Shao F, Cao Y. Virological and antigenic characteristics of SARS-CoV-2 variants LF.7.2.1, NP.1, and LP.8.1. Lancet Infect Dis. 2025 Mar;25(3):e128-e130. doi: 10.1016/S1473-3099(25)00015-5. Epub 2025 Jan 28. PMID: 39889723.
31. Liu Y, Zhao X, Shi J, Wang Y, Liu H, Hu YF, Hu B, Shuai H, Yuen TT, Chai Y, Liu F, Gong HR, Li J, Wang X, Jiang S, Zhang X, Zhang Y, Li X, Wang L, Hartnoll M, Zhu T, Hou Y, Huang X, Yoon C, Wang Y, He Y, Zhou M, Du L, Zhang X, Chan WM, Chen LL, Cai JP, Yuan S, Zhou J, Huang JD, Yuen KY, To KK, Chan JF, Zhang BZ, Sun L, Wang P, Chu H. Lineage-specific pathogenicity, immune evasion, and virological features of SARS-CoV-2 BA.2.86/JN.1 and EG.5.1/HK.3. Nat Commun. 2024 Oct 9;15(1):8728. doi: 10.1038/s41467-024-53033-7. PMID: 39379369; PMCID: PMC11461813.
32. Lu CW, Liu XF, Jia ZF. 2019-nCoV transmission through the ocular surface must not be ignored. Lancet. 2020 Feb 22;395(10224):e39. doi: 10.1016/S0140-6736(20)30313-5. Epub 2020 Feb 6. PMID: 32035510; PMCID: PMC7133551.Sallard, Erwan et al. “Tracing the origins of SARS-COV-2 in coronavirus phylogenies: a review.” Environmental chemistry letters vol. 19,2 (2021): 769-785
33. Lu S, Peluso MJ, Glidden DV, Davidson MC, Lugtu K, Pineda-Ramirez J, Tassetto M, Garcia-Knight M, Zhang A, Goldberg SA, Chen JY, Fortes-Cobby M, Park S, Martinez A, So M, Donovan A, Viswanathan B, Hoh R, Donohue K, McIlwain DR, Gaudiliere B, Anglin K, Yee BC, Chenna A, Winslow JW, Petropoulos CJ, Deeks SG, Briggs-Hagen M, Andino R, Midgley CM, Martin JN, Saydah S, Kelly JD. Early biological markers of post-acute sequelae of SARS-CoV-2 infection. Nat Commun. 2024 Aug 29;15(1):7466. doi: 10.1038/s41467-024-51893-7. PMID: 39198441; PMCID: PMC11358427.
34. Machhi, J., Herskovitz, J., Senan, A. M., Dutta, D., Nath, B., Oleynikov, M. D., Blomberg, W. R., Meigs, D. D., Hasan, M., Patel, M., Kline, P., Chang, R. C. C., Chang, L.,

Gendelman, H. E., & Kevadiya, B. D. (2020). The Natural History, Pathobiology, and Clinical Manifestations of SARS-CoV-2 Infections. In Journal of Neuroimmune Pharmacology (Vol. 15, Issue 3, pp. 359–386). Springer. https://doi.org/10.1007/s11481-020-09944-5.
35. Mahdy MAA, Younis W, Ewaida Z. An Overview of SARS-CoV-2 and Animal Infection. Front Vet Sci. 2020 Dec 11;7:596391. doi: 10.3389/fvets.2020.596391. PMID: 33363234; PMCID: PMC7759518.
36. Margarida Saramago, Cátia Bárria, Vanessa G. Costa, Caio S. Souza, Sandra C. Viegas, Susana Domingues, Diana Lousa, Cláudio M. Soares, Cecília M. Arraiano, Rute G. Matos.New targets for drug design: importance of nsp14/nsp10 complex formation for the 3'-5' exoribonucleolytic activity on SARS-CoV-2. The FEBS Journal, April 2021. https://doi.org/10.1111/febs.15815.
37. Meyerowitz EA, Richterman A, Gandhi RT, Sax PE. Transmission of SARS-CoV-2: A Review of Viral, Host, and Environmental Factors. Ann Intern Med. 2021 Jan;174(1):69-79. doi: 10.7326/M20-5008. Epub 2020 Sep 17. PMID: 32941052; PMCID: PMC7505025.
38. Meyerowitz EA, Richterman A, Gandhi RT, Sax PE. Transmission of SARS-CoV-2: A Review of Viral, Host, and Environmental Factors. Ann Intern Med. 2021 Jan;174(1):69-79. doi: 10.7326/M20-5008. Epub 2020 Sep 17. PMID: 32941052; PMCID: PMC7505025.
39. Meyerowitz EA, Richterman A. SARS-CoV-2 Transmission and Prevention in the Era of the Delta Variant. Infect Dis Clin North Am. 2022 Jun;36(2):267-293. doi: 10.1016/j.idc.2022.01.007. Epub 2022 Feb 1. PMID: 35636900; PMCID: PMC8806027.
40. Meyerowitz EA, Richterman A. SARS-CoV-2 Transmission and Prevention in the Era of the Delta Variant. Infect Dis Clin North Am. 2022 Jun;36(2):267-293. doi: 10.1016/j.idc.2022.01.007. Epub 2022 Feb 1. PMID: 35636900; PMCID: PMC8806027.
41. Mikulska M, Sepulcri C, Dentone C, Magne F, Balletto E, Baldi F, Labate L, Russo C, Mirabella M, Magnasco L, Di Grazia C, Ghiggi C, Raiola AM, Giacobbe DR, Vena A, Beltramini S, Bruzzone B, Lemoli RM, Angelucci E, Bassetti M. Triple Combination Therapy With 2 Antivirals and Monoclonal Antibodies for Persistent or Relapsed Severe Acute Respiratory Syndrome Coronavirus 2 Infection in Immunocompromised Patients. Clin Infect Dis. 2023 Jul 26;77(2):280-286. doi: 10.1093/cid/ciad181. PMID: 36976301.
42. Naqvi AAT, Fatima K, Mohammad T, Fatima U, Singh IK, Singh A, Atif SM, Hariprasad G, Hasan GM, and Hassan MI. Insights into SARS-CoV-2 genome, structure, evolution, pathogenesis and therapies: Structural genomics approach. Biochim Biophys Acta Mol Basis Dis. 2020 Oct 1; 1866(10):165878. Doi: 10.1016/j.bbadis.2020.165878. Epub 2020 Jun 13. PMID: 32544429; PMCID: PMC7293463.
43. Neerukonda SN, Katneni U. A Review on SARS-CoV-2 Virology, Pathophysiology, Animal Models, and Anti-Viral Interventions. Pathogens. 2020 May 29;9(6):426. doi: 10.3390/pathogens9060426. PMID: 32485970; PMCID: PMC7350325.
44. Paiardi G, Richter S, Oreste P, Urbinati C, Rusnati M, Wade RC. The binding of heparin to spike glycoprotein inhibits SARS-CoV-2 infection by three mechanisms. J Biol Chem. 2022 Feb;298(2):101507. doi: 10.1016/j.jbc.2021.101507. Epub 2021 Dec 18. PMID: 34929169; PMCID: PMC8683219.
45. Planas D, Staropoli I, Michel V, Lemoine F, Donati F, Prot M, Porrot F, Guivel-Benhassine F, Jeyarajah B, Brisebarre A, Dehan O, Avon L, Boland WH, Hubert M, Buchrieser J, Vanhoucke T, Rosenbaum P, Veyer D, Péré H, Lina B, Trouillet-Assant S; COVID-SER

study group; Hocqueloux L, Prazuck T, Simon-Loriere E, Schwartz O. Distinct evolution of SARS-CoV-2 Omicron XBB and BA.2.86/JN.1 lineages combining increased fitness and antibody evasion. bioRxiv [Preprint]. 2024 Feb 9:2023.11.20.567873. doi: 10.1101/2023.11.20.567873. Update in: Nat Commun. 2024 Mar 13;15(1):2254. doi: 10.1038/s41467-024-46490-7. PMID: 38045308; PMCID: PMC10690205.
46. Proal AD, Aleman S, Bomsel M, Brodin P, Buggert M, Cherry S, Chertow DS, Davies HE, Dupont CL, Deeks SG, Ely EW, Fasano A, Freire M, Geng LN, Griffin DE, Henrich TJ, Hewitt SM, Iwasaki A, Krumholz HM, Locci M, Marconi VC, Mehandru S, Muller-Trutwin M, Painter MM, Pretorius E, Price DA, Putrino D, Qian Y, Roan NR, Salmon D, Tan GS, VanElzakker MB, Wherry EJ, Van Weyenbergh J, Yonker LM, Peluso MJ. Targeting the SARS-CoV-2 reservoir in long COVID. Lancet Infect Dis. 2025 May;25(5):e294-e306. doi: 10.1016/S1473-3099(24)00769-2. Epub 2025 Feb 10. PMID: 39947217; PMCID: PMC12151306.
47. Qing E., Hantak M.P., Galpalli G.G., Gallagher T. (2020) Evaluating MERS-CoV Entry Pathways. In: Vijay R. (eds) MERS Coronavirus. Methods in Molecular Biology, vol 2099. Humana, New York, NY. doi.org/10.1007/978-1-0716-0211-9_2.
48. Rana R, Tripathi A, Kumar N, Ganguly NK. A Comprehensive Overview on COVID-19: Future Perspectives. Front Cell Infect Microbiol. 2021 Sep 14;11:744903.doi:10.3389/fcimb.2021.744903. PMID: 34595136; PMCID: PMC8476999.
49. Sallard E, Halloy J, Casane D, Decroly E, van Helden J. Tracing the origins of SARS-COV-2 in coronavirus phylogenies: a review. Environ Chem Lett. 2021;19(2):769-785. doi: 10.1007/s10311-020-01151-1. Epub 2021 Feb 4. PMID: 33558807; PMCID: PMC7859469.
50. Semenzato L, Botton J, Drouin J, Baricault B, Bertrand M, Jabagi MJ, Cuenot F, Vu SL, Dray-Spira R, Weill A, Zureik M. Characteristics associated with the residual risk of severe COVID-19 after a complete vaccination schedule: A cohort study of 28 million people in France. Lancet Reg Health Eur. 2022 Aug;19:100441. doi: 10.1016/j.lanepe.2022.100441. Epub 2022 Jun 30. PMID: 35789881; PMCID: PMC9243470.
51. Singh D, Yi SV. On the origin and evolution of SARS-CoV-2. Exp Mol Med. 2021 Apr;53(4):537-547. doi: 10.1038/s12276-021-00604-z. Epub 2021 Apr 16. PMID: 33864026; PMCID: PMC8050477.
52. Stein SR, Ramelli SC, Grazioli A, Chung JY, Singh M, Yinda CK, Winkler CW, Sun J, Dickey JM, Ylaya K, Ko SH, Platt AP, Burbelo PD, Quezado M, Pittaluga S, Purcell M, Munster VJ, Belinky F, Ramos-Benitez MJ, Boritz EA, Lach IA, Herr DL, Rabin J, Saharia KK, Madathil RJ, Tabatabai A, Soherwardi S, McCurdy MT; NIH COVID-19 Autopsy Consortium; Peterson KE, Cohen JI, de Wit E, Vannella KM, Hewitt SM, Kleiner DE, Chertow DS. SARS-CoV-2 infection and persistence in the human body and brain at autopsy. Nature. 2022 Dec;612(7941):758-763. doi: 10.1038/s41586-022-05542-y. Epub 2022 Dec 14. PMID: 36517603; PMCID: PMC9749650.
53. Taylor PC, Adams AC, Hufford MM, de la Torre I, Winthrop K, Gottlieb RL. Neutralizing monoclonal antibodies for treatment of COVID-19. Nat Rev Immunol. 2021 Jun;21(6):382-393. doi: 10.1038/s41577-021-00542-x. Epub 2021 Apr 19. PMID: 33875867; PMCID: PMC8054133.
54. Tebha SS, Tameezuddin A, Bajpai S, Zaidi AK. SARS-CoV-2-Virus structure and life cycle. Prog Mol Biol Transl Sci. 2024;202:1-23. doi: 10.1016/bs.pmbts.2023.09.001. Epub 2024 Jan 4. PMID: 38237982.

55. Touret F, Giraud E, Bourret J, Donati F, Tran-Rajau J, Chiaravalli J, Lemoine F, Agou F, Simon-Lorière E, van der Werf S, de Lamballerie X. Enhanced neutralization escape to therapeutic monoclonal antibodies by SARS-CoV-2 omicron sub-lineages. iScience. 2023 Apr 21;26(4):106413. doi: 10.1016/j.isci.2023.106413. Epub 2023 Mar 15. PMID: 36968074; PMCID: PMC10015083.
56. Trilla A, Trilla G, Aldea M, Vilella A. What Is Next for COVID-19 Vaccination? Semin Respir Crit Care Med. 2025 Feb;46(1):82-94. doi: 10.1055/a-2531-1211. Epub 2025 Mar 31. PMID: 40164121.
57. Turtle L, Thorpe M, Drake TM, Swets M, Palmieri C, Russell CD, Ho A, Aston S, Wootton DG, Richter A, de Silva TI, Hardwick HE, Leeming G, Law A, Openshaw PJM, Harrison EM; ISARIC4C investigators; Baillie JK, Semple MG, Docherty AB. Outcome of COVID-19 in hospitalised immunocompromised patients: An analysis of the WHO ISARIC CCP-UK prospective cohort study. PLoS Med. 2023 Jan 31;20(1):e1004086. doi: 10.1371/journal.pmed.1004086. PMID: 36719907; PMCID: PMC9928075.
58. Vicenti, I., Zazzi, M., & Saladini, F. (2021). SARS-CoV-2 RNA-dependent RNA polymerase as a therapeutic target for COVID-19. Expert opinion on therapeutic patents, 31(4), 325-337.
59. V'kovski P, Kratzel A, Steiner S, Stalder H, Thiel V. Coronavirus biology and replication: implications for SARS-CoV-2. Nat Rev Microbiol. 2021 Mar;19(3):155-170. doi: 10.1038/s41579-020-00468-6. Epub 2020 Oct 28. PMID: 33116300; PMCID: PMC7592455.
60. Wagoner J, Herring S, Hsiang TY, Ianevski A, Biering SB, Xu S, Hoffmann M, Pöhlmann S, Gale M Jr, Aittokallio T, Schiffer JT, White JM, Polyak SJ. Combinations of Host- and Virus-Targeting Antiviral Drugs Confer Synergistic Suppression of SARS-CoV-2. Microbiol Spectr. 2022 Oct 26;10(5):e0333122. doi: 10.1128/spectrum.03331-22. Epub 2022 Oct 3. PMID: 36190406; PMCID: PMC9718484.
61. Wrapp, D., Wang, N., Corbett, K. S., Goldsmith, J. A., Hsieh, C. L., Abiona, O., ... & McLellan, J. S. (2020). Cryo-EM structure of the 2019-nCoV spike in the prefusion conformation. Science, 367(6483), 1260-1263.
62. Xie NN, Zhang WC, Chen J, Tian FB, Song JX. Clinical Characteristics, Diagnosis, and Therapeutics of COVID-19: A Review. Curr Med Sci. 2023 Dec;43(6):1066-1074. doi: 10.1007/s11596-023-2797-3. Epub 2023 Oct 14. PMID: 37837572.
63. Yadav T, Kumar S, Mishra G, Saxena SK. Tracking the COVID-19 vaccines: The global landscape. Hum Vaccin Immunother. 2023 Dec 31;19(1):2191577. doi: 10.1080/21645515.2023.2191577. Epub 2023 Mar 30. PMID: 36995773; PMCID: PMC10101659.
64. Yang H, Rao Z. Structural biology of SARS-CoV-2 and implications for therapeutic development. Nat Rev Microbiol. 2021 Nov;19(11):685-700. doi: 10.1038/s41579-021-00630-8. Epub 2021 Sep 17. PMID: 34535791; PMCID: PMC8447893.
65. Yao H, Song Y, Chen Y, Wu N, Xu J, Sun C, Zhang J, Weng T, Zhang Z, Wu Z, Cheng L, Shi D, Lu X, Lei J, Crispin M, Shi Y, Li L, Li S. Molecular Architecture of the SARS-CoV-2 Virus. Cell. 2020 Oct 29;183(3):730-738.e13. doi: 10.1016/j.cell.2020.09.018. Epub 2020 Sep 6. PMID: 32979942; PMCID: PMC7474903.
66. Zaidi AK, Dehgani-Mobaraki P. Long Covid. Prog Mol Biol Transl Sci. 2024;202:113-125. doi: 10.1016/bs.pmbts.2023.11.002. Epub 2024 Jan 3. PMID: 38237983.
67. Hahn F, Wangen C, Häge S, Peter AS, Dobler G, Hurst B, Julander J, Fuchs J, Ruzsics Z, Überla K, et al. IMU-838, a Developmental DHODH Inhibitor in Phase II for

Autoimmune Disease, Shows Anti-SARS-CoV-2 and Broad-Spectrum Antiviral Efficacy In Vitro. Viruses. 2020; 12(12):1394. https://doi.org/10.3390/v12121394
68. Schreiber A, Rodner F, Oberberg N, Anhlan D, Bletz S, Mellmann A, Planz O, Ludwig S. The host-targeted antiviral drug Zapnometinib exhibits a high barrier to the development of SARS-CoV-2 resistance. Antiviral Res. 2024 May;225:105840. doi: 10.1016/j.antiviral.2024.105840. Epub 2024 Mar 2. PMID: 38438015.
69. Schreiber A, Ludwig S. Host-targeted antivirals against SARS-CoV-2 in clinical development - Prospect or disappointment? Antiviral Res. 2025 Mar;235:106101. doi: 10.1016/j.antiviral.2025.106101. Epub 2025 Feb 7. PMID: 39923941.
70. He Y, Zhou J, Gao H, Liu C, Zhan P, Liu X. Broad-spectrum antiviral strategy: Host-targeting antivirals against emerging and re-emerging viruses. Eur J Med Chem. 2024 Feb 5;265:116069. doi: 10.1016/j.ejmech.2023.116069. Epub 2023 Dec 21. PMID: 38160620.
71. Zheng Y, Li S, Song K, Ye J, Li W, Zhong Y, Feng Z, Liang S, Cai Z, Xu K. A Broad Antiviral Strategy: Inhibitors of Human DHODH Pave the Way for Host-Targeting Antivirals against Emerging and Re-Emerging Viruses. Viruses. 2022 Apr 28;14(5):928. doi: 10.3390/v14050928. PMID: 35632670; PMCID: PMC9146014.
72. Wang L, Wang Z, Cao L, Ge K. Constructive strategies for drug delivery systems in antivirus disease therapy by biosafety materials. Biosaf Health. 2022 Jun;4(3):161-170. doi: 10.1016/j.bsheal.2022.03.008. Epub 2022 Mar 11. PMID: 35291339; PMCID: PMC8912974.
73. Carpinteiro A, Gripp B, Hoffmann M, Pöhlmann S, Hoertel N, Edwards MJ, Kamler M, Kornhuber J, Becker KA, Gulbins E. Inhibition of acid sphingomyelinase by ambroxol prevents SARS-CoV-2 entry into epithelial cells. J Biol Chem. 2021 Jan-Jun;296:100701. doi: 10.1016/j.jbc.2021.100701. Epub 2021 Apr 23. PMID: 33895135; PMCID: PMC8062550.
74. Hashimoto K. Overview of the potential use of fluvoxamine for COVID-19 and long COVID. Discov Ment Health. 2023;3(1):9. doi: 10.1007/s44192-023-00036-3. Epub 2023 Mar 21. PMID: 36968793; PMCID: PMC10029802.
75. Hahn F, Wangen C, Häge S, Peter AS, Dobler G, Hurst B, Julander J, Fuchs J, Ruzsics Z, Überla K, Jäck HM, Ptak R, Muehler A, Gröppel M, Vitt D, Peelen E, Kohlhof H, Marschall M. IMU-838, a Developmental DHODH Inhibitor in Phase II for Autoimmune Disease, Shows Anti-SARS-CoV-2 and Broad-Spectrum Antiviral Efficacy In Vitro. Viruses. 2020 Dec 5;12(12):1394. doi: 10.3390/v12121394. PMID: 33291455; PMCID: PMC7762174.
76. White KM, Rosales R, Yildiz S, Kehrer T, Miorin L, Moreno E, Jangra S, Uccellini MB, Rathnasinghe R, Coughlan L, Martinez-Romero C, Batra J, Rojc A, Bouhaddou M, Fabius JM, Obernier K, Dejosez M, Guillén MJ, Losada A, Avilés P, Schotsaert M, Zwaka T, Vignuzzi M, Shokat KM, Krogan NJ, García-Sastre A. Plitidepsin has potent preclinical efficacy against SARS-CoV-2 by targeting the host protein eEF1A. Science. 2021 Feb 26;371(6532):926-931. doi: 10.1126/science.abf4058. Epub 2021 Jan 25. PMID: 33495306; PMCID: PMC7963220.
77. Zhu Y, Binder J, Yurgelonis I, Rai DK, Lazarro S, Costales C, Kobylarz K, McMonagle P, Steppan CM, Aschenbrenner L, Anderson AS, Cardin RD. Generation of a VeroE6 Pgp gene knock out cell line and its use in SARS-CoV-2 antiviral study. Antiviral Res. 2022 Dec;208:105429. doi: 10.1016/j.antiviral.2022.105429. Epub 2022 Oct 5. PMID: 36208677; PMCID: PMC9533647.

78. Fiaschi L, Dragoni F, Schiaroli E, Bergna A, Rossetti B, Giammarino F, Biba C, Gidari A, Lai A, Nencioni C, Francisci D, Zazzi M, Vicenti I. Efficacy of Licensed Monoclonal Antibodies and Antiviral Agents against the SARS-CoV-2 Omicron Sublineages BA.1 and BA.2. Viruses. 2022 Jun 23;14(7):1374. doi: 10.3390/v14071374. PMID: 35891355; PMCID: PMC9321742.
79. Lei C, Yang J, Hu J, Sun X. On the Calculation of TCID50 for Quantitation of Virus Infectivity. Virol Sin. 2021 Feb;36(1):141-144. doi: 10.1007/s12250-020-00230-5. Epub 2020 May 26. PMID: 32458296; PMCID: PMC7973348.
80. Vicenti, I., Martina, M. G., Boccuto, A., De Angelis, M., Giavarini, G., Dragoni, F., ... & Radi, M. (2021). System-oriented optimization of multi-target 2, 6-diaminopurine derivatives: Easily accessible broad-spectrum antivirals active against flaviviruses, influenza virus and SARS-CoV-2. European journal of medicinal chemistry, 224, 113683.
81. Yadav B, Wennerberg K, Aittokallio T, Tang J. Searching for Drug Synergy in Complex Dose-Response Landscapes Using an Interaction Potency Model. Comput Struct Biotechnol J. 2015 Sep 25;13:504-13. doi: 10.1016/j.csbj.2015.09.001. Erratum in: Comput Struct Biotechnol J. 2017 Jul 25;15:387. doi: 10.1016/j.csbj.2017.07.003. PMID: 26949479; PMCID: PMC4759128.
82. Ianevski A, Giri AK, Aittokallio T. SynergyFinder 3.0: an interactive analysis and consensus interpretation of multi-drug synergies across multiple samples. Nucleic Acids Res. 2022 Jul 5;50(W1):W739-W743. doi: 10.1093/nar/gkac382. PMID: 35580060; PMCID: PMC9252834.
83. Giammarino F, Paletti C, Bartolini N, Fiaschi L, Biba C, Varasi I, Focà E, Gulminetti R, Ferrara M, Comi L, Vicenti I, Castagna A, Zazzi M, Saladini F; PRESTIGIO Study Group. Combined doravirine and islatravir cooperate to inhibit NRTI and NNRTI resistant HIV-1 in vitro. Antiviral Res. 2025 Jul;239:106157. doi: 10.1016/j.antiviral.2025.106157. Epub 2025 Apr 18. PMID: 40254262.
84. Biba C, Fiaschi L, Varasi I, Paletti C, Bartolini N, Zazzi M, Vicenti I, Saladini F. A Comparison of Sanger Sequencing and Amplicon-Based Next Generation Sequencing Approaches for the Detection of HIV-1 Drug Resistance Mutations. Viruses. 2024 Sep 14;16(9):1465. doi: 10.3390/v16091465. Erratum in: Viruses. 2025 Jul 29;17(8):1059. doi: 10.3390/v17081059. PMID: 39339940; PMCID: PMC11437444.
85. Varasi I, Lai A, Fiaschi L, Bergna A, Gatti A, Caimi B, Biba C, Della Ventura C, Balotta C, Riva A, Zehender G, Zazzi M, Vicenti I. Neutralizing antibodies response to novel SARS-CoV-2 omicron sublineages in long-term care facility residents after the fourth dose of monovalent BNT162b2 COVID-19 vaccination. J Infect. 2023 Sep;87(3):270-272. doi: 10.1016/j.jinf.2023.06.019. Epub 2023 Jun 30. PMID: 37394012.
86. Fiaschi L, Dragoni F, Schiaroli E, Bergna A, Rossetti B, Giammarino F, Biba C, Gidari A, Lai A, Nencioni C, Francisci D, Zazzi M, Vicenti I. Efficacy of Licensed Monoclonal Antibodies and Antiviral Agents against the SARS-CoV-2 Omicron Sublineages BA.1 and BA.2. Viruses. 2022 Jun 23;14(7):1374. doi: 10.3390/v14071374. PMID: 35891355; PMCID: PMC9321742.
87. Milano G, Marchi S, Vicenti I, Biba C, Fiaschi L, Trombetta CM, Lazzeri G, Montomoli E, Manini I. SARS-CoV-2 and influenza virus coinfections in the Tuscan population during the 2021/2022 influenza season. J Prev Med Hyg. 2024 Mar 31;65(1):E11-E16. doi: 10.15167/2421-4248/jpmh2024.65.1.3179. PMID: 38706768; PMCID: PMC11066830.
88. Vicenti I, Basso M, Pirola N, Bragato B, Rossi MC, Giobbia M, Pascoli S, Vinci A, Caputo S, Varasi I, Biba C, Fiaschi L, Zazzi M, Parisi SG. SARS-CoV-2 Neutralizing Antibodies to

B.1 and to BA.5 Variant after Booster Dose of BNT162b2 Vaccine in HIV Patients COVID-Naïve and on Successful Antiretroviral Therapy. Vaccines (Basel). 2023 Apr 20;11(4):871. doi: 10.3390/vaccines11040871. PMID: 37112782; PMCID: PMC10144758.
89. Rossi S, Deidda G, Fiaschi L, Ibba R, Pieroni M, Dichiara M, Carullo G, Butini S, Ramunno A, Brogi S, Lolicato M, Arrigoni C, Cabella N, Bavagnoli L, Maga G, Varasi I, Biba C, Vicenti I, Gemma S, Crespan E, Zazzi M, Campiani G. Synthesis and biological investigation of peptidomimetic SARS-CoV-2 main protease inhibitors bearing quinoline-based heterocycles at P_3. Arch Pharm (Weinheim). 2025 Jan;358(1):e2400812. doi: 10.1002/ardp.202400812. PMID: 39873316.
90. Amodeo D, Marchi S, Fiaschi L, Raucci L, Biba C, Salvestroni V, Trombetta CM, Manini I, Zazzi M, Montomoli E, Vicenti I, Cevenini G, Messina G. Analysis of the SARS-CoV-2 inactivation mechanism using violet-blue light (405 nm). Appl Environ Microbiol. 2025 Jun 18;91(6):e0040325. doi: 10.1128/aem.00403-25. Epub 2025 May 14. PMID: 40366184; PMCID: PMC12175510.
91. Fiaschi L, Biba C, Varasi I, Bartolini N, Paletti C, Giammarino F, Saladini F, Zazzi M, Vicenti I. In Vitro Combinatorial Activity of Direct Acting Antivirals and Monoclonal Antibodies against the Ancestral B.1 and BQ.1.1 SARS-CoV-2 Viral Variants. Viruses. 2024 Jan 23;16(2):168. doi: 10.3390/v16020168. PMID: 38399944; PMCID: PMC10892871.

7. PUBLISHED PAPERS

AMERICAN SOCIETY FOR MICROBIOLOGY | Applied and Environmental Microbiology

| Virology | Full-Length Text

Analysis of the SARS-CoV-2 inactivation mechanism using violet-blue light (405 nm)

Davide Amodeo,[1] Serena Marchi,[2] Lia Fiaschi,[1] Luisa Raucci,[3] Camilla Biba,[1] Valentina Salvestroni,[2] Claudia Maria Trombetta,[2] Ilaria Manini,[2] Maurizio Zazzi,[1] Emanuele Montomoli,[2,4] Ilaria Vicenti,[1] Gabriele Cevenini,[1] Gabriele Messina[2]

AUTHOR AFFILIATIONS See affiliation list on p. 16.

ABSTRACT The study evaluated the effects of violet-blue light (VBL) on cell viability and replication, carbonylation of three structural proteins (S, E, and N) and one non-structural protein (NSP13), and direct damage to the RNA of SARS-CoV-2. The virus was exposed to increasing doses of VBL along with influenza A and B viruses to compare their susceptibility. At the highest dose (21.6 J/cm^2), SARS-CoV-2 was significantly more susceptible to VBL than the influenza viruses, with a reduction in viral titer of 2.33 $\log_{10}$. Viral RNA did not show significant changes after exposure to VBL, as demonstrated by next-generation sequencing and real-time PCR quantification, suggesting that the inactivation process does not involve direct nucleic acid damage. To exclude the role of the culture suspension in the inactivation process, virus viability experiments were performed using different dilutions of Dulbecco's modified Eagle's medium (DMEM) in phosphate-buffered saline (PBS). The results indicated that the suspension medium played a secondary role in virus inactivation, as viability did not increase with increasing DMEM dilution. Subsequent tests with three different antioxidants (NAC, AsA, and SOD) at different concentrations prevented viral inactivation, from 99.99% to 85.43% (with SOD 0.003 mM). Carbonylation of S and E proteins was more pronounced when viruses were suspended in DMEM rather than PBS, although the tests demonstrated that the intrinsic properties of the viral membrane were a crucial element to consider in relation to its susceptibility to VBL.

IMPORTANCE Light-based disinfection methods are often used in combination with other cleaning methods due to their non-invasive nature, versatility, and environmental benefits. VBL is an effective approach as it induces the production of reactive oxygen species that reduce microbial viability. In this study, lipid peroxidation was identified as an important factor affecting the structural integrity and function of the viral envelope, reducing its ability to interact with host cells and consequently its ability to be infec tious. The lipid envelope of SARS-CoV-2, composed mainly of glycerophospholipids and lacking cholesterol and sphingolipids, appears to be the critical factor in its susceptibility, distinguishing it from influenza viruses, which have a lipid profile richer in components that protect against oxidative stress.

KEYWORDS violet-blue light, reactive oxygen species, lipid peroxidation, protein carbonylation, SARS-CoV-2 envelope

The COVID-19 pandemic caused a global health crisis between 2020 and 2023, resulting in over 7 million deaths by October 2024 (1). Its impact on public health continues to influence not only health outcomes but also socio-economic and political contexts (2).

Health authorities identified the virus responsible for the pandemic in January 2020, initially referring to it as "Coronavirus 2019-nCoV" and subsequently officially as

Editor Christopher A. Elkins, Centers for Disease Control and Prevention, Atlanta, Georgia, USA

Address correspondence to Davide Amodeo, davide.amodeo@dbm.unisi.it.

E.M. is founder and Chief Scientific Officer of VisMederi Srl and VisMederi Research Srl. The other authors declare no competing interests.

Received 18 February 2025
Accepted 15 April 2025
Published 14 May 2025

SARS-CoV-2 (3). It is a single-stranded, positive-sense RNA (ssRNA+) beta-coronavirus with a genome size of approximately 30 kb, which is 80% shared with SARS-CoV (4). It encodes 11 accessory proteins (ORF3a, ORF3b, ORF3c, ORF3d, ORF6, ORF7a, ORF7b, ORF8, ORF9b, ORF9c, and ORF10), 16 non-structural proteins (NSP1–16), and 4 structural proteins (Spike [S], Envelope [E], Membrane [M], and Nucleocapsid [N]) (5). Structural proteins are essential components of the SARS-CoV-2 virion, while non-structural and accessory proteins contribute to the replication of SARS-CoV-2 RNA within the cell through different mechanisms (6). In addition, coronaviruses use a variety of host factors to infect and replicate within cells, and the expression patterns of these factors are thus co-determinants of viral tropism (4). Once the large RNA genome enters the cell and begins to translate, a cytoplasmic replication cycle begins, utilizing diverse strategies to enhance viral gene expression at both transcriptional and translational levels (7).

In response to this high replicative and adaptive capacity of the virus, international health organizations had to quickly implement appropriate preventive measures to contain and control the pandemic spread of SARS-CoV-2 (8). These included preventive and mandatory isolation of suspected or infected individuals, use of hand sanitizer, covering the nose and mouth when coughing and sneezing (to reduce aerosol transmission), use of face masks, reduction of hand-to-face contact, and use of disposable gloves to avoid direct contact with surfaces (9). In addition, several disinfection techniques have been employed to inactivate SARS-CoV-2 from contaminated surfaces or air. It is widely recognized that the virus is highly susceptible to most alcohol-based hand sanitizing solutions and detergents (10), as well as physical agents like heat (11) and UV radiation (12).

Disinfection with UV light sources has been widely employed for several decades, primarily with UVC lamps (254 nm), to inactivate pathogenic microorganisms in air, on surfaces, and in water (13–15). For example, UV light sources can provide continuous decontamination of air and surface from many respiratory pathogens, including influenza viruses (16). However, the recent pandemic has boosted this scientific sector and accelerated the technological shift from mercury vapour lamps to light-emitting diodes (LEDs), promoting a transition that had been stagnant for several years and is now increasingly recognized, particularly from an environmental perspective (17–19). The combination of (i) more versatile and longer-lasting light sources (compared to traditional lamps), (ii) an unexpected global health emergency, and (iii) a new airborne pathogen brought renewed attention to the field and encouraged the scientific community to focus on wavelengths that were previously difficult to test and expensive to implement in standard disinfection procedures (20–23). Wavelengths such as far-UVC (222 nm) and violet-blue light (VBL; at 405–450 nm) gained popularity in SARS-CoV-2 studies, during and after the pandemic, due to their significant germicidal efficacy (24, 25). Furthermore, far-UVC light exhibits a restricted penetration depth in biological tissues, primarily addressing surface pathogens while leaving deeper skin layers unaffected (26). Conversely, radiation within the 405–450 nm spectrum, especially around 405 nm, penetrates tissues more easily and exhibits antimicrobial properties by activating endogenous and exogenous photoinitiators that lead to the production of reactive oxygen species (ROS) within cells (27, 28). When viruses, bacteria, and fungi are exposed to VBL, photosensitizers such as porphyrins and flavin absorb photons, leading to the formation of ROS such as singlet oxygen ($^1O_2$) and hydrogen peroxide (H_2O_2) (29). ROS can cause damage to vital cellular components, including nucleic acids, proteins, and membrane lipids, ultimately leading to cell death (28).

Although numerous studies have demonstrated the efficacy of VBL on SARS-CoV-2, the hypotheses put forward to describe the possible mechanism of inactivation following the virus's exposure to radiation have so far remained inconclusive (30–32). Some of these studies focus on the possible photo-degradation of S protein as the primary cause of the virus inactivation. Other studies attribute the main source of ROS generation and oxidative stress promotion to the suspension medium in which the virus resides during the experiments (31, 33). This interpretation, however, would

not fully explain the different susceptibilities of other RNA viruses to VBL (34) and, more generally, why radiation appears to reduce and/or inactivate viruses (including SARS-CoV-2), bacteria, and moulds, even in in vivo studies in which the experimental factors investigated, such as culture medium and suspension, are absent (35, 36).

The aim of the study was to assess the virus inactivation mechanism using VBL (at 405 nm) by evaluating: (i) the change in viral titer of SARS-CoV-2 compared to influenza A and B viruses (IAVs and IBVs) after light exposure; (ii) the replicative cycle of the viral particle and the possible presence of oxidative stress caused by radiation; (iii) qualitative and quantitative changes in the structural components of the virus (ssRNA and proteins); and (iv) the impact of the suspension medium (Dulbecco's modified Eagle's medium [DMEM]) on virus viability.

RESULTS

$TCID_{50}$ reduction of SARS-CoV-2 and influenza A and B by VBL

The results obtained by exposing the different viruses to VBL at different doses of light energy had a significantly different impact on virus replication depending on the virus tested. As shown in Table 1, a significantly higher log_{10} reduction in $TCID_{50}$/mL was achieved for SARS-CoV-2 compared with influenza viruses. Specifically, the $TCID_{50}$/mL log reduction for SARS-CoV-2 was 0.41 log_{10} (SD = 0.14) after 22′30″ (dose of 5.4 J/cm^2), 1.33 log_{10} (SD = 0.2) after 45′ (dose of 10.8 J/cm^2), and 2.33 log_{10} (SD = 0.14) after 90′ (dose of 21.6 J/cm^2) exposure. For IAV, the $TCID_{50}$/mL mean reduction was almost 0 after 22′30″, 0.13 log_{10} (SD = 0.22) after 45′, and 0.16 log_{10} (SD = 0.26) after 90′. The results for IBV were nearly identical. In fact, the $TCID_{50}$/mL log reduction was again zero after 22′30″, 0.12 log_{10} (SD = 0.25) after 45″, and 0.17 log_{10} (SD = 0.14) after 90′.

Based on SARS-CoV-2 viral load reduction results, all further tests on the inactivation mechanism of SARS-CoV-2 were performed by exposing the virus to VBL for 90 min.

Impact of VBL on SARS-CoV-2 dsRNA and N/S protein expression and localization

To investigate the impact of VBL on different steps of viral replication, the number of viable cells and the amount and localization of viral dsRNA (indicating initiation of viral RNA transcription) and S and N proteins were assessed following VBL exposure.

Experiments were run after a 90′ VBL exposure while the virus control culture was sampled at 4, 8, and 12 h post-infection. As reported in Fig. 1, VBL exposure dramatically and comparably decreased the number of dsRNA-, S-, and N-positive cells, recovering the number of viable cells (Fig. 1A).

TABLE 1 $TCID_{50}$/mL mean reduction of SARS-CoV-2 and influenza A and B with VBL[a]

Exposure time	Energy (J/cm^2)	Virus	$TCID_{50}$/mL CV (Log_{10})	$TCID_{50}$/mL VBL exposure (Log_{10})	$TCID_{50}$/mL reduction dose (Log10)	Lower CI	Upper CI
22′30″	5.4	SARS-CoV-2	5.50	5.08	0.42	0.25	0.58
		IAV	8.75	8.75	0.00	0.00	0.14
		IBV	7.88	7.88	0.00	0.00	0.14
45′	10.8	SARS-CoV-2	5.49	4.16	1.33	1.01	1.66
		IAV	8.88	8.75	0.13	0.00	0.37
		IBV	7.75	7.63	0.12	0.00	0.40
90′	21.6	SARS-CoV-2	5.49	3.16	2.33	2.17	2.50
		IAV	8.75	8.59	0.16	0.00	0.46
		IBV	7.13	6.96	0.17	0.00	0.33

[a]Experiments were performed in triplicate for each virus exposed to VBL. The data shown in the table for both virus control (CV) and exposed virus are the means of the results obtained. The $TCID_{50}$/mL reduction, together with the 95% confidence interval (CI), was obtained by calculating the mean ratio of CV to virus exposed in each experiment.

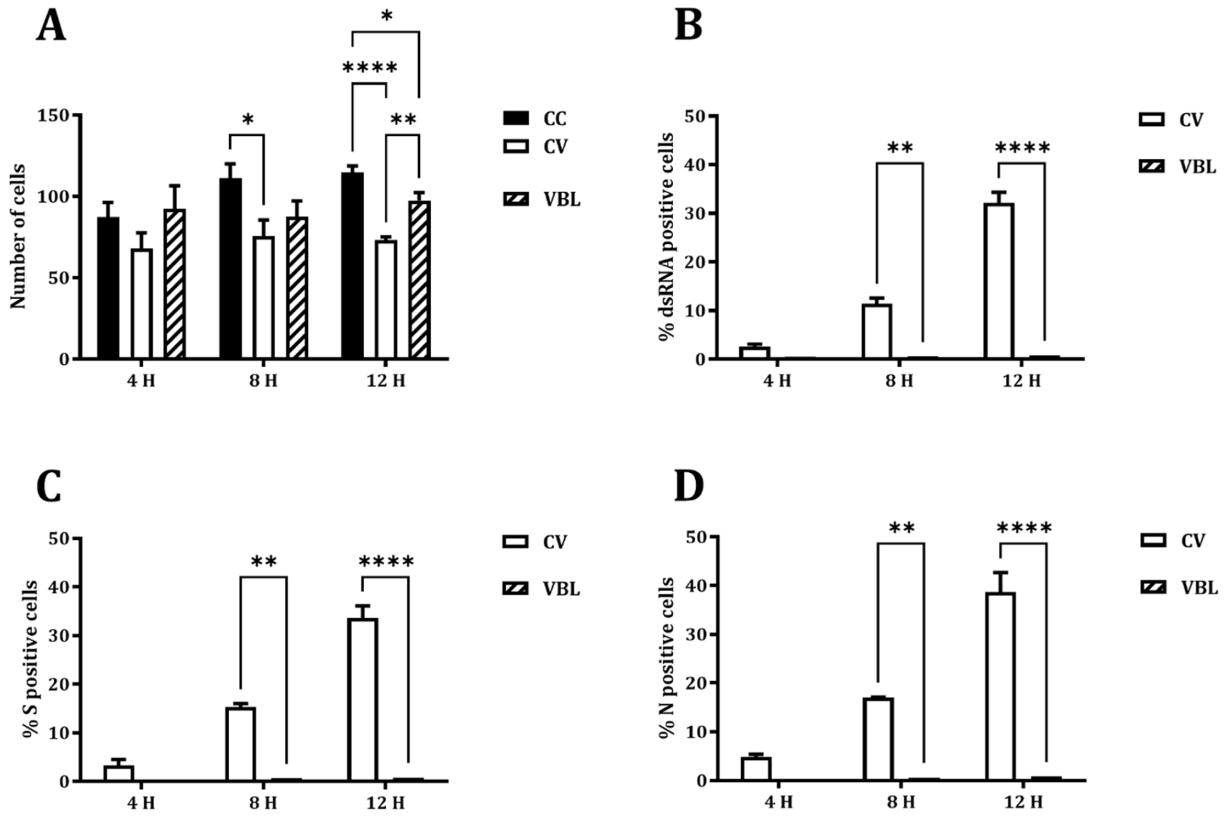

FIG 1 Effects of VBL exposure on the viral replication and protein expression of SARS-CoV-2. (A) VERO E6 cells stained with DAPI. (B) Expression of dsRNA. (C) Expression of viral S protein. (D) Expression of viral N protein. Cells were counted at 40× magnification in five random fields/slide for two replicates. Number of cells was expressed as total number; positive cells were expressed as percentage (%). Comparisons were performed by two-way ANOVA (*P < 0.05; **P < 0.01; ****P < 0.0001). CC, cell control; CV, virus control; VBL, VBL-exposed.

The time-course localization of dsRNA and viral proteins was studied through confocal microscopy. In virus control cultures, dsRNA is expressed from 4 h post-infec tion, increasing at 8 and 12 h post-infection, and localizes in peri-nuclear foci. N protein is expressed from 4 h post-infection and increases at 8 h post-infection, involving the whole cytosolic compartment. At 12 h post-infection, it moves from the cytosolic compartment toward the cell membrane. S protein is expressed at 4 h post-infection in a perinuclear location and increases at 8 and 12 h post-infection involving the whole cytosolic compartment (Fig. 2). Moreover, the co-localization of N and S starts at 8 h after infection and increases after 12 h (Fig. 3). After 90′ VBL exposure, dsRNA and viral protein expression was greatly reduced; however, similar localization patterns as for virus control were observed (Fig. 2), suggesting that VBL may globally impact cell infection but does not alter the expression and localization of the viral components.

SARS-CoV-2 RNA quantitative and qualitative analysis

Real-time PCR quantification (qRT-PCR) detected comparable levels of SARS-CoV-2 RNA in the RNA extracts obtained from the 1:3 diluted 90′ VBL-exposed and from the control virus (CV) supernatant (SN) (16.9 and 15.5 Ct, respectively). Likewise, quantification of the extracted RNA with Qubit assay showed a comparable concentration of the VBL-treated and CV SNs (0.52 and 0.45 ng/µL, respectively).

Next-generation sequencing (NGS) analysis of SARS-CoV-2 RNA was performed on 90′ VBL exposure and CV SNs at two time points (0 and 12 h post-infection). The sequences were compared with the reference vaccine strain (NCBI reference sequence: NC_045512). Neither amino acid nor nucleotide differences were observed between the VBL-exposed and CV SNs (Table 2).

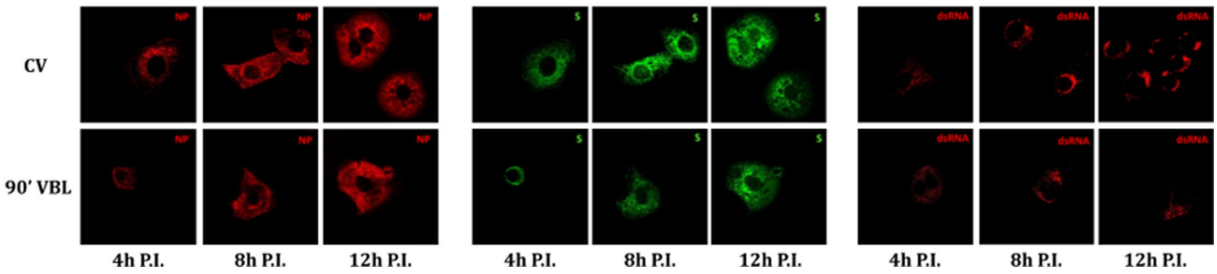

FIG 2 Intracellular localization of SARS-CoV-2 dsRNA and proteins. VERO E6 cells were infected with SARS-CoV-2 (CV) and SARS-CoV-2 after 90′ VBL exposure. Cells were stained at different time points (4, 8, and 12 h post-infection, P.I.) with NP-, S-, and dsRNA-antibody and examined by confocal microscopy.

$TCID_{50}$/mL reduction of SARS-CoV-2 after VBL exposure with different medium dilutions

Exposure of the viral SNs to VBL showed a remarkable reduction of infectious titer at all three different conditions tested (diluted 1:3, 1:20 and 1:1,000 in phosphate-buffered saline [PBS]), compared to the CV (Fig. 4). However, residual virus titer following VBL exposure was comparable in the three conditions, and the difference in fold-change reduction appeared to be driven by the decrease in untreated virus titer due to the different dilution factors. Specifically, $TCID_{50}$/mL without and with exposure to VBL decreased from 9.03 log_{10} (CI: 8.61–9.45) to 4.31 log_{10} (CI: 3.86–4.77) with 1:3 diluted SN; from 8.98 log_{10} (CI: 8.3–9.5) to 4.44 log_{10} (CI: 4.02–4.86) with 1:20 diluted SN; and from 6.93 log_{10} (CI: 6.39–7.48) to 4.31 log_{10} (CI: 3.86–4.77) with 1:1,000 diluted SN (Fig. 3). The table with extended data on viral titer and fold change values is included in the Supplementary Information (Table S1).

VBL treatment of SARS-CoV-2 with antioxidants

Antioxidants were added to the virus under the same experimental conditions as above to study the effect of oxidative stress induced by VBL exposure. The antioxidants tested included (i) 5 and 0.5 mM N-acetylcysteine (NAC), (ii) 5 and 0.5 mM ascorbic acid (AsA), and (iii) 0.03 and 0.003 mM superoxide dismutase (SOD).

As shown in Fig. 5 and Table S2, the higher concentrations of AsA and NAC at the lower SN dilutions (1:3 and 1:20) resulted in higher virus survival after VBL exposure. Specifically, at the 1:3 SN dilution, the reduction of VBL-treated virus decreased from 4.71 log_{10} in the absence of antioxidants to 3.94 log_{10} and 3.36 log_{10} with the addition of 5 mM NAC and of 5 mM AsA, respectively. As for the 1:20 diluted SN, the reduction ranged from 4.54 log_{10} in the absence of antioxidants to 3.59 log_{10} and 2.46 log_{10} with the addition of 5 mM NAC and of 5 mM AsA, respectively. Even at the lower concentra tions (0.5 mM), both NAC and AsA slightly increased virus survival with the 1:20 diluted SN, allowing a variation of −8.81% (4.15 log_{10}) and −29.51% (3.20 log_{10}), respectively, compared to the VBL-treated SNs without antioxidants (4.54 log_{10}). SOD proved to be almost ineffective in increasing SARS-CoV-2 survival at the lower SNs dilutions (1:3 and 1:20), regardless of its concentration. In contrast, at the highest SN dilution (1:1,000), SOD allowed a higher rate of virus survival than NAC and AsA. Specifically, the titer of the VBL-treated virus decreased from 2.62 log_{10} in the absence of antioxidants to 1.55 log_{10} with the addition of 5 mM NAC, 1.73 log_{10} with the addition of 5 mM AsA, and 1.51 log_{10} with the addition of 0.03 mM SOD, with a variation of −40.79%, −33.72%, and −42.16%, respectively. The increased viral survival rate disappeared at the lowest concentration of antioxidants, except for SOD. Indeed, with 0.003 mM SOD, the reduction ranged from 2.62 log_{10} to 0.83 log_{10}.

Overall, the addition of AsA (and to some extent NAC) appears to be more protective at the 1:3 and 1:20 dilutions of the virus, suggesting that the presence of residual DMEM medium and the photosensitizers that it contains may in part drive VBL-mediated oxidation of the virus.

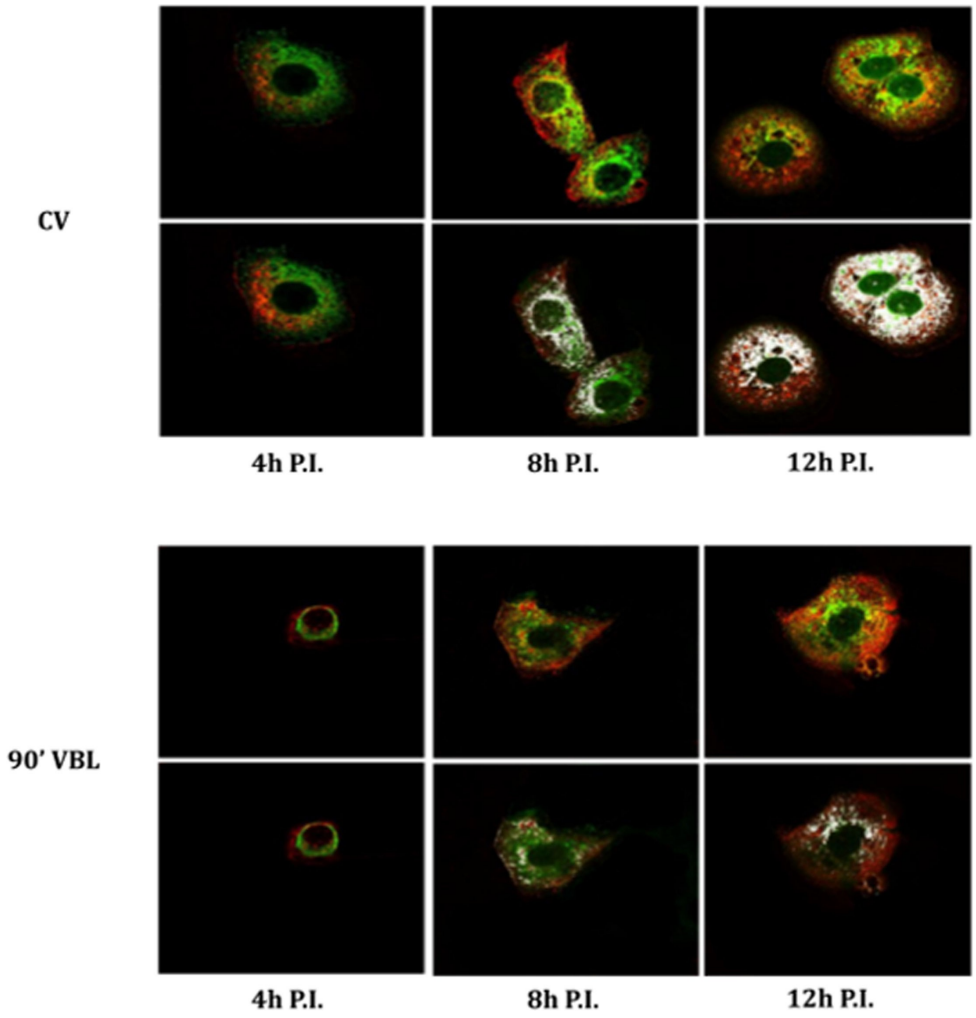

FIG 3 Co-localization of SARS-CoV-2 S and N proteins. VERO E6 cells were infected with SARS-CoV-2 (CV) and SARS-CoV-2 after 90′ VBL exposure. Cells were stained at different time points (4, 8, and 12 h post-infection, P.I.) with NP- and S-antibody and examined by confocal microscopy. Merged signals (upper panels of each condition) and co-localized points (lower panels of each condition) are shown. Co-localized points appear white.

Protein carbonylation assay

SDS-PAGE and Western blotting experiments on N, S, E, and helicase (NSP13) proteins were conducted to determine whether VBL irradiation reduces viral replication by altering viral protein structure. As shown in Fig. 6, the S and E proteins exhibited higher oxidation levels compared to the untreated control when irradiated in the presence of culture medium. Specifically, oxidation was more pronounced at the 1:3 dilution compared with the 1:20 dilution, while both conditions differed markedly from the PBS control. For the N protein, the 1:20 dilution showed a more intense band com pared with the control, along with the appearance of a fainter, higher-molecular-weight band, whose intensity was comparable to that observed in the control at the expected molecular weight. Additionally, at the 1:3 dilution, the N protein band showed a slight molecular weight shift in the VBL-exposed sample. No differences were observed for the NSP13 protein across the experimental conditions tested. These results suggest that oxidative modifications following VBL exposure primarily affect surface proteins.

TABLE 2 Whole-genome NGS analysis of SARS-CoV-2[a]

Sample	Pango lineage	Substitutions	aa substitutions
T0 control virus	B.1	C241T-C3037T-C14408T-A23403G-T23569C	ORF1b:P314L-S:0614G
T0 virus after 90′ VBL exposure	B.1	C241T-C3037T-C14408T-A23403G-T23569C	ORF1b:P314L-S:D614G
12 h P.I. control virus	B.1	C241T-C3037T-C14408T-A23403G-T23569C	ORF1b:P314L-S:D614G
12 h P.I. virus after 90′ VBL exposure	B.1	C241T-C3037T-C14408T-A23403G-T23569C	ORF1b:P314L-S:0614G

[a]The samples belong to the Pango B.1 genomic lineage and share the same genomic mutations: C241T, C3037T, C14408T, A23403G, and T23569C with respect to the reference ancestral virus. These mutations correspond to identical amino acid substitutions in each sample, namely ORF1b:P314L and S:D614G. The analysis suggests that exposure to VBL under the experimental conditions described in the text did not introduce any change in the virus genome.

DISCUSSION

The sensitivity of viruses to photodynamic inactivation was first reported in the 1930s (37). However, over the last 40 years, photodynamic procedures for virus inactiva tion have garnered increasing attention (38). This increased interest stems from the development of new active photosensitive molecules, advancements in light technolo gies (lasers, LEDs, and portability) (39), and the recent pandemic emergency.

This study investigated the mechanisms underlying SARS-CoV-2 inactivation in response to VBL exposure. The results are varied and heterogeneous, indicating the inactivation process is likely influenced by multiple interconnected mechanisms rather than a single cause.

Cell cycle regulation and RNA integrity

Initial investigation focused on potential light interference with the viral replication cycle and possible viral RNA damage.

Experimental data showed that VBL exposure does not cause significant changes in the viral replication cycle, suggesting the replication process remains largely unaffected. Indeed, analysis of the time course and cellular localization of viral components indicated the main difference between VBL-exposed and non-exposed viruses lies primarily in the concentration of viral particles infecting the cells. These results, combined with the $TCID_{50}$/mL data, led us to hypothesize that light-induced virus inactivation occurs before viral entry into the target cell. Other studies support this hypothesis, suggesting irreversible damage to viral structures occurs before host cell entry (31, 40).

Similarly, results on genetic material integrity showed that damage to ssRNA does not directly affect viral inactivation. Both qRT-PCR and NGS revealed no significant alteration of viral RNA. These findings exclude nucleic acid degradation as the primary mechanism and instead highlight other potential cellular and viral structural perturbations. Further studies support this, ruling out direct VBL-induced damage to the viral genome that could irreversibly affect the replication cycle (31, 41). Furthermore, we found no evidence that other viral components, such as structural and non-structural proteins involved in transporting and protecting genetic material within the host cell (e.g., N protein) (42), are the primary target of VBL.

Indirect assessment of oxidative stress

Results from the previous experiments allowed us to exclude, with reasonable confi-dence, some traditionally considered factors in virus inactivation, shifting the focus to remaining vital components like proteins and the cell membrane. Given the properties of the wavelength used (405 nm), an additional investigation step was necessary to identify the possible type of damage caused by VBL. Two potential mechanisms emerged: (i) oxidative damage, where photosensitive elements produce ROS, triggering a cascade

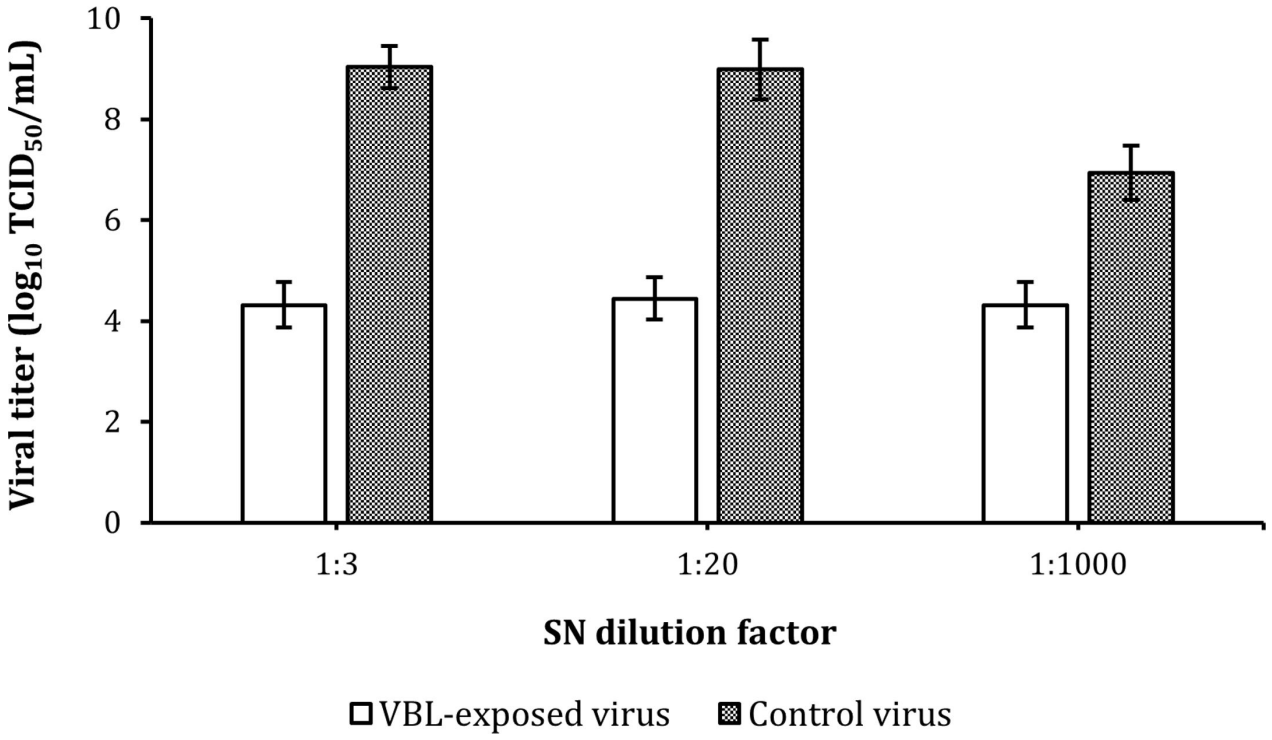

FIG 4 Viral load reduction of SARS-CoV-2 in different dilutions of culture medium exposed to VBL for 90′. The viral SN was diluted in PBS at different concentrations to reduce the presence of DMEM culture medium during VBL exposure. The results obtained showed a $TCID_{50}$/mL logarithmic reduction of the exposed samples with respect to CVs of 4.719 log_{10} (for the SN dilution factor of 1:3), 4.543 log_{10} (for the SN dilution factor of 1:20), and 2.620 log_{10} (for the SN dilution factor of 1:1,000); percentage reductions achieved were 99.998%, 99.997%, and 99.76%, respectively. The dilution of the medium certainly affected virus survival, suggesting that its presence plays a secondary but relevant role in VBL-mediated viral inactivation. Results were expressed as the logarithm of $TCID_{50}$/mL and relative 95% confidence interval (CI) obtained using the improved Kärber.

primarily damaging the membrane and proteins (43), and/or (ii) conformational changes in key viral structural proteins (44), potentially compromising virus adhesion and cellular uptake, thus preventing replication.

Experiments incubating the virus with antioxidants (initially only in 1× PBS) during VBL exposure tested the first hypothesis, revealing that oxidative damage significantly contributes to VBL-induced virus inactivation. Indeed, treatment with NAC, AsA, and SOD at different concentrations partially but significantly prevented SARS-CoV-2 inactivation (reducing it from 99.99% without antioxidants to 99.96% with NAC 0.5 mM and 85.43% with SOD 0.003 mM) (Fig. 5). These data highlight the role of ROS produced during VBL exposure as mediators of oxidative stress, indicating their interaction with viral components potentially affects structural stability and functionality (39).

Based on the hypothesis that oxidative stress is a key inactivation mechanism, we evaluated DMEM cell culture medium as a potential primary source of ROS production. Several studies suggest photosensitive molecules like riboflavin in suspension media may act as primary ROS sources upon VBL exposure, potentially compromising viral viability before cell culture incubation (31, 40). In this context, our results seem to partially diminish the role of DMEM medium as the primary source of ROS production. The same reduction (>99.99%) was achieved when the virus was exposed to VBL at 1:3 and 1:20 dilutions in PBS. Therefore, there appears to be no significant difference in virus viability regardless of the culture medium concentration used. However, exposing the virus to VBL at a 1:1,000 dilution in PBS yielded 99.76% inactivation. While this slight difference seems biologically insignificant, it does not allow us to completely exclude the suspension medium's role as an adjunct in the inactivation process, suggesting it may play a secondary rather than a central role. Several studies appear to confirm

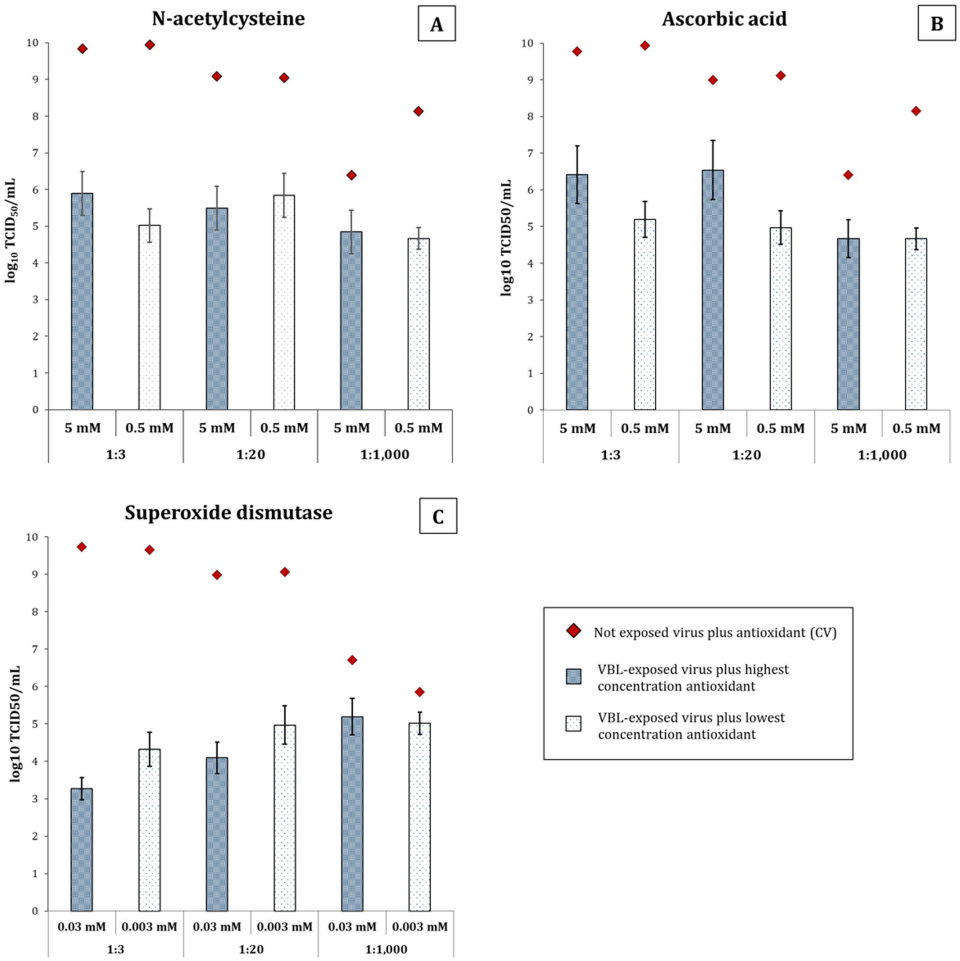

FIG 5 Evaluation of antioxidant protection against VBL-induced inactivation of SARS-CoV-2 in different dilutions of culture medium. The viability of SARS-CoV-2, as measured by $\log_{10}$ $TCID_{50}$/mL, is depicted in this figure after a 90-min exposure to VBL. The virus was incubated in DMEM diluted 1:3, 1:20, or 1:1,000 in PBS during irradiation, and various antioxidants were added at two concentrations. The goal was to ascertain whether these antioxidants could shield the virus from the oxidative stress caused by VBL. In the panels, the results are presented for (A) NAC at 5 mM (blue patterned bars) and 0.5 mM (white patterned bars), (B) AsA at 5 and 0.5 mM, and (C) SOD at 0.03 and 0.003 mM. The whiskers of the bars represent the 95% confidence interval. The titers of the non-exposed control virus (CV) are represented by red diamonds. The CV was incubated under identical conditions (medium dilution, antioxidant type, concentration, and time) without VBL exposure, and they served as a baseline for maximum viability. The titers of the CV range from 8 to 10 $\log_{10}$ $TCID_{50}$/mL, according to the specific condition.

this hypothesis (32, 33, 45), and our IAV and IBV inactivation results also seem to corroborate it. Indeed, although the suspension media differed (UltraMDCK for IAV/IBV vs DMEM for SARS-CoV-2), photosensitive components should also be present and contribute to influenza virus inactivation, yielding similar results to those seen with SARS-CoV-2. However, this was not observed, suggesting the inactivation process is likely driven by intrinsic features of the virus morphology. This remains speculative, as comparing photosensitive element concentrations between DMEM and the propriet ary UltraMDCK medium is not possible. Subsequent experiments, exposing the virus to different DMEM dilutions and antioxidant concentrations, partially confirmed the medium's secondary role in inactivation, showing a minimal but measurable increase in cell viability correlating with its concentration. This increase was proportional to both medium and antioxidant concentrations, with AsA generally showing better a ability to reduce oxidative stress. Survival increased to a maximum of 0.5% with 5 mM AsA in

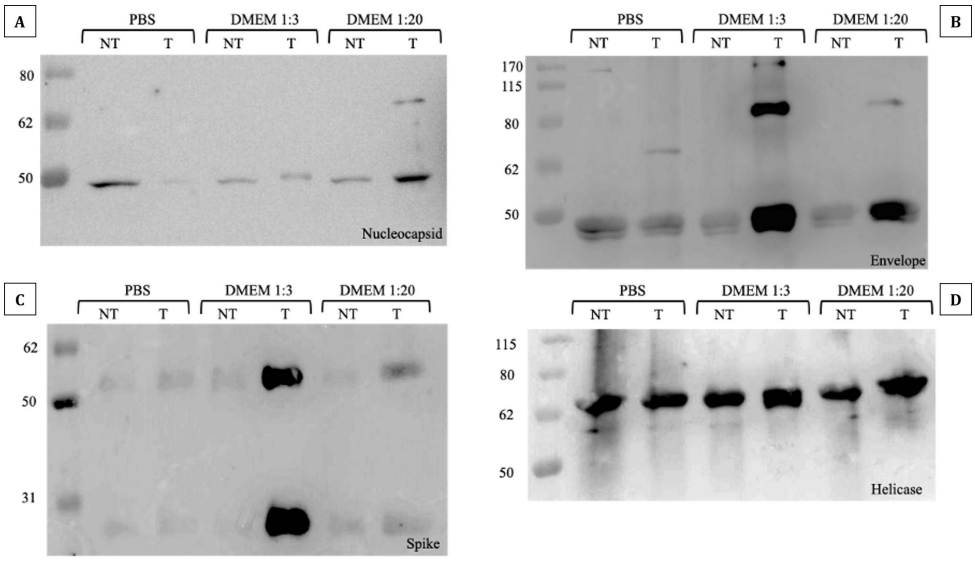

FIG 6 Protein carbonylation assay results. Detection of carbonylated proteins derivatized with DNPH and analyzed by Western blot in the presence (T) or absence (NT) of VBL exposure. (A) Protein N exposed to VBL showed no visible signs of carbonylation compared to unexposed controls and different incubation conditions with different dilutions of the culture medium. In general, slight protein oxidation seems to be visible in all samples, probably due to the experimental conditions under which the tests were carried out. (B) Protein E showed signs of carbonylation in samples exposed to VBL and incubated with DMEM medium dilutions of 1:3 and 1:20. In this case, the presence of higher medium concentrations seems to have affected the oxidative state of the protein. Again, a slight presence of protein oxidation is visible in all samples, probably due to the experimental conditions of the assay. (C) Protein S showed significant carbonylation in the 1:3 dilution of medium exposed to VBL, although a slight level of carbonylation is also present in the sample incubated with the 1:20 dilution. Again, it appears that the concentration of medium increases the degree of protein carbonylation in the presence of VBL. (D) Protein NSP13 showed signs of extensive carbonylation regardless of the variables examined. Again, the results could be due to a combination of factors related to the intrinsic properties of the protein and the experimental conditions under which the tests were carried out. Nevertheless, no differences were found between the samples exposed and those not exposed to VBL.

DMEM 1:20. Although minimal, this increase may offer a partial estimate of the medium's effect, but additional tests are required for accurate measurements with high confidence.

Protein oxidation and structural integrity

Experiments were conducted on three structural (S, N, and E) and one non-structural (NSP13) SARS-CoV-2 protein to test the hypothesis that oxidative stress could be induced by light-sensitive endogenous or exogenous molecules. Proteins were incubated in neutral medium (1× PBS) and different DMEM dilutions (matching cell viability tests) to evaluate the direct effect of light. The aim was to confirm literature findings suggesting significant culture medium involvement in S protein (and partial N protein) oxidation (31, 34, 46, 47), or to partially validate our previous results with DMEM. The hypothesis of VBL-induced conformational change or protein damage was not completely rejected; however, confirming it depended on detecting protein degradation via SDS-PAGE and Western blotting, which was not observed.

Exposing the proteins to VBL in 1× PBS showed no significant oxidative stress-induced changes or molecular weight alterations. This ruled out the possibility that the protein alone promotes viral inactivation. Supporting this, oxidative damage to viral proteins was most evident in tests using DMEM as the incubation medium (particularly with S and E proteins), suggesting DMEM could act as a secondary ROS producer in the presence of VBL. This suggests oxidative stress might affect the structural and functional integrity of these proteins, partially confirming literature reports (39, 48). The S protein, critical for SARS-CoV-2 entry and interaction with the host cell ACE2 receptor (49), showed oxidative

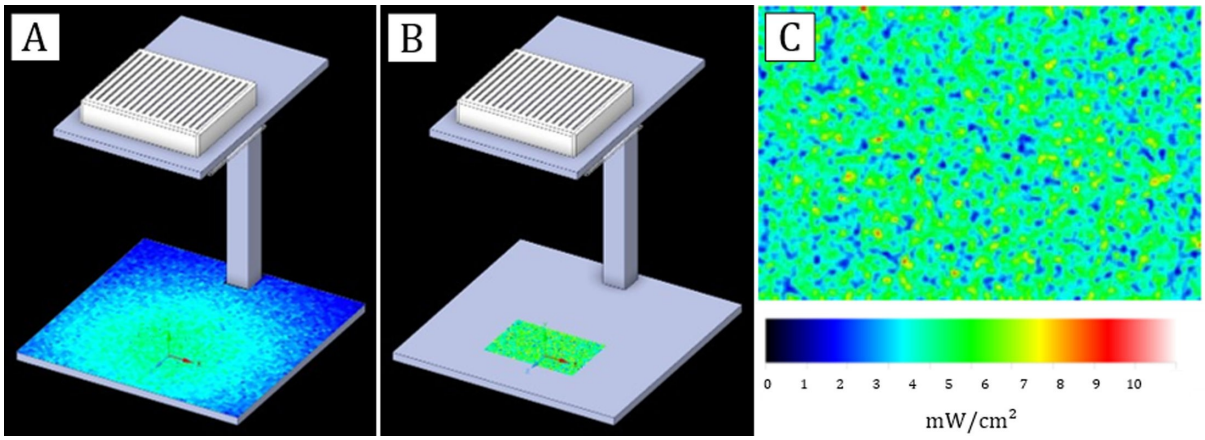

FIG 7 3D representation of the light source and VBL light distribution. (A) Light irradiance simulation on the plane realised with Ansys Speos software. The radio-photometric simulation was carried out considering the power of each light source (the nine LEDs at 405 nm), the distance of the light sources from the plane, and empirical measurements taken at various points on the plane using the Avantes ULS2048CL EVO spectrophotometer. As expected, the highest irradiance (section in green) was measured on the perpendicular plane section below the source (4.3 mW/cm^2), while an average irradiance decrease of 83% (0.7 mW/cm^2) was recorded on the lateral plane sections (section in blue). (B) Irradiance on the multi-well plate. The marked area on the plane (in green) represents the point, where the multi-well plate is positioned during the virus and protein exposure experiments. Before starting the experiments, the temperature at the point of maximum light exposure was measured to exclude it as a possible risk factor. The measured temperature was not different from room temperature (23°C, 50% relative humidity). (C) Detail of the light distribution on the plate.

changes that could affect its binding affinity or conformational stability. Such structural changes could hinder viral infection, as damaged S proteins might be unable to perform their cellular entry function, primarily via the endosomal pathway (50), consistent with entry dynamics observed in VERO E6 cells (51).

Indeed, oxidative processes can induce post-translational modifications altering protein structure, folding, net charge, and hydrophobic/hydrophilic balance (52). However, this assay cannot determine whether these oxidative modifications led to conformational changes affecting protein interaction or stability, and thus potentially impacting viral infectivity. Furthermore, the relationship between function loss and protein oxidative damage is not direct. Nitration and carbonylation can negatively impact target proteins, but under stress conditions, these modifications might even be beneficial (53). An oxidized protein might retain normal or only slightly reduced function (54), without affecting cellular structure or viral replication. This latter point is strongly supported by the cell viability results, leading to the hypothesis that: (i) proteins most likely do not undergo direct VBL-induced alterations; (ii) the suspension medium has a secondary effect, contributing to inactivation likely via membrane protein oxidation; but (iii) medium-induced protein oxidation alone cannot explain the inactivation results obtained, even at the 1:1,000 DMEM dilution.

SARS-CoV-2 membrane composition and phospholipid oxidation

While protein oxidation alone may not fully explain viral inactivation, combining it with membrane phospholipid oxidation might help clarify the complex phenomenon observed, assigning a secondary but supportive role to protein oxidative damage in reducing virus survival.

Lipid peroxidation, mainly ROS-driven, is well-studied and known to adversely affect membrane integrity by altering lipid bilayer fluidity and permeability. The lack of oxidative damage control mechanisms exposes viral envelope phospholipids to oxidative changes (55). Free radicals such as AAPH (2,2′-Azobis(2-amidinopropane) dihydrochloride) (56) and DBHN (di-tert-butyl hyponitrite) (57) can accelerate oxidation, increasing the structural instability of viral phospholipids. VBL-based inactivation could

target this viral membrane vulnerability, as lipid peroxidation can compromise the viral envelope, rendering it non-functional and limiting its ability to infect host cells.

This assumption seems supported by two key previous findings: (i) the different survival rates of IAV/IBV vs. SARS-CoV-2 after VBL exposure, and (ii) the higher SARS-CoV-2 survival when co-incubated with SOD during VBL exposure.

Regarding the first finding, differences in the lipid bilayer composition of the two virus types could account for their varying susceptibility to oxidative stress and VBL exposure. Indeed, according to a recent study by Saud et al. (58), the SARS-CoV-2 lipid bilayer is composed mainly of phosphatidylcholine), phosphatidylethanolamine (PE), and phosphatidylinositol (PI), with modest amounts of phosphatidylserine (PS), phosphati dylglycerol (PG), and sphingolipids (SLs) like ceramide and dihydroceramide (DHCer). Conversely, cholesterol, triacylglycerols, free cholesterol, and sphingomyelin (SM) appear largely absent (58). These latter components, more resistant to oxidative stress than glycerophospholipids, are essential for maintaining membrane fluidity and flexibility and provide additional support against prolonged stress (55). The influenza virus membrane presents a different composition. It is composed mainly of cholesterol (up to 40%) (59), SLs such as SM, glucosyl/galactosylceramide, and DHCer, phospholipids (PL) including PS and PE, and small amounts of PG (60). The virus's complex homeostatic equilibrium may depend on this intrinsic variability in membrane composition, where type I or II photoinitiators (e.g., Fe(III) atoms, O•–, hydroxyl radicals, ozone, and H_2O_2) can trigger widespread, irreversible lipid peroxidation (61), induced by stressors like VBL.

For the second finding, lipid peroxidation could explain SOD's superior perform ance compared to the other antioxidants. In oxygenated solutions, ionizing radiation generates superoxide, while in deoxygenated water, it produces hydroxyl radicals and solvated electrons triggering lipid autoxidation cascades. At low concentrations, SOD neutralizes superoxide radicals, acting as a control mechanism for oxidative stress in complex systems like eukaryotic cells (55). In our study, the most protective effects were seen when SOD was incubated and exposed in the 1:1,000 supernatant dilution in PBS. When incubated with the virus and DMEM, the results were negligible (regardless of concentration), likely due to the secondary ROS generation process caused by DMEM.

Further studies using advanced techniques are necessary to definitively assess the preservation state of the viral membrane after VBL exposure and confirm its precise role in the virus inactivation mechanism.

Conclusion

VBL inhibits SARS-CoV-2 and influenza virus replication primarily by inducing oxidative stress to the viral membrane, with an emphasis on phospholipids and, to a lesser degree, viral proteins. The results obtained allow us to hypothesise that the oxidative degrada tion of phospholipids and the reduced presence of cholesterol and sphingolipids can alter the viral membrane, reducing the ability of the virus to maintain its structural integrity or interact with host cells. The results of this study underscore the potential of VBL as a non-invasive disinfection tool for inactivating viruses such as SARS-CoV-2. This method may be particularly useful in situations when direct viral exposure is unavoida ble, such as in healthcare facilities or air filtering systems.

In conclusion, VBL has great potential as an innovative, affordable, and scalable disinfection tool, including against viruses. However, further studies are needed to optimize its use, particularly in settings where safety and efficacy must be ensured. Integrating antioxidant therapies with VBL could be a more effective viral inactivation strategy than using VBL alone, thus improving therapeutic applications and environ mental disinfection. However, it is essential to recognize some limitations of the study, including the limited number of viruses tested and the need to consider the complexity of real-world settings. In this regard, in vivo studies might be useful to better assess prospects. The potential of VBL as an environmentally friendly and safe alternative to traditional disinfection methods is considerable, but further research is needed to define

the optimal application parameters, such as the amount of energy, duration, source distance, and exposure time that could be most effective to achieve viral inactivation.

MATERIALS AND METHODS

Experimental setting and photoradiometric simulation

The VBL prototype lamp consisted of nine LEDs centred at 405 nm (±4 nm) positioned on a square metal stand. The light source was supported by a metal scaffold attached to a 30 cm × 30 cm square base at 32 cm from the light sources, on which the profile of a multi-well plate was outlined to perform the tests correctly (Fig. 7A).

The characterization of the electromagnetic spectrum was performed using an Avantes ULS2048CL EVO spectrophotometer (Avantes, Apeldoorn, the Netherlands). The energy map of the multi-well plate was measured to obtain the distribution of light irradiance (Fig. 7B). The average irradiance measured within the wells of the plate was 4 mW/cm^2.

The test setup, the number of LEDs, and their position in the device were designed using Ansys Speos software. Subsequently, a simulation was conducted to ensure that the light distribution was uniform in all wells of the plate, and then empirically con firmed the simulated values by measuring the light distribution at 405 nm (Fig. 7C). The following photometric simulation parameters were set:

- radiant flux of VBL LEDs = 1.4 W, taken from the LED datasheet as the median value of the intermediate production bin;
- Lambertian type of intensity with an aperture angle of 130°; and
- 7% absorption of VBL by the polymer cover protecting the LEDs.

Fig. S1 shows the specifications of the type of LEDs used and the characterization of their light spectrum, carried out using the Avasoft measurement software (Avantes, Apeldoorn, the Netherlands).

SARS-CoV-2 and influenza viruses

The SARS-CoV-2 variant used for the experiments was the wild-type B.1 (GISAID code EPI_ISL_2472896), kindly provided by the Department of Biomedical and Clinical Sciences, Luigi Sacco, University of Milan, Italy. The cell line used to propagate the viral stock was VERO E6, a cell line with epithelial morphology originally isolated from the kidney of an African green monkey (ATCC CRL-1586). VERO E6 cells were propagated in DMEM high glucose medium (Euroclone, Pero, Italy) supplemented with 10% fetal bovine serum (FBS; Euroclone, Pero, Italy) and 1% streptomycin/penicillin (PS) (Euroclone, Pero, Italy) in a humidified incubator at 37°C with 5% CO_2. After propagation, the viral stock was titrated in VERO E6 as previously described (62). To perform viral infection, the same DMEM medium but with 1% FBS concentration was used.

The influenza viruses used for the experiments were A/Wisconsin/588/2019 (H1N1), as representative of IAVs, and B/Austria/1359417/2021 (B/Victoria lineage) (NIBSC 21/218), representative of IBVs. The cell line used to propagate both viruses was the Madin-Darby Canine Kidney (MDCK) (ATCC CCL-34). MDCK cells were cultured in Eagle's minimum essential medium (Lonza, Milano, Italy) supplemented with 2 mM L-Glutamine (Lonza, Milano, Italy), 1% non-essential amino acid solution (Sigma-Aldrich, St. Louis, MO, USA), 100 units/mL PS mixture (Lonza, Milano, Italy) and 10% FBS (Euroclone, Pero, Italy), in a humidified incubator at 37°C with 5% CO_2. To perform viral infection, UltraMDCK serum-free medium (Lonza, Milano, Italy) with 1% PS and 1 µg/mL Trypsin TPCK treated (Sigma-Aldrich, St. Louis, MO, USA) was used. After propagation, the viral stock was titrated in MDCK cells as previously described (63).

Virus exposure to VBL

Viral suspensions of SARS-CoV-2 and influenza (IAV and IBV) were exposed to VBL, in DMEM or UltraMCDK medium in microtiter wells (300 µL per well) of a multi-well plate, at different doses of light energy: 22′30″ (dose of 5.4 J/cm^2), 45′ (10.8 J/cm^2), and 90′ (21.6 J/cm^2). In all exposures, a non-VBL-exposed virus was used as control.

In all subsequent experiments, the SARS-CoV-2 SN was exposed for 90′ of continuous irradiation under the VBL lamp at a 30 cm distance from the light source, with an irradiation of 4 mW/cm^2. Each virus SN was tested at 1:3, 1:20, and 1:1,000 dilution in PBS to account for the cell culture medium effect. The same experiments were performed with the addition of alternative antioxidants: NAC (5 and 0.5 mM) (VWR International, Radnor, PA, USA), AsA (5 and 0.5 mM) (VWR International, Radnor, PA, USA), and SOD (0.03 and 0.003 mM) (Thermo Fisher Scientific, Waltham, MA, USA). In all experiments, non-VBL-exposed SARS-CoV-2 (without the addition of antioxidants) was used as control.

Immunofluorescence assay

The spatiotemporal distribution of the SARS-CoV-2 N protein, S protein, and dsRNA was investigated by immunofluorescence on VERO E6 cells infected with the VBL-exposed and unexposed virus. The cells were seeded 24 h before infection on 24-well plates and covered with sterile borosilicate cover glasses (diameter 13 mm, thickness no. 1.5, VWR International). On the day of infection, the SARS-CoV-2 stock was irradiated under the VBL lamp for 90′ and then used to infect the pre-seeded VERO E6 cells. In parallel, VERO E6 cells were infected with the unexposed CV at 0.2 MOI, and uninfected cells were used as cell control. The infected cells, both with the VBL-exposed virus and with the CV, and the uninfected cells were then fixed with 10% paraformaldehyde for 20′ at 4, 8, and 12 h post-infection.

The immunofluorescence assay was then performed as previously reported (62). Briefly, after the permeabilization step (0.5% Triton X-100, 7′), non-specific binding sites were blocked in 3% bovine serum albumin (BSA; Life Technologies, Carlsbad, CA, USA) for 1 h, then cells were incubated overnight with primary antibody (anti-dsRNA, anti-NP, or anti-S) diluted in PBS containing 0.5% BSA + 0.5% Triton X-100. After washing steps (PBS containing 0.5% BSA + 0.5% Triton X-100 + 0.05% Tween20), the cells were incubated for 1 h with AlexaFluor 488- or 568-labeled secondary antibody (Life Technologies, Carlsbad, CA) diluted in PBS with 0.5% BSA + 0.5% Triton X-100. Coverslips were mounted in Fluoromount Aqueous Mounting Medium (Merck, Darmstadt, Germany) and pictures of stained cells were taken through a confocal microscope (Zeiss LSM500; Carl Zeiss, Germany). The number of viable cells was determined by the count of cells stained with 4′,6-diamidino-2-phenylindole (DAPI; Sigma-Aldrich, St. Louis, MO, USA) and randomly (five fields) counted at 40× original magnification to the confocal microscope. To determine the percentage of SARS-CoV-2 infection, dsRNA-, N-, or S-expressing cells were counted, and data were reported as the percentage of positive cells/slide. Reagents for immunofluorescence (PBS, Triton X-100, and Tween20) and anti-dsRNA, anti-N, and anti-S antibodies were obtained from Merck (Darmstadt, Germany).

The number of cells was determined by the count of cells stained with DAPI and randomly counted (five fields) at 40× original magnification. dsRNA-, S-, and N-express ing cells were counted, and data were reported as the percentage of positive cells/slide. Images were pre-processed using ImageJ software (US National Institutes of Health, Bethesda, MD, USA). The colocalization of S and N proteins was represented as white dots using the colocalization plug-in.

Virus titration after VBL irradiation

All viral SNs were harvested and titrated to evaluate the rate of virus inactivation and to test whether the SN retained the ability to infect cells. At the end of VBL exposure to SARS-CoV-2, IAV, and IBV, titration was performed as previously reported (62–64).

At the beginning, SARS-CoV-2, IAV, and IBV were titrated in serial 1 $\log_{10}$ dilutions to obtain a $TCID_{50}$ on 96-well culture plates of VERO E6 or MDCK cells, respectively. After 72

h of incubation at 37°C with 5% CO_2, plates were observed for the presence of cytopathic effect (CPE) by means of an inverted optical microscope. The viral titer was calculated using the Reed-Muench method and expressed as $TCID_{50}$/mL.

ELISA assay and quantification of CPE were initially performed as screening experi ments to optimize experimental conditions, to identify influencing variables, and to determine the most suitable readout for subsequent analyses. Notably, all three titrations revealed a 3 log_{10} reduction of the VBL-exposed virus titer compared to the untreated control, as we can observe in Table S3. Considering these results, we decided to proceed using the quantification of CPE as readout for all subsequent experiments.

For the titration of SARS-CoV-2 after VBL exposure with and without antioxidants, the virus was titrated by performing fivefold serial dilutions of irradiated and control SNs in 96-well adhesion plates. The dilutions were used to infect pre-seeded VERO E6 cells at 70% confluence. After 72 h, cell viability was measured by the CellTiterGLO 2.0 assay (Promega, La Jolla, CA, USA). The viral titer was calculated using the improved Kärber method and expressed as $TCID_{50}$/mL.

Detection and quantification of SARS-CoV-2 RNA by qRT-PCR, Qubit assay, and NGS analysis

Viral RNA extraction was performed from the VBL-exposed and the CV SNs using a homemade guanidine thiocyanate-based (GuSCN) extraction method. Then, cDNA was generated using the LunaScript RT SuperMix Kit (New England Biolabs, MA, USA). qRT-PCR was performed using the Luna Universal Probe qPCR MasterMix (Euroclone, Pero, Italy) in a total volume of 20 µL containing 5 µL of cDNA, 10 µL of 2× Luna MasterMix, 10 pM each forward and reverse primer, 2.5 pM FAM-labeled probe and RNase-free sterile water to the final volume. The samples were then loaded on a Rotor-Gene Q instrument (Qiagen, Hilden, Germany) to detect the fluorescence intensity of the FAM-TaqMan probe in each sample, and results were analyzed using the Rotor-Gene Q 2.3.1 software. Each cDNA was quantified in duplicate, with primers and probes designed on the NC_045512.2 reference strain targeting the SARS-CoV-2 polybasic cleavage site in the spike region. To quantify viral RNA in culture SNs, a standard curve obtained by diluting a control plasmid that was previously quantified by ddPCR (65) was used in each qRT-PCR run to interpolate the cycle threshold (Ct) generated by SNs. Eventually, RNA concentration of the CV and of the VBL-treated virus was evaluated with fluorimetric Qubit assay (Qubit 4 Fluorometer) based on binding of RNA-selective fluorescent dyes, using the RNA Assay Kit (Life Technologies, Waltham, MA, USA).

The NGS analysis was carried out using the MiSeq system (Illumina, San Diego, CA, USA). The VBL-exposed and the CV SN-extracted RNAs were used to prepare the library for SARS-CoV-2 whole-genome sequencing by using the COVIDSeq Assay (Illumina, San Diego, CA, USA) and Artic V4.1 SARS-CoV-2 primers, following the manufacturer's instructions. SARS-CoV-2 sequences were assembled with the DRAGEN COVID lineage software (version 4.0.6).

Protein carbonyls labeling with DNPH

Purified SARS-CoV-2 (2019-nCoV) Nucleocapsid Protein (His tag), SARS-CoV-2 (2019-nCoV) Spike Protein (RBD, His Tag), SARS-CoV-2 (2019-nCoV) envelope (CoV-E) protein, and SARS-CoV-2 (2019-nCoV) Helicase-His Recombinant Protein were purchased (Sino Biological, Eschborn, Germany), to facilitate their individual characterization. Specifically,we aimed to determine whether exposure to light could induce oxidative damage using the DNPH assay.

The 2,4-dinitro-phenylhydrazin (DNPH) is a specific probe that reacts with protein carbonyl groups, forming protein-conjugated dinitrophenylhydrazones (DNP). These protein-DNP adducts are recognized by specific primary antibodies, allowing DNPH to be used for the derivatization of protein carbonyls and subsequent analysis by the Western Blot method. For each protein, 3 µg per condition were exposed to VBL in 1× PBS, 1:3 DMEM in PBS, and 1:20 DMEM in PBS at room temperature for 90 min. Untreated samples

were kept under the same conditions, away from VBL, in Eppendorf tubes. The samples were derivatized by adding an equal volume of derivatization solution (DNPH 5 mM, TFA 5% vol/vol, and SDS 6% wt/vol) and incubated for 30 min at room temperature in the dark, vortexing every 10 min. An equal volume of neutralization solution (Tris 1 M, 30% glycerol, 2% beta-mercaptoethanol, and bromophenol blue traces) was added to stop the derivatization reaction. Finally, the samples were boiled for 5 min at 95°C and resolved by SDS-PAGE.

SDS-PAGE and western blot

Immunoblot was performed according to a previous study (66). The samples were resolved by SDS-PAGE using 4–12% Bis-Tris gels (Invitrogen), transferred to PVDF membrane, and incubated overnight at 4°C with a primary anti-dinitrophenyl antibody (Merck KGaA, Darmstadt, Germany) diluted 1:10,000 in 3% milk-0.1% Triton X-100 in 1× PBS. The following day, membranes were washed three times in 3% milk-0.1% Triton X-100 in 1× PBS for 10 min each, then incubated for 2 h at room temperature with a secondary anti-rabbit-HRP conjugated antibody (Merck KGaA, Darmstadt, Germany) diluted 1:5,000 in 3% milk-0.1% Triton X-100 in 1× PBS. Membranes were washed three times in the same solution. In the end, membranes were washed for 15 min with Triton X-100 in 1× PBS and two times with Tris-HCl 0.05 M pH 6.8. The chemiluminescent signal was detected with Lite Up (Euroclone S.p.A., Milan, Italy) and captured with Imagine Quant Las 4000 (GE Healthcare, Milan, Italy). Ponceau red staining (SERVA Electrophoresis GmbH Heidelberg, Germany) was performed as a control (Fig. S2).

Statistical analysis

All viral viability data collected during the study were entered into a database, includ ing the following variables: test date, test identifier, $TCID_{50}$/mL, virus species, and test inoculum concentrations. Descriptive statistics of the empirical data were calculated as the mean of the logarithmic reduction in base 10 (log_{10}) of the $TCID_{50}$/mL together with 95% confidence intervals to assess the reliability of the measurements. Microsoft Excel software (ver. 2021) was used to organize the database. Statistical analysis was performed with Stata software (ver. 17). For the immunofluorescence assay, statistical analyses were performed using Prism 9 software (GraphPad Software, La Jolla, CA, USA). Differences between VBL exposure and virus control were estimated using a two-way ANOVA. Values were expressed as the mean ± SD and $P < 0.05$ was considered statisti cally significant.

ACKNOWLEDGMENTS

We thank the company Ansys, Inc. for providing the educational version of the photo metric simulation software (Ansys Speos 2024).

Conceptualization of the study: G.M., E.M., M.Z., I.V., and G.C. Methodology: G.M., S.M., L.F., L.R., I.M., and D.A. Software acquisition of photonic measurements: G.C. Resources: G.M., E.M., and M.Z. Data curation: G.M., G.C., D.A., S.M., and I.V. Writing—original draft preparation: G.M., S.M., L.F., L.R., I.V., and D.A. Writing—review and editing: G.C, D.A., M.Z., C.M.T., and E.M. Supervision: G.M., E.M., and M.Z. Investigation for the tests: D.A., S.M., L.F., L.R., C.B.,V.S., and I.M. All authors have read and agreed to the published version of the manuscript.

AUTHOR AFFILIATIONS

[1]Department of Medical Biotechnologies, University of Siena, Siena, Italy
[2]Department of Molecular and Developmental Medicine, University of Siena, Siena, Italy
[3]Department of Biotechnology, chemistry and pharmacy, University of Siena, Siena, Italy
[4]VisMederi srl, Siena, Italy

AUTHOR ORCIDs

Davide Amodeo http://orcid.org/0000-0003-2022-9964

AUTHOR CONTRIBUTIONS

Davide Amodeo, Data curation, Investigation, Methodology, Writing – original draft, Writing – review and editing | Serena Marchi, Data curation, Investigation, Methodol ogy, Writing – original draft | Lia Fiaschi, Investigation, Methodology, Writing – original draft | Luisa Raucci, Investigation, Methodology, Writing – original draft | Camilla Biba, Investigation | Valentina Salvestroni, Investigation | Claudia Maria Trombetta, Writing – review and editing | Ilaria Manini, Investigation, Methodology | Maurizio Zazzi, Concep tualization, Resources, Supervision, Writing – review and editing | Emanuele Monto moli, Conceptualization, Resources, Supervision, Writing – review and editing | Ilaria Vicenti, Conceptualization, Data curation, Writing – original draft | Gabriele Cevenini, Conceptualization, Data curation, Software, Writing – review and editing | Gabriele Messina, Conceptualization, Data curation, Methodology, Resources, Supervision, Writing – original draft

DATA AVAILABILITY

The data that support the findings of this study are available from the corresponding authors upon request. Source data are provided with this paper and its supplemental material.

ADDITIONAL FILES

The following material is available online.

Supplemental Material

Supplemental material (AEM00403-25-S0001.docx). Figures S1 and S2; Tables S1 to S3.

REFERENCES

1. 2024. COVID-19 deaths | WHO COVID-19 dashboard datadot. Available from: https://data.who.int/dashboards/covid19/cases
2. Tang JW, Caniza MA, Dinn M, Dwyer DE, Heraud JM, Jennings LC, Kok J, Kwok KO, Li Y, Loh TP, Marr LC, Nara EM, Perera N, Saito R, Santillan-Salas C, Sullivan S, Warner M, Watanabe A, Zaidi SK. 2022. An exploration of the political, social, economic and cultural factors affecting how different global regions initially reacted to the COVID-19 pandemic. Interface Focus 12:20210079. https://doi.org/10.1098/rsfs.2021.0079
3. Hui DS, Azhar E, Madani TA, Ntoumi F, Kock R, Dar O, Ippolito G, Mchugh TD, Memish ZA, Drosten C, Zumla A, Petersen E. 2020. The continuing 2019-nCoV epidemic threat of novel coronaviruses to global health - the latest 2019 novel coronavirus outbreak in Wuhan, China. Int J Infect Dis 91:264–266. https://doi.org/10.1016/j.ijid.2020.01.009
4. Yang H, Rao Z. 2021. Structural biology of SARS-CoV-2 and implications for therapeutic development. Nat Rev Microbiol 19:685–700. https://doi.org/10.1038/s41579-021-00630-8
5. Redondo N, Zaldívar-López S, Garrido JJ, Montoya M. 2021. SARS-CoV-2 accessory proteins in viral pathogenesis: knowns and unknowns. Front Immunol 12:708264. https://doi.org/10.3389/fimmu.2021.708264
6. Justo Arevalo S, Castillo-Chávez A, Uribe Calampa CS, Zapata Sifuentes D, Huallpa CJ, Landa Bianchi G, Garavito-Salini Casas R, Quiñones Aguilar M, Pineda Chavarría R. 2023. What do we know about the function of SARS-CoV-2 proteins? Front Immunol 14:1249607. https://doi.org/10.3389/fimmu.2023.1249607
7. V'kovski P, Kratzel A, Steiner S, Stalder H, Thiel V. 2021. Coronavirus biology and replication: implications for SARS-CoV-2. Nat Rev Microbiol 19:155–170. https://doi.org/10.1038/s41579-020-00468-6
8. Güner R, Hasanoğlu I, Aktaş F. 2020. COVID-19: prevention and control measures in community. Turk J Med Sci 50:571–577. https://doi.org/10.3906/sag-2004-146
9. Krittanawong C, Maitra N, Kumar A, Hahn J, Wang Z, Carrasco D, Zhang HJ, Sun T, Jneid H, Virani SS. 2022. COVID-19 and preventive strategy. Am J Cardiovasc Dis 12:153–169.
10. Kratzel A, Todt D, V'kovski P, Steiner S, Gultom M, Thao TTN, Ebert N, Holwerda M, Steinmann J, Niemeyer D, Dijkman R, Kampf G, Drosten C, Steinmann E, Thiel V, Pfaender S. 2020. Inactivation of severe acute respiratory syndrome coronavirus 2 by WHO-recommended hand rub formulations and alcohols. Emerg Infect Dis 26:1592–1595. https://doi.org/10.3201/eid2607.200915
11. Harapan H, Johar E, Maroef CN, Sriyani IY, Iqhrammullah M, Kusuma HI, Syukri M, Razali R, Hamdani H, Kurniawan R, Irwansyah I, Sofyan SE, Myint KS, Mahlia TMI, Rizal S. 2022. Effect of elevated temperature on SARS-CoV-2 viability. F1000Res 11:403. https://doi.org/10.12688/f1000research.110305.2
12. Biasin M, Bianco A, Pareschi G, Cavalleri A, Cavatorta C, Fenizia C, Galli P, Lessio L, Lualdi M, Tombetti E, Ambrosi A, Redaelli EMA, Saulle I, Trabattoni D, Zanutta A, Clerici M. 2021. UV-C irradiation is highly effective in inactivating SARS-CoV-2 replication. Sci Rep 11:6260. https://doi.org/10.1038/s41598-021-85425-w
13. Reed NG. 2010. The history of ultraviolet germicidal irradiation for air disinfection. Public Health Rep 125:15–27. https://doi.org/10.1177/003335491012500105
14. Memarzadeh F. 2021. A review of recent evidence for utilizing ultraviolet irradiation technology to disinfect both indoor air and surfaces. Appl Biosaf 26:52–56. https://doi.org/10.1089/apb.20.0056
15. Astrid F, Beata Z, Julia E, Elisabeth P, Magda DE. 2021. The use of a UV-C disinfection robot in the routine cleaning process: a field study in an Academic hospital. Antimicrob Resist Infect Control 10:84. https://doi.org/10.1186/s13756-021-00945-4

16. McDevitt JJ, Rudnick SN, Radonovich LJ. 2012. Aerosol susceptibility of influenza virus to UV-C light. Appl Environ Microbiol 78:1666–1669. https://doi.org/10.1128/AEM.06960-11
17. Nicolau T, Gomes Filho N, Padrão J, Zille A. 2022. A comprehensive analysis of the UVC LEDs' applications and decontamination capability. Materials (Basel) 15:2854. https://doi.org/10.3390/ma15082854
18. Martín-Sómer M, Pablos C, Adán C, van Grieken R, Marugán J. 2023. A review on LED technology in water photodisinfection. Sci Total Environ 885:163963. https://doi.org/10.1016/j.scitotenv.2023.163963
19. Pizzichetti R, Martín-Gamboa M, Pablos C, Reynolds K, Stanley S, Dufour J, Marugán J. 2024. Environmental life cycle assessment of UV-C LEDs vs. mercury lamps and oxidant selection for diclofenac degradation. Sustain Mater Technol 41:e01002. https://doi.org/10.1016/j.susmat.2024.e01002
20. Atari N, Mamane H, Silberbush A, Zuckerman N, Mandelboim M, Gerchman Y. 2023. Disinfection of SARS-CoV-2 by UV-LED 267 nm: comparing different variants. Sci Rep 13:8229. https://doi.org/10.1038/s4 1598-023-35247-9
21. Gidari A, Sabbatini S, Bastianelli S, Pierucci S, Busti C, Bartolini D, Stabile AM, Monari C, Galli F, Rende M, Cruciani G, Francisci D. 2021. SARS-CoV-2 survival on surfaces and the effect of UV-C light. Viruses 13:408. https://doi.org/10.3390/v13030408
22. van der Schans M, Yu J, de Vries A, Martin G. 2024. Estimation of the UV susceptibility of aerosolized SARS-CoV-2 to 254 nm irradiation using CFD-based room disinfection simulations. Sci Rep 14:15963. https://doi.org/10.1038/s41598-024-63472-3
23. Messina G, Della Camera A, Ferraro P, Amodeo D, Corazza A, Nante N, Cevenini G. 2021. An emerging innovative UV disinfection technology (part ii): virucide activity on SARS-CoV-2. Int J Environ Res Public Health 18:3873. https://doi.org/10.3390/ijerph18083873
24. Robinson RT, Mahfooz N, Rosas-Mejia O, Liu Y, Hull NM. 2022. UV222 disinfection of SARS-CoV-2 in solution. Sci Rep 12:14545. https://doi.org/10.1038/s41598-022-18385-4
25. Frilli E, Amodeo D, Cevenini G, Nante N, Messina G. 2023. Effectiveness of near-UVA in SARS-CoV-2 inactivation. Epidemiol Infect 151:e76. https://doi.org/10.1017/S0950268823000560
26. Görlitz M, Justen L, Rochette PJ, Buonanno M, Welch D, Kleiman NJ, Eadie E, Kaidzu S, Bradshaw WJ, Javorsky E, et al. 2024. Assessing the safety of new germicidal far-UVC technologies. Photochem Photobiol 100:501–520. https://doi.org/10.1111/php.13866
27. Maclean M, McKenzie K, Anderson JG, Gettinby G, MacGregor SJ. 2014. 405 nm light technology for the inactivation of pathogens and its potential role for environmental disinfection and infection control. J Hosp Infect 88:1–11. https://doi.org/10.1016/j.jhin.2014.06.004
28. Amodeo D, Lucarelli V, De Palma I, Puccio A, Nante N, Cevenini G, Messina G. 2022. Efficacy of violet-blue light to inactive microbial growth. Sci Rep 12:20179. https://doi.org/10.1038/s41598-022-24563-1
29. Haridas D, Atreya CD. 2022. The microbicidal potential of visible blue light in clinical medicine and public health. Front Med (Lausanne) 9:905606. https://doi.org/10.3389/fmed.2022.905606
30. Biasin M, Strizzi S, Bianco A, Macchi A, Utyro O, Pareschi G, Loffreda A, Cavalleri A, Lualdi M, Trabattoni D, Tacchetti C, Mazza D, Clerici M. 2022. UV and violet light can neutralize SARS-CoV-2 infectivity. J Photochem Photobiol 10:100107. https://doi.org/10.1016/j.jpap.2021.100107
31. Terrosi C, Anichini G, Docquier JD, Gori Savellini G, Gandolfo C, Pavone FS, Cusi MG. 2021. Efficient inactivation of SARS-CoV-2 and other RNA or DNA viruses with blue LED light. Pathogens 10:1590. https://doi.org/10.3390/pathogens10121590
32. Rathnasinghe R, Jangra S, Miorin L, Schotsaert M, Yahnke C, García-Sastre A. 2021. The virucidal effects of 405 nm visible light on SARS-CoV-2 and influenza A virus. Sci Rep 11:19470. https://doi.org/10.1038/s 41598-021-97797-0
33. Gorman S. 2023. The inhibitory and inactivating effects of visible light on SARS-CoV-2: a narrative update. J Photochem Photobiol 15:100187. https://doi.org/10.1016/j.jpap.2023.100187
34. Hessling M, Lau B, Vatter P. 2022. Review of virus inactivation by visible light. Photonics 9:113. https://doi.org/10.3390/photonics9020113
35. Amodeo D, Manzi P, De Palma I, Puccio A, Nante N, Barcaccia M, Marini D, Pietrella D. 2023. Efficacy of violet-blue (405 nm) LED lamps for disinfection of high-environmental-contact surfaces in healthcare facilities: leading to the inactivation of microorganisms and reduction of MRSA contamination. Pathogens 12:1338. https://doi.org/10.3390/patho gens12111338
36. Sinclair LG, Dougall LR, Ilieva Z, McKenzie K, Anderson JG, MacGregor SJ, Maclean M. 2023. Laboratory evaluation of the broad-spectrum antibacterial efficacy of a low-irradiance visible 405-nm light system for surface-simulated decontamination. Health Technol 13:615–629. https://doi.org/10.1007/s12553-023-00761-3
37. Schultz EW. 1928. Inactivation of staphyloccus bacteriophage by methylene blue. Exp Biol Med (Maywood) 26:100–101. https://doi.org/10.3181/00379727-26-4158
38. Käsermann F, Kempf C. 1998. Buckminsterfullerene and photodynamic inactivation of viruses. Rev Med Virol 8:143–151. https://doi.org/10.1002/(sici)1099-1654(199807/09)8:3<143::aid-rmv214>3.0.co;2-b
39. Costa L, Faustino MAF, Neves MGPMS, Cunha A, Almeida A. 2012. Photodynamic inactivation of mammalian viruses and bacteriophages. Viruses 4:1034–1074. https://doi.org/10.3390/v4071034
40. De Santis R, Luca V, Näslund J, Ehmann RK, De Angelis M, Lundmark E, Nencioni L, Faggioni G, Fillo S, Amatore D, Regalbuto E, Molinari F, Petralito G, Wölfel R, Stefanelli P, Rezza G, Palamara AT, Antwerpen M, Forsman M, Lista F. 2021. Rapid inactivation of SARS-CoV-2 with LED irradiation of visible spectrum wavelengths. J Photochem Photobiol 8:100082. https://doi.org/10.1016/j.jpap.2021.100082
41. Kocher J, Arwood L, Roberts RC, Henson I, Annas A, Emerson D, Stasko N, Fulcher ML, Brotton M, Randell SH, Cockrell AS. 2022. Visible blue light inactivates SARS-CoV-2 variants and inhibits delta replication in differentiated human airway epithelia. bioRxiv. https://doi.org/10.1101/ 2022.01.25.477616
42. Cubuk J, Alston JJ, Incicco JJ, Singh S, Stuchell-Brereton MD, Ward MD, Zimmerman MI, Vithani N, Griffith D, Wagoner JA, Bowman GR, Hall KB, Soranno A, Holehouse AS. 2021. The SARS-CoV-2 nucleocapsid protein is dynamic, disordered, and phase separates with RNA. Nat Commun 12:1936. https://doi.org/10.1038/s41467-021-21953-3
43. Itri R, Junqueira HC, Mertins O, Baptista MS. 2014. Membrane changes under oxidative stress: the impact of oxidized lipids. Biophys Rev 6:47–61. https://doi.org/10.1007/s12551-013-0128-9
44. Schmid GH. 1980. Conformational changes caused by blue light, p 198–204. In Senger H (ed), The blue light syndrome. Springer, Berlin, Heidelberg.
45. Oh P, Kang KW, Ryu SR, Lim S, Sohn M, Lee S, Jeong H. 2022. Evaluation of photobiogoverning role of blue light irradiation on viral replication. Photochem & Photobiology 98:461–470. https://doi.org/10.1111/php.13 514
46. Gardner A, Ghosh S, Dunowska M, Brightwell G. 2021. Virucidal efficacy of blue LED and far-UVC light disinfection against feline infectious peritonitis virus as a model for SARS-CoV-2. Viruses 13:1436. https://doi.o rg/10.3390/v13081436
47. Grzelak A, Rychlik B, Bartosz G. 2001. Light-dependent generation of reactive oxygen species in cell culture media. Free Radic Biol Med 30:1418–1425. https://doi.org/10.1016/s0891-5849(01)00545-7
48. Wiehe A, O'Brien JM, Senge MO. 2019. Trends and targets in antiviral phototherapy. Photochem Photobiol Sci 18:2565–2612. https://doi.org/10.1039/c9pp00211a
49. Jackson CB, Farzan M, Chen B, Choe H. 2022. Mechanisms of SARS-CoV-2 entry into cells. Nat Rev Mol Cell Biol 23:3–20. https://doi.org/10.1038/s4 1580-021-00418-x
50. Le K, Kannappan S, Kim T, Lee JH, Lee HR, Kim KK. 2023. Structural understanding of SARS-CoV-2 virus entry to host cells. Front Mol Biosci 10:1288686. https://doi.org/10.3389/fmolb.2023.1288686
51. Pires De Souza GA, Le Bideau M, Boschi C, Wurtz N, Colson P, Aherfi S, Devaux C, La Scola B. 2022. Choosing a cellular model to study SARS-CoV-2. Front Cell Infect Microbiol 12:1003608. https://doi.org/10.3389/fci mb.2022.1003608
52. Kehm R, Baldensperger T, Raupbach J, Höhn A. 2021. Protein oxidation - formation mechanisms, detection and relevance as biomarkers in human diseases. Redox Biol 42:101901. https://doi.org/10.1016/j.redox.2 021.101901
53. Cai Z, Yan LJ. 2013. Protein oxidative modifications: beneficial roles in disease and health. J Biochem Pharmacol Res 1:15–26.
54. Wong CM, Cheema AK, Zhang L, Suzuki YJ. 2008. Protein carbonylation as a novel mechanism in redox signaling. Circ Res 102:310–318. https://doi.org/10.1161/CIRCRESAHA.107.159814
55. Duché G, Sanderson JM. 2024. The chemical reactivity of membrane lipids. Chem Rev 124:3284–3330. https://doi.org/10.1021/acs.chemrev.3 c00608
56. Barclay LRC, Locke SJ, MacNeil JM, Vankessel J. 1985. Quantitative studies of the autoxidation of linoleate monomers sequestered in phosphatidylcholine bilayers. absolute rate constants in bilayers. Can J Chem 63:2633–2638. https://doi.org/10.1139/v85-437

57. Pliss EM, Loshadkin DV, Grobov AM, Kuznetsova TS, Rusakov AI. 2015. Kinetic study and simulation of methyl linoleate oxidation in micelles. Russ J Phys Chem B 9:127–131. https://doi.org/10.1134/S199079311501 0091
58. Saud Z, Tyrrell VJ, Zaragkoulias A, Protty MB, Statkute E, Rubina A, Bentley K, White DA, Rodrigues PDS, Murphy RC, et al. 2022. The SARS-CoV2 envelope differs from host cells, exposes procoagulant lipids, and is disrupted in vivo by oral rinses. J Lipid Res 63:100208. https://doi.org/1 0.1016/j.jlr.2022.100208
59. Sun X, Whittaker GR. 2003. Role for influenza virus envelope cholesterol in virus entry and infection. J Virol 77:12543–12551. https://doi.org/10.1 128/jvi.77.23.12543-12551.2003
60. Petrich A, Chiantia S. 2023. Influenza A virus infection alters lipid packing and surface electrostatic potential of the host plasma membrane. Viruses 15:1830. https://doi.org/10.3390/v15091830
61. Casalino E, Sblano C, Landriscina C. 1996. A possible mechanism for initiation of lipid peroxidation by ascorbate in rat liver microsomes. Int J Biochem Cell Biol 28:137–149. https://doi.org/10.1016/1357-2725(95)00 131-X
62. Vicenti I, Martina MG, Boccuto A, De Angelis M, Giavarini G, Dragoni F, Marchi S, Trombetta CM, Crespan E, Maga G, Eydoux C, Decroly E, Montomoli E, Nencioni L, Zazzi M, Radi M. 2021. System-oriented optimization of multi-target 2,6-diaminopurine derivatives: easily accessible broad-spectrum antivirals active against flaviviruses, influenza virus and SARS-CoV-2. Eur J Med Chem 224:113683. https://doi.org/10.1 016/j.ejmech.2021.113683
63. Pavulraj S, Bergmann T, Trombetta CM, Marchi S, Montomoli E, AlamiSSE, Ragni-Alunni R, Osterrieder N, Azab W. 2021. Immunogenicity of calvenza-03 EIV/EHV vaccine in horses: comparative in vivo study. Vaccines 9:166. https://doi.org/10.3390/vaccines9020166
64. Manenti A, Maggetti M, Casa E, Martinuzzi D, Torelli A, Trombetta CM, Marchi S, Montomoli E. 2020. Evaluation of SARS-CoV-2 neutralizing antibodies using a CPE-based colorimetric live virus micro-neutralization assay in human serum samples. J Med Virol 92:2096–2104. https://doi.or g/10.1002/jmv.25986
65. Luongo FP, Dragoni F, Boccuto A, Paccagnini E, Gentile M, Canosi T, Morgante G, Luddi A, Zazzi M, Vicenti I, Piomboni P. 2022. SARS-CoV-2 infection of human ovarian cells: a potential negative impact on female fertility. Cells 11:1431. https://doi.org/10.3390/cells11091431
66. Pierantozzi E, Raucci L, Buonocore S, Rubino EM, Ding Q, Laurino A, Fiore F, Soldaini M, Chen J, Rossi D, Vangheluwe P, Chen H, Sorrentino V. 2023. Skeletal muscle overexpression of sAnk1.5 in transgenic mice does not predispose to type 2 diabetes. Sci Rep 13:8195. https://doi.org/10.1038/s 41598-023-35393-0

Antiviral Research 239 (2025) 106157

Contents lists available at ScienceDirect

Antiviral Research

journal homepage: www.elsevier.com/locate/antiviral

Combined doravirine and islatravir cooperate to inhibit NRTI and NNRTI resistant HIV-1 *in vitro*

Federica Giammarino [a,b,1], Chiara Paletti [b,1], Niccolo Bartolini [b,1], Lia Fiaschi [b], Camilla Biba [b], Ilenia Varasi [b], Emanuele Foca [c], Roberto Gulminetti [d], Micol Ferrara [e], Laura Comi [f], Ilaria Vicenti [b], Antonella Castagna [g], Maurizio Zazzi [b], Francesco Saladini [b,*], PRESTIGIO Study Group[2]

[a] *Division of Infectious Diseases, Department of Medicine Huddinge, Karolinska Institutet, Stockholm, Sweden*
[b] *Department of Medical Biotechnologies, University of Siena, Siena, Italy*
[c] *Unit of Infectious and Tropical Diseases, Department of Clinical and Experimental Sciences, University of Brescia and ASST Spedali Civili di Brescia, Brescia, Italy*
[d] *Fondazione IRCCS Policlinico San Matteo, Pavia, Italy*
[e] *Ospedale Amedeo di Savoia, Torino, Italy*
[f] *ASST Papa Giovanni XXIII, Bergamo, Italy*
[g] *San Raffaele Vita-Salute University, Milan, Italy*

ARTICLE INFO

Keywords:
HIV-1
Multidrug resistance
Islatravir
Doravirine
Combinatorial activity

ABSTRACT

Doravirine and islatravir have shown promising activity against multidrug resistant HIV-1. In this study we aimed to evaluate the *in vitro* susceptibility to doravirine and islatravir as well as their combinatorial activity in a panel of 38 recombinant viruses harboring multiple NRTI and NNRTI mutations. One additional recombinant virus had the M184V mutation alone. According to the IC_{50} fold-change (FC) values calculated with respect to the NL4-3 wild-type strain, full susceptibility to doravirine was detected in 15/39 (38.5 %) samples, while high-level resistance was mainly associated with specific doravirine resistance mutations. Decreased susceptibility to islatravir was associated with the presence of the M184V/I mutation and increasing numbers of TAMs and NRTI resistance mutations. According to ZIP model of the SynergyFinder Plus tool, the combination of doravirine and islatravir showed additive activity in 37/40 (92.5 %) viruses (including the NL4-3 strain), while synergy and antagonism in one and two cases, respectively. The combination sensitivity score calculated by SynergyFinder Plus indicated a cooperative effect between doravirine and islatravir higher than that observed for the reference NL4-3 strain in 22 (56 %) recombinant viruses. The Multi-dimensional Synergy of Combinations (MuSyC) tool predicted synergy and antagonism in 25 (62.5 %, including NL4-3 virus) and 15 (37.5 %) cases, respectively. MuSyC scores showed a negative correlation with doravirine FC values, number of NRTI mutations and presence of M184V/I, but not with islatravir FC values. Doravirine and islatravir may cooperatively inhibit NRTI and NNRTI resistant viruses despite complex mutational profiles, however the accumulation of resistance mutations may reduce the combinatorial activity.

1. Introduction

Doravirine is an HIV-1 non-nucleoside reverse transcriptase inhibitor (NNRTI) approved in 2018 both as first-line regimen and as maintenance option in virologically suppressed people living with HIV-1 (PLWH). Doravirine has shown to retain *in vitro* activity against different HIV-1 subtypes harboring the most common NNRTI resistance associated mutations selected by older NNRTI, including K103N, Y181C, G190A, and K103N/Y181C double mutants (Lai et al., 2014; Feng et al., 2016; Asante-Appiah et al., 2021). Doravirine demonstrated high genetic barrier to resistance with both wild-type and NNRTI resistant isolates *in vitro*, resulting in delayed viral breakthrough compared to

* Corresponding author.
E-mail address: saladini6@unisi.it (F. Saladini).
[1] These authors equally contributed to the work.
[2] The members of the study group are listed in the section PRESTIGIO Study Group.

https://doi.org/10.1016/j.antiviral.2025.106157
Received 26 February 2025; Received in revised form 5 April 2025; Accepted 9 April 2025
Available online 18 April 2025

other NNRTI such as rilpivirine, etravirine or efavirenz (Feng et al. 2015, 2016). The substitutions emerging during these experiments included V106A/M, V108I, F227C/I/L, and L234I, which were shown to reduce susceptibility to doravirine but not to other NNRTI, indicating a partially distinct resistance profile. Other mutations emerging during clinical trials and associated with reduced phenotypic susceptibility to doravirine were A98G, V106I, Y188L, H221Y, P225H, Y318F, always detected as multiple mutations except for Y188L which emerged as single mutant in one case and was associated with high level resistance. The viruses with emerging mutations retained activity against rilpivirine and etravirine in most cases, confirming the partly unique resistance profile among the NNRTI class (Martin et al., 2020; Orkin et al., 2023). However, susceptibility to doravirine may be reduced by complex patterns of NNRTI mutations, particularly in the presence of more than three aminoacidic substitutions, even in absence of specific doravirine resistance signature mutations (Saladini et al., 2021, 2023; Asante-Appiah et al., 2021).

Islatravir is an investigational first-in-class nucleoside reverse transcriptase translocation inhibitor (NRTTI), currently under phase III clinical evaluation. Different from nucleoside/nucleotide reverse transcriptase inhibitors (NRTI), islatravir is a deoxyadenosine analog with a 3—OH group allowing either to act as immediate or delayed chain terminator, depending on the interaction of the *4′*-ethynyl group with a conserved hydrophobic pocket in the polymerase active site, resulting in a strong inhibition of translocation of viral RT and synthesis of viral DNA (Michailidis et al., 2009). Islatravir was shown to retain activity across different subtypes and superior potency against variable patterns of NRTI mutations (Kawamoto et al., 2008; Maeda et al., 2014; Grobler et al., 2018; Njenda et al., 2018; Diamond et al., 2022). Interestingly, the NRTI mutations K65R and L74V have been shown to confer hypersusceptibility to islatravir (Kawamoto et al., 2008; Diamond et al., 2022; Grobler et al., 2018). Resistance to islatravir is mainly driven by the M184V/I mutation, which has been selected *in vitro* alone or together with V90I, A114S or I142V + T165R, although these substitutions had a minimal or no impact on islatravir susceptibility in the absence of M184V/I (Kawamoto et al., 2008; Oliveira et al., 2017; Cilento et al., 2021; Diamond et al., 2022).

Recent *in vitro* dual selection experiments with doravirine/islatravir resulted in the limited emergence of resistance mutations starting from both wild-type and NRTI and/or NNRTI resistant viruses, suggesting a highly favorable interaction between the two drugs (Brenner et al., 2023).

In this study we performed *in vitro* isobolographic analysis of combinations of islatravir and doravirine to evaluate their combinatory activity against HIV-1 isolates harboring NRTI and/or NNRTI mutations derived from highly treatment-experienced PLWH.

2. Materials and methods

2.1. Clinical samples

Plasma samples were mainly collected from individuals enrolled in the Italian PRESTIGIO Registry (NCT04098315), which includes PLWH with documented genotypic resistance to NRTI, NNRTI, protease inhibitors (PI) and integrase strand transfer inhibitors (INSTI) (Clemente et al., 2024). Genotypic resistance to a drug class was defined as at least intermediate resistance to at least one drug in the class, according to the Stanford HIVdb algorithm, version 9.7. Additional plasma samples were collected at the University Hospital in Siena, Italy, following completion of routine HIV genotyping tests and patient informed consent, as approved by the local Ethics Committee of the University Hospital.

2.2. Cells and reagents

293T Lenti-X cells (Takara Bio) were cultured in DMEM high glucose with L-glutamine, supplemented with 10 % fetal bovine serum (FBS), 100 U/mL penicillin, and 100 μg/mL streptomycin. The TZM-bl and MT-2 cell lines were obtained from the Centre for AIDS Reagent of the National Institute for Biological Standards and Control. TZM-bl cells were cultured in DMEM high glucose with L-glutamine, supplemented with 10 % FBS, 100 U/mL penicillin and 100 μg/mL streptomycin, while MT-2 cells were cultured in RPMI with 2 mM L-glutamine, supplemented with 10 % FBS, 100 U/mL penicillin and 100 μg/mL streptomycin. All cell culture media and reagents were obtained from EuroClone.

2.3. Antiviral drugs

Doravirine and islatravir were kindly provided by Merck Sharp & Dohme LLC.

2.4. Generation of recombinant viruses

Recombinant viruses were generated through homologous recombination between a modified NL4-3 vector lacking the region encompassing the Gag cleavage sites, the protease and the first 290 amino acids of reverse transcriptase (pNL4-3ΔPR-RT, HXB2 nucleotide coordinates of deletion 1850–3420) and a clinically derived PCR fragment corresponding to the deletion (Saladini et al., 2018). For the amplification of the target region, viral RNA was extracted from the bottom 0.4mL following centrifugation of 1.5mL of plasma at 20,000×*g* for 90 min, by using the EZ1 automatic system and the DSP Virus Kit (Qiagen) according to the manufacturer's instructions. The reverse transcription and first-round PCR were performed using the SuperScript III One-Step RT-PCR System with Platinum Taq High Fidelity (Invitrogen) using the primers P210 (5′-ACCCTTCAGGAACAAATAGSATGGA-3′, HXB2 nucleotide coordinates 1513–1537) and P220 (5′-TTCTGCTATT AAGTCTTTTGMTGGGTCRTA-3′, HXB2 3504–3533). Two microliters of the first-round PCR were used as the template for a nested PCR including the Q5 Hot Start High-Fidelity DNA Polymerase (New England Biolabs) and the primers P240 (5′-CAAAGGAACCCTTYAGAGAYTATGT-3′, HXB2 1655–1679) and P533 (5′- GCTAYTAARTCTTTTGWTGGGTCATA-3′, HXB2 3504–3529). Triplicate nested PCRs of each sample were purified, combined with 10 μg of linearized pNL4-3ΔPR-RT and co-transfected in 293T Lenti-X cells through a calcium phosphate method as previously described (Saladini et al., 2018). Supernatants harboring recombinant viruses were harvested 48 h post transfection and expanded in MT-2 cells to increase viral titers. In presence of large cellular syncytia, supernatants were harvested and stored at −80 °C.

2.5. Determination of the in vitro susceptibility to doravirine and islatravir

In vitro susceptibility to doravirine and islatravir was determined in duplicate through a TZM-bl cell-based assay previously shown to correlate well with the reference phenotypic Phenosense Assay (Saladini et al., 2018). Briefly, 10,000 TZM-bl cells/well were infected with the wild-type NL4-3 strain or NRTI/NNRTI resistant recombinant viruses at multiplicity of infection of 0.03 in the presence of five-fold dilution of doravirine (range 10 μM–0.00512 nM) and islatravir (range 5 μM–0.00256 nM). After 48 h, cells were treated with the Glo-Lysis buffer (Promega) and virus replication was measured as relative luminescence units by using the Bright-Glo Luciferase Assay with the GloMax Discover instrument (Promega) and elaborated with GraphPad software to calculate half-maximal inhibitory concentration (IC_{50}) values. The IC_{50} fold-change (FC) values were calculated with respect to the IC_{50} value obtained with the NL4-3 wild-type strain. Viruses with FC > 100 were considered as FC = 100 for statistical analyses. For doravirine, the 3-fold biological cut-off as determined by Monogram Biosciences was considered to infer clinical resistance. Currently, neither clinical nor biological cut-offs are available for islatravir.

2.6. HIV-1 sequencing, subtyping and genotypic prediction of drug activity

PCR amplicons generated to produce recombinant viruses were sequenced by Sanger population sequencing using primers P214 (5′-TTTGCCAGGAAAATGGAAACCAAAAATGAT-3′, HXB2 2363–2392) and P533. The HIV-1 subtype was assigned by using the COMET HIV-1 subtyping tool (Struck et al., 2014). According to the Stanford HIVdb algorithm version 9.7, the following NNRTI mutations with score equal to or higher than 15 were considered as associated with resistance to doravirine: L100I, V106A/L/M, Y188F/L, G190E/S/Q, P225H, F227C/I/L/V, M230L, L234I, Y318F.

2.7. Determination of the combinatorial activity of doravirine and islatravir

The combinatorial activity or doravirine and islatravir was determined in a 6 × 6 drug concentration matrix assay by infecting 10,000 TZM-bl cells/well with the wild-type NL4-3 strain or NRTI/NNRTI resistant viruses at least in duplicate. The NL4-3 virus was used as a reference to evaluate the combinatorial activity in the absence of resistance mutations. For each virus, the concentrations of doravirine and islatravir used in the combination matrix were chosen based on the respective dose-response curve. In particular, the range of concentrations was selected to obtain from no effect to complete inhibition of viral replication according to the activity of each drug, thus viruses showing lower susceptibility to an individual drug required higher concentrations of that drug in the drug combination analysis. Dilutions of drugs were combined in a checkerboard format, meaning that serial dilutions of one drug are distributed across rows, while the dilutions of the other drug are distributed among columns. After 48 h, luminescence values were normalized to calculate the percentage of inhibition of viral replication and elaborated with the SynergyFinder Plus tool (https://synergyfinder.org/) to calculate synergy scores using the Zero Interaction Potency (ZIP) model (Yadav et al., 2015; Zheng et al., 2022). Values lower than 10, from 10 to 10 and higher than 10 are associated with antagonistic, additive and synergistic effect, respectively. SynergyFinder Plus was also used to calculate the combination sensitivity score (CSS), which represents a quantitative measure of the overall efficacy of a drug combination, providing a single metric that summarizes the drug pair's effectiveness and potency across the concentrations tested in the drug combination analysis. The score is calculated by considering both the level of inhibition and the changes in the shapes of the dose-response curves across all drug combinations with respect to the curves of single drugs. (Malyutina et al., 2019). Data from concentration matrices were also analyzed through the Multi-dimensional Synergy of Combinations (MuSyC) tool (https://musyc.lolab.xyz/), which has been developed to address two types of synergy in drug combinations (Meyer et al., 2019; Wooten et al., 2021). MuSyC extends the Hill equation into a two-dimensional (2D) model, allowing differentiation between synergistic potency and efficacy. The MuSyC software analyzes the effect of combination of drugs using two different indicators. The β parameter represents the percentage change in the effect of a drug combination over the most effective single drug. For synergistic efficacy (β > 0), the combination effect at the maximum concentration of both drugs exceeds the maximum effect of either drug alone. Conversely, for antagonistic interaction (β < 0), one or both drugs are more effective as single agents than when used in combination. The α parameter measures how the effective dose (IC_{50}) of one drug is influenced by the presence of the other. Since each drug can independently affect the potency of the other, α12 and α21 (effect of drug1 on potency of drug 2 and vice versa, respectively) values are calculated for both drugs. This allows to describe cases where a drug combination exhibits synergistic potency in one direction (α12 > 0) and antagonistic potency in the other (α21 < 0), or vice versa. In this study, drug 1 was islatravir and drug 2 was doravirine.

2.8. Statistical analysis

The Spearman test was used to test the correlation between fold-change values, ZIP and CSS scores from SynergyFinder Plus analysis, number of TAM and NRTI mutations, α and β scores from MuSyC analysis. The Jonckheere-Terpstra test was used to analyze the association of phenotypic drug susceptibility of doravirine with the Stanford HIVdb susceptibility level. The Mann-Whitney test was used to compare phenotypic susceptibility values of either doravirine or islatravir depending on the presence of specific doravirine resistance mutations or the presence of M184V/I mutation, respectively. All statistical analyses were performed by SPSS (IBM Corporation) version 20.

3. Results

3.1. Clinical samples

We selected 39 plasma samples from 38 PLWH harboring virus with NRTI and/or NNRTI resistance mutations. According to the information available from 33 PLWH, at sample collection the median viral load was 4.3 [IQR 3.4–5.1] log copies HIV-1 RNA/mL, 13 (39.4 %) and 2 (6.1 %) were on treatment with NRTI or NNRTI, respectively, while 12 (36.4 %) were receiving both NRTI and NNRTI. The NRTI included in the treatment were lamivudine or emtricitabine in 21 (63.6 %) cases, tenofovir DF or alafenamide in 19 (57.6 %) cases, and zidovudine in 1 (3.1 %) case, while the NNRTI were etravirine in 12 (36.4 %) cases, rilpivirine and doravirine in 1 case each (3.0 %).

3.2. In vitro susceptibility to doravirine and islatravir

According to the 3-fold biological FC cut-off, 15/39 (38.5 %) viruses were fully susceptible to doravirine, while 9/39 (23.1 %) showed high-level resistance with >100 FC. The 13 viruses (33.3 %) with doravirine resistance mutations had a significantly higher median FC value compared to viruses without (100 [16.4–100] vs. 2.4 [0.6–6.6], P < 0.0001). The distribution of FC values strongly correlated with the levels of predicted susceptibility to doravirine as determined by the HIVdb

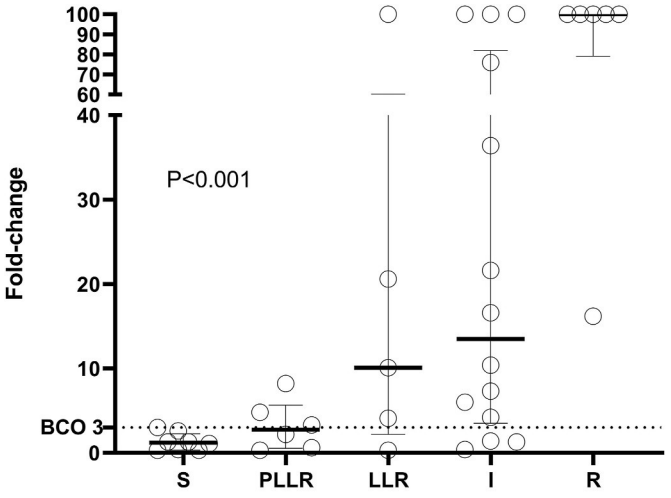

	S	PLLR	LLR	I	R
N	8	6	5	14	5
Median	1.2	2.8	10.1	13.5	100
IQR	0.3-2.3	0.5-5.7	2.2-60.3	3.5-82	79-100

Fig. 1. Distribution of doravirine IC_{50} fold-change values according to the predicted susceptibility levels as determined by the Stanford HIVdb algorithm. Abbreviations: S, susceptible; PLLR, potential low-level resistance; LLR, low-level resistance; I, intermediate resistance; R, high-level resistance; BCO, biological foldchange cut-off value.

algorithm (P < 0.0001) (Fig. 1). However, viruses with predicted low-level or intermediate resistance were associated with a wide range of FC values, with 5/19 (26.3 %) viruses showing a FC < 3 suggesting full susceptibility (Table 1). Enhanced susceptibility to doravirine (fold-change <0.4) was detected in four viruses, two from the same patient with NNRTI mutations E138A + G190A (cases 19 and 31), and two with K103N + Y181I (case 17) or K101E + E138K (case 35).

The median FC values to islatravir in the whole virus panel was 3.9 [1.3–10.4], with viruses harboring the M184V/I mutation (n = 26) showing a higher median FC value compared with those without (7.7 [3.6–13.2] vs. 1.3 [0.8–2.2], respectively; p < 0.0001). Both the total number of NRTI resistance mutations and the number of TAMs had a strong positive correlation with islatravir FC values (rho = 0.342, p = 0.03; rho = 0.597, p < 0.001; respectively). Increasing numbers of TAMs resulted in higher resistance to islatravir also in the subset of viruses harboring the M184V/I mutation (Fig. 2). The only one virus harboring the M184V mutation alone (case 32) showed a FC value of 10.4. Enhanced susceptibility to islatravir was detected in two cases, one with mixed L74LI (case 38), one with a complex pattern of mutations including A62V, D67N, K70E, V75I, Y115F, F116Y, Q151M, M184V (case 29).

3.3. Evaluation of the combinatorial activity using the SynergyFinder plus software

According to the synergy scores calculated through the ZIP model, the combination of doravirine and islatravir was additive in 37/40 (92.5 %) cases, including the wild-type NL4-3 virus which showed a ZIP score

Table 1
Genotypic and phenotypic susceptibility of viruses harbouring NRTI and NNRTI resistance associated mutations (RAM).

Virus	Subtype	NRTI RAM	NNRTI RAM	Doravirine fold-change	Islatravir fold-change	Predicted doravirine resistance
1	B	M41L, D67G, S68G, K70R, L74I, M184V, T215Y, K219E	A98G, K103N, Y181C, P225H	16.2	7.3	R
2	B	M41ML, T215F	E138EG, Y181C	1.3	3.4	S
3	B	M41L, A62V, V75I, L210W, T215CHRY	K103N, Y181V	8.2	2.5	PLLR
4	B	L74V	L100I, K103N, K238N	10.4	0.6	I
5	B	M41L, T215Y	K103N, Y181C	4.8	1.3	PLLR
6	B	D67N, T69D, K70R, M184MV, T215TAIV, K219Q	K103NS, Y181C, G190S	21.6	2.8	I
7	B	D67N, K70R, M184V, T215F, K219E	V108I, E138A, Y181V	10.1	14.9	LLR
8	B	M41L, T69D, M184V, L210W, T215Y	V108I, Y181C	4.1	8.5	LLR
9	B	D67N, K70R, M184V, T215F, K219Q	A98G	3.3	13.7	PLLR
10	B	M41L, E44D, S68G, L74V, M184V, L210W, T215Y, K219N	L100I, E138R, V179L	20.6	3.8	LLR
11	F1	D67N, K70R, T215L, K219E	K101E, Y181C, G190A	6	1.3	I
12	B	D67N, T69D, L74LI, V75S, T215L, K219Q	A98G, L100I, K103N, E138Q	>100	1.8	I
13	B	M41L, D67N, L74V, L210W, T215C, K219N	L100I, K103N, E138G	7.3	0.7	I
14	B	K70Q, M184MV, T215F	E138Q, V179E, Y181C	1.1	3.9	S
15	B	K65R, Y115F, M184V	Y181C, H221Y, M230I	76	2.4	I
16	B	D67G, S68SG, K70KE, V75IT, M184V	K103KR, V108VI, V179E, Y181C, G190A, H221Y	4.2	6.6	I
17	B	M41L, E44D, D67N, T69D, M184V, L210W, T215Y, K219KR	K103N, Y181I	0.3	8	PLLR
18	B	M41L, E44D, D67N, K70KQ, V75M, F77L, M184I, L210W, T215Y	K101KE, E138A, V179F, Y181V	0.4	16	I
19*	B	M41L, E44D, D67N, K70Q, V75M, F77L, M184I, L210W, T215Y, K219R	E138A, G190A	0.3	37.8	S
20	B	M41L, L74V, Y115F, M184V, T215Y	Y181C	2.6	3.1	S
21	B	M41L, D67N, V75I, M184MV, L210W, T215Y, K219N	L100I, K103N, V179T	16.6	4.5	I
22	B	M41L, A62AV, D67N, K70G, V75I, M184MV, L210W, T215Y, K219Q	K101E, Y181C, G190A	1.4	2.3	I
23	F1	M41L, D67N, T69S_ES, F77L, L210W, T215Y	K103N	0.4	8.1	S
24	B	D67N, K70R, T215E, K219Q	K101H, V108I, Y181C, G190A	36.4	1	I
25	B	M41L, S68G, M184V, L210W, T215C, K219E	Y181I	1.3	5.5	I
26	B	M41L, E44D, L74V, M184V, L210W, T215Y	K103N, E138A, P225H, M230L	>100	20.9	R
27	B	M41L, E44D, D67G, V75M, M184V, L210W, T215Y, K219N	L100V, K101H, V179F, Y181C, G190A	>100	26.4	I
28	B	M41L, M184V, L210W, T215Y, K219E	K101E, E138A, G190Q	>100	9.8	I
29	B	A62V, D67N, K70E, V75I, Y115F, F116Y, Q151M, M184V	L100I, V179D, G190Q, F227L	>100	0.2	R
30	B	M41L, M184V, L210W, T215Y, K219E	L100I, K103S	>100	10.4	LLR
31*	B	M41L, E44D, D67N, V75M, F77L, M184I, L210W, T215Y, K219R	E138A, G190A	0.3	5.4	S
32	B	M184V	None	3	10.4	S
33	B	D67G, T69ins, K70T, T215Y	K103N, G190A	1.3	0.8	S
34	B	M41L, D67del, T69G, K70R, M184V, T215F, K219E	K103N, Y181C	2.2	12.6	PLLR
35	CRF01_AE	S68G, K70G	K101E, E138K	0.3	0.9	LLR
36	B	M41L, D67N, T215Y	K103N, Y181I	0.6	1.4	PLLR
37	B	M41L, M184V, T215Y	V106I, Y188L	>100	13	R
38	B	L74LI	E138K, G190E	>100	0.3	R
39	B	A62V, D67N, K70E, V75I, Y115F, F116Y, Q151QKLM, M184MV	L100I, V179D, G190Q, F227L	>100	0.8	R

Abbreviations: S, susceptible; PLLR, potential low-level resistance; LLR, low-level resistance; I, intermediate resistance; R, high-level resistance. *Samples 19 and 31 were obtained from the same subject at different time points.

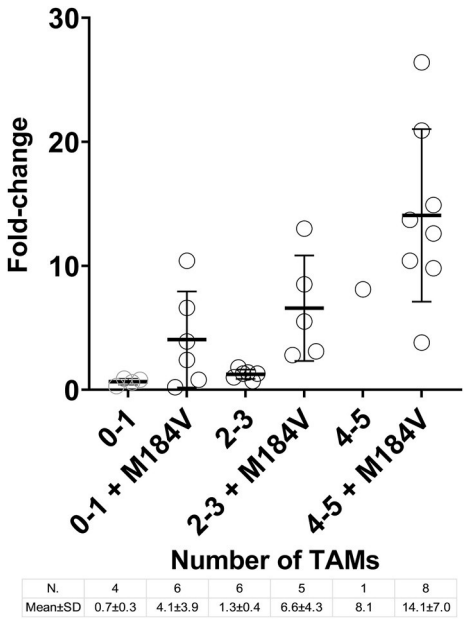

Fig. 2. Distribution of islatravir IC_{50} fold-change values according to the number of thymidine analogue mutations (TAMs) and the presence of the M184V mutation. Mean fold-change values and standard deviation for each group are indicated below the graph.

of 0.95 (Fig. 3). Synergistic activity was identified only with sample 17, which showed enhanced susceptibility to doravirine, although other samples with increased susceptibility to doravirine showed variable ZIP scores (range 0.62/-9.24) and were all associated with additive activity. By contrast, antagonistic activity of doravirine and islatravir was observed only with samples 38 and 39, both with high-level resistance to doravirine and full susceptibility to islatravir. However, FC values > 100 to doravirine measured in 9 samples were mostly associated with additive activity, suggesting that high-level resistance to doravirine does not compromise the combinatorial effect with islatravir. Globally, fold-change values of neither doravirine nor islatravir correlated with ZIP scores (p = 0.203 and p = 0.812, respectively), indicating that the combinatorial activity is not influenced by the susceptibility to either individual drug.

The SynergyFinder Plus software also calculates the Combination Sensitivity Score (CSS), which indicates a quantitative measure of the overall efficacy of a drug combination, providing a single metric that summarizes the drug pair's effectiveness and potency. When compared to the wild-type NL4-3 virus, 22/39 (56 %) of the NRTI/NNRTI resistant viruses showed higher CSS values, further supporting that the presence of resistance mutations does not impair the combinatorial activity of doravirine and islatravir (Fig. 4). By contrast, 17 viruses showed both ZIP scores and CSS values lower than those observed for NL4-3 virus, suggesting lower cooperation between doravirine and islatravir. The presence of M184V/I, the number of TAMs, and the doravirine and islatravir fold-changes did not correlate with the CSS value.

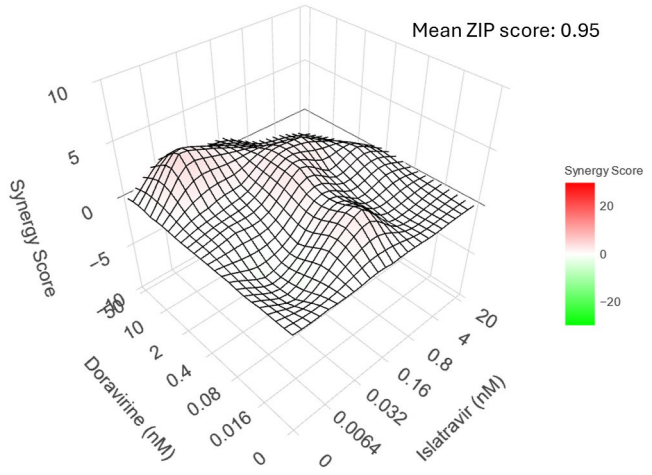

Fig. 3. Synergy landscape of the combination of doravirine and islatravir against the wild-type NL4-3 virus, calculated using the Zero Interaction Potency (ZIP) model through the SynergyFinder Plus software (https://synergyfinder.org/).

3.4. Evaluation of the combinatorial activity using the MuSyC software

According to the MuSyC β parameter, 25/40 (62.5 %) viruses, including the wild-type NL4-3 virus, showed synergy. Globally, β value showed strong positive correlation with both CSS and ZIP (rho = 0.568, P < 0.001 and rho = 0.482, P = 0.002; respectively), although one remarkable exception was virus 11, which showed the lowest β value but had a ZIP score of 4.77, indicating additive activity. β values showed a negative correlation with the fold-change values of doravirine but not with those of islatravir (rho = 0.409, P = 0.009 and rho = 0.211, P = 0.191; respectively), suggesting that susceptibility to doravirine might have a higher impact on the combinatorial activity compared with susceptibility to islatravir. However, the number of NRTI mutations and the presence of M184V/I were negatively correlated with β values (rho = 0.328, P = 0.039, and rho = 0.377, P = 0.018; respectively), suggesting that the accumulation of resistance to NRTI, irrespective of the susceptibility to islatravir, may contribute to reduce the combinatorial activity of doravirine and islatravir.

According to the α parameter, the highest islatravir dose was synergistic with doravirine IC_{50} in 24/37 (64.9 %) cases (not calculated for samples 37, 38 and 39 where only 10 μM was tested), while doravirine was synergistic with islatravir IC_{50} in 19/40 (47.5 %) cases. Confirmed synergy and antagonism based on both α12 and α21 was observed in 16 (40 %) and 11 (27.5 %) cases, respectively, although the associated β value was not consistent with this result in 9/27 (33 %) cases, probably because the β value is calculated on the full set of drug combinations. Regarding α12 and α21, we found that α21 negatively correlated with the number of NRTI mutations (rho = 0.377, P = 0.016), while no other correlations were found with other factors such as doravirine and islatravir fold-changes, number of NRTI or TAMs and the presence of M184V/I mutation.

4. Discussion

Our study suggests that doravirine and islatravir, both alone and in combination, have the potential to inhibit viruses harboring extensive NRTI and NNRTI resistance. These *in vitro* findings are in agreement with a small clinical trial (35 participants) where the combination of doravirine and islatravir plus optimized background was investigated in a group of viremic heavily treatment-experienced individuals with resistance to NRTI and NNRTI (NCT04233216, 2024). In this clinical study, viral replication was suppressed in nearly 70 % of participants with a slight increase of $CD4^+$ T-cell count despite the use of 0.75 mg dose of islatravir, later shown to be lymphocytotoxic. Further studies are required to investigate if the newly investigated 0.25 mg dose of islatravir is able to achieve the same efficacy against viruses harboring resistance mutations selected by licensed reverse transcriptase inhibitors.

For doravirine, the data of the present study extend our previous analysis of a smaller panel of NNRTI resistant viruses (Saladini et al., 2023). However, the lack of established FC clinical cut-offs does not allow to translate this data on expected in vivo activity nor identify cases of partially retained activity which could still be beneficial in salvage therapy. We also confirm other studies showing that M184V/I plus TAM

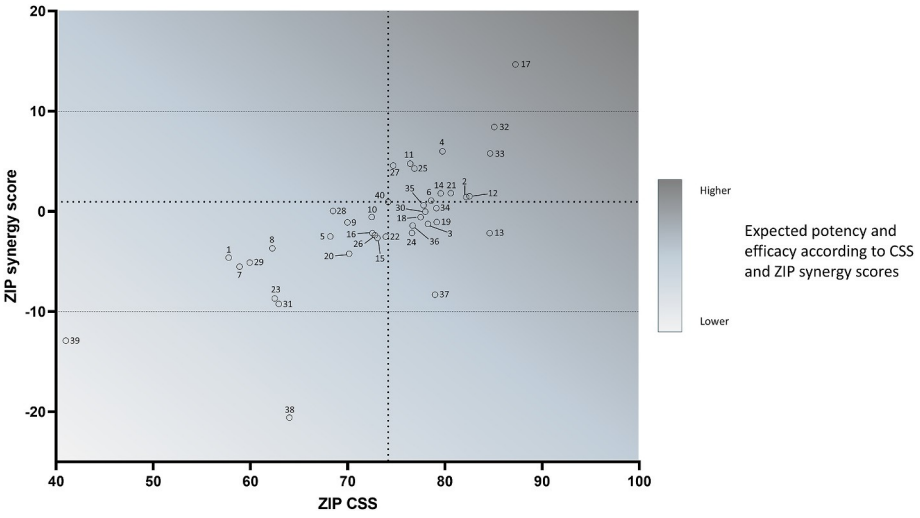

Fig. 4. Scatter plot of ZIP synergy scores and combination sensitivity scores (CSS) of doravirine and islatravir activity as calculated by the SynergyFinder plus software for the 40 viruses tested. Dotted lines intercepting X at 74.17 and Y at 0.95 refer to the CSS and ZIP scores calculated for the NL4-3 wild-type virus, respectively, labelled as number 40. Lines intercepting Y at 10 and -10 identify the thresholds of ZIP synergy scores associated with synergy (Y > 10), additivity (10<Y < 10) and antagonism (Y < 10). Labels indicate the ID of the viruses as described in Table 1. According to both CSS and ZIP synergy scores, the combinatorial activity of doravirine and islatravir is expected to be higher for viruses in the top right, lower in the bottom left area.

causes cross-resistance between islatravir and NRTI (Kawamoto et al., 2008; Cilento et al., 2023; Diamond et al., 2022). Interestingly, sample 32 with the M184V mutation alone had fold-change value of 10.4, higher than the values calculated for some viruses with M184V plus other NRTI mutations. However, similarly high FC values were previously reported among recombinant viruses with M184V alone in a panel showing a wide range of FC values (Aulicino et al., 2024). These findings suggest that the broad levels of resistance to islatravir in presence of M184V might be influenced not only by the addition of other NRTI mutations, but also by the variability of the amino acids that may modulate the interactions between islatravir and the active site of the reverse transcriptase, although off-target effects cannot be excluded as well. A notable exception is represented by sample 29, where hypersusceptibility to islatravir was detected in the presence of a complex pattern of NRTI mutations including M184V. In this case, enhanced susceptibility might be caused by the presence of Q151M, as previously described (Grobler et al., 2018). Similarly to doravirine, the lack of defined phenotypic FC clinical cut-offs for islatravir prevents distinguishing cases of full susceptibility from residual or no in vivo activity.

To our knowledge, this is the first attempt to evaluate the combinatorial activity of a drug combination on different clinically derived recombinant HIV-1 isolates harboring complex patterns of resistance mutations, although using a limited panel of clinical samples. We queried two user-friendly web tools, such as SynergyFinder Plus and MuSyC, which showed a strong positive correlation in the distribution of scores used to calculate the combinatorial activity for each virus, although the thresholds used in the two tools provided different interpretations in several cases. Indeed, while the MuSyC model infers only synergy or antagonism, SynergyFinder Plus attributes also an intermediate level of cooperation defined as additivity. The correlation among the two systems, particularly when using the ZIP model, can be attributed to the common focus on the assessment of how a drug combination deviates from what would be expected if the drugs were non-interacting, based on dose-response curves (e.g., single drug effect) (Yadav et al., 2015; Wooten et al., 2021). Irrespective of the levels of interaction between drugs assigned by the two tools, we can extrapolate some findings of biological meaning. As compared to the NL4-3 wild-type virus, not all the mutational patterns including NRTI and NNRTI mutations appeared to reduce the combinatorial activity of doravirine and islatravir, although either or both drugs may show lower individual activity. However, MuSyC suggested that high-level phenotypic resistance to doravirine, higher numbers of NRTI mutations and the presence of M184V/I decrease the cooperation between doravirine and islatravir. Although the number of NRTI mutations and the presence of M184V/I are known to impair susceptibility to islatravir, islatravir FC values did not correlate with combinatorial activity. On the other hand, the accumulation of resistance to NRTI appeared to affect the activity of doravirine when combined with islatravir.

The two tools for predicting the efficacy of drug combinations queried in this study have been mostly applicated in the field of cancer research but recently extended to antiviral agents, mostly against SARS-CoV-2 (Mast et al., 2021; Liu et al., 2021; Mirabelli et al., 2021; Cochin et al., 2022; Pérez-Vargas et al., 2023; Tang et al., 2024; Fiaschi et al., 2024). However, it must be noted that the clinical utility of these predicting models has been poorly explored (Ling and Huang, 2020) and alternative models have been proposed in recent years (Foucquier and Guedj, 2015). Clearly, matching clinical outcomes with *in vitro* evidence is necessary to clarify if such tools are adequate for a deeper investigation of drug combinations, particularly for antiviral agents.

In conclusion, our study indicates that doravirine and islatravir may cooperate and play a valuable role in the treatment of multidrug resistant HIV-1, even in presence of extensive drug resistance derived from previous exposure to NRTI and NNRTI. By screening larger panels of resistant viruses, further refinements of *in vitro* combinatorial analysis systems together with the definition of the clinical cutoffs are awaited to inform the best use of this drug combination.

CRediT authorship contribution statement

Federica Giammarino: Visualization, Methodology, Investigation. **Chiara Paletti:** Visualization, Methodology, Investigation. **Niccolo Bartolini:** Visualization, Methodology, Investigation. **Lia Fiaschi:** Writing – review & editing, Methodology. **Camilla Biba:** Writing – review & editing, Methodology. **Ilenia Varasi:** Writing – review & editing, Methodology. **Emanuele Foca:** Writing – review & editing, Validation. **Roberto Gulminetti:** Writing – review & editing, Validation. **Micol Ferrara:** Writing – review & editing, Validation. **Laura Comi:** Writing – review & editing, Validation. **Ilaria Vicenti:** Writing – review & editing, Methodology. **Antonella Castagna:** Writing – review & editing, Validation. **Maurizio Zazzi:** Writing – review & editing, Supervision, Funding acquisition, Conceptualization. **Francesco Saladini:** Writing –

original draft, Formal analysis, Conceptualization.

Declaration of competing interest

The authors declare the following financial interests/personal relationships which may be considered as potential competing interests: Francesco Saladini received speaker's honoraria from ViiV Healthcare. Emanuele Focà received speakers' honoraria, research grants and payments for advisory board from Gilead Sciences, MSD, Viiv Healthcare and Astrazeneca. Laura Comi received speaker's honoraria from ViiV Healthcare and Gilead Sciences and payments for advisory board from MSD. Antonella Castagna received personal fees for advisory boards, speaker panels and educational materials from Gilead Sciences, ViiV Healthcare, Janssen-Cilag, MSD and Theratechnlogies. Maurizio Zazzi received grants for his institution from MSD and personal fees from MSD, ViiV Healthcare and Gilead Sciences. All other authors have no conflicts of interest to declare.

Acknowledgements

This work has been supported in part by a research grant from Investigator-Initiated Studies Program of Merck Sharp & Dohme LLC. The opinions expressed in this paper are those of the authors and do not necessarily represent those of Merck Sharp & Dohme LLC.

The PRESTIGIO Registry was approved by the Ethics Committee of the coordinating centre (IRCCS San Raffaele Scientific Institute, Milan, Italy, protocol number: 41/int/December 2017) and by the Ethics Committees of all the participating centres. The Centro San Luigi (CSL) HIV Cohort was approved by the Ethics Committee of IRCCS San Raffaele Scientific Institute, Milan, Italy (protocol number: 34/int/December 2017). Anonymized data of people with HIV included in the PRESTIGIO Registry and in the CSL HIV Cohort were used for research studies following written informed consent and Good Clinical Practice.

PRESTIGIO Study Group

STEERING COMMITTEE: Antonella Castagna (Coordinator), Vincenzo Spagnuolo (Operative coordinator), Daniele Armenia, Stefano Bonora, Leonardo Calza, Anna Maria Cattelan, Giovanni Cenderello, Adriana Cervo, Laura Comi, Antonio Di Biagio, Emanuele Focà, Roberta Gagliardini, Andrea Giacomelli, Filippo Lagi, Giulia Marchetti, Stefano Rusconi, Francesco Saladini, Maria Mercedes Santoro, Maurizio Zazzi. **VIROLOGY TEAM AND BIOLOGICAL BANK:** Andrea Galli, Daniele Armenia, Francesco Saladini, Maria Mercedes Santoro, Maurizio Zazzi, BioRep SRL. **STUDY COORDINATORS:** Elisabetta Carini, Sabrina Bagaglio, Girolamo Piromalli. **STATISTICAL AND MONITORING TEAM:** Riccardo Lolatto. **ENROLLING CENTRES: ANCONA:** Marcello Tavio, Alessandra Mataloni Paggi; **AVIANO:** Ornella Schioppa, Valentina Da Ros; **BARI:** Annalisa Saracino, Flavia Balena; **BERGAMO:** Laura Comi, Daniela Valenti, Claudia Suardi; **BOLOGNA:** Pierluigi Viale, Leonardo Calza, Federica Malerba, Silvia Cretella, Riccardo Riccardi; **BRESCIA:** Francesco Castelli, Emanuele Focà, Davide Minisci, Francesca Pennati; **BUSTO ARSIZIO:** Barbara Menzaghi, Maddalena Farinazzo; **CATANIA:** Bruno Cacopardo, Maurizio Celesia, Michele Salvatore Paternò Raddusa, Carmen Giarratana; **CATANZARO:** Paolo Fusco, Vincenzo Olivadese; **CREMONA:** Angelo Pan, Chiara Fornabaio, Paola Brambilla; **FIRENZE:** Alessandro Bartoloni, Filippo Lagi, Paola Corsi, Seble Tekle Kiros, Filippo Ducci, Susanna Giache, Cecilia Costa, Alessio Bellucci, Elisa Mirabelli; **FOGGIA:** Teresa Santantonio, Sergio Lo Caputo, Sergio Ferrara, Arianna Narducci; **GENOVA:** Emanuele Pontali, Marcello Feasi, Antonio Sarà, Matteo Bassetti, Antonio Di Biagio, Sabrina Blanchi; **MILANO:** Antonella Castagna, Vincenzo Spagnuolo, Camilla Muccini, Elisabetta Carini, Sabrina Bagaglio, Riccardo Lolatto, Andrea Galli, Rebecka Papaioannu Borjesson, Tommaso Clemente, Girolamo Piromalli, Spinello Antinori, Andrea Giacomelli, Tiziana Formenti, Fabiola Schiavo, Giulia Marchetti, Lidia Gazzola, Fabiana Trionfo Fineo, Massimo Puoti, Cristina Moioli, Federico D'Amico; **MODENA:** Cristina Mussini, Adriana Cervo; **NAPOLI:** Elio Manzillo, Amedeo Lanzardo; **PADOVA:** Anna Maria Cattelan, Maria Mazzitelli; **PALERMO:** Antonio Cascio, Marcello Trizzino; **PARMA:** Elisa Fronti, Diletta Laccabue, Federica Carli; **PAVIA:** Roberto Gulminetti, Layla Pagnucco, Mattia Demitri; **PERUGIA:** Daniela Francisci, Giuseppe De Socio, Elisabetta Schiaroli; **REGGIO EMILIA:** Elisa Garlassi, Romina Corsini; **ROMA:** Roberta Gagliardini, Marisa Fusto, Loredana Sarmati, Vincenzo Malagnino, Tiziana Mulas, Mirko Compagno Carlo Torti, Simona Di Giambenedetto, Silvia Lamonica, Pierluigi Francesco Salvo; **SANREMO:** Giovanni Cenderello, Rachele Pincino; **SIENA:** Mario Tumbarello, Massimiliano Fabbiani, Francesca Panza, Ilaria Rancan; **TORINO:** Giovanni Di Perri, Stefano Bonora, Micol Ferrara, Andrea Calcagno, Silvia Fantino; **VERONA:** Stefano Nardi, Marta Fiscon. **SUPPORTED BY:** ViiV Healthcare, Gilead Sciences, Merck Sharp & Dohme, Janssen-Cilag.

Appendix A. Supplementary data

Supplementary data to this article can be found online at https://doi.org/10.1016/j.antiviral.2025.106157.

Data availability

Data will be made available on request.

References

Asante-Appiah, E., Lai, J., Wan, H., Yang, D., Martin, E.A., Sklar, P., Hazuda, D., Petropoulos, C.J., Walworth, C., Grobler, J.A., 2021. Impact of HIV-1 resistance-associated mutations on susceptibility to doravirine: analysis of real-world clinical isolates. Antimicrob. Agents Chemother. 65 (12), e0121621. https://doi.org/10.1128/AAC.01216-21. Epub 2021 Sep 27. PMID: 34570651; PMCID: PMC8597775.

Aulicino, P.C., Sharma, S., Truong, K., Kukunoor, V., Ghei, K., Arazi-Caillaud, S., Taicz, M., Bologna, R., Mangano, A., Kimata, J.T., 2024. Variable antiviral activity of islatravir against M184I/V mutant HIV-1 selected during antiretroviral therapy. J. Antimicrob. Chemother. 79 (2), 370–374. https://doi.org/10.1093/jac/dkad390. PMID: 38153245.

Brenner, B.G., Oliveira, M., Ibanescu, R.I., Routy, J.P., Thomas, R., 2023. Doravirine responses to HIV-1 viruses bearing mutations to NRTIs and NNRTIs under *in vitro* selective drug pressure. J. Antimicrob. Chemother. 78 (8), 1921–1928. https://doi.org/10.1093/jac/dkad184. PMID: 37303226.

Cilento, M.E., Reeve, A.B., Michailidis, E., Ilina, T.V., Nagy, E., Mitsuya, H., Parniak, M. A., Tedbury, P.R., Sarafianos, S.G., 2021. Development of human immunodeficiency virus type 1 resistance to 4′-ethynyl-2-fluoro-2′-deoxyadenosine starting with wild-type or nucleoside reverse transcriptase inhibitor-resistant strains. Antimicrobial Agents and Chemotherapy 65 (12), e0116721. https://doi.org/10.1128/AAC.01167-21.

Cilento, M.E., Wen, X., Reeve, A.B., Ukah, O.B., Snyder, A.A., Carrillo, C.M., Smith, C.P., Edwards, K., Wahoski, C.C., Kitzler, D.R., Kodama, E.N., Mitsuya, H., Parniak, M.A., Tedbury, P.R., Sarafianos, S.G., 2023. HIV-1 resistance to islatravir/tenofovir combination therapy in wild-type or NRTI-resistant strains of diverse HIV-1 subtypes. Viruses 15 (10), 1990. https://doi.org/10.3390/v15101990. PMID: 37896768; PMCID: PMC10612037.

Clemente, T., Galli, L., Lolatto, R., Gagliardini, R., Lagi, F., Ferrara, M., Cattelan, A.M., Foca, E., Di Biagio, A., Cervo, A., Calza, L., Maggiolo, F., Marchetti, G., Cenderello, G., Rusconi, S., Zazzi, M., Santoro, M.M., Spagnuolo, V., Castagna, A., PRESTIGIO Study Group, 2024. Cohort profile: PRESTIGIO, an Italian prospective registry-based cohort of people with HIV-1 resistant to reverse transcriptase, protease and integrase inhibitors. BMJ Open 14 (2), e080606. https://doi.org/10.1136/bmjopen-2023-080606. PMID: 38341206; PMCID: PMC10862296.

Cochin, M., Touret, F., Driouich, J.S., Moureau, G., Petit, P.R., Laprie, C., Solas, C., de Lamballerie, X., Nougairede, A., 2022. Hydroxychloroquine and azithromycin used alone or combined are not effective against SARS-CoV-2 ex vivo and in a hamster model. Antivir. Res. 197, 105212. https://doi.org/10.1016/j.antiviral.2021.105212. Epub 2021 Nov 24. PMID: 34838583; PMCID: PMC8611861.

Diamond, T.L., Ngo, W., Xu, M., Goh, S.L., Rodriguez, S., Lai, M.T., Asante-Appiah, E., Grobler, J.A., 2022. Islatravir has a high barrier to resistance and exhibits a differentiated resistance profile from approved nucleoside reverse transcriptase inhibitors (NRTIs). Antimicrob. Agents Chemother. 66 (6), e0013322. https://doi.org/10.1128/aac.00133-22. Epub 2022 May 12. PMID: 35546110; PMCID: PMC9211433.

Feng, M., Sachs, N.A., Xu, M., Grobler, J., Blair, W., Hazuda, D.J., Miller, M.D., Lai, M.T., 2016. Doravirine suppresses common nonnucleoside reverse transcriptase inhibitor-associated mutants at clinically relevant concentrations. Antimicrob. Agents Chemother. 60 (4), 2241–2247. https://doi.org/10.1128/AAC.02650-15. PMID: 26833152; PMCID: PMC4808216.

Feng, M., Wang, D., Grobler, J.A., Hazuda, D.J., Miller, M.D., Lai, M.T., 2015. *In vitro* resistance selection with doravirine (MK-1439), a novel nonnucleoside reverse transcriptase inhibitor with distinct mutation development pathways. Antimicrob. Agents Chemother. 59 (1), 590–598. https://doi.org/10.1128/AAC.04201-14. Epub 2014 Nov 10. PMID: 25385110; PMCID: PMC4291404.

Fiaschi, L., Biba, C., Varasi, I., Bartolini, N., Paletti, C., Giammarino, F., Saladini, F., Zazzi, M., Vicenti, I., 2024. *In vitro* combinatorial activity of direct acting antivirals and monoclonal antibodies against the ancestral B.1 and BQ.1.1 SARS-CoV-2 viral variants. Viruses 16 (2), 168. https://doi.org/10.3390/v16020168. PMID: 38399944; PMCID: PMC10892871.

Foucquier, J., Guedj, M., 2015. Analysis of drug combinations: current methodological landscape. Pharmacol. Res Perspect 3 (3), e00149. https://doi.org/10.1002/prp2.149. Epub 2015 May 20. Erratum in: Pharmacol Res Perspect. 2019 Dec;7(6): e00549. doi: 10.1002/prp2.549. PMID: 26171228; PMCID: PMC4492765.

Grobler, J.A., Huang, Q., Hazuda, D.J., Lai, M.T., 2018. Efficacy of MK-8591 against diverse HIV-1 subtypes and NRTI-resistant clinical isolates. J. Int. AIDS Soc. 21, e25187. https://doi.org/10.1002/jia2.25187.

Kawamoto, A., Kodama, E., Sarafianos, S.G., Sakagami, Y., Kohgo, S., Kitano, K., Ashida, N., Iwai, Y., Hayakawa, H., Nakata, H., Mitsuya, H., Arnold, E., Matsuoka, M., 2008. 2′-deoxy-4′-C-ethynyl-2-halo-adenosines active against drug-resistant human immunodeficiency virus type 1 variants. Int. J. Biochem. Cell Biol. 40 (11), 2410–2420. https://doi.org/10.1016/j.biocel.2008.04.007. Epub 2008 Apr 11. PMID: 18487070.

Lai, M.T., Feng, M., Falgueyret, J.P., Tawa, P., Witmer, M., DiStefano, D., Li, Y., Burch, J., Sachs, N., Lu, M., Cauchon, E., Campeau, L.C., Grobler, J., Yan, Y., Ducharme, Y., Côté, B., Asante-Appiah, E., Hazuda, D.J., Miller, M.D., 2014. *In vitro* characterization of MK-1439, a novel HIV-1 nonnucleoside reverse transcriptase inhibitor. Antimicrob. Agents Chemother. 58 (3), 1652–1663. https://doi.org/10.1128/AAC.02403-13. Epub 2013 Dec 30. PMID: 24379202; PMCID: PMC3957832.

Ling, A., Huang, R.S., 2020. Computationally predicting clinical drug combination efficacy with cancer cell line screens and independent drug action. Nat. Commun. 11 (1), 5848. https://doi.org/10.1038/s41467-020-19563-6. PMID: 33203866; PMCID: PMC7673995.

Liu, H., Yuan, M., Huang, D., Bangaru, S., Zhao, F., Lee, C.D., Peng, L., Barman, S., Zhu, X., Nemazee, D., Burton, D.R., van Gils, M.J., Sanders, R.W., Kornau, H.C., Reincke, S.M., Prüss, H., Kreye, J., Wu, N.C., Ward, A.B., Wilson, I.A., 2021. A combination of cross-neutralizing antibodies synergizes to prevent SARS-CoV-2 and SARS-CoV pseudovirus infection. Cell Host Microbe 29 (5), 806–818.e6. https://doi.org/10.1016/j.chom.2021.04.005. Epub 2021 Apr 15. PMID: 33894127; PMCID: PMC8049401.

Maeda, K., Desai, D.V., Aoki, M., Nakata, H., Kodama, E.N., Mitsuya, H., 2014. Delayed emergence of HIV-1 variants resistant to 4′-ethynyl-2-fluoro-2′-deoxyadenosine: comparative sequential passage study with lamivudine, tenofovir, emtricitabine and BMS-986001. Antivir. Ther. 19 (2), 179–189. https://doi.org/10.3851/IMP2697. Epub 2013 Oct 25. PMID: 24162098.

Malyutina, A., Majumder, M.M., Wang, W., Pessia, A., Heckman, C.A., Tang, J., 2019. Drug combination sensitivity scoring facilitates the discovery of synergistic and efficacious drug combinations in cancer. PLoS Comput. Biol. 15 (5), e1006752. https://doi.org/10.1371/journal.pcbi.1006752. PMID: 31107860; PMCID: PMC6544320.

Martin, E.A., Lai, M.T., Ngo, W., Feng, M., Graham, D., Hazuda, D.J., Kumar, S., Hwang, C., Sklar, P., Asante-Appiah, E., 2020. Review of doravirine resistance patterns identified in participants during clinical development. J. Acquir. Immune Defic. Syndr. 85 (5), 635–642. https://doi.org/10.1097/QAI.0000000000002496. PMID: 32925358; PMCID: PMC7655028.

Mast, F.D., Fridy, P.C., Ketaren, N.E., Wang, J., Jacobs, E.Y., Olivier, J.P., Sanyal, T., Molloy, K.R., Schmidt, F., Rutkowska, M., Weisblum, Y., Rich, L.M., Vanderwall, E. R., Dambrauskas, N., Vigdorovich, V., Keegan, S., Jiler, J.B., Stein, M.E., Olinares, P. D.B., Herlands, L., Hatziioannou, T., Sather, D.N., Debley, J.S., Fenyö, D., Sali, A., Bieniasz, P.D., Aitchison, J.D., Chait, B.T., Rout, M.P., 2021. Highly synergistic combinations of nanobodies that target SARS-CoV-2 and are resistant to escape. Elife 10, e73027. https://doi.org/10.7554/eLife.73027. PMID: 34874007; PMCID: PMC8651292.

Meyer, C.T., Wooten, D.J., Paudel, B.B., Bauer, J., Hardeman, K.N., Westover, D., Lovly, C.M., Harris, L.A., Tyson, D.R., Quaranta, V., 2019. Quantifying drug combination synergy along potency and efficacy axes. Cell Syst 8 (2), 97–108.e16. https://doi.org/10.1016/j.cels.2019.01.003. Epub 2019 Feb 20. PMID: 30797775; PMCID: PMC6675406.

Michailidis, E., Marchand, B., Kodama, E.N., Singh, K., Matsuoka, M., Kirby, K.A., Ryan, E.M., Sawani, A.M., Nagy, E., Ashida, N., Mitsuya, H., Parniak, M.A., Sarafianos, S.G., 2009. Mechanism of inhibition of HIV-1 reverse transcriptase by 4′-Ethynyl-2-fluoro-2′-deoxyadenosine triphosphate, a translocation-defective reverse transcriptase inhibitor. J. Biol. Chem. 284 (51), 35681–35691. https://doi.org/10.1074/jbc.M109.036616. PMID: 19837673; PMCID: PMC2790999.

Mirabelli, C., Wotring, J.W., Zhang, C.J., McCarty, S.M., Fursmidt, R., Pretto, C.D., Qiao, Y., Zhang, Y., Frum, T., Kadambi, N.S., Amin, A.T., O'Meara, T.R., Spence, J. R., Huang, J., Alysandratos, K.D., Kotton, D.N., Handelman, S.K., Wobus, C.E., Weatherwax, K.J., Mashour, G.A., O'Meara, M.J., Chinnaiyan, A.M., Sexton, J.Z., 2021. Morphological cell profiling of SARS-CoV-2 infection identifies drug repurposing candidates for COVID-19. Proc. Natl. Acad. Sci. U. S. A. 118 (36), e2105815118. https://doi.org/10.1073/pnas.2105815118. PMID: 34413211; PMCID: PMC8433531.

NCT04233216, 2024. Doravirine/islatravir (DOR/ISL) in heavily treatment-experienced (HTE) participants for human immunodeficiency virus type 1 (HIV-1) infection (MK-8591A-019). https://clinicaltrials.gov/study/NCT04233216. (Accessed 2 April 2025).

Njenda, D.T., Aralaguppe, S.G., Singh, K., Rao, R., Sönnerborg, A., Sarafianos, S.G., Neogi, U., 2018. Antiretroviral potency of 4′-ethnyl-2′-fluoro-2′-deoxyadenosine, tenofovir alafenamide and second-generation NNRTIs across diverse HIV-1 subtypes. J. Antimicrob. Chemother. 73 (10), 2721–2728. https://doi.org/10.1093/jac/dky256. PMID: 30053052; PMCID: PMC6148215.

Oliveira, M., Brenner, B.G., Xu, H., Ibanescu, R.I., Mesplède, T., Wainberg, M.A., 2017. M184I/V substitutions and E138K/M184I/V double substitutions in HIV reverse transcriptase do not significantly affect the antiviral activity of EFdA. J. Antimicrob. Chemother. 72 (11), 3008–3011. https://doi.org/10.1093/jac/dkx280.

Orkin C, Kuritzkes D, Katlama C, Su F-H, Teal V, Plank RM, Lahoulou R, Asante-Appiah E. Doravirine resistance patterns identified through week 192 in the DRIVE-FORWARD and DRIVE-AHEAD phase 3 clinical trials. 12th IAS Conference on HIV Science, 23-26 July 2023, Brisbane, Australia..

Pérez-Vargas, J., Worrall, L.J., Olmstead, A.D., Ton, A.T., Lee, J., Villanueva, I., Thompson, C.A.H., Dudek, S., Ennis, S., Smith, J.R., Shapira, T., De Guzman, J., Gang, S., Ban, F., Vuckovic, M., Bielecki, M., Kovacic, S., Kenward, C., Hong, C.Y., Gordon, D.G., Levett, P.N., Krajden, M., Leduc, R., Boudreault, P.L., Niikura, M., Paetzel, M., Young, R.N., Cherkasov, A., Strynadka, N.C.J., Jean, F., 2023. A novel class of broad-spectrum active-site-directed 3C-like protease inhibitors with nanomolar antiviral activity against highly immune-evasive SARS-CoV-2 Omicron subvariants. Emerg. Microb. Infect. 12 (2), 2246594. https://doi.org/10.1080/22221751.2023.2246594. PMID: 37555275; PMCID: PMC10453993.

Saladini, F., Giannini, A., Boccuto, A., Vicenti, I., Zazzi, M., 2018. Agreement between an in-house replication competent and a reference replication defective recombinant virus assay for measuring phenotypic resistance to HIV-1 protease, reverse transcriptase, and integrase inhibitors. J. Clin. Lab. Anal. 32 (1), e22206. https://doi.org/10.1002/jcla.22206. Epub 2017 Mar 17. PMID: 28303602; PMCID: PMC6816933.

Saladini, F., Giammarino, F., Hosseini, B.A., Giannini, A., Boccuto, A., Dragoni, F., Vicenti, I., Shafer, R.W., Zazzi, M., 2021. *In vitro* cross-resistance to doravirine in a panel of HIV-1 clones harbouring multiple NNRTI resistance mutations. J. Antimicrob. Chemother. 76 (1), 130–134. https://doi.org/10.1093/jac/dkaa401. PMID: 32974670; PMCID: PMC8453390.

Saladini, F., Giammarino, F., Maggiolo, F., Ferrara, M., Cenderello, G., Celesia, B.M., Martellotta, F., Spagnuolo, V., Corbelli, G.M., Gianotti, N., Santoro, M.M., Rusconi, S., Zazzi, M., Castagna, A., PRESTIGIO Study Group, 2023. Residual phenotypic susceptibility to doravirine in multidrug-resistant HIV-1 from subjects enrolled in the PRESTIGIO Registry. Int. J. Antimicrob. Agents 61 (3), 106737. https://doi.org/10.1016/j.ijantimicag.2023.106737. Epub 2023 Jan 25. PMID: 36708743.

Struck, D., Lawyer, G., Ternes, A.M., Schmit, J.C., Bercoff, D.P., 2014. COMET: adaptive context-based modeling for ultrafast HIV-1 subtype identification. Nucleic Acids Res. 42 (18), e144. https://doi.org/10.1093/nar/gku739. Epub 2014 Aug 12. PMID: 25120265; PMCID: PMC4191385.

Tang, W.-F., Chang, Y.-H., Lin, C.-C., Jheng, J.-R., Hsieh, C.-F., Chin, Y.-F., Chang, T.-Y., Lee, J.-C., Liang, P.-H., Lin, C.-Y., Lin, G.-H., Cai, J.-Y., Chen, Y.-L., Chen, Y.-S., Tsai, S.-K., Liu, P.-C., Yang, C.-M., Shadbahr, T., Tang, J., Hsu, Y.-L., Huang, C.-H., Wang, L.-Y., Chen, C.C., Kau, J.-H., Hung, Y.-J., Lee, H.-Y., Wang, W.-C., Tsai, H.-P., Horng, J.-T., 2024. BPR3P0128, a non-nucleoside RNA-dependent RNA polymerase inhibitor, inhibits SARS-CoV-2 variants of concern and exerts synergistic antiviral activity in combination with remdesivir. Antimicrob. Agents Chemother. 68 (4), e0095623. https://doi.org/10.1128/aac.00956-23. Epub 2024 Mar 6. PMID: 38446062; PMCID: PMC10989008.

Wooten, D.J., Meyer, C.T., Lubbock, A.L.R., Quaranta, V., Lopez, C.F., 2021. MuSyC is a consensus framework that unifies multi-drug synergy metrics for combinatorial drug discovery. Nat. Commun. 12 (1), 4607. https://doi.org/10.1038/s41467-021-24789-z. PMID: 34326325; PMCID: PMC8322415.

Yadav, B., Wennerberg, K., Aittokallio, T., Tang, J., 2015. Searching for drug synergy in complex dose-response landscapes using an interaction potency model. Comput. Struct. Biotechnol. J. 13, 504–513. https://doi.org/10.1016/j.csbj.2015.09.001. Erratum in: Comput Struct Biotechnol J. 2017 Jul 25;15:387. doi: 10.1016/j.csbj.2017.07.003. PMID: 26949479; PMCID: PMC4759128.

Zheng, S., Wang, W., Aldahdooh, J., Malyutina, A., Shadbahr, T., Tanoli, Z., Pessia, A., Tang, J., 2022. SynergyFinder plus: toward better interpretation and annotation of drug combination screening datasets. Genom. Proteom. Bioinform. 20 (3), 587–596. https://doi.org/10.1016/j.gpb.2022.01.004. Epub 2022 Jan 25. PMID: 35085776; PMCID: PMC9801064.

Received: 15 October 2024 | Revised: 23 December 2024 | Accepted: 7 January 2025 DOI: 10.1002/ardp.202400812

ARCH PHARM DPhG Archiv der Pharmazie

FULL PAPER

Synthesis and biological investigation of peptidomimetic SARS-CoV-2 main protease inhibitors bearing quinoline-based heterocycles at P_3

Sara Rossi[1] | Graziano Deidda[2] | Lia Fiaschi[3] | Roberta Ibba[1] | Mariachiara Pieroni[1] | Maria Dichiara[1] | Gabriele Carullo[1] | Stefania Butini[1] | Anna Ramunno[4] | Simone Brogi[5] | Marco Lolicato[6] | Cristina Arrigoni[6] | Noemi Cabella[2] | Laura Bavagnoli[2] | Giovanni Maga[2] | Ilenia Varasi[3] | Camilla Biba[3] | Ilaria Vicenti[3] | Sandra Gemma[1] | Emmanuele Crespan[2] | Maurizio Zazzi[3] | Giuseppe Campiani[1]

[1]Department of Biotechnology, Chemistry and Pharmacy, University of Siena, Siena, Italy

[2]Institute of Molecular Genetics IGM-CNR 'Luigi Luca Cavalli-Sforza', Pavia, Italy

[3]Department of Medical Biotechnologies, University of Siena, Siena, Italy

[4]Department of Pharmacy, University of Salerno, Fisciano, Salerno, Italy

[5]Department of Pharmacy, University of Pisa, Pisa, Italy

[6]Department of Molecular Medicine, University of Pavia, Pavia, Italy

Correspondence
Sandra Gemma, Department of Biotechnology, Chemistry and Pharmacy, University of Siena, via Aldo Moro 2, 53100, Siena, Italy.
Email: gemma@unisi.it

Funding information
EU funding within the NextGeneration EU- MUR PNRR Extended Partnership initiative on Emerging Infectious Diseases, Project no. PE00000007, INF-ACT; Project of National Interest PRIN, Grant/Award Number: 2022TLZRXT - DEFENCE; "Fondo di Beneficenza di Intesa Sanpaolo", Grant/Award Number: B/2020/0113; AVITHRAPID project, European Union HORIZON-HLTH-2023-DISEASE-03-04, Grant/Award Number: 101137192; Italian Association for Cancer Research, Grant/Award Number: AIRC IG 24448

Abstract

In the last few years, severe acute respiratory syndrome coronavirus 2 (SARS-CoV-2) has been the cause of a worldwide pandemic, highlighting the need for novel antiviral agents. The main protease (M^{pro}) of SARS-CoV-2 was immediately identified as a crucial enzyme for viral replication and has been validated as a drug target. Here, we present the design and synthesis of peptidomimetic M^{pro} covalent inhibitors charac-terized by quinoline-based P_3 moieties. Structure–activity relationships (SARs) were also investigated at P_1 and P_2, as well as for different warheads. The binding modes of the designed inhibitors were assessed using X-ray crystallographic and molecular docking studies. The identified M^{pro} inhibitors were tested for their antiviral activities in cell-based assays, and the results were encouraging. The SAR studies presented here can contribute to the future design of improved inhibitors by addressing some of the current or prospective issues regarding M^{pro} inhibitors currently used in therapy.

KEYWORDS
live virus antiviral assay, main protease, peptidomimetics, SARS-CoV-2, X-ray crystallography

Sara Rossi and Graziano Deidda contributed equally to this study.

Emmanuele Crespan, Maurizio Zazzi, and Giuseppe Campiani are equal senior authors.

1 | INTRODUCTION

Coronaviruses are commonly known to cause pulmonary and gas-trointestinal diseases in humans and animals such as the common cold or bronchial pneumonia.[1] In the last few decades, three strains of coronaviruses with animal ancestral origins have attracted atten-tion worldwide for their pathogenicity and infectivity, causing global epidemics and pandemics. In fact, in November 2019, a massive outbreak of severe acute respiratory syndrome coronavirus 2 (SARS- CoV-2) has been identified as the causative agent for coronavirus disease 2019 (COVID-19) pathology, highlighting once again the urgent need for effective antiviral agents. SARS-CoV-2 belongs to the betacoronavirus genus, as well as SARS-CoV and Middle East respiratory syndrome coronavirus (MERS-CoV), which gave rise to an outbreak of pneumonia and numerous deaths. These strains possess a high degree of similarity with one another in their genomic sequence and share the same ancestral lineage from bats. The single- stranded RNA genome sequence of SARS-CoV-2 encodes for two partially overlapping polyproteins pp1a and pp1ab, which are cleaved into 16 nonstructural proteins by two viral proteases: papain-like protease (PL^{pro}) and 3-chymotrypsin-like or main protease (M^{pro}). Both enzymes were rapidly recognized as promising anti-viral tar-gets.[2] M^{pro} is a 33.8 kDa homodimeric cysteine protease that pro-cesses the viral polyproteins, allowing the cleavage of most non-structural proteins during viral replication. The cleavage specificity is unique, with a specific amino acidic sequence Leu-Gln-Ser in P_2-P_1- P_1', which is not recognizable by mammalian proteases, rendering its inhibition less prompt for off-target effects.[2,3] In this context, the M^{pro} of SARS-CoV-2 has emerged as the preferential target in terms of conservation across coronaviruses allowing the design and syn-thesis of effective antiviral agents, as confirmed by the final approval of nirmatrelvir (NRM) (1, Figure 1) in combination with ritonavir for the treatment of mild to moderate COVID-19 in adult patients.[4,5] Currently, there is ample room for optimization in the development of M^{pro} inhibitors, starting from the need to expand the patient popu-lation eligible for therapy, to address potential interference with other medications caused by the co-administration of the metabolic booster ritonavir, or the need for an expansion of the antiviral spectrum and to address the potential emergence of therapy-resistant viruses. A number of peptidomimetic M^{pro} inhibitors have been identified to date,[6,7] leading to the approval of new M^{pro} inhibitors in China (simnotrelvir, 2)[8,9] and in Japan (ensitrelvir, 3),[10] whereas other inhibitors are currently under preclinical or clinical investigation. Among the inhibitors under investigation today, both nonpeptide- and peptide-based M^{pro} inhibitors have been widely studied. Among covalent inhibitors, an electrophilic warhead (WH) is usually incorporated to covalently bind the catalytic cysteine at position 145 (C145). Nitriles, aldehydes, halo-methyl ketones, and various Michael acceptors are commonly used as reactive WHs.[11,12] These functional groups are associated with glutamine bioisosteres such as the pyrrolidin-2-one, as shown in Figure 2 for the reference inhibitor GC-376 (4).[13] The pyrrolidin-2-one moiety is crucial for maintaining protease binding affinity at the S_1 site. Various natural and non-natural amino acids interact with the subpocket S_2, even though they are usually small lipophilic groups. The $S_{3/4}$ subpockets can accommodate several functionalities.[14–17] In this study, we fo-cused on exploring $S_{3/4}$ of the active site. Generally, these pockets are shallower and therefore more exposed to solvents than the S_1 and S_2 subpockets; hence, different groups may be accommodated in this position. These groups may differ in size and nature due to the loops of the surface that can rearrange upon ligand binding. Examples of $P_{3/4}$ moieties are exemplified for compounds 5–7 (Figure 2). To obtain differently decorated peptidomimetics and to explore the ef-fects of heterocyclic rings as $P_{3/4}$ residues, we decided to investigate quinoline- and isoquinoline-derived scaffolds. Quinolines and quino-lones are privileged structures in medicinal chemistry and can also be considered as bioisosteric replacements of the indole moieties or rigidified analogs of pyridone-based M^{pro} inhibitors exemplified by

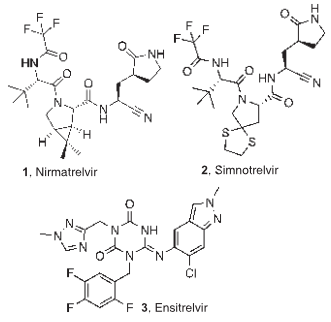

FIGURE 1 Clinically approved M^{pro} inhibitors (1–3).

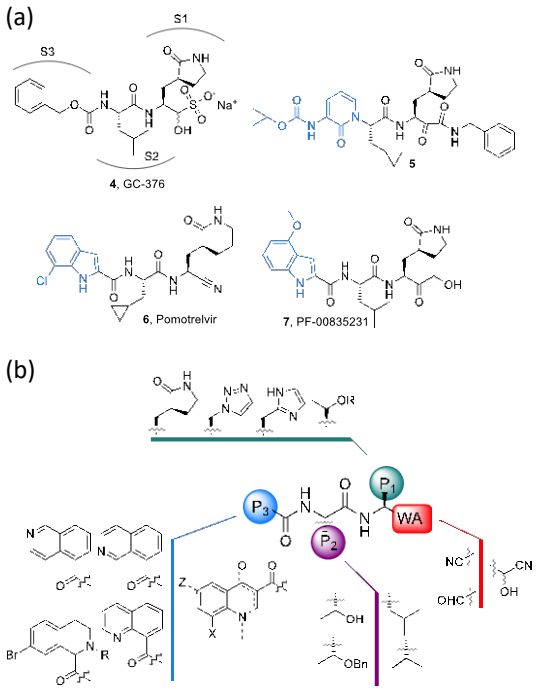

FIGURE 2 (a) Reference M^{pro} inhibitors 4–7. (b) Schematic representation of P_1–P_3 positions explored in this article (the structures of compounds synthesized are reported in Table 1).

5.[18–21] We have synthesized a series of peptide-based inhibitors bearing a nitrile group as an alternative to the more reactive aldehyde group as an electrophilic WH, and various quinolines, isoquinolines, N-methylquinolones, and tetrahydroisoquinoline, differently substituted and spatially oriented, were included at P_3 in order to investigate the structure–activity relationships (SARs) at the S_3/S_4 subsite.

A graphical representation of the P_1' and $P_{1-3/4}$ moieties used for exploring the SARs is shown in Figure 2b. A brief exploration of substituents at the P_1 and P_2 positions of the peptidomimetic scaffold was also performed in addition to different electrophilic WHs. All synthesized compounds were tested in vitro against M^{pro} of SARS- CoV-2 to determine the ID_{50} values. A crystal structure of the M^{pro} with one of the peptide-based compounds has been solved (PDB ID: 9GF7), allowing us to confirm the binding mode, while docking studies were performed in order to confirm the mechanism of interaction, binding modes, and complement SAR studies. Assays using infected VERO E6 cells were used to determine the antiviral activity of selected inhibitors.

2 | RESULTS AND DISCUSSION

2.1 | Chemistry

2.1.1 | P_3- and P_2-modified derivatives

The synthesis of the target compounds 13a–i bearing different heterosubstituents coupled to a leucine residue as P_2 was accomplished as described in Scheme 1. In the same scheme, the syn-thesis of compounds 14a and 14b is also described, bearing free or benzyl-protected threonine side chains as R_1, coupled to an 8-chloro-1-methyl-4-oxo-1,4-dihydro-3-quinolyl- substituent at R_2. Starting from building block 8, prepared as described previously in the literature,[22] trifluoroacetic acid (TFA)-mediated deprotection of the amino-group was followed by a coupling reaction with Boc-Leu-OH, Boc-Thr-OH, or Fmoc-Thr(Bzl)-OH to afford intermediates 9a–c. For the coupling reaction, 1-[bis(dimethylamino)methylene]-1H-1,2,3-triazolo[4,5-b]pyridinium 3-o-xide hexafluorophosphate (HATU) was used as a coupling agent in the presence of triethylamine (TEA). In the next step of the synthetic pro-tocol, TFA-mediated deprotection of 9a, followed by a coupling reaction, under the same conditions described before, with the appropriate car-boxylic acids afforded the ester intermediates 10a–i. Compounds 10j,k were obtained through a similar two-steps protocol by the reaction of 8-chloro-1-methyl-4-oxo-1,4-dihydroquinoline-3-carboxylic acid with 9b and 9c, respectively. The ester groups of 10a–k were subsequently converted into the corresponding primary amides 11a–i and 12a,b by treatment with ammonia solution (7N in MeOH). Finally, the nitrile de-rivatives 13a–i and 14a,b were obtained by the dehydration reaction of the primary amides carried out with trifluoroacetic anhydride (TFAA) and TEA at 0°C. Compound 13d was subjected to hydrolytic cleavage of the Boc moiety with a methanolic solution of HCl, yielding the final compound (R/S)-15, while intermediate 13i was converted into 16 by the reduction of the nitro moiety with iron powder and NH_4Cl. The extended analog 20, bearing a Val at P_3 and the capping 8-chloro-1-methyl-4-oxo-1,4-dihydroquinolin-3-carbonyl group at P_4, was synthesized as reported in Scheme 2. Intermediate 9a was converted into 17 by an initial Boc cyclic R_2 cleavage and subsequent coupling reaction with Boc-Val-OH. A second

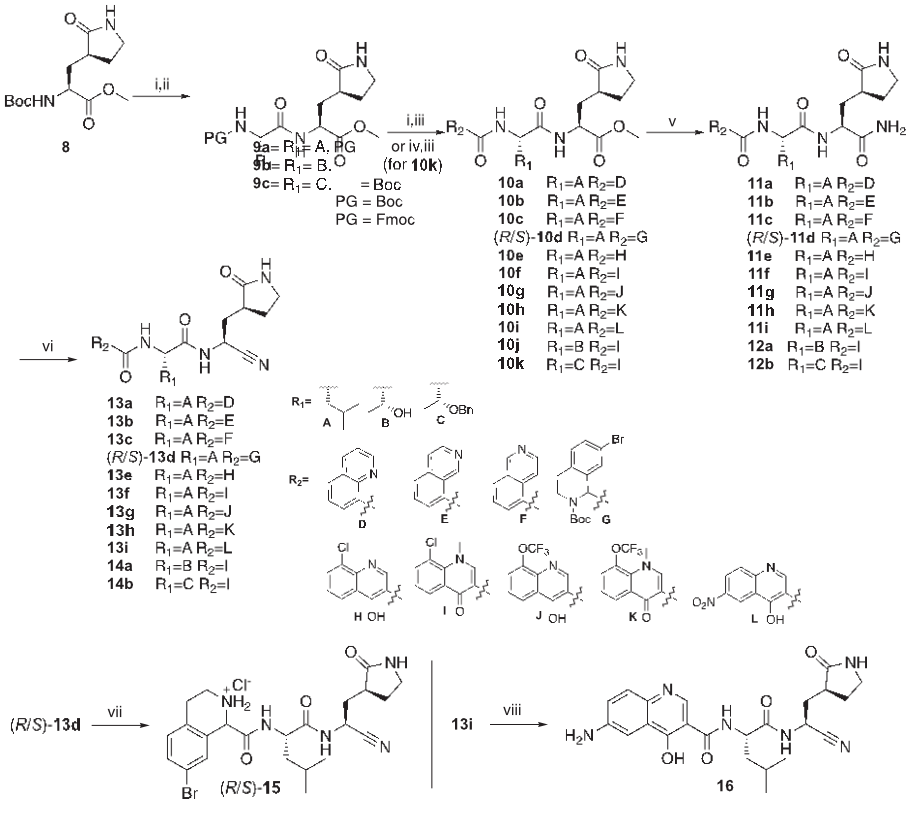

SCHEME 1 Synthesis of compounds 13a–i, 14a,b, (R/S)-15, and 16. Reagents and conditions: (i) TFA, DCM, 0°C, 1 h; (ii) Boc-Leu-OH, Boc-Thr-OH or Fmoc-Thr (Bzl)-OH, HATU, TEA, DCM, 0°C, 4 h; (iii) appropriate carboxylic acid, HATU, TEA, DCM, 0°C, 4 h; (iv) Et_2NH, DCM, rt, 1 h; (v) ammonia solution (7 N in MeOH), MeOH, rt, 12 h; (vi) TFAA, TEA, DCM or DMF, 0°C, 3 h; (vii) HCl in MeOH, 0°C, 1 h; and (viii) Fe powder, NH_4Cl, EtOH/H_2O (5:1), 55°C, 30 min. DCM, dichloromethane; HATU, 1-[bis (dimethylamino)methylene]-1H-1,2,3-triazolo[4,5-b]pyridinium 3-oxide hexafluorophosphate; TEA, triethylamine; TFA, trifluoroacetic acid; TFAA, trifluoroacetic anhydride.

deprotection and coupling reaction with 8-chloro-1-methyl-4-oxo-1,4-dihydroquinoline-3-carboxylic acid yielded intermediate 18, which allowed to obtain the primary amide 19 upon treatment with ammonia solution (7 N in MeOH). Subsequent dehydration yielded the final compound 20.

2.1.2 | P_1-modified derivatives

The effect of modification of the P_1 position with different heteroaliphatic moieties was investigated using the N-methylquinolinone moiety as the P_3 residue and a leucine as the P_2 residue. The synthetic procedure to obtain the target compounds 25a–c and the mixture of diasteroisomers (R/S)-26 is shown in Scheme 3. Boc-Leu-OH 22 was reacted with the triazole derivative 21a, prepared as described in the Supporting Information file (Scheme S1), with H-His-OMe 21b or with H-Thr-OMe 21c to obtain dipeptides 23a–c. TFA-mediated Boc cleavage, followed by coupling of the resulting amine with 8-chloro-1-methyl-4-oxo-1,4-dihydroquinoline-3-carboxylic acid, afforded intermediates 24a–c in good overall yield. The conversion of esters 24a–c into the corre-sponding primary amides was accomplished by treatment with ammonia solution (7 N in MeOH), followed by the dehydration reaction, which gave rise to the final nitrile derivatives 25a–c. The final compound 25c was also converted in the O-acetal derivative (R/S)-26 upon treatment with 2,3-dihydrofuran (DHF) in the presence of p-toluenesulfonic acid (PTSA).

2.1.3 | WH-modified derivatives

The synthesis of 30a,b and 34, bearing an aldehyde as WH and the cyanohydrine derivative (R/S)-31, was performed as described in Scheme 4. For the synthesis of aldehydes 30a,b, the key common in-cyclic and termediates were the esters 10a (prepared as described previously) and the analog 28 bearing an Ile moiety as a P_2 residue. The latter was prepared, starting from 8, through two consecutive deprotection and coupling reactions to introduce the Ile amino acid (intermediate 27) and the 8-quinoline capping group. The ester intermediates 10a and 28 were reduced by means of $NaBH_4$ in MeOH, affording the corresponding al-cohols 29a,b, which were oxidized using Dess Martin Periodinane (DMP) at 0°C to obtain the final compounds 30a,b. The WH of 30b was then converted into the corresponding cyanohydrin (R/S)-31. The synthesis of aldehyde 34 involved a slightly different procedure. Accordingly, the ester derivative 9a was reduced to 32; afterward, the latter compound was subjected to amine deprotection and coupling reaction with the 8-chloroquinolone carboxylic acid to yield the derivative 33, which was finally oxidized with DMP to target compound 34.

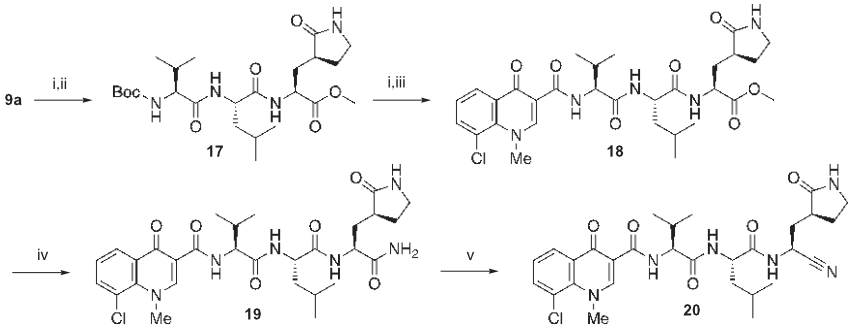

SCHEME 2 Synthesis of compound 20. Reagents and conditions: (i) TFA, DCM, 0°C, 1 h; (ii) Boc-Val-OH, HATU, TEA, DCM, 0°C, 4 h; (iii) 8-chloro-1-methyl-4-oxo-1,4-dihydroquinoline-3-carboxylic acid, HATU, TEA, DMF, 0°C, 6 h; (iv) ammonia solution (7 N in MeOH), MeOH, rt, 20 h; and (v) TFAA, TEA, DMF, 0°C, 6 h. DCM, dichloromethane; HATU, 1-[bis(dimethylamino)methylene]-1H-1,2,3-triazolo[4,5-b]pyridinium 3-oxide hexafluorophosphate; TEA, triethylamine; TFA, trifluoroacetic acid, TFAA, trifluoroacetic anhydride.

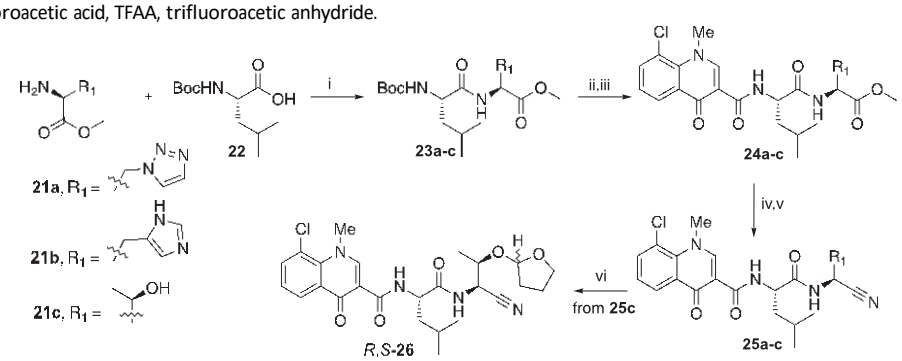

SCHEME 3 Synthesis of compounds 25a–c and R,S-26. Reagents and conditions: (i) HATU, TEA, DCM, 0°C, 4 h; (ii) TFA, DCM, 0°C, 1 h; (iii) 8-chloro-1-methyl-4-oxo-1,4-dihydroquinoline-3-carboxylic acid, HATU, TEA, DCM, 0°C, 4 h; (iv) ammonia solution (7 N in MeOH), rt, 12 h; (v) TFAA, TEA, DCM, 0°C, 3 h; and (vi) PTSA, DHF, THF, rt, 2 h. DCM, dichloromethane; HATU, 1-[bis(dimethylamino)methylene]-1H-1,2,3-triazolo[4,5-b] pyridinium 3-oxide hexafluorophosphate; PTSA, p-toluenesulfonic acid; TEA, triethylamine; TFA, trifluoroacetic acid; TFAA, trifluoroacetic anhydride.

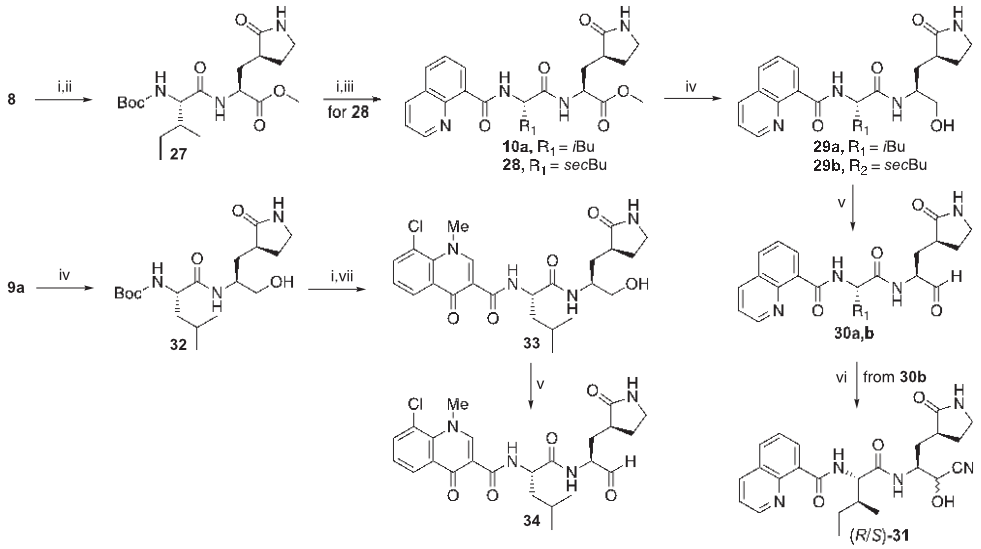

SCHEME 4 Synthesis of compounds 30a,b, 31, and 34. Reagents and conditions: (i) TFA, DCM, 0°C, 2 h; (ii) Boc-Ile-OH, HATU, TEA, DCM, 0°C, 4 h; (iii) 8-quinolinecarboxylic acid, HATU, TEA, DCM, 0°C, 4 h; (iv) $NaBH_4$, MeOH, 0-25°C, 12 h; (v) DMP, DCM, 0°C, 1 h; (vi) $NaHSO_3$ aq s.s., KCN; g) $NaBH_4$, MeOH, 0–25°C, 12 h; and (vii) 8-chloro-1-methyl-4-oxo-1,4-dihydroquinoline-3-carboxylic acid, HATU, TEA, DCM, 0°C, 4 h. DMP, Dess Martin Periodinane; DCM, dichloromethane; HATU, 1-[bis(dimethylamino)methylene]-1H-1,2,3-triazolo[4,5-b]pyridinium 3-oxide hexafluorophosphate; TEA, triethylamine.

2.2 | M^{pro} inhibition and SARs investigation

The inhibitory ability of the synthesized compounds was evaluated in vitro using recombinant M^{pro} by the fluorescence resonance en-ergy transfer (FRET) assay. A number of compounds were able to inhibit the M^{pro} in the micromolar or submicromolar range, as shown in Table 1.

Starting from the reference inhibitor 4 (Table 1), bearing a leucine at the P_2 position and the N-pyrrolidinone heterocycle as the P_1 substituent, we first investigated the effect of variously substituted quinolyl and iso-quinolyl moieties coupled to a nitrile group as a WH (13a–e, (R/S)-15 and 16). The choice of the nitrile in place of the more electrophilic aldehyde moiety of 4 as WH is due to its better drug-like properties. However, to facilitate a direct comparison with reference inhibitor 4, the aldehyde derivative 30a was also synthesized. While the latter showed an inhibi-tory potency comparable to that of 4, the analog 13a bearing the nitrile WH was less potent.

However, X-ray crystal studies coupled with molecular modeling (see the next paragraphs) revealed comparable binding modes for both compounds. Isoquinoline derivatives 13b,c showed better inhibitory activities than quinoline 13a, even though the latter inhibitor displayed higher activity in the antiviral assay (vide infra), most reasonably due to different cell penetration properties. The corresponding tetrahydroisoquinolin-1-yl derivatives (R/S)-13d and (R/S)-15 were also prepared, showing moderate and low inhibitory potency, respectively. Regarding the quinoline-3-yl series of deriva-tives bearing oxygenated substituents at C4, compound 13f showed 10 times higher potency than the 8-quinolyl-derivative 13a. The amino group at C6 (16) did not improve the inhibitory potency. The expansion of the inhibitor toward the S4 pocket through the syn-thesis of tetrapeptide 20 was detrimental to the activity. Due to its interesting activity, the 8-chloro-1-methyl-4-oxo-3-quinolyl moiety 13f was used to further explore SARs. Investigation of the P_2 position was accomplished through the synthesis of 14a,b bearing a free and O-benzyl-protected threonine moiety, respectively, but no improve-ment in the inhibitory potency with respect to 13f was obtained. Also, the brief investigation of alternative moieties at P_1 (25a–c and 26) did not yield any noteworthy activity. Finally, regarding the electrophilic WH, three compounds were synthesized with an alde-hyde WH, namely, 30a, which is an analog of nitrile 13a, 30b, which presents an isoleucine residue instead of the leucine of 30a, and 34 as an analog of 13f. All compounds showed submicromolar activities, confirming the reactivity of the aldehyde group toward the cysteine catalytic residue (C145). A different WH, namely, the cyanohydrine (R/S)-31, was prepared and showed an enzyme-inhibitory activity against M^{pro} in the same range as the aldehyde analog 30b.

2.3 | X-ray crystallography study

X-ray crystallography was used to solve the structure of compound 30a. The structure, solved at 1.9 Å resolution, shows the formation of a covalent adduct between the thiol of C145 and the aldehyde of compound 30a (Figure 3a). Moreover, 30a forms H-bond interactions with both the carboxylic acid and backbone NH of Glu166, while the pyrrolidone NH forms an H bond with a water molecule in turn in-teracting with Asn142. As shown in Figure 3b, the binding pose of 30a matches that of compound 4 (GC-376) (PDB: 6WTT). However, the bulkier but slightly shorter compound 30a causes a rearrangement of the β-hairpin loop residues 166–172, the α-helix residues 45–51, and the loop residues 186–193, which all move closer to the bound molecule, framing it more tightly.

TABLE 1 Structure, enzymatic (IC_{50}), and antiviral (EC_{50}) activity, and selectivity indexes (SI) of inhibitors 13a–h, 14a,b, 15–16, 20, 25a–c, (R/S)-26, 30a–b, (R/S)-31, and 34, and reference inhibitors 1 and 4.

Cmpd	Structure	IC_{50} (μM)	K_i (μM)	EC_{50} (μM)	SI (CC_{50}/EC_{50} ratio)
13a	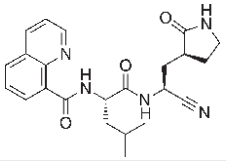	6.57 ± 1.31	3.65 ± 0.71	6.8 ± 1.5	44.1
13b	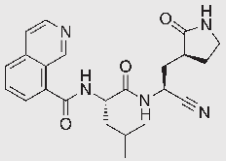	1.28 ± 0.20	0.48 ± 0.07	24.0 ± 6.5	12.5
13c	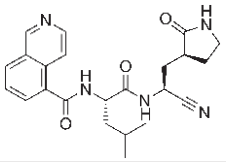	3.38 ± 1.04	1.42 ± 0.38	16.2 ± 0.1	>200
(R/S)-13d	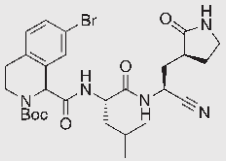	>10	n.d.	n.t.	-
13e	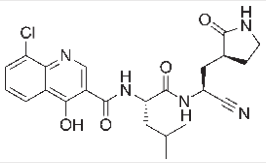	6.0 ± 0.67	2.23 ± 0.25	n.a.	-
13f	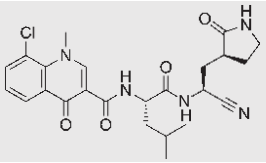	0.56 ± 0.07	0.30 ± 0.04	1.6 ± 0.5	187.5
13g	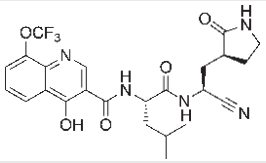	13.85 ± 2.14	7.5 ± 1.15	n.a.	-
13h	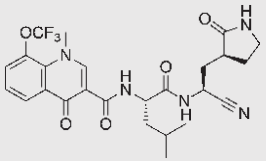	5.89 ± 1.21	3.2 ± 0.65	n.a.	-
14a	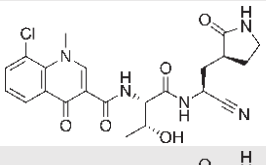	>10	n.d.	n.t.	-
14b	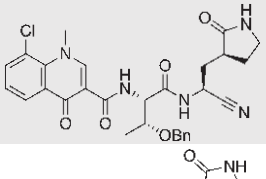	>10	n.d.	n.t.	-
(R/S)-15	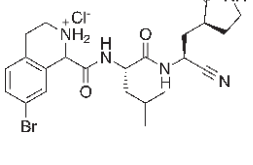	>10	n.d.	n.t.	-

TABLE 1 (Continued)

Cmpd	Structure	IC_{50} (μM)	K_i (μM)	EC_{50} (μM)	SI (CC_{50}/EC_{50} ratio)
16	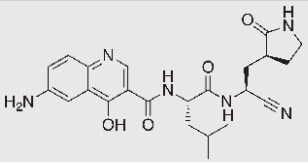	>10	n.d.	n.t.	-
20	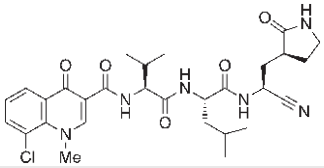	4.25 ± 0.28	1.58 ± 0.1	n.a.	-
25a	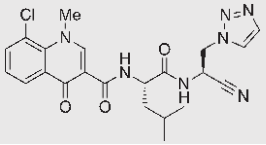	>100	n.d.	n.t.	-
25b	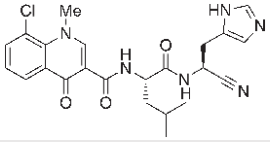	>10	n.d.	n.t.	-
25c	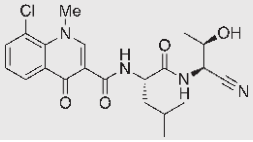	>10	n.d.	n.t.	-
(R/S)-26	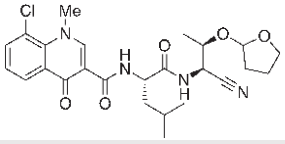	>10	n.d.	n.t.	-
30a	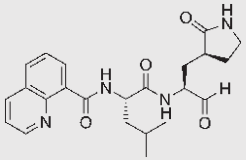	0.43 ± 0.04	0.16 ± 0.01	8.0 ± 2.5	6.6
30b	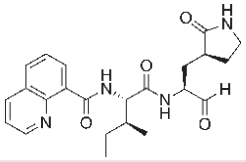	0.51 ± 0.01	0.27 ± 0.06	n.t.	-
(R/S)-31	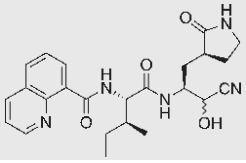	1.81 ± 0.5	0.67 ± 0.18	1.8 ± 0.1	91.6
34	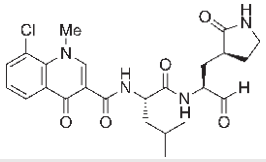	0.65 ± 0.04	0.24 ± 0.02	n.t.	-
GC376 (4)		0.14 ± 0.04	0.074 ± 0.22	0.16 ± 0.1	
NRM (1)		n.t.	0.0031[5]	0.05	874.8

Abbreviations: IC_{50}, half-maximal inhibitory concentration; EC_{50}, half-maximal effective concentration; n.a., not active; n.d, not determined; n.t, not tested.

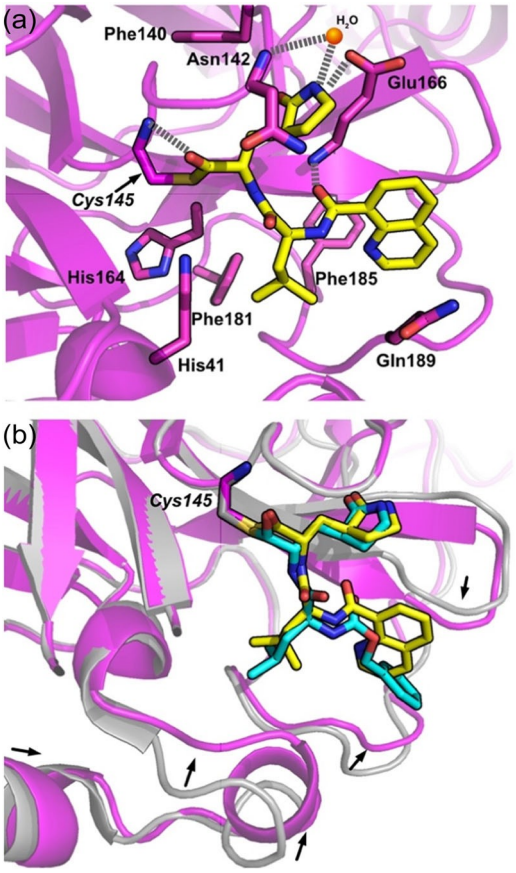

FIGURE 3 (a) X-ray co-crystal structure of M^{pro} in complex with inhibitor 30a (yellow sticks) (PDB ID 9GF7). Enzyme residues interacting with inhibitors are displayed as magenta sticks. Residues framing the inhibitor are indicated. The residues involved in polar contacts with the molecule 30a are indicated by dashed gray lines. The active site Cys145 is indicated with an arrow. (b) Superposition of the crystal structure of M^{pro} in complex with compound 30a (magenta cartoon, yellow sticks) and reference inhibitor 4[13] (gray cartoon, cyan sticks). Regions of the protein that move closer to the molecule are highlighted by black arrows. The image was prepared using PyMOL.

2.4 | Molecular docking

The molecular docking calculation of 30a within the M^{pro} binding site, before the formation of the covalent adduct with C145, allowed us to understand how the electrophilic moiety of the compound was ori-ented during the binding and to compare it to the nitrile WH present in 13a. As shown in Figure 4, compound 13a was able to interact well with all the subregions of the M^{pro} binding site. In particular, nitrile is in a suitable position for nucleophilic attack from C145 to form a tetrahedral intermediate. In fact, the distance between the sulfur of C145 and the electrophilic groups of both compounds is appropriate for a possible covalent attack (S-C145/carbon of aldehyde group 3.1 Å; S-C145/carbon of nitrile group 3.4 Å). Moreover, both com-pounds similarly interacted at the S1 and S4 sites, targeting H163 and E166 by H bonds, whereas they established hydrophobic interactions with M165 and P168. At the S1' site, compound 30a established additional polar contacts with F140, G143, and S144.

In agreement with the different number of target residues, the docking scores obtained, although comparable, were slightly different. In fact, the score of 13a was found to be slightly higher than that of 30a (13a = –9.128 kcal/mol; 30a = –9.694 kcal/mol). The in vitro results highlighted that 31a was more potent than the derivative 13a, which maintained a significant inhibitory potency against the enzyme. In addi-tion, the replacement of leucine with isoleucine, as in 30b, was well tolerated, and no significant differences in the binding mode with respect to 30a were observed. Accordingly, 13a could be a good starting point for optimizing the structure to develop a novel series of derivatives con-taining nitrile as a WH as M^{pro} inhibitors. Subsequently, we investigated the role of nitrogen at different positions of the quinoline moiety with respect to compound 13a. This resulted in compounds 13b and 13c. As

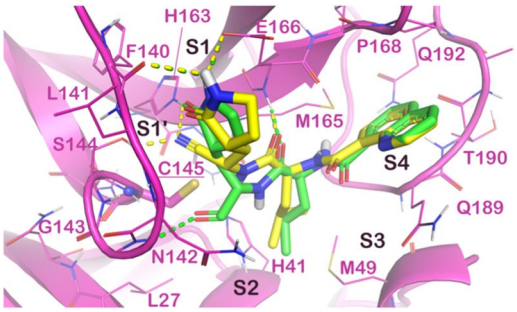

FIGURE 4 Superposition of docked poses of 30a (green sticks) and 13a (yellow sticks) within SARS-CoV-2 M^{pro} (magenta cartoon; PDB ID 9GF7). The key regions and residues involved in the binding site are highlighted by lines. H bonds are represented by colored dotted lines, according to the color of the related compound. The image was prepared using PyMOL (The PyMOL Molecular Graphics System, v1.8; Schrödinger, LLC, 2015).
SARS-CoV-2, severe acute respiratory syndrome coronavirus 2.

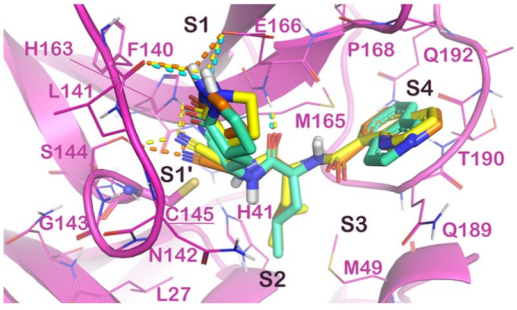

FIGURE 5 Superposition of docked poses of 13a (yellow sticks), 13b (orange sticks), and 13c (cyan sticks) within SARS-CoV-2 M^{pro} (magenta cartoon; PDB ID 9GF7). The key regions and residues involved in the binding site are highlighted by lines. H bonds are represented by colored dotted lines, according to the color of the related compound. The image was prepared using PyMOL (The PyMOL Molecular Graphics System, v1.8; Schrödinger, LLC, 2015).
SARS-CoV-2, severe acute respiratory syndrome coronavirus 2.

illustrated in Figure 5, the binding mode was largely comparable, con-sidering that residues F140, H163, and E166 were targeted by H bonds, whereas residues M165 and P168 were targeted by hydrophobic inter-actions with compounds 13b and 13c. The nitrile group of the mentioned compounds was in a suitable position for a possible nucleophilic attack from C145.

In fact, the distance between S-C145 and the carbon of the nitrile group was found to be 3.2 Å for compound 13b (orange sticks, Figure 5) and 3.5 Å for compound 13c (cyan stick, Figure 5). Inter-estingly, according to the distance from S-C145, derivative 13b was one of the most potent inhibitors of the series. The docking scores were perfectly comparable (13a = –9.096 kcal/mol; 13b = –9.117 kcal/ mol; 13c = –9.038 kcal/mol). The next investigation aimed to identify a bioisosteric replacement of the quinoline nucleus with a different substituted quinoline. The most potent compound obtained from this step was compound 13f (Figure 5). The nitrile group was maintained as the WH, substituting the moiety interacting with the S_4 subsite of the enzyme. Interestingly, the introduction of a slightly more flexible and bulkier nucleus produces a proper arrangement that allows the com-pound to appropriately interact within the binding site of the enzyme. In fact, compound 13f was able to establish the same contacts as described previously (H bonds with F140, H163, and E166 and hydrophobic interactions with M165 and P168). Moreover, the nitrile group established a strong H-bond network with G143, S144, and C145. The distance between S-C145 and the carbon of the nitrile group was found to be 3.0 Å, indicating a suitable distance for nucle-ophilic attack. The mentioned binding mode accounted for a docking score of –9.577 kcal/mol, suggesting the significant capability of the compound to interact within the selected binding site, as experimen-tally confirmed. Finally, because of the interesting activity observed for compound (R/S)-31, we investigated whether a different activity between the two diasteroisomers could be predicted. As reported in Figure 6, the R- and S-diasteroisomers (Figure 7a,b, respectively)

showed the same pattern of interaction, being able to target residues

F140, H163 (H bonds), M165, and P168 (hydrophobic interactions). In addition, the S-enantiomer established an additional H bond with E166. Moreover, the nitrile group of both derivatives was at a suitable distance for covalent interaction with C145 (distance between S-C145 and the carbon of the nitrile group: R-diasteroisomer 2.6 Å, S- diasteroisomer 3.3 Å). According to the similar binding mode and tar-

geting residues, the docking score was similar (R-diasteroisomer –8.914 kcal/mol, S-diasteroisomer –9.037 kcal/mol), thus neither indicating stereoselective mode of interaction with the enzyme.

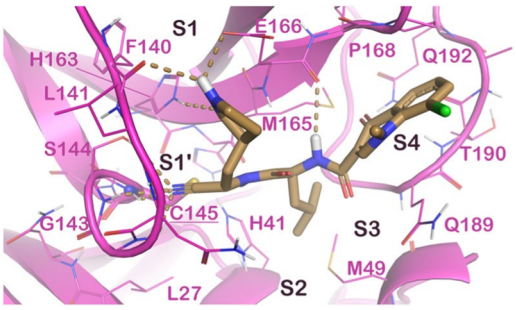

FIGURE 6 Docked poses of 13f (sand sticks) within the SARS- CoV-2 M^{pro} (magenta cartoon; PDB ID 9GF7). The key regions and residues involved in the binding site are highlighted by lines. H bonds are represented by colored dotted lines, according to the color of the related compound. The image was prepared using PyMOL (The PyMOL Molecular Graphics System, v1.8; Schrödinger, LLC, 2015).
SARS-CoV-2, severe acute respiratory syndrome coronavirus 2.

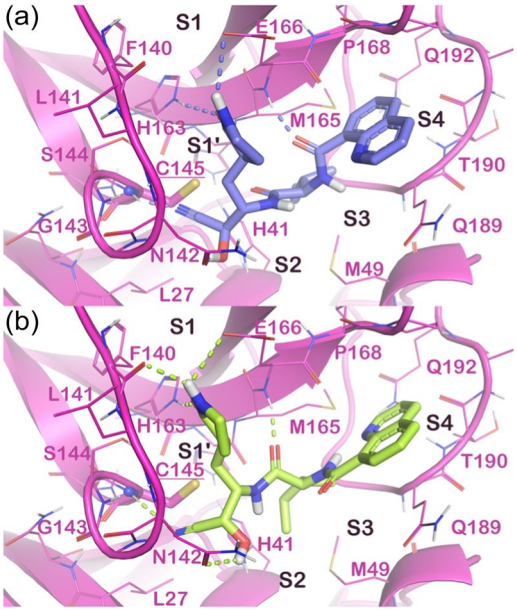

FIGURE 7 Docked poses of (a) R-diasteroisomer (light blue sticks) and (b) S-diasteroisomer (lemon sticks) of compound (R/S)-31 within the SARS-CoV-2 M^{pro} (magenta cartoon; PDB ID 9GF7). The key regions and residues involved in the binding site are highlighted by lines. H bonds are represented by colored dotted lines, according to the color of the related compound. Images were prepared using PyMOL (The PyMOL Molecular Graphics System, v1.8; Schrödinger, LLC, 2015). M^{pro}, main protease; SARS-CoV-2, severe acute respiratory syndrome coronavirus 2.

2.5 | Antiviral activity in VERO E6 cells against SARS-CoV-2

Inhibitors 13a–c, 13f–h, 20, 30a, and (R/S)-31 were then investigated in a cell-based assay using a live delta SARS-CoV-2 (EPI_ISL_2840619) virus to determine their ability to halt virus rep-lication. Anti-SARS-CoV-2 activity was evaluated using a direct yield reduction assay in VERO E6 cells. Since this cell line overexpresses the efflux P-glycoprotein (P-gp), VERO E6 were pretreated with CP- 100356 hydrochloride, which is a P-gp inhibitor.

After incubation with the P-gp inhibitor, cells were treated with scalar nontoxic doses of each compound and subsequently chal-lenged with the virus at MOI 0.001. The licensed M^{pro} inhibitor NRM (MCE® cat. HY-104077) was used as the reference compound. The inhibitory activity of each compound was determined by measuring

the nucleocapsid expression by immunodetection and expressed as the half-maximal effective concentration (EC_{50}). Among the nine compounds tested, six of them (13a, 13b,c, 13f, 30a, and (R/S)-31) were active against the delta SARS-CoV-2 lineage in the micromolar range (Table 1). The low micromolar activity observed by the enzy-matic assay for 13b and 30a was not confirmed by the live virus antiviral assay, with 18-fold loss of activity (13b, EC_{50}: 24.0 ± 6.5 μM; 30a, EC_{50}: 8.0 ± 2.5 μM). Instead, the antiviral activity of 13a (EC_{50}: 6.8 ± 1.5 μM), 13f (EC_{50}: 1.6 ± 0.5 μM), and (R/S)-31 (EC_{50}: 1.8 ± 0.1 μM) was comparable with respect to that observed by the enzymatic assay. The selectivity index (SI), defined as the ratio between the half-maximal toxic concentration (CC_{50}) and the half-maximal effective concentration (EC_{50}) of each compound, was above 10 for all compounds, except for 30a (SI 6.6). A high SI is associated with a more potent and safer drug, able to eliminate the target virus at concentrations much lower than its cytotoxic concentration.

CONCLUSIONS

Here, we reported the synthesis and M^{pro}-inhibitory activity of nitrile-based peptidomimetic compounds bearing different quinoline and isoquinoline systems at P_2. SARs studies were complemented by X-ray crystal structure determination and molecular modeling investigations. The antiviral activity in a cell-based system of the selected inhibitors was assessed, resulting in the identification of 13f and (R/S)-31 showing anti-SARS-CoV-2 activity in the low micro-molar range both in the enzymatic and in the live virus assay with good SI (187.5 and 91.7 for 13f and (R/S)-31, respectively). Although the EC_{50} and the SI values of these compounds were weaker and less selective those of NRM (IC_{50}: 0.05 μM; SI: 874.8), their simple molecular scaffold allows further structure-based optimization, providing important information for future structure-based design studies.

4 | EXPERIMENTAL SECTION

| Chemistry

4.1.1 | General remarks

All the reagents used were commercially available and purchased from Merck. Reaction progress was monitored by TLC using silica gel 60 F_{254} with detection by UV (254 nm). ^1H NMR and ^{13}C NMR spectra (see the Supporting Information) were recorded on a Varian 300 MHz spectrometer or a Bruker 400 MHz spectrometer using the residual signal of the deuterated solvent as the internal standard. Splitting patterns are described as singlet (s), doublet (d), triplet (t), and quartet (q); the value of chemical shifts (δ) is given in ppm, and coupling constants (J) are given in hertz (Hz). Electrospray ionization mass spectrometry (ESI-MS) spectra were performed using an Agilent 1100 series LC/MSD spectrometer. Yields refer to purified products and are not optimized. ESI-HRMS spectra were acquired using a linear ion trap Orbitrap hybrid mass spectrometer (LTQ Orbitrap XL) (Thermo Fisher Scientific) operating in positive electrospray ioniza-tion mode. Data were collected and analyzed using Xcalibur 2.2 software provided by the manufacturer.

The InChI codes of the investigated compounds, together with some biological activity data, are provided as the Supporting Information.

4.1.2 | Synthesis of inhibitors 13a–h and 14a,b

General procedure for the Boc-deprotection and coupling reaction exemplified with compound methyl (S)-2-{(S)-2-[(tert-butoxycarbonyl) amino]-4-methylpentanamido}-3-((S)-2-oxopyrrolidin-3-yl)propanoate (9a): In a round-bottom flask, methyl (S)-2-[(tert-butoxycarbonyl) amino]-3-((S)-2-oxopyrrolidin-3-yl)propanoate 8 (154 mg, 1 eq) was solubilized in dry dichloromethane (DCM) (7 mL, 0.07 M) at 0°C, and 3 | then, TFA (1.64 mL, 40 eq) was slowly added. The reaction mixture was stirred for 1 h, then the mixture was dried under N_2 flux, and the crude product (yellowish amorphous solid obtained in quantitative yield) was used without any further purification for the next reaction. The coupling reaction was carried out in a two-necked oven-dried round-bottom flask under a N_2 atmosphere. Boc-Leu-OH (118 mg, 1 eq) was solubilized in anhydrous DCM (2 mL, 0.15 M), the mixture was cooled at 0°C, and then HATU (293 mg, 1.5 eq) and TEA (0.20 mL, 3 eq) were added. The mixture was stirred for 30 min and then a solution of the previously deprotected amine (100 mg, 1.05 eq) in DCM (1.5 mL, 0.15 M) and TEA (0.15 mL, 2 eq) were slowly added. The reaction mixture was stirred a 0°C for 4 h. After completion of the reaction, checked by TLC, a saturated aqueous solution of NH_4Cl (4 mL) was added to the reaction mixture, and the resulting aqueous phase was extracted with DCM (3 × 3 mL). The organic phases were combined, dried over anhydrous Na_2SO_4, filtered, and concentrated under reduced pressure. The crude mixture was purified by SiO_2 column chromatography eluting with (20:1, DCM/MeOH), to yield a pale yellow oil (187 mg, 87% yield). Spectroscopic data are in agreement with those reported previously in the literature.[22]

Methyl (S)-2-{(2S,3S)-2-[(tert-butoxycarbonyl)amino]-3-hydroxy- 4.1 butanamido}-3-((S)-2-oxopyrrolidin-3-yl)propanoate (9b): Compound 9b was prepared following the general procedures for Boc cleavage and coupling reaction, using Boc-Thr-OH as the appropriate carboxylic acid. The mixture was purified by SiO_2 column chromatography (30:1, DCM/MeOH), yielding a colorless oil (43% yield). ESI-MS m/z 388 $[M+H]^+$, 410 $[M+Na]^+$.

Methyl (S)-2-[(2S,3S)-2-({[(9H-fluoren-9-yl)methoxy]carbonyl}amino)-3-(benzyloxy)butanamido]-3-((S)-2-oxopyrrolidin-3-yl)propanoate (9c): Compound 9c was prepared following general procedures for Boc cleavage and coupling reaction, with Fmoc-Thr(Bzl)-OH as the appropri-ate carboxylic acid. The mixture was purified by SiO_2 column chroma-tography using (30:1, DCM/MeOH), yielding a colorless oil (89% yield). ESI-MS m/z 600 $[M+H]^+$, 622 $[M+Na]^+$. ^1H NMR (300 MHz, CD_3OD) δ 8.55 (m, 1H), 7.75 (d, J = 7.5 Hz, 2H), 7.71–7.54 (m, 2H), 7.43–7.14

(m, 9H), 4.67–3.99 (m, 7H), 3.64 (s, 3H), 3.20–2.92 (m, 2H), 2.46–2.02 (m, 3H), 1.85–1.53 (m, 2H), 1.21 (m, 3H).

Methyl (S)-2-[(S)-4-methyl-2-(quinoline-8-carboxamido) pentan amido]-3-((S)-2-oxopyrrolidin-3-yl)propanoate (10a): Compound 10a was prepared following the general procedures for Boc cleav-age and coupling reaction, using quinoline-8-carboxylic acid as the appropriate carboxylic acid. The mixture was purified by SiO_2 col-umn chromatography using (40:1, $CHCl_3$/MeOH), yielding a color-less oil (36% yield). ESI-MS m/z 455 $[M+H]^+$, 477 $[M+Na]^+$. ^1H NMR (300 MHz, $CDCl_3$) δ 11.66 (m, 1H), 8.98–8.88 (m, 1H), 8.73 (m, 1H), 8.29–8.20 (m, 1H), 8.02 (d, J = 7.3 Hz, 1H), 7.97–7.88 (m, 1H), 7.62 (m, 1H), 7.47 (m, 1H), 6.89 (s, 1H), 5.01–4.70 (m, 1H), 4.52 (m, 1H), 4.19–4.03 (m, 1H), 3.67 (d, J = 5.5 Hz, 3H), 3.38–3.09 (m, 2H), 2.50–2.16 (m, 2H), 1.98–1.47 (m, 4H), 1.32–1.17 (m, 1H), 1.05–0.89 (m, 6H).

Methyl (S)-2-[(S)-2-(isoquinoline-8-carboxamido)-4-methyl-pen tanamido]-3-((S)-2-oxopyrrolidin-3-yl)propanoate (10b): Compound 10b was synthesized according to the general procedures for Boc cleavage and coupling reaction, using isoquinoline-8-carboxylic acid as the appropriate carboxylic acid. The compound was purified by SiO_2 column chromatography (30:1 DCM/MeOH), yielding a color-less oil (57% yield). ESI-MS m/z 455 $[M+H]^+$, 477 $[M+Na]^+$. ^1H NMR (300 MHz, $CDCl_3$) δ 9.76–9.62 (m, 1H), 8.75 (d, J = 7.0 Hz, 1H), 8.50 (m, 1H), 8.42 (d, J = 6.6 Hz, 1H), 7.84 (d, J = 8.2 Hz, 1H), 7.73 (t, J = 5.6 Hz, 1H), 7.62 (dd, J = 10.1, 4.9 Hz, 1H), 7.13 (m, 1H), 6.94 (d, J = 12.1 Hz, 1H), 4.95 (m, 1H), 4.63–4.37 (m, 1H), 3.72 (s, 3H), 3.37–3.22 (m, 2H), 2.52–2.15 (m, 3H), 1.94–1.62 (m, 5H), 1.07–0.93 (m, 6H).

Methyl (S)-2-[(S)-2-(isoquinoline-5-carboxamido)-4-methyl-pen tanamido]-3-((S)-2-oxopyrrolidin-3-yl)propanoate (10c): Compound 10c was synthesized according to the general procedures for Boc cleavage and coupling reaction, using isoquinoline-5-carboxylic acid as the appropriate carboxylic acid. The compound was purified by SiO_2 column chromatography (30:1 DCM/MeOH), yielding a color-less oil (55% yield). ESI-MS m/z 455 $[M+H]^+$, 477 $[M+Na]^+$. ^1H NMR (300 MHz, CD_3OD) δ 9.27 (s, 1H), 8.48 (dd, J = 7.3, 3.1 Hz, 1H), 8.27–8.13 (m, 2H), 7.99 (dd, J = 7.2, 1.0 Hz, 1H), 7.72 (t, 1H), 4.80–4.57 (m, 2H), 3.74 (d, J = 4.7 Hz, 3H), 3.38–3.22 (m, 2H), 2.77–2.11 (m, 3H), 1.92–1.65 (m, 5H), 1.03 (dd, J = 6.4, 2.6 Hz, 6H).

tert-Butyl (R/S)-7-bromo-1-[((S)-1-{[(S)-1-methoxy-1-oxo-3-((S)-2-oxopyrrolidin-3-yl)propan-2-yl]amino}-4-methyl-1-oxopentan-2-yl) carbamoyl]-3,4-dihydroisoquinoline-2(1H)-carboxylate (R/S-10d): Compound 10d was synthesized according to the general procedures for Boc cleavage and coupling reaction, using 8-bromo-2-(tert-butoxycarbonyl)-1,2,3,4-tetrahydroisoquinoline-1-carboxylic acid as the appropriate carboxylic acid. The colorless crude product was purified by SiO_2 column chromatography with (30:1, DCM/MeOH), as an eluent (71% yield). ESI-MS m/z 638 $[M+H]^+$. ^1H NMR (300 MHz, CD_3OD) δ 7.66 (m, 1H), 7.41–7.29 (m, 1H), 7.10 (t, J = 7.3 Hz, 1H), 5.35 (s, 1H), 4.64–4.33 (m, 3H), 4.04–3.84 (m, 1H), 3.69 (s, 3H), 3.60–3.42 (m, 1H), 3.23–3.10 (m, 1H), 3.01–2.88 (m, 2H), 2.55–2.02 (m, 3H), 1.90–1.56 (m, 5H), 1.49 (d, J = 2.0 Hz, 9H), 0.92 (m, 6H).

Methyl (S)-2-[(S)-2-(8-chloro-4-hydroxyquinoline-3-carboxam ido)-4-methylpentanamido]-3-((S)-2-oxopyrrolidin-3-yl)propanoate (10e): Compound 10e was synthesized according to the general procedures for Boc cleavage and coupling reaction, using 8-chloro-4-hydroxyquinoline-3-carboxylic acid as the appropriate carboxylic acid. The mixture was purified through SiO_2 column chromatog-raphy (30:1, DCM/MeOH), yielding a colorless oil (65% yield). ^1H NMR (300 MHz, $CDCl_3$) δ 9.34 (m, 1H), 9.22 (m, 1H), 8.15–8.02 (m, 1H), 7.67–7.52 (m, 1H), 7.41 (d, J = 8.3 Hz, 1H), 4.75–4.46 (m, 2H), 3.66 (d, J = 4.2 Hz, 3H), 3.35–3.16 (m, 2H), 2.47–2.02 (m, 4H), 2.00–1.58 (m, 5H), 0.96–0.87 (m, 6H).

Methyl (S)-2-[(S)-2-(8-chloro-1-methyl-4-oxo-1,4-dihydroquino line-3-carboxamido)-4-methylpentanamido]-3-((S)-2-oxopyrrolidin-3-yl)propanoate (10f): Compound 10f was synthesized according to the general procedures for Boc cleavage and coupling reaction, using 8-chloro-1-methyl-4-oxo-1,4-dihydroquinoline-3-carboxylic acid as the appropriate carboxylic acid. The target molecule was purified by SiO_2 column chromatography (40:1, $CHCl_3$/MeOH), yielding a colorless oil (43% yield). ESI-MS m/z 520 $[M+H]^+$, 542 $[M+Na]^+$. ^1H NMR (300 MHz, $CDCl_3$) δ 10.01 (m, 1H), 8.58–8.51 (m, 1H), 8.36–8.19 (m, 1H), 7.92 (s, 1H), 7.82 (t, J = 8.6 Hz, 1H), 7.56 (m, 1H), 7.28–7.16 (m, 1H), 4.62 (m, 1H), 4.51 (m, 1H), 4.25 (s, 3H), 3.63 (s, 3H), 3.23 (m, 2H), 2.45–2.09 (m, 3H), 1.84–1.59 (m, 5H), 0.93–0.78 (m, 6H).

Methyl (S)-2-{(S)-2-[4-hydroxy-8-(trifluoromethoxy)quinoline-3-carboxamido]-4-methylpentanamido}-3-((S)-2-oxopyrrolidin-3-yl) propanoate (10g): Compound 10g was synthesized according to the general procedures for Boc cleavage and coupling reaction, using 4-hydroxy-8-(trifluoromethoxy)quinoline-3-carboxylic acid as the appropriate carboxylic acid. The target molecule was purified by SiO_2 column chromatography (40:1, $CHCl_3$/MeOH), yielding a colorless oil (67% yield). ESI-MS m/z 555 $[M+H]^+$, 577 $[M+Na]^+$. ^1H NMR (300 MHz, $CDCl_3$) δ 12.58 (s, 1H), 10.24 (s, 1H), 8.76 (m, 1H), 8.41–8.15 (m, 2H), 7.66 –7.41 (m, 2H), 4.76–4.52 (m, 2H), 3.72 (s, 3H), 3.55–3.07 (m, 3H), 2.70–2.25 (m, 3H), 2.09–1.63 (m, 4H), 1.10–0.78 (m, 6H).

Methyl (S)-2-{(S)-4-methyl-2-[1-methyl-4-oxo-8-(trifluorometho xy)-1,4-dihydroquinoline-3-carboxamido]pentanamido}-3-((S)-2-oxo pyrrolidin-3-yl)propanoate (10h): Compound 10h was synthesized according to the general procedures for Boc cleavage and coupling reaction, using 1-methyl-4-oxo-8-(trifluoromethoxy)-1,4-dihydroqui noline-3-carboxylic acid as the appropriate carboxylic acid. The target molecule was purified by SiO_2 column chromatography (40:1, $CHCl_3$/MeOH), yielding a colorless oil (78% yield). ESI-MS m/z 569 $[M+H]^+$, 591 $[M+Na]^+$. ^1H NMR (300 MHz, DMSO-d_6) δ 10.00 (d, J = 7.7 Hz, 1H), 8.74 (s, 1H), 8.68 (d, J = 7.3 Hz, 1H), 8.39 (d, J = 8.1 Hz, 1H), 7.88 (d, J = 7.6 Hz, 1H), 7.66–7.53 (m, 2H), 4.73–4.58 (m, 1H), 4.38–4.26 (m, 1H), 4.12 (s, 3H), 3.61 (s, 3H), 3.19–2.99 (m, 4H), 2.3–1.97 (m, 4H), 1.72–1.44 (m, 4H), 0.96–0.84 (m, 6H).

Methyl (S)-2-[(S)-2-(4-hydroxy-6-nitroquinoline-3-carboxamido)-4-m-ethylpentanamido]-3-((S)-2-oxopyrrolidin-3-yl)propanoate (10i): Compound 10i was synthesized according to the general procedures for Boc cleavage and coupling reaction, using 4-hydroxy-6-nitroquinoline-

3-carboxylic acid as the appropriate carboxylic acid. The crude mixture was purified by SiO_2 column chromatography (30:1, DCM/MeOH), yielding a bright yellow oil (61% yield). ESI-MS m/z 516 $[M+H]^+$, 538 $[M+Na]^+$. ^1H NMR (300 MHz, CD_3OD) δ 10.23 (m, 1H), 9.72 (d, J = 7.1 Hz, 1H), 9.00–8.56 (m, 3H), 8.42 (m, 1H), 7.78–7.65 (m, 1H), 4.69–4.42 (m, 2H), 3.73 (s, 3H), 3.26–3.02 (m, 2H), 2.70–2.09 (m, 2H), 1.94–1.67 (m, 5H), 1.02 (m, 6H).

Methyl (S)-2-[(2S,3S)-2-(8-chloro-1-methyl-4-oxo-1,4-dihydroquinoline-3-carboxamido]-3-hydroxybutanamido)-3-((S)-2-oxopyrrolidin-3-yl)propanoate (10j): Compound 10j was synthesized according to the general procedures for Boc cleavage and coupling reaction, using 8-chloro-1-methyl-4-oxo-1,4-dihydroquinoline-3-carboxylic acid as the appropriate carboxylic acid. The crude mixture was purified by SiO_2 column chromatography (30:1, DCM/MeOH), yielding a colorless oil (70% yield). ESI-MS m/z 507 $[M+H]^+$. ^1H NMR (300 MHz, CD_3OD) δ 8.55 (s, 1H), 8.28–8.19 (m, 1H), 7.70 (m, 1H), 7.32 (m, 1H), 4.78–4.52 (m, 3H), 4.30 (s, 3H), 3.74 (s, 3H), 2.80–2.22 (m, 3H), 1.94–1.72 (m, 2H), 1.25 (d, J = 6.4 Hz, 3H).

Methyl (S)-2-[(2S,3S)-3-(benzyloxy)-2-(8-chloro-1-methyl-4-oxo-1,4-dihydroquinoline-3-carboxamido)butanamido]-3-((S)-2-oxopyrrolidin-3-yl) propanoate (10k): Compound 10k was synthesized starting from the Fmoc cleavage of intermediate 9c. In a round-bottom flask, compound 9c (400 mg, 1 eq) was solubilized in dry DCM (1.1 mL, 0.6 M), and then diethylamine (0.96 mL, 14 eq) was slowly added. The reaction mixture was stirred at 25°C for 2 h, then the mixture was dried under N_2 flux, and the crude product was used without any further purification. The de-protected amino-intermediate was then subjected to a coupling reaction, using 8-chloro-1-methyl-4-oxo-1,4-dihydroquinoline-3-carboxylic acid as the appropriate carboxylic acid. The mixture was purified by SiO_2 column chromatography (30:1, DCM/MeOH), affording the target molecule as a colorless oil (83% yield). ESI-MS m/z 597 $[M+H]^+$, 619 $[M+Na]^+$. ^1H NMR (300 MHz, CD_3OD) δ 10.60 (d, J = 8.0 Hz, 1H), 8.63 (s, 1H), 8.40–8.26 (m, 1H), 7.82–7.70 (m, 1H), 7.32 (m, 6H), 4.75–4.51 (m, 5H), 4.33 (s, 3H), 3.68 (d, J = 1.9 Hz, 3H), 3.11–2.91 (m, 1H), 2.56–2.10 (m, 4H), 1.87–1.62 (m, 3H), 1.28 (d, J = 4.6 Hz, 3H).

General procedure for the conversion of the ester intermediates into primary amides exemplified for compound N-((S)-1-{[(S)-1-amino-1-oxo-3-((S)-2-oxopyrrolidin-3-yl)propan-2-yl]amino}-4-methyl-1-oxopentan-2-yl)quinoline-8-carboxamide (11a): In an oven-dried round-bottom flask, the ester intermediate 10a (25 mg, 0.051 mmol) was solubilized in the smallest quantity of MeOH (0.2 mL), then NH_3 7 N in MeOH (0.86 mL) was slowly added to the reaction, and the flask was closed with a rubber stopper. The reaction mixture was stirred at 20°C for 12 h. Then, the solvent was evaporated and the crude product, a white amorphous solid, was used without any further purification (76% yield). ESI-MS m/z 440 $[M+H]^+$, 462 $[M+Na]^+$.

N-((S)-1-{[(S)-1-Amino-1-oxo-3-((S)-2-oxopyrrolidin-3-yl)propan-2-yl]amino}-4-methyl-1-oxopentan-2-yl)isoquinoline-8-carboxamide (11b): For the synthesis of compound 11b, the general procedure for the primary amide conversion was followed using 10b as the starting material. The crude product, a white amorphous solid, was used for the following reaction without any further purification (72% yield). ESI-MS m/z 440 $[M+H]^+$, 462 $[M+Na]^+$.

N-((S)-1-{[(S)-1-Amino-1-oxo-3-((S)-2-oxopyrrolidin-3-yl)propan-2-yl]amino}-4-methyl-1-oxopentan-2-yl)isoquinoline-5-carboxamide (11c): For the synthesis of compound 11c, the general procedure for the primary amide conversion was followed using 10c as the starting material. The crude product, a white amorphous solid, was used for the following reaction without any further purification (69% yield). ESI-MS m/z 440 $[M+H]^+$, 462 $[M+Na]^+$.

tert-Butyl (R/S)-1-[((S)-1-{[(S)-1-amino-1-oxo-3-((S)-2-oxopyrrolidin-3-yl)propan-2-yl]amino}-4-methyl-1-oxopentan-2-yl)carbamoyl]-7-bromo-3,4-dihydroisoquinoline-2(1H)-carboxylate (R/S-11d): For the syn-thesis of compound 11d, the general procedure for the primary amide conversion was followed using 10d as the starting material. The crude product was used for the following reaction without any further purification, yielding a white amorphous solid (83% yield). ESI-MS m/z 622 $[M+H]^+$, 644 $[M+Na]^+$.

N-((S)-1-{[(S)-1-Amino-1-oxo-3-((S)-2-oxopyrrolidin-3-yl)propan-2-yl]amino}-4-methyl-1-oxopentan-2-yl)-8-chloro-4-hydroxyquinoline-3-carboxamide (11e): For the synthesis of compound 11e, the general procedure for the primary amide conversion was followed using 10e as the starting material. The crude product was used for the following reaction without any further purification, yielding a white amorphous solid (68% yield). ESI-MS m/z 490 $[M+H]^+$.

N-((S)-1-{[(S)-1-Amino-1-oxo-3-((S)-2-oxopyrrolidin-3-yl)propan-2-yl]amino}-4-methyl-1-oxopentan-2-yl)-8-chloro-1-methyl-4-oxo-1,4-dihydroquinoline-3-carboxamide (11f): For the synthesis of compound 11f, the general procedure for the primary amide conversion was followed using 10f as the starting material. The crude product, a white amorphous solid (79% yield), was used for the following reaction without any further purification. ESI-MS m/z 504 $[M+H]^+$.

N-((S)-1-{[(S)-1-Amino-1-oxo-3-((S)-2-oxopyrrolidin-3-yl)propan-2-yl]amino}-4-methyl-1-oxopentan-2-yl)-4-hydroxy-8-(trifluoromethoxy) quinoline-3-carboxamide (11g): For the synthesis of compound 11g, the general procedure for the primary amide conversion was followed using 10g as the starting material. The crude product, a white amorphous solid (66% yield), was used for the following reaction without any further purification. ESI-MS m/z 540 $[M+H]^+$.

N-((S)-1-{[(S)-1-Amino-1-oxo-3-((S)-2-oxopyrrolidin-3-yl)propan-2-yl]amino}-4-methyl-1-oxopentan-2-yl)-1-methyl-4-oxo-8-(trifluor-omethoxy)-1,4-dihydroquinoline-3-carboxamide (11h): For the synthesis of compound 11h, the general procedure for the primary amide conversion was followed using 10h as the starting material. The crude product, a white amorphous solid (76% yield), was used for the following reaction without any further purification. ESI-MS m/z 553 $[M+H]^+$.

N-((S)-1-{[(S)-1-Amino-1-oxo-3-((S)-2-oxopyrrolidin-3-yl)propan-2-yl]amino}-4-methyl-1-oxopentan-2-yl)-4-hydroxy-6-nitroquinoline -3-carboxamide (11i): For the synthesis of compound 11i, the general procedure for the primary amide conversion was followed using 10i as the starting material. The crude product, a bright yellow amor-phous solid, was used for the following reaction without any further purification (64% yield). ESI-MS m/z 501 $[M+H]^+$, 523 $[M+Na]^+$.

N-((2S,3S)-1-{[(S)-1-Amino-1-oxo-3-((S)-2-oxopyrrolidin-3-yl)propan-2-yl)amino}-3-hydroxy-1-oxobutan-2-yl)-8-chloro-1-methyl-4-oxo-

1,4-dihydroquinoline-3-carboxamide (12a): For the synthesis of compound 12a, the general procedure for the primary amide conversion was followed using 10j as the starting material. The crude product, a white amorphous solid, was used for the following reaction without any further purification (84% yield). ESI-MS m/z 492 $[M+H]^+$, 515 $[M+Na]^+$.

N-((2S,3S)-1-{[(S)-1-Amino-1-oxo-3-((S)-2-oxopyrrolidin-3-yl)propan-2-yl]amino}-3-(benzyloxy)-1-oxobutan-2-yl)-8-chloro-1-methyl-4-oxo-1,4-dihydroquinoline-3-carboxamide (12b): For the synthesis of com-pound 12b, the general procedure for the primary amide conversion was followed using 10k as the starting material. The crude product, a white amorphous solid, was used for the following reaction without any further purification (83% yield). ESI-MS m/z 583 $[M+H]^+$, 605 $[M+Na]^+$.

General procedure for the primary amide conversion in the nitrile moiety exemplified with compound N-((S)-1-{[(S)-1-cyano-2-((S)-2-oxopyrrolidin-3-yl)ethyl]amino}-4-methyl-1-oxopentan-2-yl)quinoline-8-carboxamide (13a): In an oven-dried round-bottom flask under a N_2 atmosphere, the amide intermediate 11a (35 mg, 1 eq) was solubilized in anhydrous DCM (2 mL, 0.04 M) and the reaction mixture was cooled at 0°C, and then anhydrous TEA (22 µL, 2 eq) was slowly added, followed by TFAA (33 µL, 3 eq). The reaction mixture was stirred at 0°C for 2 h, then brine solution (2 mL) was added to the mixture, and the reaction mixture was allowed to reach room temperature and extracted with DCM (3 × 2 mL). The collected organic phases were combined, dried over anhydrous Na_2SO_4, filtered, and concentrated under reduced pressure to obtain the crude mixture. The crude mixture was purified by SiO_2 column chromatography (20:1, $CHCl_3$/MeOH), yielding a colorless amorphous solid. Elution solvent DCM/MeOH (20:1), 7 mg (21% yield). ESI-MS m/z 422 $[M+H]^+$, 444 $[M+Na]^+$. ^1H NMR (300 MHz, $CDCl_3$) δ 11.75 (d, J = 7.6 Hz, 1H), 8.97 (dd, J = 4.2, 1.6 Hz, 1H), 8.76 (d, J = 7.4 Hz, 1H), 8.41 (d, J = 7.1 Hz, 1H), 8.29 (dd, J = 8.3, 1.5 Hz, 1H), 7.97 (d, J = 8.1 Hz, 1H), 7.66 (t, J = 7.7 Hz, 1H), 7.51 (dd, J = 8.3, 4.3 Hz, 1H), 6.45 (s, 1H), 4.98–4.81 (m, 2H), 3.38–3.15 (m, 2H), 2.53–2.26 (m, 3H), 1.99–1.64 (m, 5H), 1.00 (dd, J = 8.2, 6.3 Hz, 6H). ^{13}C NMR (75 MHz, $CDCl_3$) δ 178.6, 172.9, 166.3, 149.6, 145.5, 137.8, 133.8, 132.4, 128.5, 127.9, 126.4, 121.1, 118.5, 52.3, 40.8, 40.3, 39.1, 37.7, 33.9, 29.7, 28.1, 25.1, 23.1, 22.1. ESI-HRMS m/z $[M+H]^+$ calcd for $[C_{23}H_{28}N_5O_3]^+$ 422.2187, found 422.2194; m/z $[M+Na]^+$ calcd for $[C_{23}H_{27}N_5O_3Na]^+$ 444.2006, found 444.2008; m/z $[M+K]^+$ calcd for $[C_{23}H_{27}N_5O_3K]^+$ 460.1745, found 460.1746.

N-((S)-1-{[(R)-1-Cyano-2-((S)-2-oxopyrrolidin-3-yl)ethyl]amino}-4-methyl-1-oxopentan-2-yl)isoquinoline-8-carboxamide (13b): The conversion of the primary amide 11b into the corresponding nitrile derivative 13b was carried out following the general procedure for the nitrile WH formation. The crude mixture was purified using SiO_2 column chromatography (20:1, DCM/MeOH), yielding a colorless oil (23% yield). ESI-MS m/z 422 $[M+H]^+$, 444 $[M+Na]^+$. ^1H NMR (300 MHz, CD_3OD) δ 9.59 (s, 1H), 8.49 (d, J = 5.7 Hz, 1H), 8.07 (d, J = 8.2 Hz, 1H), 7.95–7.76 (m, 3H), 5.09 (dd, J = 13.9, 7.1 Hz, 1H), 4.63 (m, 1H), 3.19–2.86 (m, 2H), 2.78–2.20 (m, 3H), 2.07–1.48 (m, 5H), 1.12–0.98 (m, 6H). ^{13}C NMR (75 MHz, CD_3OD) δ 179.7, 173.4, 169.3, 149.6, 136.4, 134.3, 130.2, 128.9, 127.2, 121.4, 119.7, 52.8, 40.0, 39.9, 38.4, 37.7, 33.8, 24.8, 21.9. ESI-HRMS m/z $[M+H]^+$ calcd for $[C_{23}H_{28}N_5O_3]^+$ 422.2187, found 422.2176; m/z $[M+Na]^+$ calcd for $[C_{23}H_{27}N_5O_3Na]^+$ 444.2006, found 444.1995.

N-((S)-1-{[(R)-1-Cyano-2-((S)-2-oxopyrrolidin-3-yl)ethyl]amino}-4-methyl-1-oxopentan-2-yl)isoquinoline-5-carboxamide (13c): The conversion of the primary amide 11c into the corresponding nitrile derivative 13c was carried out following the general procedure for the nitrile WH formation. The crude mixture was purified using SiO_2 column chromatography (20:1, DCM/MeOH), yielding a colorless oil (37% yield). ESI-MS m/z 422 $[M+H]^+$, 444 $[M+Na]^+$. ^1H NMR (300 MHz, CD_3OD) δ 9.30 (s, 1H), 8.50 (s, 1H), 8.21 (m, 1H), 8.02 (dd, J = 9.6, 4.8 Hz, 1H), 7.75 (t, J = 7.6 Hz, 1H), 5.13 (dd, J = 10.3, 5.5 Hz, 1H), 4.60 (dd, J = 9.2, 5.5 Hz, 1H), 3.80–3.58 (m, 2H), 2.74–2.19 (m, 3H), 2.05–1.53 (m, 5H), 1.07–0.87 (m, 6H). ^{13}C NMR (75 MHz, CD_3OD) δ 179.6, 173.4, 169.5, 142.3, 133.2, 132.5, 131.8, 130.3, 130.2, 128.7, 126.7, 126.7, 118.4, 52.7, 40.0, 39.9, 37.7, 31.6, 27.2, 24.8, 22.3, 21.9, 20.6. ESI-HRMS m/z $[M+H]^+$ calcd for $[C_{23}H_{28}N_5O_3]^+$ 422.2187, found 422.2181; m/z $[M+Na]^+$ calcd for $[C_{23}H_{27}N_5O_3Na]^+$ 444.2006, found 444.1999.

tert-Butyl (R/S)-7-bromo-1-[((S)-1-{[(S)-1-cyano-2-((S)-2-oxopyrrolidin-3-yl)ethyl]amino}-4-methyl-1-oxopentan-2-yl)carbamoyl]-3,4-dihydroisoquinoline-2(1H)-carboxylate (R/S-13d): The conversion of the primary amide 11d into the corresponding nitrile derivative 13d was carried out following the general procedure for the nitrile WH formation. The crude mixture was purified by SiO_2 column chromatography (20:1, DCM/MeOH), yielding a colorless oil (26% yield). ESI-MS m/z 604 $[M+H]^+$, 626 $[M+Na]^+$. ^1H NMR (300 MHz, CD_3OD) δ 7.65 (m, 1H), 7.37 (t, J = 8.9 Hz, 1H), 7.11 (dd, J = 12.5, 8.9 Hz, 1H), 5.39– 5.25 (m, 1H), 5.11–4.93 (m, 1H), 4.48–4.28 (m, 2H), 3.72 (m, 2H), 3.08–2.86 (m, 2H), 2.62–2.18 (m, 4H), 2.10–1.96 (m, 1H), 1.87–1.62 (m, 5H), 1.49 (s, 9H), 1.01–0.83 (m, 6H). ^{13}C NMR (75 MHz, CD_3OD) δ 179.5, 172.9, 172.7, 171.9, 135.1, 134.2, 130.3, 130.2, 129.9, 129.9, 119.4, 118.3, 115.4, 51.9, 51.4, 40.2, 39.9, 37.4, 33.6, 29.3, 27.4, 27.2, 27.2, 26.9, 24.7, 24.4, 22.3. ESI-HRMS m/z $[M+H]^+$ calcd for $[C_{28}H_{39}BrN_5O_5]^+$ 604.2129, found 604.2116; m/z $[M+Na]^+$ calcd for $[C_{28}H_{38}BrN_5O_5Na]^+$ 626.1949, found 626.1928.

8-Chloro-N-((S)-1-{[(S)-1-cyano-2-((S)-2-oxopyrrolidin-3-yl)ethyl]amino}-4-methyl-1-oxopentan-2-yl)-4-hydroxyquinoline-3-carboxamide (13e): The conversion of the primary amide 11e into the corresponding nitrile derivative 13e was carried out following the general procedure for the nitrile WH formation. The target mole-cule was purified by SiO_2 column chromatography (20:1, DCM/MeOH), yielding a colorless oil (11% yield). ESI-MS m/z 473 $[M+H]^+$, 495 $[M+Na]^+$. ^1H NMR (300 MHz, CD_3OD) δ 8.77 (s, 1H), 8.34 (d, J = 8.1 Hz, 1H), 7.89 (d, J = 7.8 Hz, 1H), 7.48 (t, J = 8.0 Hz, 1H), 5.01 (dd, J = 9.4, 4.3 Hz, 1H), 4.65–4.48 (m, 1H), 3.70–3.47 (m, 2H), 2.79–2.11 (m, 3H), 2.00–1.69 (m, 5H), 1.00 (dd, J = 12.4, 6.3 Hz, 6H). ^{13}C NMR (75 MHz, CD_3OD) δ 179.5, 173.6, 165.4, 144.1, 132.7, 125.2, 124.7, 111.1, 52.0, 40.9, 40.0, 39.4, 38.4, 37.7, 33.7, 33.2, 29.4, 29.3, 27.5, 27.2, 24.8, 22.0, 20.6. ESI-HRMS m/z $[M+H]^+$ calcd for $[C_{23}H_{27}ClN_5O_4]^+$ 4.76–472.1746, found 472.1754.

8-Chloro-N-((S)-1-{[(S)-1-cyano-2-((S)-2-oxopyrrolidin-3-yl)ethyl]amino}-4-methyl-1-oxopentan-2-yl)-1-methyl-4-oxo-1,4-dihydroquinoline-3-carboxamide (13f): The conversion of the primary amide

11f into the corresponding nitrile derivative 13f was carried out the general procedure for the nitrile WH formation. mixture was purified by SiO_2 column chromatography (20:1, DCM/MeOH), yielding a colorless oil (21% yield). ESI-MS m/z 487 $[M+H]^+$, 509 $[M+Na]^+$. ^1H NMR (300 MHz, $CDCl_3$) δ 10.14 (d, J = 7.1 Hz, 1H), 8.64 (s, 1H), 8.45 (d, J = 8.0 Hz, 1H), 7.74 (d, J = 7.6 Hz, 1H), 7.37 (t, J = 7.8 Hz, 1H), 6.57 (s, 1H), 5.55 (s, 1H), 4.68–4.54 (m, 1H), 4.35 (s, 3H), 3.83–3.23 (m, 2H), 2.88–2.28 (m, 2H), 1.99–1.56 (m, 6H), 0.95 (m, 6H).^{13}C NMR (75 MHz, CD_3OD) δ 179.5, 175.7, 173.3, 164.9, 152.3, 152.3, 137.7, 136.7, 130.5, 125.9, 125.6, 122.5, 118.4, 110.5, 109.9, 40.9, 40.0, 38.4, 37.7, 33.8, 27.2, 24.8, 22.0, 20.7. ESI-HRMS m/z $[M+Na]^+$ calcd for $[C_{24}H_{28}ClN_5O_4Na]^+$ 508.1722, found 508.1726.

N-((S)-1-{[(S)-1-Cyano-2-((S)-2-oxopyrrolidin-3-yl)ethyl]amino}-4-methyl-1-oxopentan-2-yl)-4-hydroxy-8-(trifluoromethoxy)quinoline-3-carboxamide (13g): The conversion of the primary amide 11g into the corresponding nitrile derivative 13g was carried out following the general procedure for the nitrile WH formation. The target molecule was purified by SiO_2 column chromatography (20:1, DCM/MeOH), yielding a colorless oil (33% yield). ESI-MS m/z 522 $[M+H]^+$, 544 $[M+Na]^+$. ^1H NMR (300 MHz, CD_3OD) δ 8.72 (s, 1H), 8.33 (d, J = 4.9 Hz, 1H), 7.79 (d, J = 7.8 Hz, 1H), 7.54 (t, J = 8.1 Hz, 1H), 5.17–4.88 (m, 1H), 4.65–4.45 (m, 1H), 2.72–2.19 (m, 4H), 2.01–1.61 (m, 6H), 1.01 (dd, J = 12.7, 5.0 Hz, 6H). ^{13}C NMR (75 MHz, CD_3OD) δ 192.1, 179.5, 179.3, 176.5, 176.4, 173.5, 173.2, 143.9, 138.6, 132.3, 128.2, 124.6, 124.4, 123.7, 111.3, 40.9, 40.1, 40.0, 39.4, 38.2, 37.7, 33.2, 27.5, 24.8, 22.0, 20.6. ESI-HRMS m/z $[M+H]^+$ calcd for $[C_{24}H_{27}F_3N_5O_5]^+$ 522.1929, found 522.1962; m/z $[M+Na]^+$ calcd for $[C_{24}H_{26}F_3N_5O_5Na]^+$ 544.1778, found 544.1778; m/z $[M+K]^+$ calcd for $[C_{24}H_{26}F_3N_5O_5K]^+$ 560.1518, found 560.1519.

N-((S)-1-{[(S)-1-Cyano-2-((S)-2-oxopyrrolidin-3-yl)ethyl]amino}-4-methyl-1-oxopentan-2-yl)-1-methyl-4-oxo-8-(trifluoromethoxy)-1,4-dihydroquinoline-3-carboxamide (13h): The conversion of the primary amide 11h into the corresponding nitrile derivative 13h was carried out following the general procedure for the nitrile WH formation. The target molecule was purified by SiO_2 column chromatography (20:1, DCM/MeOH), yielding a pale yellow oil (24% yield). ESI-MS m/z 536 $[M+H]^+$, 558 $[M+Na]^+$. ^1H NMR (300 MHz, CD_3OD) δ 8.75–8.68 (m, 1H), 8.55–8.44 (m, 1H), 7.83 (d, J = 8.0 Hz, 1H), 7.58 (dd, J = 11.7, 4.4 Hz, 1H), 5.08–4.88 (m, 1H), 4.72–4.42 (m, 1H), 4.20 (s, 3H), 2.68–2.17 (m, 4H), 1.99–1.64 (m, 6H), 1.10–0.92 (m, 6H). ^{13}C NMR (75 MHz, CD_3OD) δ 175.3, 173.3, 152.0, 133.6, 130.2, 126.5, 125.8, 125.3, 118.9, 118.3, 117.8, 110.8, 40.9, 40.0, 39.3, 38.2, 37.7, 33.2, 27.4, 27.1, 24.8, 22.0, 20.5. ESI-HRMS m/z $[M+H]^+$ calcd for $[C_{25}H_{29}F_3N_5O_5]^+$ 536.2115, found 536.2108; m/z $[M+Na]^+$ calcd for $[C_{25}H_{28}F_3N_5O_5Na]^+$ 558.1935, found 558.1929.

N-((S)-1-{[(S)-1-Cyano-2-((S)-2-oxopyrrolidin-3-yl)ethyl]amino}-4-methyl-1-oxopentan-2-yl)-4-hydroxy-6-nitroquinoline-2-carboxamide (13i): The conversion of the primary amide 11i into the corresponding nitrile derivative 13i was carried out following the general procedure for the nitrile WH formation. The target molecule was purified by SiO_2 column chromatography following (20:1, DCM/MeOH), yielding a bright yellow oil (43% yield). ESI-MS The m/z 483 $[M+H]^+$, 505 $[M+Na]^+$. ^1H NMR (300 MHz, CD_3OD) δ 10.34 (s, 1H), 8.77 (d, J = 3.9 Hz, 1H), 8.53 (m, 1H), 7.78 (dd, J = 9.1, 1.6 Hz, 1H), 5.14–4.97 (m, 1H), 4.68–4.50 (m, 1H), 3.59 (m, 2H), 2.71–2.18 (m, 3H), 1.85 (m, 5H), 1.02 (m, 6H). ^{13}C NMR (75 MHz, CD_3OD) δ 179.5, 179.3, 176.6, 173.3, 145.1, 144.6, 142.8, 126.6, 125.9, 125.9, 121.9, 120.4, 111.8, 40.8, 40.1, 37.7, 33.2, 27.5, 27.2, 24.8, 22.1, 20.7, 20.6. ESI-HRMS m/z $[M+H]^+$ calcd for $[C_{23}H_{27}N_6O_6]^+$ 483.1987, found 483.1986; m/z $[M+Na]^+$ calcd for $[C_{23}H_{26}N_6O_6Na]^+$ 505.1806, found 505.1785.

8-Chloro-N-((2S,3 R)-1-{[(S)-1-cyano-2-((S)-2-oxopyrrolidin-3-yl) ethyl]amino}-3-hydroxy-1-oxobutan-2-yl)-1-methyl-4-oxo-1,4,4a,8a-tetrahydroquinoline-3-carboxamide (14a): The conversion of the primary amide 12a into the corresponding nitrile derivative 14a was carried out following the general procedure for the nitrile WH formation. The crude mixture was purified through SiO_2 column chromatography (30:1, DCM/MeOH), yielding a colorless oil (27% yield). ESI-MS m/z 474 $[M+H]^+$, 496 $[M+Na]^+$. ^1H NMR (300 MHz, CD_3OD) δ 10.57 (d, J = 7.3 Hz, 1H), 8.68 (s, 1H), 8.41 (dd, J = 8.1, 1.5 Hz, 1H), 7.88–7.79 (m, 1H), 7.54–7.31 (m, 1H), 5.11 (dd, J = 10.1, 6.0 Hz, 1H), 4.47 (dd, J = 7.3, 3.7 Hz, 1H), 4.38 (s, 3H), 4.34 (dd, J = 6.4, 3.6 Hz, 1H), 3.20 (dd, J = 14.8, 7.5 Hz, 1H), 2.68–2.22 (m, 4H), 2.01–1.65 (m, 2H), 1.25 (d, J = 6.4 Hz, 3H). ^{13}C NMR (75 MHz, CD_3OD) δ 179.6, 171.6, 165.6, 152.4, 137.7, 136.6, 130.5, 125.9, 125.9, 125.5, 122.5, 118.4, 110.7, 66.8, 64.6, 59.2, 53.4, 40.0, 37.6, 33.8, 27.2, 19.1. ESI- HRMS m/z $[M+H]^+$ calcd for $[C_{22}H_{25}ClN_5O_5]^+$ 474.1539, found 474.1527; m/z $[M+Na]^+$ calcd for $[C_{22}H_{24}ClN_5O_5Na]^+$496.1358, found 496.1341.

(2 R,3S)-3-(8-Chloro-1-methyl-4-oxo-1,4,4a,8a-tetrahydroquinoline-3-carboxamido)-4-{[(S)-1-cyano-2-((S)-2-oxopyrrolidin-3-yl)ethyl]amino}-4-oxobutan-2-yl benzoate (14b): The conversion of the primary amide 12b into the corresponding nitrile derivative 14b was carried out following the general procedure for the nitrile WH formation. The crude mixture was purified through SiO_2 column chromatography (30:1, DCM/MeOH), yielding a colorless oil (36% yield). ESI-MS m/z 564 $[M+H]^+$, 586 $[M+Na]^+$. ^1H NMR (300 MHz, CD_3OD) δ 8.73 (s, 1H), 8.46 (dd, J = 8.1, 1.6 Hz, 1H), 7.92–7.85 (m, 1H), 7.52–7.14 (m, 6H), 5.06 (dd, J = 10.1, 5.9 Hz, 1H), 4.77–4.47 (m, 3H), 4.39 (d, J = 3.7 Hz, 3H), 4.30 (dd, J = 6.3, 2.9 Hz, 1H), 3.24–2.94 (m, 2H), 2.49–2.10 (m, 3H), 1.90–1.65 (m, 2H), 1.29 (d, J = 2.2 Hz, 3H). ^{13}C NMR (75 MHz, CD_3OD) δ 179.4, 175.5, 171.3, 171.1, 170.8, 165.5, 165.4, 165.2, 152.4, 138.4, 137.4, 136.6, 130.2, 127.9, 127.4, 127.1, 127.1, 125.7, 125.4, 122.4, 118.5, 110.5, 74.4, 70.7, 58.1, 39.9, 37.5, 33.6, 26.9, 15.3. ESI-HRMS m/z $[M+H]^+$ calcd for $[C_{29}H_{31}ClN_5O_5]^+$ 564.2008, found 564.2004; m/z $[M+Na]^+$ calcd for $[C_{29}H_{30}ClN_5O_5Na]^+$ 586.1828, found 586.1829.

(R/S)-7-Bromo-N-((S)-1-{[(S)-1-cyano-2-((S)-2-oxopyrrolidin-3-yl)ethyl]amino}-4-methyl-1-oxopentan-2-yl)-1,2,3,4-tetrahydroisoquinoline-1-carboxamide (R/S-15): Final compound 13d was deprotected, allowing to obtain the final compound 15. In a round-bottom flask, the final com-pound 13d (20 mg, 1 eq) was solubilized in MeOH (0.66 mL, 0.05 M), the solution was cooled at 0°C, and then HCl in MeOH (20 eq, 1 M) was slowly added. The reaction mixture was stirred at the same temperature

for 1 h, then the mixture was concentrated under N_2 flux, and the crude mixture was purified by SiO_2 column chromatography (30:1, $CHCl_3$/ MeOH), yielding a pale yellow oil (40% yield). ESI-MS m/z 504 $[M+H]^+$, 526 $[M+Na]^+$. ^1H NMR (300 MHz, CD_3OD) δ 7.89 (s, 1H), 7.46 (d, J = 9.9 Hz, 1H), 7.30 (d, J = 8.3 Hz, 1H), 7.09–7.00 (m, 1H), 4.69–4.32 (m, 3H), 3.00–2.68 (m, 4H), 2.57–2.43 (m, 2H), 2.33–2.07 (m, 3H), 1.98–1.50 (m, 5H), 1.09–0.74 (m, 6H). ^{13}C NMR (101 MHz, CD_3OD) δ 172.8, 172.7, 172.4, 171.7, 171.3, 167.2, 166.5, 131.8, 131.7, 131.5, 131.1, 131.0, 130.9, 129.9, 129.5, 129.0, 128.6, 120.6, 120.3, 56.7, 56.6, 53.2, 52.3, 50.8, 40.5, 40.2, 39.9, 39.7, 37.8, 33.1, 29.4, 27.4, 27.3,
24.8, 24.6, 24.1, 22.4, 22.4, 22.0, 21.9, 20.9, 20.7, 20.7, 19.6, 19.4, 12.1. ESI-HRMS m/z $[M+H]^+$ calcd for $[C_{23}H_{31}BrN_5O_3]^+$ 504,1605, found 504.1592.

6-Amino-N-((S)-1-{[(S)-1-cyano-2-((S)-2-oxopyrrolidin-3-yl)ethyl] amino}-4-methyl-1-oxopentan-2-yl)-4-hydroxyquinoline-2-carboxamide (16): To a solution of compound 13i (40 mg, 1 eq) in a mixture of EtOH/H_2O (5:1, 0.82 mL, 0.1 M), NH_4Cl (15 mg. 3,3 eq) and Fe powder (15 mg, 3.3 eq) were added. The reaction mixture was stirred at 55°C for 30 min, then the solid was filtered on celite, and washed with EtOH (3 × 1 mL). The solute was concentrated under reduced pressure, solubilized with EtOAc (3 mL), and washed with aqueous $NaHCO_3$ (3 × 2 mL), and then the combined organic phase was dried over anhydrous Na_2SO_4, filtered, and concentrated under reduced pressure. The final compound was purified by SiO_2 column chromatography (20:1, DCM/MeOH), yielding a pale yellow oil (95% yield). ESI-MS m/z 453 $[M+H]^+$, 475 $[M+Na]^+$. ^1H NMR (300 MHz, CD_3OD) δ 8.58 (s, 1H), 7.98 (bs, 1H), 7.87 (t, J = 7.2 Hz, 1H), 7.75–7.44 (m, 4H), 7.33–7.14 (m, 2H), 6.97 (d, J = 7.6 Hz, 1H), 4.64–4.47 (m, 2H), 3.77–3.59 (m, 1H), 3.25–3.08 (m, 1H), 2.68–2.22 (m, 3H), 2.04–1.63 (m, 5H), 1.00 (dd, J = 12.7, 6.1 Hz, 6H). ^{13}C NMR (75 MHz, CD_3OD) δ 180.7, 177.1, 172.8, 153.8, 139.7, 139.5, 138.0, 129.3, 128.8, 128.5, 127.3, 119.7, 75.7,
72.0, 58.7, 41.2, 39.8, 39.7, 38.8, 30.7, 28.4, 28.3, 16.7. ESI-HRMS m/z $[M+H]^+$ calcd for $[C_{23}H_{29}N_6O_4]^+$ 453.2245, found 453.2234; m/z $[M+Na]^+$ calcd for $[C_{23}H_{28}N_6O_4Na]^+$ 475.2064, found 475.2052.

4.1.3 | Synthetic procedure for the preparation of compound 20

Methyl (6S,9S,12S)-9-isobutyl-6-isopropyl-2,2-dimethyl-4,7,10-trioxo-12-[((S)-2-oxopyrrolidin-3-yl)methyl]-3-oxa-5,8,11-triazatridecan-13-oate (17): Compound 17 was synthesized according to the general procedures for Boc cleavage and coupling reaction using (tert-butoxycarbonyl)-L- valine as the appropriate carboxylic acid and the previously prepared ester intermediate 9a as the starting material. ESI-MS and ^1H NMR data are in accordance with those reported in the literature.[23]

Methyl (S)-2-{(S)-2-[(R)-2-(8-chloro-1-methyl-4-oxo-1,4-dihydroquinoline-3-carboxamido)-3-methylbutanamido]-4-methylpentanamido}-3-((S)-2-oxopyrrolidin-3-yl)propanoate (18): Compound 18 was synthesized according to the general procedures for Boc cleavage and coupling reaction using 8-chloro-1-methyl-4-oxo-1,4-dihydroquinoline-3-carboxylic acid as the appropriate carboxylic acid. The mixture was purified by SiO_2 column chromatography (30:1, DCM/MeOH), yielding a colorless oil (61% yield). ESI-MS m/z 618 $[M+H]^+$ 640 $[M+Na]^+$. ^1H NMR (300 MHz, $CDCl_3$) δ 10.36 (m, 1H), 8.67 (m, 1H), 8.40 (d, J = 7.8 Hz, 1H), 8.13 (m, 1H), 7.86–7.58 (m, 1H), 7.36–7.18 (m, 2H), 6.87 (s, 1H), 4.72–4.40 (m, 3H), 4.34 (s, 3H), 3.67 (s, 3H), 3.37–3.18 (m, 2H), 2.58–2.19 (m, 4H), 1.91–1.39 (m, 5H), 1.12–0.75 (m, 12H).

N-{(S)-1-[((S)-1-{[(S)-1-Amino-1-oxo-3-((S)-2-oxopyrrolidin-3-yl) propan-2-yl]amino}-4-methyl-1-oxopentan-2-yl)amino]-3-methyl-1-oxobutan-2-yl}-8-chloro-1-methyl-4-oxo-1,4-dihydroquinoline-3-carbox-amide (19): For the synthesis of compound 19, the general procedure for the primary amide conversion was followed using the ester inter-mediate 18 as the starting material. The crude product, a white amorphous solid, was used for the following reaction without any further purification (88% yield). ESI-MS m/z 604 $[M+H]^+$ 626 $[M+Na]^+$.

8-Chloro-N-{(S)-1-[((S)-1-{[(S)-1-cyano-2-((S)-2-oxopyrrolidin-3-yl) ethyl]amino}-4-methyl-1-oxopentan-2-yl)amino]-3-methyl-1-oxobutan-2-yl}-1-methyl-4-oxo-1,4-dihydroquinoline-3-carboxamide (20): The conversion of the primary amide 19 into the corresponding nitrile derivative 20 was carried out following the general procedure for the nitrile WH formation. The mixture was purified by SiO_2 column chromatography (30:1, DCM/MeOH), yielding a colorless oil (18% yield). ESI-MS m/z 586 $[M+H]^+$, 608 $[M+Na]^+$. ^1H NMR (300 MHz, CD_3OD) δ 10.58–10.47 (m, 1H), 8.80–8.68 (m, 1H), 8.58 (m, 1H), 8.47–8.39 (m, 1H),
8.23 (d, J = 8.5 Hz, 1H), 7.89 (d, J = 7.5 Hz, 1H), 7.73 (dd, J = 8.8, 4.3 Hz,
1H), 7.47 (t, J = 7.9 Hz, 1H), 4.40 (s, 3H), 4.70–4.13 (m, 3H), 3.23–3.07 (m,
1H), 2.58–2.15 (m, 5H), 1.92–1.57 (m, 5H), 1.12–0.87 (m, 12H). ^{13}C NMR (75 MHz, CD_3OD) δ 175.8, 173.3, 172.5, 152.4, 137.8, 136.7, 130.5, 125.9, 125.6, 122.6, 110.7, 59.0, 51.6, 51.3, 40.1, 38.4, 32.3, 30.7, 29.5, 29.3, 27.9, 27.7, 24.4, 22.3, 21.9, 20.5, 18.7, 16.9. ESI-HRMS m/z $[M+H]^+$ calcd for $[C_{29}H_{38}ClN_6O_5]^+$ 585.2587, found 585.2565; m/z $[M+Na]^+$
calcd for $[C_{29}H_{37}ClN_6O_5Na]^+$ 607.2406, found 607.2382.

4.1.4 | Synthetic procedure for the preparation of compounds 25a–c and 26

Methyl (S)-2-{(S)-2-[(tert-butoxycarbonyl)amino]-4-methylpentanamido}-3-(1H-1,2,3-triazol-1-yl)propanoate (23a): Compound 23a was synthesized according to the general procedure for a coupling reaction using the modified amino acid 21a (synthesis reported in supporting information) and Boc-Leu-OH as the appropriate carboxylic acid. The mixture was used without any further purification, yielding a colorless oil (89% yield). ESI-MS m/z 384 $[M+H]^+$, 406 $[M+Na]^+$.

Methyl (tert-butoxycarbonyl)-L-leucyl-L-histidinate (23b): Compound 23b was synthesized according to the general procedures for Boc cleavage and coupling reaction using the natural amino acid 21b as the starting material and Boc-Leu-OH as the appropriate carbox-ylic acid. ESI-MS and ^1H NMR data are in accordance with those reported in the literature.[24]

Methyl (tert-butoxycarbonyl)-L-leucyl-L-threoninate (23c): Compound 23c was synthesized according to the general procedures for Boc cleavage and coupling reaction using the natural amino acid 21c and Boc-Leu-OH as the appropriate carboxylic acid. ESI-MS and ^1H NMR data are in accordance with those reported in the literature.[25]

Methyl (S)-2-[(S)-2-(8-chloro-1-methyl-4-oxo-1,4-dihydroquinoline-3-carboxamido)-4-methylpentanamido]-3-(1H-1,2,3-triazol-1-yl)propano-ate (24a): Compound 24a was synthesized according to the general procedures for Boc cleavage and coupling reaction using compound 23a and 8-chloro-1-methyl-4-oxo-1,4-dihydroquinoline-3-carboxylic acid as the appropriate carboxylic acid. The crude mixture was purified by SiO_2 column chromatography (30:1, DCM/MeOH), yielding a colorless oil (64% yield). ESI-MS m/z 504 $[M+H]^+$, 526 $[M+Na]^+$. ^1H NMR (300 MHz, CD_3OD) δ 10.29 (d, J = 6.7 Hz, 1H), 8.70 (d, J = 2.8 Hz, 1H), 8.40 (d, J = 8.1 Hz, 1H), 8.05 (dd, J = 8.6, 0.9 Hz, 1H), 7.87 (m, 1H), 7.74–7.64 (m, 1H), 7.44 (m, 1H), 5.13–4.72 (m, 3H), 4.57 (m, 1H), 4.40 (d, J = 1.5 Hz, 3H), 3.76 (s, 3H), 1.83–1.56 (m, 3H), 0.96 (m, 6H).

Methyl (8-chloro-1-methyl-4-oxo-1,4-dihydroquinoline-3-carbonyl)-L-leucyl-L-histidinate (24b): Compound 24b was synthesized according to general procedures for Boc cleavage and coupling reaction using compound 23b and 8-chloro-1-methyl-4-oxo-1,4-dihydroquinoline-3-carboxylic acid as the appropriate carboxylic acid. The mixture was purified by SiO_2 column chromatography (30:1, DCM/MeOH), yielding a colorless oil (68% yield). ESI-MS m/z 502 $[M+H]^+$, 524 $[M+Na]^+$. ^1H NMR (300 MHz, CD_3OD) δ 10.36 (d, J = 6.5 Hz, 1H), 8.67 (s, 1H), 8.38 (t, J = 6.9 Hz, 1H), 7.90–7.76 (m, 1H), 7.43 (t, J = 8.2 Hz, 1H), 6.92 (s, 1H), 4.69 (m, 1H), 4.52 (m, 1H), 4.43–4.25 (s, 3H), 3.4 (s, 3H), 3.30 (dt, J = 3.4, 1.8 Hz, 1H), 3.22–2.95 (m, 1H), 1.89– 1.54 (m, 3H), 1.06 (m, 6H).

Methyl (8-chloro-1-methyl-4-oxo-1,4-dihydroquinoline-3-carbonyl)-L-leucyl-L-threoninate (24c): Compound 24c was synthesized according to the general procedures for Boc cleavage and coupling reaction using compound 23c and 8-chloro-1-methyl-4-oxo-1,4-dihydroquinoline-3-carboxylic acid as the appropriate carboxylic acid. The mixture was purified by SiO_2 column chromatography (30:1, DCM/MeOH), yielding a pale yellow oil (61% yield). ESI-MS m/z 466 $[M+H]^+$, 488 $[M+Na]^+$. ^1H NMR (300 MHz, Acetone-d_6) δ 10.23 (d, J = 7.7 Hz, 1H), 8.69 (s, 1H), 8.41 (m, 1H), 7.89–7.84 (m, 1H), 7.48 (dd, J = 7.9, 3.2 Hz, 1H), 4.90–4.78 (m, 1H), 4.43 (s, 1H), 4.31–4.26 (m, 1H), 3.92 (m, 1H), 3.69 (s, 1H), 2.05 (m, 1H), 1.86–1.68 (m, 3H), 1.17 (d, J = 6.3 Hz, 3H), 0.97 (dd, J = 11.3, 5.9 Hz, 6H).

8-Chloro-N-((S)-1-{[(S)-1-cyano-2-(1H-1,2,3-triazol-1-yl)ethyl]amino}-4-methyl-1-oxopentan-2-yl)-1-methyl-4-oxo-1,4-dihydroquinoline-3-carboxamide (25a): For the synthesis of compound 25a, the general procedure for the primary amide conversion was followed using 24a as the starting material. The crude product, a white amorphous solid, was used immediately for the following reaction without any further purification (95% yield). ESI-MS m/z 489 $[M+H]^+$, 511 $[M+Na]^+$. The conversion of the primary amide into the corresponding nitrile derivative 25a was carried out following the general procedure for the nitrile WH formation. The crude mixture was purified by SiO_2 column chromatography (20:1, DCM/MeOH), yielding a colorless oil (37%). ESI-MS m/z 470 $[M+H]^+$, 492 $[M+Na]^+$. ^1H NMR (300 MHz, CD_3OD) δ 10.33 (d, J = 5.8 Hz, 1H), 8.71 (d, J = 3.6 Hz, 1H), 8.48–8.37 (m, 1H), 8.10 (m, 1H), 7.89 (m, 1H), 7.74 (d, J = 3.7 Hz, 1H), 7.46 (m, 1H), 5.42 (m, 1H), 4.95–4.87 (m, 2H), 4.50 (m, 1H), 4.39 (d, J = 4.8 Hz, 3H), 1.78–1.54 (m, 3H), 1.01–0.90 (m, 6H). ^{13}C NMR (75 MHz, CD_3OD) δ 175.7, 173.4, 165.0, 152.4, 137.8, 136.7, 133.3, 130.5, 125.9, 125.6, 125.5, 122.6, 115.5, 110.4, 52.0, 51.9, 49.6, 40.7, 24.7, 21.9, 20.5. ESI-HRMS m/z $[M+H]^+$ calcd for $[C_{22}H_{25}ClN_7O_3]^+$ 470.1702, found 470.1698; m/z $[M+Na]^+$ calcd for $[C_{22}H_{24}ClN_7O_3Na]^+$ 492.1521, found 492.1514.

8-Chloro-N-((S)-1-{[(S)-1-cyano-2-(1H-imidazol-4-yl)ethyl]amino}-4-methyl-1-oxopentan-2-yl)-1-methyl-4-oxo-1,4-dihydroquinoline-3-carboxamide (25b): For the synthesis of compound 25b, the general procedure for the primary amide conversion was followed using the ester intermediate 24b as the starting material. The crude product, a white amorphous solid, was used for the following reaction without any further purification (88% yield). ESI-MS m/z 470 $[M+H]^+$, 492 $[M+Na]^+$. The conversion of the primary amide into the corresponding nitrile derivative 25b was carried out following the general procedure for the nitrile WH formation. The mixture was purified by SiO_2 column chromatography the (30:1, DCM/MeOH), yielding a colorless oil (37% yield). ESI-MS m/z 470 $[M+H]^+$, 492 $[M+Na]^+$. ^1H NMR (300 MHz, CD_3OD) δ 8.72 (s, 1H), 8.45 (dd, J = 8.1, 1.5 Hz, 1H), 7.94–7.84 (m, 1H), 7.59 (s, 1H), 7.48 (t, J = 7.9 Hz, 1H), 7.02 (s, 1H), 5.05 (t, J = 7.4 Hz, 1H), 4.56 (dd, J = 9.2, 5.7 Hz, 1H), 4.40 (s, 3H), 3.13 (dd, J = 7.3, 4.0 Hz, 1H), 1.84–1.54 (m, 4H), 0.98 (dd, J = 12.2, 6.3 Hz, 6H). ^{13}C NMR (75 MHz, CD_3OD) δ 175.6, 173.1, 165.0, 152.3, 137.7, 136.7, 130.4, 125.9, 125.6, 122.6, 117.7, 110.4, 78.0, 51.9, 40.9, 40.6, 31.3, 29.3, 24.7, 22.0, 20.6, 12.9. ESI-HRMS m/z $[M+H]^+$ calcd for $[C_{23}H_{26}ClN_6O_3]^+$ 469.1749, found 469.1749; m/z $[M+Na]^+$ calcd for $[C_{23}H_{25}ClN_6O_3Na]^+$ 491.1569, found 491.1572.

8-Chloro-N-{(S)-1-[((1R,2R)-1-cyano-2-hydroxypropyl)amino]-4-methyl-1-oxopentan-2-yl}-1-methyl-4-oxo-1,4-dihydroquinoline-3-carboxamide (25c): For the synthesis of compound 25c, the general procedure for the primary amide conversion was followed using the ester intermediate 24c as the starting material. The crude product, a white amorphous solid, was used immediately for the following reaction without any further purification (68% yield). ESI- MS m/z 470 $[M+H]^+$, 492 $[M+Na]^+$. The conversion of the primary amide into the corresponding nitrile derivative 25c was carried out following the general procedure for the nitrile WH formation. The mix-ture was purified by SiO_2 column chromatography (30:1, DCM/MeOH), yielding a colorless oil (41% yield). ESI-MS m/z 434 $[M+H]^+$. ^1H NMR (300 MHz, CD_3OD) δ 10.39 (d, J = 6.9 Hz, 1H), 8.70 (s, 1H), 8.43 (dd, J = 8.1, 1.5 Hz, 1H), 7.89 (dd, J = 7.7, 1.5 Hz, 1H), 7.46 (t, J = 7.9 Hz, 1H), 4.63 (d, J = 4.1 Hz, 1H), 4.38 (s, 3H), 4.04 (dd, J = 11.9, 5.7 Hz, 1H), 1.76 (m, 3H), 1.28 (d, J = 6.3 Hz, 3H), 1.16 (dd, J = 15.4, 7.0 Hz, 1H), 1.01 (dd, J = 11.8, 6.2 Hz, 6H). ^{13}C NMR (75 MHz, CD_3OD) δ 175.7, 173.4, 165.0, 152.3, 137.7, 136.7, 130.5, 125.9, 125.6, 122.5, 117.2, 110.4, 66.5, 51.9, 40.9, 24.8, 22.1, 20.6, 17.7. ESI-HRMS m/z $[M+H]^+$ calcd for $[C_{21}H_{26}ClN_4O_4]^+$ 433.1637, found 433.1626; m/z $[M+Na]^+$ calcd for $[C_{21}H_{25}ClN_4O_4Na]^+$ 455.1456, found 455.1441.

8-Chloro-N-[(S)-1-({(1R,2R)-1-cyano-2-[((R/S)-tetrahydrofuran-2-yl)oxy]propyl}amino)-4-methyl-1-oxopentan-2-yl]-1-methyl-4-oxo-1,4-dihydroquinoline-3-carboxamide (R/S-26): In a glass vial under a N_2 atmosphere, the final compound 25c (10 mg, 1 eq) was solubilized in anhydrous DCM (0.5 mL, 0.04 M), and then 2,3-dihydrofuran (3 mg, 1.5 eq) was added, followed by a solution (0.006 M) of PTSA (2 mg, 0.15 eq) in DCM (0.5 mL). The reaction mixture was stirred for 12 h at

20°C, and then the mixture was dried under N_2 flux. The mixture was directly purified by SiO_2 column chromatography (30:1, $CHCl_3$/MeOH), yielding a white amorphous solid (44% yield). ESI-MS m/z 504 $[M+H]^+$. ^1H NMR (300 MHz, CD_3OD) δ 8.71 (s, 1H), 8.46 (d, J = 8.1 Hz, 1H), 7.91 (d, J = 7.9 Hz, 1H), 7.48 (t, J = 7.9 Hz, 1H), 4.69–4.57 (m, 1H), 4.39 (s, 3H), 4.14–3.72 (m, 2H), 2.09–1.51 (m, 5H), 1.44–1.17 (m, 8H), 1.08–0.73 (m, 6H). ^{13}C NMR (101 MHz, CD_3OD) δ 182.1, 174.5, 160.1, 159.7, 157.1, 138.4, 117.1, 108.7,
105.0, 66.5, 66.4, 57.3, 56.6, 53.8, 49.4, 39.9, 31.7, 24.5, 23.0, 22.0, 20.3, 17.7. ESI-HRMS m/z $[M+H]^+$ calcd for $[C_{25}H_{32}ClN_4O_5]^+$ 503.2056, found 503.2062; m/z $[M+Na]^+$ calcd for $[C_{25}H_{31}ClN_4O_5\text{-}Na]^+$ 525.1875, found 525.1876.

4.1.5 | Synthetic procedure for the preparation of compounds 30a–b, 31, and 34

Methyl (S)-2-{(2S,3S)-2-[(tert-butoxycarbonyl)amino]-3-methylpentanamido}-3-((S)-2-oxopyrrolidin-3-yl)propanoate (27): Compound 27 was synthesized according to the general procedures for Boc cleavage and coupling reaction using Boc-Ile-OH as the appropriate carboxylic acid. The crude mixture was purified through SiO_2 column chromatography (30:1, DCM/MeOH), yielding a colorless oil (91% yield). ESI-MS m/z 400 $[M+H]^+$ 422 $[M+Na]^+$. ^1H NMR (300 MHz, $CDCl_3$) δ 7.79 (d, J = 7.1 Hz, 1H), 5.25 (d, J = 6.3 Hz, 1H), 4.16–3.96 (m, 2H), 3.71 (d, J = 3.2 Hz, 3H), 3.32 (d, J = 6.5 Hz, 2H), 2.55–2.28 (m, 2H), 2.22–1.72 (m, 5H), 1.40 (s, 9H), 1.28–1.20 (m, 1H), 0.92 (dd,
J = 9.8, 6.4 Hz, 6H).

Methyl (S)-2-[(2S,3S)-3-methyl-2-(quinoline-8-carboxamido) pentanamido]-3-((S)-2-oxopyrrolidin-3-yl)propanoate (28): Compound 28 was synthesized according to the general procedures for Boc cleavage and coupling reaction using quinoline-8-carboxlic acid as the appropriate carboxylic acid. The mixture was purified by SiO_2 column chromatography (20:1, DCM/MeOH), yielding a colorless oil (66% yield). ESI-MS m/z 455 $[M+H]^+$ 477 $[M+Na]^+$. ^1H NMR (300 MHz, $CDCl_3$) δ 11.88 (d, J = 8.4 Hz, 1H), 8.98 (d, J = 3.9 Hz, 1H), 8.78 (d, J = 7.4 Hz, 1H), 8.26 (d, J = 8.3 Hz, 1H), 7.95 (d, J = 8.1 Hz, 1H), 7.64 (t, J = 7.7 Hz, 1H), 7.48 (dd, J = 7.3, 4.3 Hz, 1H), 7.02–6.55 (m, 1H), 5.00–4.42 (m, 2H), 3.70 (s, 3H), 3.27 (m, 2H), 2.54–2.01 (m, 4H), 1.95–1.59 (m, 2H), 1.47–1.13 (m, 2H), 1.14–0.90 (m, 6H).

General procedure for ester reduction to alcohol exemplified with compound N-((S)-1-{[(S)-1-hydroxy-3-((S)-2-oxopyrrolidin-3-yl)propan-2-yl]amino}-4-methyl-1-oxopentan-2-yl)quinoline-8-carboxamide (29a): In a round-bottom flask, the ester intermediate 10a (60 mg, 1 eq) was solubilized in anhydrous MeOH (0.8 mL, 0.15 M) in a N_2 atmosphere and cooled at 0°C. Then, $NaBH_4$ (40 mg, 8 eq) was carefully added, the reaction mixture was allowed to reach 20°C and stirred for 10 h. Sub-sequently, an aqueous solution of NH_4Cl (1 mL) was slowly added, and the water phase was extracted with EtOAc (3 × 3 mL). The combined organic phase was dried over anhydrous Na_2SO_4, filtered, and con-centrated under vacuum. The crude mixture was then purified by SiO_2 column chromatography (20:1, DCM/MeOH), yielding a white amorphous solid (68% yield). ESI-MS m/z 427 $[M+H]^+$ 449 $[M+Na]^+$.

N-((2S,3S)-1-{[(S)-1-Hydroxy-3-((S)-2-oxopyrrolidin-3-yl)propan-2-yl]amino}-3-methyl-1-oxopentan-2-yl)quinoline-8-carboxamide (29b): Compound 29b was synthesized starting from ester intermediate 28 following the general procedure for ester reduction to alcohol reported previously. The mixture was purified by SiO_2 column chromatography (20:1, DCM/MeOH), yielding a colorless oil (65% yield). ESI-MS m/z 427 $[M+H]^+$ 449 $[M+Na]^+$. ^1H NMR (300 MHz, CD_3OD) δ 11.94 (m, 1H), 9.02 (dd, J = 4.2, 1.7 Hz, 1H),
8.77–8.56 (m, 1H), 8.46 (dd, J = 8.4, 1.6 Hz, 1H), 8.30–8.00 (m, 1H), 7.89–7.45 (m, 2H), 5.48 (s, 1H), 4.69–4.49 (m, 1H), 4.17–3.90 (m, 1H), 3.64–3.39 (m, 2H), 3.23–3.07 (m, 2H), 2.62–2.24 (m, 2H), 2.17–1.93 (m, 2H), 1.80–1.32 (m, 4H), 1.12 –0.95 (m, 6H).

General procedure for the conversion of the alcohol moiety in aldehyde WH exemplified by compound N-((S)-4-methyl-1-oxo-1-{[(S)-1-oxo-3-((S)-2-oxopyrrolidin-3-yl)propan-2-yl]amino}pentan-2-yl)quinoline-8-carboxamide (30a): In a two-necked oven-dried round-bottom flask under a N_2 atmosphere, the alcohol intermediate 29a (36 mg, 1 eq) was solubilized in anhydrous DCM (1.2 mL, 0.07 M) and cooled at 0°C. Then Dess–Martin periodinane (DMP) (286 mg, 8 eq) was added in one portion. The reaction mixture was stirred at 0°C for 30 min, an aqueous solution of $NaHCO_3$ (2 mL) was added, and the water phase was extracted with DCM (3 × 2 mL). The combined organic phase was washed with $Na_2S_2O_3$ (3 × 1 mL) and brine (3 × 1 mL), dried over anhydrous Na_2SO_4, filtered, and concentrated under vacuum. The crude mixture was purified by SiO_2 column chromatography (15:1, DCM/MeOH), yielding a col-orless oil (72% yield). ESI-MS m/z 425 $[M+H]^+$ 447 $[M+Na]^+$. ^1H
NMR (300 MHz, $CDCl_3$) δ 11.67 (d, J = 7.2 Hz, 1H), 9.56 (s, 1H), 8.96 (d, J = 2.5 Hz, 1H), 8.80 (d, J = 7.4 Hz, 1H), 8.29 (d, J = 8.2 Hz, 1H), 7.98 (d, J = 7.9 Hz, 1H), 7.67 (t, J = 7.8 Hz, 1H), 7.51 (dd, J = 8.2, 4.3 Hz, 1H), 4.96–4.81 (m, 1H), 4.62–4.39 (m, 1H), 3.21 (m, 2H), 2.61–1.67 (m, 8H), 1.09–0.88 (m, 6H). ^{13}C NMR (75 MHz, $CDCl_3$) δ 199.7, 172.8, 168.7, 166.2, 149.6, 141.4, 137.8, 133.9, 132.6, 131.4, 127.8, 126.5, 121.0, 94.4, 58.9, 57.5, 40.7, 37.2, 28.3, 25.3, 16.0, 15.1, 11.6. ESI-HRMS m/z $[M+H]^+$ calcd for $[C_{23}H_{29}N_4O_4]^+$ 425.2183, found 425.2168.

N-((2S,3S)-3-Methyl-1-oxo-1-{[(S)-1-oxo-3-((S)-2-oxopyrrolidin-3-yl)propan-2-yl]amino}pentan-2-yl)quinoline-8-carboxamide (30b): The final aldehydic compound 30b was synthesized starting from the alcohol intermediate 29b, following the general procedure for the conversion of the alcohol moiety in aldehyde WH reported previously. The crude mixture was purified by SiO_2 column chro-matography (15:1, DCM/MeOH), (71% yield). ESI-MS m/z 425 $[M+H]^+$ 447 $[M+Na]^+$. ^1H NMR (300 MHz, CD_3OD) δ 12.07–11.81 (m, 1H), 9.53 (s, 1H), 9.02 (dd, J = 4.3, 1.7 Hz, 1H), 8.63 (d, J = 7.3 Hz, 1H), 8.47 (dd, J = 8.3, 1.4 Hz, 1H), 8.12 (dd, J = 11.9, 5.1 Hz, 1H), 7.71 (t, J = 7.8 Hz, 1H), 7.62 (dd, J = 8.3, 4.3 Hz, 2H), 4.68–4.57 (m, 1H), 4.57– 4.43 (m, 1H), 4.08–3.95 (m, 1H), 3.24–3.03 (m, 2H), 2.59–2.01 (m, 3H), 1.84–1.33 (m, 4H), 1.16–0.95 (m, 6H). ^{13}C NMR (75 MHz, CD_3OD) δ 181.3, 172.8, 166.6, 149.9, 145.3, 137.8, 132.8, 132.5, 128.7, 128.0, 126.0, 121.3, 98.2, 59.1, 51.5, 40.0, 38.0, 37.3, 29.1, 27.4, 24.9, 14.9, 10.4. ESI-HRMS m/z $[M+H]^+$ calcd for $[C_{23}H_{29}N_4O_4]$ 425.2183, found 425.2193.

N-((2S,3 R)-1-{[(1 R/S,2S)-1-Cyano-1-hydroxy-3-((S)-2-oxopyrrolidin-3-yl)propan-2-yl]amino}-3-methyl-1-oxopentan-2-yl)quinoline-8-carboxamide (R/S-31): In a round-bottom flask, the final compound 30b (30 mg, 1 eq) was solubilized in DCM (1.3 mL, 0.05 M), and then an aqueous solution (8 M) of $NaHSO_3$ (10 mg, 1.3 eq) was added drop by drop. The reaction mixture was stirred at 20°C for 30 min, and then an aqueous solution (1.6 M) of KCN (5.5 mg, 1.2 eq) was slowly added. The reaction mixture was stirred at 20°C for 12 h. Then, the reaction mixture was extracted with DCM (3 × 2 mL), and the organic phase was dried over anhydrous Na_2SO_4, filtered, and concentrated under vacuum. The crude mixture was purified by SiO_2 column chromatography (20:1, DCM/MeOH), yielding a colorless oil (63% yield). ESI-MS m/z 452 $[M+H]^+$ 474 $[M+Na]^+$. ^{1}H NMR (300 MHz, CD_3OD) δ 9.02 (d, J = 4.0 Hz, 1H), 8.65 (d, J = 6.8 Hz, 1H), 8.47 (d, J = 7.0 Hz, 1H), 8.14 (d, J = 8.0 Hz, 1H), 7.72 (t, J = 7.8 Hz, 1H), 7.62 (dd, J = 8.3, 4.3 Hz, 1H), 4.70–4.43 (m, 1H), 4.29–4.16 (m, 1H), 3.26–3.06 (m, 2H), 2.67–1.99 (m, 4H), 1.88–1.36 (m, 4H), 1.17–0.95 (m, 6H). ^{13}C NMR (75 MHz, CD_3OD) δ 181.3, 180.9, 173.2, 172.8, 166.6, 149.9, 145.3, 137.9, 132.9, 132.6, 128.7, 126.0, 121.3, 98.2, 59.2, 40.0, 38.0, 37.3, 29.3, 29.1, 27.4, 24.9, 15.0, 10.3. ESI-HRMS m/z $[M+H]^+$ calcd for $[C_{24}H_{30}N_5O_4]^+$ 452.2292; found 452.2287; m/z $[M+Na]^+$ calcd for $[C_{24}H_{29}N_5O_4Na]^+$ 474.2112 found, 474.2106.

tert-Butyl ((S)-1-{[(S)-1-hydroxy-3-((S)-2-oxopyrrolidin-3-yl)propan-2-yl]amino}-4-methyl-1-oxopentan-2-yl)carbamate (32): Compound 32 was synthesized starting from ester intermediate 9a following the general procedure for ester reduction to alcohol reported previously. The mixture was used without any further purification, yielding a colorless oil (46% yield). ESI-MS m/z 372 $[M+H]^+$ 394 $[M+Na]^+$. ESI- MS m/z 371 $[M+H]^+$. ^{1}H NMR (400 MHz, $CDCl_3$) δ 7.35–7.24 (m, 1H), 6.43 (s, 1H), 5.17–5.00 (m, 1H), 4.31–4.15 (m, 1H), 3.38–3.26 (m, 2H), 3.21 (m, 1H), 2.44–2.31 (m, 2H), 2.16–1.93 (m, 1H), 1.83–1.73 (m, 1H), 1.71–1.44 (m, 5H), 1.40 (s, 9H), 0.90 (d, J = 6.4 Hz, 6H).

8-Chloro-N-((S)-1-{[(S)-1-hydroxy-3-((S)-2-oxopyrrolidin-3-yl)propan-2-yl]amino}-4-methyl-1-oxopentan-2-yl)-1-methyl-4-oxo-1,4-dihydroquinoline-3-carboxamide (33): Compound 33 was synthesized according to the general procedures for Boc cleavage and coupling reaction using 8-chloro-1-methyl-4-oxo-1,4-dihydroquinoline-3-carboxylic acid as the appropriate carboxylic acid. The mixture was purified by SiO_2 column chromatography (30:1, DCM/MeOH), yielding a colorless oil (41% yield). ESI-MS m/z 492 $[M+H]^+$ 514 $[M+Na]^+$. ^{1}H NMR (300 MHz, CD_3OD) δ 8.85 (s, 1H), 8.49 (d, J = 9.4 Hz, 1H), 8.00 (d, J = 7.7 Hz, 1H), 7.56 (t, J = 7.9 Hz, 1H), 4.66–4.50 (m, 1H), 4.46 (s, 3H), 4.09–3.92 (m, 1H), 3.61–3.37 (m, 2H), 3.03–2.91 (m, 1H), 2.57–2.20 (m, 3H), 2.09–1.46 (m, 6H), 1.06–0.85 (m, 6H).

8-Chloro-1-methyl-N-((S)-4-methyl-1-oxo-1-{[(S)-1-oxo-3-((S)-2-oxopyrrolidin-3-yl)propan-2-yl]amino}pentan-2-yl)-4-oxo-1,4-dihydroquinoline-3-carboxamide (34): The final aldehydic compound 34 was synthesized starting from the alcohol intermediate 33, following the general procedure for the conversion of the alcohol moiety in aldehyde WH reported previously. The crude mixture was purified by SiO_2 column chromatography (30:1, DCM/MeOH), (36% yield). ESI-MS m/z 490 $[M+H]^+$ 512 $[M+Na]^+$. ^{1}H NMR (300 MHz, CD_3OD) δ 10.34 (d, J = 7.2 Hz, 1H), 9.50 (s, 1H), 8.71 (d, J = 3.1 Hz, 1H), 8.45 (d, J = 8.3 Hz, 1H), 7.84 (d, J = 8.1 Hz, 1H), 7.71–7.60 (m, 1H), 7.47 (t, J = 7.9 Hz, 1H), 7.34 (d, J = 8.8 Hz, 1H), 4.67–4.43 (m, 2H), 4.39 (s, 3H), 3.26–3.16 (m, 2H), 2.36 (m, 3H), 1.91–1.47 (m, 5H), 1.00 (dd, J = 12.6, 6.2 Hz, 6H). ^{13}C NMR (101 MHz, CD_3OD) δ 181.4, 175.7, 173.7, 164.9, 152.3, 137.7, 136.7, 130.5, 126.0, 122.6, 110.6, 98.1, 78.1, 52.2, 51.3, 41.1, 40.1, 38.0, 29.9, 29.5, 27.5, 24.8, 22.1, 20.9.

4.2 | Protein expression and purification

Plasmid expressing SARS-CoV-2 M^{pro} (ORF1ab polyprotein residues 3264-3569, GenBank code: MN908947.3) was a gift from Prof. Rolf Hilgenfeld and the protein was purified according to reference[26], with minor modifications.

Culture ad lysis: overnight pre-inoculation of Escherichia coli BL21 ΔE3 cells in 20 mL of Luria broth (LB) medium with 100 mg/mL ampicillin was inoculated to a 2 L culture until OD_{600} = 0.6 at 37°C, followed by overnight induction at 16°C with 0.5 mM Isopropil-β-D-1-tiogalattopiranoside. Cells were then collected by centrifugation and pellets were stored at –80°C. The cell pellet (~15 g) was resuspended in 45 mL of Buffer A (20 mM Tris Cl, pH 8.0, 300 mM NaCl), 1× protease inhibitor cocktail (Merck S8820), 1 mg/mL lysozyme, and 1 mM phe-nylmethylsulfonyl fluoride. Lysated bacteria were then sonicated in an ice bath until the cell lysate became clear. Finally, 20 µL of Dnase 10 U/µL was added and the cell lysate was left under rotation for 15 min at 4°C prior to centrifugation at 20,000 rpm (HITACHI, rotor R20A2 rotor) for 45 min to retrieve the supernatant. Purification: ~40 mL of supernatant was loaded onto 1 mL of a His-Trap HP (GE) affinity chromatography column, washing with 10 CV of Buffer A and 10 CV of 10% Buffer B (20 mM TrisCl, pH 8.0, 300 mM NaCl, 300 mM imidazole). Two steps of elution were performed using 25% and 100% of Buffer B. Eluted histidine-tagged M^{pro} was (uncut) concentrated in 1 mL in Storage Buffer (50 mM TrisCl, pH 7.3, 75 mM NaCl, 1 mM ethylendiaminetetracetic acid (EDTA), 1 mM DTT) using a 30 MWCO concentrator. The histidine tag was removed by adding 200 µL of 40 µM HRV3C in HRV-3C Cut Buffer 3X (Tris Cl 150 mM, pH 8.0, NaCl 900 mM, Glycerol 5%, DTT 3 mM). The digestion reaction was left under rotation for 16 h at +4°C. Histidine-free M^{pro} was then diluted in a Storage Buffer, loaded on a second 1 mL HisTrap HP, collected as flow-through, concentrated to 1 mL in the Storage Buffer, and stored at –80°C.

4.3 | Protease assay

Compounds' activity was evaluated in vitro using a FRET assay. Peptide substrate HiLyte Fluor488–ESATLQSGLRKAK–QXL520-NH2 was pur-chased from Anaspec and used as an M^{pro} substrate. Substrate cleavage was monitored by applying an excitation wavelength filter at 475 nm and an emission wavelength filter at 500–550 nm on a Glomax Discover Microplate reader (Promega). Reactions were performed for 30 min at 30°C using 0.5 µM M^{pro}, 2 µM, or 4 µM peptide substrate, 20 mM hydroxyethylpiperazine ethane sulfonic acid, pH 7.5, 150 mM NaCl, 4%

glycerol, 2 mM DTT, 0.4 mM EDTA, and 5% DMSO in a final volume of 50 µL in a black 384-well plate (Perkin Elmer). GraphPad Prism 5.0 was used to determine IC_{50} values according to the following equation:

$$v = V[1 + (I/IC_{50})],$$

where v is the enzyme velocity of the reaction, V is the apparent enzyme velocity in the absence of inhibitors, I is the inhibitor con-centration, and IC_{50} is the inhibitor concentration that determines 50% reduction of V.

Apparent affinity (K_m) for the peptidic substrate was calculated according to the Michaelis–Menten method and was 2.36 ± 0.51 µM. K_i values were calculated according to the Cheng–Prusoff equation:

$$K_i = IC_{50}/(1 + [S]/K_m),$$

where K_i represents the inhibitory constant, defined as the equilibrium concentration of an inhibitory ligand when 50% of the receptor sites are occupied if no competing substrate is present, and [S] is the peptide concentration.

4.4 | Crystallization and structure determination

Purified M^{pro} protein was concentrated to 50 mg/mL and mixed 1:1 with a 6 mM stock of compound 30a to yield a final protein and compound concentration of 25 mg/mL and 3 mM, respectively. The protein–compound mixture was incubated on ice for 1 h before setting up the crystallization plates. The crystallization reaction was initiated by mixing 1 mL of the protein–compound mixture and 1 mL of reservoir solution in a sitting-drop configuration. Plates were sealed and incubated at 17°C. Crystals appeared within 1 week under the following conditions: 22%–27% PEG1500 and 100 mM MTT buffer [DL-Malic acid, 4-Morpholine Ethane Sulfonic acid (MES) monohydrate, and 2-amino-2-(hydroxymethyl)-1,3-propanediol (TRIS)-HCl), pH=6.0]. Crystals were cryoprotected with 30% PEG1500, 100 mM MTT buffer, and 20% glycerol and flash-frozen in liquid nitrogen. Several data sets were collected at ESRF (European Synchrotron Radiation Facility) beamline ID23-2. The best diffracting crystal achieved a visual resolution of about 2 Å was used for further processing. Collected images were processed with XDS,[27] merged with Aimless,[28] and refined with several cycles of REFMAC[29] and PHENIX[26] with manual rebuilding in COOT.[30] The refined structure was optimized with PDB_REDO[31] and diffracted at 1.9 Å resolution with an R/Rfree value of 0.263/0.296 with excellent geometry (Supporting Information S2: Table S1).

| Molecular modeling studies

| Protein and ligand preparation

the included drawing tools in the Maestro molecular modeling environment (Maestro release 2020, Schrödinger, LLC, 2020), peptide-based derivatives were generated as described previously.[14,32,33] MacroModel (MacroModel release 2020, Schrödinger, LLC, 2020) software was used to minimize the energy of the designed com-pounds using OPLS3 as the force field.[34] Subsequently, LigPrep appli-cation (LigPrep release 2020, Schrödinger, LLC, 2020) was used to obtain the probable ionization state of compounds at pH 7.4 ± 0.2 to mimic physiological conditions. The generalized born surface area (GBSA) model was used with "no cutoff" for nonbonded interactions to mimic solvent effects. The potential energy was minimized using the Polak-Ribiere conjugate gradient) method (5000 maximum iterations and threshold for gradient convergence = 0.001). The experimental structure of the SARS- CoV-2 M^{pro} enzyme in complex with inhibitor 30a was experimentally solved and used for computational investigation in this study (PDB ID 9GF7). The mentioned structure was optimized for in silico analysis. In particular, the covalent bond between C145 and the aldehyde WH of compound 30a was broken to restore the native arrangement of the protein. Furthermore, according to the literature data[35,36], C145 was deprotonated and the resulting structure was refined using the Protein Preparation Wizard protocol accessible in Maestro to obtain a reasonable starting structure for further computational studies, as described previously.[14,37]

4.5.2 | Molecular docking

Docking studies were conducted in Maestro using Glide software (Glide release 2020, Schrödinger, LLC, 2020) with standard precision SP scoring as described by us recently.[14] The default values for preparing the en-ergy grid for docking were used (1.0 Å for protein atom-scaling factor), and the crystallized ligand was used to generate the calculation box. The docked solutions selected for the post-docking minimization procedure were 1000. In addition, using the Prime/MM-GBSA technique, we estimated the ligand binding energy for each complex originating from molecular docking studies (Prime release 2020, Schrödinger, LLC, 2020). This technique computes the variation between the free and complex states of both the ligand and the enzyme after energy minimization.[14]

4.6 | Cell-based assays and

To determine the anti-SARS-CoV-2 activity of the candidate com-pounds, a live virus cell-based assay was performed adapting a pre-viously published protocol.[38] Briefly, the VERO E6 monkey cell line (ATCC® CRL-1586) was used to determine the cytotoxicity and the antiviral activity of the candidate compounds. Cells were propagated in Dulbecco's modified eagle medium High-Glucose medium (Euroclone) supplemented with 10% fetal bovine serum (FBS) and 1% 4.5 streptomycin/penicillin (PS) (Euroclone) in a humidified incubator at 37°C with 5% CO_2. VERO E6 cells were pretreated with 0.5 µM CP- 4.5.1 100356 hydrochloride inhibitor to reduce the efflux activity of P-gp, which is overexpressed by this cell line. The SARS-CoV-2 delta var-Using iant (GISAID code EPI_ISL_2840619) used for the experiments was expanded in VERO E6 cells and titrated as described previously.[38]

To determine the cytotoxicity of all investigated compounds, cells viability was calculated using the CellTiter Glo 2.0 Luminescent Cell Viability Assay (Promega); luminescence values were measured using the GloMax® Discover Multimode Microplate Reader (Promega) and elaborated with GraphPad PRISM software version 9.0. The half-maximal cytotoxic concentration (CC_{50}) and the com-pound concentration allowing 90% cell viability (CC_{10}) were calcu-lated using a nonlinear regression analysis of the dose–response curves and the ECanything GraphPad function. The CC_{10} was used for each compound as the starting concentration in the antiviral activity assay.

To determine the antiviral activity of each compound against delta SARS-CoV-2, we performed a direct yield reduction assay, based on the infection of cells in the presence of serial drug dilutions. The day before the infection, 10.000 VERO E6 cells per well were preseeded on 96-well adhesion plates to ensure 70% confluence on the day of infection. Cells were treated with fourfold decreasing concentrations of each candidate compound and after a 1 h incuba-tion at 37°C with 5% CO_2, cells were infected at 0.001 multiplicity of infection (MOI). After 24 h incubation, the antiviral activity was measured on the cell monolayer by measuring the nucleocapsid ex-pression with an immunodetection assay, adapting a previously published protocol,[39] calculated using a nonlinear fit normalization curve (GraphPad 6.01) and expressed as the half-maximal effective concentration (EC_{50}). Each experiment was performed in at least two independent runs including a mock infection control, a virus back titration, and the licensed M^{pro} inhibitor NRM (cat. HY-138687) as the reference compound.

ACKNOWLEDGMENTS

This research was supported by EU funding within the NextGen-eration EU-MUR PNRR Extended Partnership initiative on Emerging Infectious Diseases (Project no. PE00000007,INF-ACT). Si. Bro. (UniPI) was a recipient of INF-ACT Cascade Open Call 2023 (COC- 1-2023-CNR). This research was supported by the Project of National Interest PRIN 2022TLZRXT - DEFENCE to G.M. This research was supported in part by "Fondo di Beneficenza di Intesa Sanpaolo" (Grant Number B/2020/0113). This project was partly funded by the AVITHRAPID project, European Union HORIZON- HLTH-2023-DISEASE-03-04 grant agreement No 101137192. E.C. was supported by the Italian Association for Cancer Research (AIRC IG 24448).

CONFLICT OF INTEREST STATEMENT

The authors declare no conflicts of interest.

DATA AVAILABILITY STATEMENT

The data that support the findings of this study are available from the corresponding author upon reasonable request.

ORCID

Mariachiara Pieroni https://orcid.org/0009-0004-5014-6961
https://orcid.org/0000-0002-1619-3295
Simone Brogi http://orcid.org/0000-0001-9375-6242
Sandra Gemma http://orcid.org/0000-0002-8313-2417
Giuseppe Campiani https://orcid.org/0000-0001-5295-9529

REFERENCES

[1] B. Hu, H. Guo, P. Zhou, Z. L. Shi, Nat. Rev. Microbiol. 2021, 19, 141. [2] J. Cui, F. Li, Z. L. Shi, Nat. Rev. Microbiol. 2019, 17, 181.
[3] G. La Monica, A. Bono, A. Lauria, A. Martorana, J. Med. Chem. 2022, 65, 12500.
[4] B. Halford, ACS Cent. Sci. 2022, 8, 405.
[5] D. R. Owen, C. M. N. Allerton, A. S. Anderson, L. Aschenbrenner, M. Avery, S. Berritt, B. Boras, R. D. Cardin, A. Carlo, K. J. Coffman, A. Dantonio, L. Di, H. Eng, R. Ferre, K. S. Gajiwala, S. A. Gibson, S. E. Greasley, B. L. Hurst, E. P. Kadar, A. S. Kalgutkar, J. C. Lee, J. Lee, W. Liu, S. W. Mason, S. Noell, J. J. Novak, R. S. Obach, K. Ogilvie, N. C. Patel, M. Pettersson, D. K. Rai, M. R. Reese, M. F. Sammons, J. G. Sathish, R. S. P. Singh, C. M. Steppan, A. E. Stewart, J. B. Tuttle, L. Updyke, P. R. Verhoest, L. Wei, Q. Yang, Y. Zhu, Science 2021, 374, 1586.
[6] X. Li, Y. Song, Eur. J. Med. Chem. 2023, 260, 115772.
[7] X. Liu, X. Ren, M. Hua, F. Liu, X. Ren, C. Sui, Q. Li, F. Luo, Z. Jiang, Z. Xia, J. Chen, B. Yang, Chem. Biol. Drug Des. 2024, 103, e14425.
[8] X. Jiang, H. Su, W. Shang, F. Zhou, Y. Zhang, W. Zhao, Q. Zhang, H. Xie, L. Jiang, T. Nie, F. Yang, M. Xiong, X. Huang, M. Li, P. Chen, S. Peng, G. Xiao, H. Jiang, R. Tang, L. Zhang, J. Shen, Y. Xu, Nat. Commun. 2023, 14, 6463.
[9] B. Cao, Y. Wang, H. Lu, C. Huang, Y. Yang, L. Shang, Z. Chen, R. Jiang, Y. Liu, L. Lin, P. Peng, F. Wang, F. Gong, H. Hu, C. Cheng, X. Yao, X. Ye, H. Zhou, Y. Shen, C. Liu, C. Wang, Z. Yi, B. Hu, J. Xu, X. Gu, J. Shen, Y. Xu, L. Zhang, J. Fan, R. Tang, C. Wang, N. Engl. J. Med. 2024, 390, 230.
[10] Y. Y. Syed, Drugs 2024, 84, 721.
[11] A. Citarella, D. Gentile, A. Rescifina, A. Piperno, B. Mognetti, G. Gribaudo, M. T. Sciortino, W. Holzer, V. Pace, N. Micale, Int. J. Mol. Sci. 2021, 22. 1398.
[12] S. Brogi, R. Ibba, S. Rossi, S. Butini, V. Calderone, S. Gemma, G. Campiani, Molecules 2022, 27, 2561.
[13] C. Ma, M. D. Sacco, B. Hurst, J. A. Townsend, Y. Hu, T. Szeto, X. Zhang, B. Tarbet, M. T. Marty, Y. Chen, J. Wang, Cell Res. 2020, 30, 678.
[14] S. Brogi, S. Rossi, R. Ibba, S. Butini, V. Calderone, G. Campiani, S. Gemma, Computation 2022, 10, 69.
[15] R. Cannalire, C. Cerchia, A. R. Beccari, F. S. Di Leva, V. Summa, J. Med. Chem. 2022, 65, 2716.
[16] C. Capasso, A. Nocentini, C. T. Supuran, Expert Opin. Ther. Pat. 2021, 31, 309.
[17] Z. Jin, X. Du, Y. Xu, Y. Deng, M. Liu, Y. Zhao, B. Zhang, X. Li, L. Zhang, C. Peng, Y. Duan, J. Yu, L. Wang, K. Yang, F. Liu, R. Jiang, X. Yang, T. You, X. Liu, X. Yang, F. Bai, H. Liu, X. Liu, L. W. Guddat, W. Xu, G. Xiao, C. Qin, Z. Shi, H. Jiang, Z. Rao, H. Yang, Nature 2020, 582, 289.
[18] S. Richter, C. Parolin, M. Palumbo, G. Palu, Curr. Drug Target -Infect. Disord. 2004, 4, 111.
[19] Y. S. Shin, J. Y. Lee, S. Jeon, S. Myung, H. J. Gong, S. Kim, H. R. Kim, L. S. Jeong, C. M. Park, Bioorg. Med. Chem. Lett. 2023, 85, 129214.
[20] S. Gemma, C. Camodeca, S. Sanna Coccone, B. P. Joshi, M. Bernetti, V. Moretti, S. Brogi, M. C. Bonache de Marcos, L. Savini, D. Taramelli, N. Basilico, S. Parapini, M. Rottmann, R. Brun, S. Lamponi, S. Caccia, G. Guiso, R. L. Summers, R. E. Martin, S. Saponara, B. Gorelli, E. Novellino, G. Campiani, S. Butini, J. Med. Chem. 2012, 55, 6948.
[21] P. Kushwaha, Curr. Top. Med. Chem. 2024, 24, 2377.
[22] H. Wang, R. Pei, X. Li, W. Deng, S. Xing, Y. Zhang, C. Zhang, S. He, H. Sun, S. Xiao, J. Xiong, Y. Zhang, X. Chen, Y. Wang, Y. Guo, B. Zhang, L. Shang, Eur. J. Med. Chem. 2022, 238, 114458.
[23] I. Stefanelli, A. Corona, C. Cerchia, E. Cassese, S. Improta, E. Costanzi, Gabriele Carullo S. Pelliccia, S. Morasso, F. Esposito, A. Paulis, S. Scognamiglio,

F. S. Di Leva, P. Storici, M. Brindisi, E. Tramontano, R. Cannalire, V. Summa, Eur. J. Med. Chem. 2023, 253, 115311.

[24] H. Chen, W. Jiao, M. A. Jones, J. M. Coxon, J. D. Morton, R. Bickerstaffe, A. D. Pehere, O. Zvarec, A. D. Abell, Chem. Biodiversity 2012, 9, 2473.

[25] A. M. Krieg, R. Subramanian, J. McSwiggen, J. T. Lee, RaNa Therapeutics, Inc., 2015.

[26] P. D. Adams, P. V. Afonine, G. Bunkóczi, V. B. Chen, I. W. Davis, N. Echols, J. J. Headd, L. W. Hung, G. J. Kapral, R. W. Grosse- Kunstleve, A. J. McCoy, N. W. Moriarty, R. Oeffner, R. J. Read, D. C. Richardson, J. S. Richardson, T. C. Terwilliger, P. H. Zwart, Acta Crystallogr. D. Biol. Crystallogr. 2010, 66, 213.

[27] W. Kabsch, Acta Crystallogr. D. Biol. Crystallogr. 2010, 66, 125. [28] J. Agirre, M. Atanasova, H. Bagdonas, C. B. Ballard, A. Baslé, J. Beilsten-Edmands, R. J. Borges, D. G. Brown, J. J. Burgos-Mármol, J. M. Berrisford, P. S. Bond, I. Caballero, L. Catapano, G. Chojnowski, A. G. Cook, K. D. Cowtan, T. I. Croll, J. É. Debreczeni, N. E. Devenish, E. J. Dodson, T. R. Drevon, P. Emsley, G. Evans, P. R. Evans, M. Fando, J. Foadi, L. Fuentes-Montero, E. F. Garman, M. Gerstel, R. J. Gildea, K. Hatti, M. L. Hekkelman, P. Heuser, S. W. Hoh, M. A. Hough, H. T. Jenkins, E. Jiménez, R. P. Joosten, R. M. Keegan, N. Keep, E. B. Krissinel, P. Kolenko, O. Kovalevskiy, V. S. Lamzin, D. M. Lawson, A. A. Lebedev, A. G. W. Leslie, B. Lohkamp, F. Long, M. Malý, A. J. McCoy, S. J. McNicholas, A. Medina, C. Millán, J. W. Murray, G. N. Murshudov, R. A. Nicholls, M. E. M. Noble, R. Oeffner, N. S. Pannu, J. M. Parkhurst, N. Pearce, J. Pereira, A. Perrakis, H. R. Powell, R. J. Read, D. J. Rigden, W. Rochira, M. Sammito, F. Sánchez Rodríguez, G. M. Sheldrick, K. L. Shelley, F. Simkovic, A. J. Simpkin, P. Skubak, E. Sobolev, R. A. Steiner, K. Stevenson, I. Tews, J. M. H. Thomas, A. Thorn, J. T. Valls, V. Uski, I. Usón, A. Vagin, S. Velankar, M. Vollmar, H. Walden, D. Waterman, K. S. Wilson, M. D. Winn, G. Winter, M. Wojdyr, K. Yamashita, Acta Crystallogr. D Struct. Biol. 2023, 79, 449.

[29] G. N. Murshudov, P. Skubák, A. A. Lebedev, N. S. Pannu, R. A. Steiner, R. A. Nicholls, M. D. Winn, F. Long, A. A. Vagin, Acta Crystallogr. D. Biol. Crystallogr. 2011, 67, 355.

[30] P. Emsley, K. Cowtan, Acta Crystallogr. D. Biol. Crystallogr. 2004, 60, 2126.

[31] R. P. Joosten, F. Long, G. N. Murshudov, A. Perrakis, IUCrJ 2014, 1, 213.

[32] S. Brogi, S. Giovani, M. Brindisi, S. Gemma, E. Novellino, G. Campiani, M. J. Blackman, S. Butini, J. Mol. Graph. Model. 2016, 64, 121.

[33] S. Giovani, M. Penzo, S. Brogi, M. Brindisi, S. Gemma, E. Novellino, L. Savini, M. J. Blackman, G. Campiani, S. Butini, Bioorg. Med. Chem. Lett. 2014, 24, 3582.

[34] W. L. Jorgensen, D. S. Maxwell, J. Tirado-Rives, J. Am. Chem. Soc. 1996, 118, 11225.

[35] L. Polgár, Eur. J. Biochem. 1973, 33, 104.

[36] D. W. Kneller, G. Phillips, K. L. Weiss, S. Pant, Q. Zhang, H. M. O'Neill, L. Coates, A. Kovalevsky, J. Biol. Chem. 2020, 295, 17365.

[37] C. C. Maquiaveli, J. F. Lucon-Júnior, S. Brogi, G. Campiani, S. Gemma, P. C. Vieira, E. R. Silva, J. Nat. Prod. 2016, 79, 1459.

[38] L. Fiaschi, C. Biba, I. Varasi, N. Bartolini, C. Paletti, F. Giammarino, F. Saladini, M. Zazzi, I. Vicenti, Viruses 2024, 16, 168.

[39] I. Vicenti, M. G. Martina, A. Boccuto, M. De Angelis, G. Giavarini, F. Dragoni, S. Marchi, C. M. Trombetta, E. Crespan, G. Maga, C. Eydoux, E. Decroly, E. Montomoli, L. Nencioni, M. Zazzi, M. Radi, Eur. J. Med. Chem. 2021, 224, 113683.

SUPPORTING INFORMATION

Additional supporting information can be found online in the Supporting Information section at the end of this article.

How to cite this article: S. Rossi, G. Deidda, L. Fiaschi, R. Ibba, M. Pieroni, M. Dichiara, G. Carullo, S. Butini, A. Ramunno, S. Brogi, M. Lolicato, C. Arrigoni, N. Cabella, L. Bavagnoli, G. Maga, I. Varasi, C. Biba, I. Vicenti, S. Gemma, E. Crespan, M. Zazzi, G. Campiani, Arch. Pharm. 2025, 358, e2400812. https://doi.org/10.1002/ardp.202400812

viruses

MDPI

Article

A Comparison of Sanger Sequencing and Amplicon-Based Next Generation Sequencing Approaches for the Detection of HIV-1 Drug Resistance Mutations

Camilla Biba †, Lia Fiaschi †, Ilenia Varasi, Chiara Paletti, Niccolò Bartolini, Maurizio Zazzi, Ilaria Vicenti * and Francesco Saladini

Department of Medical Biotechnologies, University of Siena, 53100 Siena, Italy; camilla.biba@student.unisi.it (C.B.); lia.fiaschi@unisi.it (L.F.); ilenia.varasi@student.unisi.it (I.V.); c.paletti@student.unisi.it (C.P.); niccolo.bartolini@student.unisi.it (N.B.); zazzi@unisi.it (M.Z.); saladini6@unisi.it (F.S.)

* Correspondence: vicenti@unisi.it

† These authors contributed equally to this work.

Abstract: Background: Next-generation sequencing (NGS) kits are needed to finalise the transition from Sanger sequencing to NGS in HIV-1 genotypic drug resistance testing. Materials and Methods: We compared a homemade NGS amplicon-based protocol and the AD4SEQ HIV-1 Solution v2 (AD4SEQ) NGS kit from Arrow Diagnostics for identifying resistance-associated mutations (RAMs) above the 5% threshold in 27 plasma samples where Sanger sequencing previously detected at least one RAM. Results: The samples had a median 4.9 log [IQR 4.6–5.2] HIV-1 RNA copies/mL and were mostly subtype B (59%) and CRF02_AG (15%). Homemade NGS had a lower rate of samples with low-coverage regions (2/27) compared with AD4SEQ (13/27) ($p < 0.001$). Homemade NGS and AD4SEQ identified additional mutations with respect to Sanger sequencing in 12/27 and 9/27 samples, respectively. However, there were two and eight cases where mutations detected by Sanger sequencing were missed by homemade NGS and AD4SEQ-SmartVir, respectively. The discrepancies between NGS and Sanger sequencing resulted in a few minor differences in drug susceptibility interpretation, mostly for NNRTIs. Conclusions: Both the NGS systems identified additional mutations with respect to Sanger sequencing, and the agreement between them was fair. However, AD4SEQ should benefit from technical adjustments allowing higher sequence coverage.

Keywords: HIV genotype; drug resistance mutations; NGS; antiretroviral

Citation: Biba, C.; Fiaschi, L.; Varasi, I.; Paletti, C.; Bartolini, N.; Zazzi, M.; Vicenti, I.; Saladini, F. A Comparison of Sanger Sequencing and Amplicon-Based Next Generation Sequencing Approaches for the Detection of HIV-1 Drug Resistance Mutations. Viruses 2024, 16, 1465. https://doi.org/10.3390/v16091465

Academic Editor: Thomas Klimkait

Received: 22 August 2024
Revised: 10 September 2024
Accepted: 13 September 2024
Published: 14 September 2024
Corrected: 29 July 2025

1. Introduction

In recent years, advances in antiretroviral therapy (ART) have significantly improved the life expectancy for people living with HIV (PLWH). Indeed, several drugs targeting different steps of the HIV-1 replication cycle are now available, with improved convenience, reduced toxicity and higher genetic barrier, while several other investigational antiretro-virals have shown promising results in clinical trials [1]. Despite these improvements, all the currently available drugs, including those belonging to the newer classes, are at risk of losing their full efficacy due to emergence of resistance mutations, thus compromising the success of long-term therapy [2]. Indeed, real-world evidence shows that even the second-generation integrase inhibitor dolutegravir, which is recommended by the WHO as the preferred drug for first-line and second-line ART in all populations due to its high genetic barrier to resistance [3], can occasionally lead to the selection of resistance mutations within integrase, particularly in the presence of nucleoside reverse transcriptase inhibitor resistance [4]. For these reasons, the international guidelines recommend the execution of HIV-1 genotypic tests on viral RNA to evaluate transmitted and acquired drug resistance at HIV diagnosis and at treatment failure, respectively (EACS guidelines v12.0).

Dideoxynucleoside Sanger sequencing has been the standard method for HIV-1 drug resistance testing in clinical settings over the last two decades [5]. Despite widespread use and clinical effectiveness, Sanger sequencing identifies the predominant HIV-1 quasispecies but fails to detect mutations occurring at frequencies lower than 20–30% of the viral population [6]. This limitation has been overcome with the advent of next-generation sequencing (NGS). NGS can detect mutations that occur at frequencies lower than 5% with an accuracy greater than 99% [7]. NGS includes different applications that allow the sequencing of specific genomic fragments as well as of the whole virus genome [8]. Thus, most laboratories are transitioning from Sanger sequencing to NGS for HIV-1 genotypic drug resistance testing. While NGS platforms and chemistry are evolving at a fast pace, Illumina NGS technology, based on sequencing by synthesis, has gained widespread popularity due to low error rates [9] and high throughput with a relatively simple workflow at a reasonable cost [10]. However, until a few years ago, most NGS platforms were certified for research use only and thus were not suitable for clinical diagnostic applications. Recently,
three NGS systems have been approved by the FDA for HIV-1 genotypic resistance testing in a diagnostic setting: the Sentosa® SQ HIV Genotyping Assay by Vela Diagnostics (The Kendall, Singapore), the DeepChek® Assay HIV-1 Full PR/RT/INT Drug Resistance system by ABL Diagnostics (Woippy, France) and the AD4SEQ HIV-1 Solution v2 by Arrow Diagnostics (Genoa, Italy). While the Sentosa® assay is based on Ion Torrent technology (PMID: 35269868), both the assays by Arrow Diagnostics and ABL Diagnostics are based on Illumina technology. The aim of this study was to compare the sensitivity of the latter two NGS methods in identifying resistance-associated mutations (RAMs) detected by Sanger sequencing in clinical HIV-1 samples.

2. Materials and Methods

2.1. Samples

Access to residual anonymised plasma samples derived from clinical practice was initially obtained through patients' informed consent as approved by the local Ethics Com-mittee at the University Hospital of Siena. A total of 27 HIV-1 viremic plasma samples with a previous Sanger sequencing-based genotypic resistance test performed at the Micro-biology and Virology Unity of the University Hospital of Siena, Italy, were selected. All samples had at least one RAM to protease inhibitors (PIs), nucleoside and non-nucleoside reverse transcriptase inhibitors (NRTIs and NNRTIs) or integrase inhibitors (INIs). The viral load of each sample was available as quantified by the Cobas® 6800 system (Roche Diagnostic, Basel, Switzerland) for routine testing.

2.2. HIV-1 RNA Extraction and Amplification

Viral RNA was extracted from 1 mL of plasma with the eMAG automated system (bioMérieux, Craponne, France). HIV-1 RNA extracts were reverse-transcribed with the ImProm-II Reverse Transcriptase (Promega, Madison, WI, USA). Two consecutive PCR reactions (outer and inner PCR, Table 1) were performed to amplify the reverse transcriptase (RT, amino acids 1-400), the whole protease (PR) and the whole integrase (IN) coding regions. The outer PCR included 5 µL of cDNA, 10 µL of 5× Colourless GoTaq® Flexi buffer (Promega, Madison, WI, USA), 2.5 mM $MgCl_2$, 80 µM dNTPs, 3 pmol of primers (Table 1), 1 U of GoTaq® Flexi DNA Polymerase (Promega, Madison, WI, USA) and sterile DNAse-/RNAse-free water to a final volume of 50 µL. The thermal profile included a denaturation step of 4 min at 95 °C followed by 5 cycles of 56 °C for 30 s, 68 °C for 2 min and 95 °C for 40 s, 25 cycles of 54 °C for 30 s, 68 °C for 2 min and 95 °C for 40 s and then two final steps at 54 °C for 1 min and 68 °C for 8 min. A total of 2 µL of the outer PCR mixture was used as the template for the nested PCR including 6 µL of 5× Green GoTaq® Flexi Buffer, 2.5 mM $MgCl_2$, 80 µM dNTPs, 3 pmol of primers (Table 1), 1 U of GoTaq® Flexi DNA Polymerase and sterile DNAse-/RNAse-free water to a final volume of 30 µL. The thermal profile included a denaturation step of 4 min at 95 °C, followed by 5 cycles of 56 °C for 30 s, 68 °C for 2 min and 95 °C for 40 s, 30 cycles of 54 °C for 30 s, 68 °C for 2 min

and 95 °C for 40 s and then two final steps at 54 °C for 1 min and 68 °C for 8 min. A total of 5 µL of the inner PCR was loaded onto a 1.5% Seakem agarose gel and was run at 6 V/cm for 50 min, and the presence of expected bands was checked under a transilluminator after gel staining with GelRed dye solution (Biotium, Fremont, CA, USA). The amplicons obtained were used both for Sanger sequencing and for the homemade amplicon-based NGS protocol.

Table 1. Primers used to amplify the protease, reverse transcriptase (amino acid 1–400) and integrase coding regions for Sanger sequencing and homemade NGS. _F, forward primer; _R, reverse primer; PR, protease; RT, reverse transcriptase; IN, integrase.

Primer	Sequence (5′-3′)	Target Region	HIV-1 HXB2 Coordinates	PCR Round
P534_F	AAAARGGYTGTTGGAAATGTGG	PR-RT	2018–2039	Outer
P1069_R	TCCCAYTCAGGAATCCAGGT		3774–3793	
P688_F	CATGGGTACCAGCACACAAAGG	IN	4150–4171	Outer
P689_R	CCCAAATGCCAGTCTCTTTCTCCTG		5261–5285	
P535_F	GARAGRCAGGCTAATTTTTTAGGGA	PR-RT	2071–2095	Inner
P1070_R	AATCCAGGTRGCYTGCCAATA		3762–3782	
P690_F	AGGRATTGGAGGAAATGAACA	IN	4169–4189	Inner
P691_R	GGGATGTGTACTTCTGAACTTA		5192–5213	

2.3. Sanger Sequencing

All sequencing reactions were performed on a 3500xL Dx Genetic Analyzer (Applied Biosystems, Waltham, MA, USA). PCR amplicons (PR-RT and IN) were diluted to a final concentration of 1–3 ng/µL; then, 10 µL was purified by adding 2 µL of ExoSAP-IT for PCR Product Clean-Up (Affymetrix, Santa Clara, CA, USA) at 37 °C for 15 min, followed by an inactivation step at 80 °C for 15 min. Each sequencing reaction included 3 µL of purified PCR product, 3.2 pmol of sequencing primer (Table 1), 2 µL of BigDye® Terminator v1.1 Ready Reaction Mix (Life Technologies, Waltham, MA, USA), 1 µL of 5× Sequencing Buffer and sterile DNAse-/RNAse-free water, giving a final volume of 10 µL. The thermal cycler profile for this reaction included an initial denaturation step at 94° for 4 min, followed by 25 cycles at 50 °C for 1 min, 68 °C for 4 min, and 94 °C for 1 min. Sequencing reactions were treated with the X-Terminator® Purification kit (Applied Biosystems, Waltham, MA, USA) in a 96-well plate as suggested by the manufacturer and loaded into a capillary electrophoresis sequencer. Chromatograms were assembled and edited with the DNAStar 7.1.0 SeqMan module to generate the FASTA files that were submitted to the Stanford online HIVdb system (https://hivdb.stanford.edu/; accessed on 1 August 2024) for the interpretation of RAMs.

2.4. Homemade Amplicon-Based NGS

Amplicons (Table 1) were obtained as described above for Sanger sequencing, purified with the Agencourt® AMPure® magnetic beads (Beckman Coulter, Brea, CA, USA), quanti-fied with the Qubit fluorometer in dsDNA HS Buffer (Qiagen, Venlo, The Netherlands) and diluted to a final concentration of 0.8 ng/µL. PR-RT and IN amplicons derived from the same sample were pooled together for the subsequent steps. Tagmentation was performed with the Nextera® XT DNA Library Preparation Kit (Illumina, San Diego, CA, USA), ac-cording to the manufacturer's instructions. Tagmented samples were indexed with IDT for Illumina DNA/RNA UD Indexes (Illumina, San Diego, CA, USA) and pooled together to obtain the library that was diluted to a final concentration of 9 pM. The library was then spiked-in with 10% 9 pM PhiX control library (Illumina, San Diego, CA, USA), loaded on a Nano MiSeq Reagent Kit v2 (2 × 250 bp paired-end reads, 8.5 Gb output, Illumina, San Diego, CA, USA) and run on an Illumina MiSeq instrument.

2.5. AD4SEQ HIV-1 Solution v2 Kit

The RNA extracts were obtained as described above and, according to the AD4SEQ HIV-1 Solution v2 protocol (Arrow Diagnostic, Genoa, Italy), samples with viremia above 20,000 HIV-1 RNA copies/mL were five-fold diluted in sterile DNase-/RNase-free wa-ter. Then, one-step RNA reverse transcription was performed, followed by amplifica-tion of the target regions in two separate PCRs, defined as Target PCR. Target PCR amplifies the following regions of the HIV-1 genome: PR (codons 1–99), RT (codons 1–440), IN (codons 1–289) and gp120 (codons 266–366). Once the reaction was completed, amplification products were visualised by electrophoresis. Then, for each sample, the two separated Target PCR reactions were combined in a single tube and purified with magnetic beads (Agentcourt® AMPure® magnetic beads, Beckman Coulter, Brea, CA, USA). Individual samples were indexed using the index adaptors provided by the kit (Index PCR), purified as described above, and amplification was checked again by elec-trophoresis. The concentration of each purified Index PCR was determined with the Qubit fluorometer in dsDNA HS Buffer (Qiagen, Venlo, The Netherlands), and the mo-larity of each sample was calculated using the following formula: sample concentration [nM] = (sample concentration [ng/µL] × 10^6)/(656.6 × AMPpb), where AMPbp is the av-erage length of the amplicons in base pairs. After quantification, each sample was diluted to 20 pM, and 3 µL was pooled in the library. After purification, the library was diluted to a final concentration of 9 pM and spiked-in with 20% of 9 pM PhiX control library (Illumina, San Diego, CA, USA), loaded on a Nano MiSeq Reagent Kit v2 (2 × 250 bp paired-end reads, 8.5 Gb output, Illumina, San Diego, CA, USA) and run on an Illumina MiSeq instrument.

2.6. HIV-1 Subtyping and Drug Resistance Interpretation

The assignment of HIV-1 subtypes was performed by the COMET HIV-1 tool [11]. NGS data generated by AD4SEQ were analysed both with the dedicated SmartVir software version 1.0.6 provided by Arrow Diagnostics (AD4SEQ-SmartVir) and by the online HIVdb Drug Resistance Database system (AD4SEQ-HIVdb) (Stanford University; https://hivdb. stanford.edu/; accessed on 1 August 2024). NGS data generated by the homemade system were analysed only by HIVdb. The FASTA files obtained from Sanger sequencing were analysed directly, while the FASTQ files obtained from NGS were first converted to CodFreq files and then analysed to detect RAMs. The CodFreq files list the frequency of the mutations of each nucleotide triplet within the sequenced region. For the analysis of FASTQ files, the minimum read depth parameter was set at >100 reads per position with a mutation detection threshold of 5%, both for SmartVir and for HIVdb, independently of whether the position was associated with drug resistance or not. The Stanford HIVdb 9.6 algorithm was used to infer drug susceptibility from the RAMs identified by the two NGS systems and by Sanger sequencing. Mutations were defined as RAMs when associated with a score for at least one drug or included in a combination rule changing the score for at least one drug in the HIVdb 9.6 algorithm. Agreement among the RAMs reported by the different systems was qualitatively defined when identical RAMs were reported.

2.7. Statistical Analysis

Continuous variables were reported as median and interquartile ranges (IQRs). The difference in proportions was analysed by a chi-square test followed by a post hoc z test with the Bonferroni adjustment for multiple comparisons. The difference between numerical values obtained with paired samples were analysed by a Wilcoxon signed-rank test. All the analyses were performed using the SPSS version 20 package (IBM Corp., Armonk, NY, USA).

3. Results

3.1. Samples Included in This Study

All the 27 plasma samples included in this study (Table 2) had detectable viremia with a median viral load of 4.9 log [IQR 4.6–5.2] HIV-1 RNA copies/mL. Subtype B was identified in 16 (59%) cases and CRF02_AG in 4 (15%).

Table 2. Subtype and viral load of the 27 plasma samples included in this study.

Sample	Subtype	HIV-1 RNA log10 Copies/mL 4.3	
5826	B 5974	4.9	3.1
F1 6003	CRF02_AG	6.0	4.9
6006	F1 6084	4.9	4.6
	B 6092	4.8	6.3
	B 6107	5.4	4.8
	B 6216	4.9	4.8
	B 6222	3.7	5.1
	B 6322	4.1	4.5
A6 6363	B 6408	5.0	4.7
	B 6436	5.3	3.1
CRF02_AG 6471	B 6493	5.0	5.4
CRF01_AE 6570	B 6592	4.3	6.3
	C 6669	4.8	5.9
CRF02_AG 6695	B 6750		
	B 6762		
	B 6813		
	B 6817		
	B 6835		
	B 6880		
F1 7312	G		
7347	CRF02_AG		

3.2. Comparison Between Homemade NGS and AD4SEQ: Identification of Drug Resistance Mutations

The RAMs reported by the two different data processing methods, SmartVir for the data generated by the AD4SEQ HIV-1 Solution v2 Kit, and HIVdb for Sanger and homemade NGS, are listed in Supplementary Table S1. RAMs to PIs, NRTIs, NNRTIs and INIs were detected in 6, 18, 20 and 6 samples, respectively, by at least one method (Table 3). Homemade NGS and AD4SEQ-SmartVir identified additional mutations with respect to Sanger sequencing in 12/27 and 9/27 samples, respectively.

Agreement between the NGS methods and Sanger sequencing for PIs was observed in 24/27 cases (88.9%). In two cases (samples 5826 and 6570), both NGS methods detected additional RAMs with respect to Sanger sequencing. In one sample (6813), homemade NGS was more sensitive in detecting additional RAMs with respect to Sanger sequencing and AD4SEQ-SmartVir.

With NRTIs, complete agreement among the NGS methods and Sanger sequencing was observed in only 18/27 (66.6%) cases. In three cases (samples 5826, 5974 and 7312), homemade NGS-HIVdb reported additional mutations with respect to AD4SEQ-SmartVir and Sanger sequencing, while in one case (sample 7312), AD4SEQ-SmartVir detected an additional mutation with respect to homemade NGS and Sanger sequencing. However, in four cases (samples 6003, 6006, 6436 and 6493), Sanger sequencing and homemade NGS-HIVdb gave comparable results, and AD4SEQ-SmartVir did not report the S68G mutation. Differently from Sanger sequencing and AD4SEQ-SmartVir, homemade NGS

failed to identify mutations D67N and K219E in sample 6471. Agreement between the NGS methods with respect to Sanger sequencing was observed only in one case (sample 6835). A strong discordance among the three methods was observed in sample 7312. Indeed, Sanger sequencing detected the D67N, T69G and K219Q mutations, homemade NGS-HIVdb reported mixed populations at codon 67 (D67ΔN), the additional mutation S68G and a deletion at position 69, while AD4SEQ-SmartVir reported a combination of mutations at position D67(N/E) and the T69N/G mutation.

Table 3. Drug resistance mutations to (A) PIs (protease inhibitors), (B) NRTIs (nucleoside reverse transcriptase inhibitors) and NNRTI (non-NRTI) and (C) INI (integrase inhibitors) identified. The table lists the samples in which RAMs were detected by at least one of the three sequencing methods, highlighted in bold. The frequency of each mutation identified by NGS is shown in brackets.

(A)

Sample	Sequencing System and Data Processing Method	PIs
5826	Sanger-HIVdb	V32I, L33F, M46I, I47V, I54M, Q58E, T74P
	Homemade NGS-HIVdb	V32I (99%), L33F (99%), M46I (99%), I47V (99%), I50V (29%), I54M (99%), Q58E (99%), T74P (27%)
	AD4SEQ-SmartVir	V32I (99%), L33F (99%), M46I (99%), I47V (99%), I50V (24%), I54M (99%), Q58E (99%), T74P (45%)
5979	Sanger-HIVdb Homemade NGS-HIVdb AD4SEQ-SmartVir	L33F, I84V L33F (98%), I54T (10%), I84V (98%) L33F (98%), I84V (98%)
6084	Sanger-HIVdb Homemade NGS-HIVdb AD4SEQ-SmartVir	L10F, M46I, T74P L10F (98%), M46I (99%), T74P (64%)
6092	Sanger-HIVdb Homemade NGS-HIVdb AD4SEQ-SmartVir	L10F (98%), M46I (98%), T74P (69%) L90M L90M (98%) L90M (99%)
6408	Sanger-HIVdb Homemade NGS-HIVdb AD4SEQ-SmartVir	L33F, M46L, L90M L33F (99%), M46L (99%), L90M (98%) L33F (98%), M46L (97%), L90M (99%) None
6570	AD4SEQ-SmartVir Sanger-HIVdb Homemade NGS-HIVdb	K20T (14%) K20T (9.6%) Q58E
6813	AD4SEQ-SmartVir	Q58E (99%), G73S (7.3%) Q58E (98%)

(B)

Sample	Sequencing System and Data Processing Method	NRTIs	NNRTIs
5826	Sanger-HIVdb	K70T, M184V	None
	Homemade NGS-HIVdb	K70T (78%), V75I (6.5%), M184V (96%)	None
	AD4SEQ-SmartVir	K70T (70%), M184V (99%)	None

Table 3. Cont.

5974	Sanger-HIVdb	S68G	K103N, N348I
	Homemade NGS-HIVdb	S68G (99%), K219Q (7.1%)	K103N (99%), V106I (10%), N348I (99%)
	AD4SEQ-SmartVir	None	K103N (99%), N348I (99%)
5979	Sanger-HIVdb	M41L, D67N, T215Y	K103N, Y181I
	Homemade NGS-HIVdb	M41L (99%), D67N (95%), T215Y (91%)	K103N (97%), Y181I (97%)
	AD4SEQ-SmartVir	D67N (98%), T215Y (88%)	K103N (99%), Y181I (90%)
6003	Sanger-HIVdb	S68G, M184V	K103N, K238N
	Homemade NGS-HIVdb	S68G (99%), M184V (99%)	K103N (98%), K238N (99%)
	AD4SEQ-SmartVir	M184V (98%) S68G	K103N (95%), K238N (96%)
6006	Sanger-HIVdb	S68G (99%)	K103N, N348I
	Homemade NGS-HIVdb	None	K103N (98%), N348I (98%)
	AD4SEQ-SmartVir	D67N, T215C D67N	K103N (99%), N348I (99%)
6084	Sanger-HIVdb	(92%), T215C (97%) D67N	None None
	Homemade NGS-HIVdb	(98%), T215C (97%)	None None
	AD4SEQ-SmartVir	M41ML, M184V, T215TNSY	None
6092	Sanger-HIVdb	M41L (28%), M184V (97%), T215Y (23%)	None
	Homemade NGS-HIVdb	M41L (36%), M184V (97%), T215Y (13%)	Y181C Y181C
	AD4SEQ-SmartVir	K219N K219N	(98%) Y181C
6107	Sanger-HIVdb	(99%) K219N	(99%) None
	Homemade NGS-HIVdb	(98%) M41L,	None None
	AD4SEQ-SmartVir	T215D	V106I, G190A V106I
6216	Sanger-HIVdb	M41L (97%), T215D (98%)	(91%), G190A (99%) V106I
	Homemade NGS-HIVdb	M41L (94%), T215D (90%)	(92%), G190A (98%)
	AD4SEQ-SmartVir	None None	E138A, G190GS E138A
6222	Sanger-HIVdb	None None	(90%), G190S (41%) E138A
	Homemade NGS-HIVdb	None None	(89%), G190S (38%)
	AD4SEQ-SmartVir	M184V	V106A, F227L V106A
6322	Sanger-HIVdb	M184V (92%)	(97%), F227L (93%) V106A
	Homemade NGS-HIVdb	M184V (98%)	(97%), F227L (97%)
	AD4SEQ-SmartVir	T215V T215V	None
6363	Sanger-HIVdb	(95%) T215V	None
	Homemade NGS-HIVdb	(98%) S68G	None
	AD4SEQ-SmartVir	S68G (85%)	K103N
6408	Sanger-HIVdb	None	K103N (98%), K238T (7.8%), N348I (6.8%)
	Homemade NGS-HIVdb		K103N (99%)
	AD4SEQ-SmartVir		
6436	Sanger-HIVdb		
	Homemade NGS-HIVdb		
	AD4SEQ-SmartVir		

Table 3. Cont.

6471	Sanger-HIVdb	M41L, D67N, M184V, L210W, T215Y, K219KE	L100I, K103N, N348I
	Homemade NGS-HIVdb	M41L (98%), M184V (98%), L210W (98%), T215Y (95%)	L100I (96%), K103N (98%), N348I (98%)
	AD4SEQ-SmartVir	M41L (98%), D67N (19%), M184V (91%), L210W (98%), T215Y (92%), K219E (9%)	L100I (99%), K103N (97%), N348I (99%)
6493	Sanger-HIVdb	D67G, S68G, K70R, M184V, T215I, K219E	K103N, V108I, K238T, N348I
	Homemade NGS-HIVdb	D67G (99%), S68G (97%), K70R (98%), M184V (98%), T215I (87%), K219E (78%)	K103N (98%), V108I (98%), V179D (7%), Y181C (34%), K238T (98%), N348I (98%)
	AD4SEQ-SmartVir	D67G (98%), K70R (99%), M184V (92%), K219E (87%)	K103N (98%), V108I (99%), Y181C (26%), K238T (97%), N348I (99%)
6570	Sanger-HIVdb	M41L, M184MV M41L	None
	Homemade NGS-HIVdb	(44%), M184V (43%) M41L	None
	AD4SEQ-SmartVir	(66%), M184V (70%)	None
6592	Sanger-HIVdb	None	E138EK
	Homemade NGS-HIVdb	None	K101E (40%), E138K (23%)
	AD4SEQ-SmartVir	None	K101E (13%), E138K (29%)
6669	Sanger-HIVdb	None	K103KN, V106M
	Homemade NGS-HIVdb	None	K103N (75%), V106M (24%) K103N
	AD4SEQ-SmartVir	None	(45%), V106M (54%), Y181C (7%)
6695	Sanger-HIVdb	None	A98G A98G
	Homemade NGS-HIVdb	None	(99%) A98G
	AD4SEQ-SmartVir	None	(90%) E138A
6750	Sanger-HIVdb	V75M	E138A (99%)
	Homemade NGS-HIVdb	V75M (96%)	E138A (97%)
	AD4SEQ-SmartVir	V75M (95%)	K103N, V179T, Y181C, H221Y
6762	Sanger-HIVdb	D67N, K219Q	K103N (99%), V179T (T 76%), Y181C (98%), H221Y (99%)
	Homemade NGS-HIVdb	D67N (90%), K219Q (98%)	K103N (99%), V179T (T 76%), Y181C (98%), H221Y (98%)
	AD4SEQ-SmartVir	D67N (92%), K219Q (98%)	E138A, G190A, M230L
6813	Sanger-HIVdb	None	E138A (99%), G190A (99%), M230L (98%)
	Homemade NGS-HIVdb	None	K103N (7%), E138A (92%), G190A (95%), M230L (96%)
	AD4SEQ-SmartVir	None	K103KN, V179T
6817	Sanger-HIVdb	None	K103N (67%), V106I (5.4%), V179T (99%)
	Homemade NGS-HIVdb	None	K103N (69%) None
	AD4SEQ-SmartVir	None	None
6835	Sanger-HIVdb	L210W, T215S	None
	Homemade NGS-HIVdb	M41L (30%), L210W (99%), T215DS (D: 19%, S 79%)	None
	AD4SEQ-SmartVir	M41L (19%), L210W (98%), T215DS (D: 25%, S: 72%)	

Table 3. Cont.

6880	Sanger-HIVdb	None	E138G E138G
	Homemade NGS-HIVdb	None	(96%) E138G
	AD4SEQ-SmartVir	None	(97%) A98G,
7312	Sanger-HIVdb	D67Δ, T69G, K219Q	V106I
	Homemade NGS-HIVdb	D67ΔN (Δ: 8.9%, N: 53%), S68G (52%), T69Δ (93%), K219Q (96%)	A98G (99%), V106I (94%), Y181C (55%)
	AD4SEQ-SmartVir	D67NE (N: 8%, E: 88%), T69NG (N: 6%, G: 89%), K219Q (96%)	A98G (97%), V106I (98%), Y181C (66%)
7347	Sanger-HIVdb	None	K101E, Y181C, N348I
	Homemade NGS-HIVdb	None	K101E (99%), V106I (16%), Y181C (99%), N348I (99%)
	AD4SEQ-SmartVir	None	K101E (99%), V106I (15%), Y181C (96%), N348I (96%)

(C)

Sample	Sequencing System and Data Processing Method	INIs	
5979	Sanger-HIVdb Homemade NGS-HIVdb AD4SEQ-SmartVir	T97A, E138K, G140S, Q148H T97A (100%), E138K (99%), G140S (99%), Q148H (99%) T97A (94%), E138K (94%), G140S (93%), Q148H (94%) R263K	
6003	Sanger-HIVdb Homemade NGS-HIVdb AD4SEQ-SmartVir	R263K (96%) None	R263K (98%)
6669	Sanger-HIVdb Homemade NGS-HIVdb AD4SEQ-SmartVir	E157Q (7.1%) E157Q (11%)	
6813	Sanger-HIVdb Homemade NGS-HIVdb AD4SEQ-SmartVir	L74M, G140S, Q148K L74M (98%) G140S (99%), Q148K (98%) L74M (97%), G140S (97%), Q148K (98%) None	
6835	Sanger-HIVdb Homemade NGS-HIVdb AD4SEQ-SmartVir	None L74M (10%) Q95QK Q95K (35%) Q95K	
6880	Sanger-HIVdb Homemade NGS-HIVdb AD4SEQ-SmartVir	(36%) None T97A (6%) None	
7347			

With NNRTIs, similar to NRTIs, 18/27 (66.7%) cases showed complete agreement across the NGS methods and Sanger sequencing. In four cases (samples 5974, 6436, 6493 and 6817), homemade NGS-HIVdb reported additional mutations with respect to AD4SEQ-SmartVir and Sanger sequencing, while in two cases (samples 6669 and 6813), AD4SEQ-SmartVir reported additional mutations with respect to homemade NGS and Sanger sequencing. Additional mutations detected by both NGS methods but not by Sanger sequencing were observed in three cases (samples 6592, 7312 and 7347).

For INIs, complete agreement among all methods was observed in 24/27 cases (88.9%). In one case (sample 6669), both NGS methods detected the minority RAM E157Q, which was not reported by Sanger sequencing. Homemade NGS was more sensitive in detecting the additional minority RAM T97A with respect to Sanger sequencing and AD4SEQ-SmartVir in sample 7347, while AD4SEQ-SmartVir was more sensitive than homemade NGS with sample 6835, detecting L74M.

In conclusion, AD4SEQ-SmartVir did not report one or more RAMs detected by at least one of the other two systems in 1 (3.7%), 7 (25.9%), 4 (14.8%) and 1 (3.7%) samples for PIs, NRTIs, NNRTIs and INIs, respectively, while homemade NGS-HIVdb did not identify one or more RAMs in 0, 2 (7.4%), 2 (7.4%) and 1 (3.7%) samples detected by at least one of the other two systems for PIs, NRTIs, NNRTIs and INIs, respectively. Differently from HIVdb, AD4SEQ-SmartVir did not report the mutation S68G and mutations identified by Sanger sequencing and homemade NGS with a frequency >20% in one case (sample 6817). By contrast, homemade NGS-HIVdb gave a slightly different identification of RAMs at two amino acid positions that were detected as predominant by Sanger sequencing or with frequency >20% by AD4SEQ-SmartVir in sample 7312.

3.3. Comparison of SmartVir and HIVdb NGS Data Processing

Notably, SmartVir and HIVdb generated different outputs for read depth, i.e., median read depth vs. max. and min. coverage, respectively (Supplementary Table S2). Other parameters, such as the regions sequenced with a coverage depth of <100 reads per base, were instead reported by both interpretation systems (Table 4). To compare the two NGS data processing methods, we analysed the FASTQ files obtained by AD4SEQ both with SmartVir (AD4SEQ-SmartVir) and with HIVdb (AD4SEQ-HIVdb). Homemade NGS generated low-coverage data in 2/27 samples, both subtype B, in the initial part of the integrase coding region (Table 4). A coverage depth <100 was more frequent both with AD4SEQ-HIVdb (16/27 cases) and with AD4SEQ-SmartVir (12/27) with respect to homemade NGS (2/27) ($p < 0.001$ and $p = 0.004$, respectively) while the difference between AD4SEQ-HIVdb and AD4SEQ-SmartVir was not statistically significant. The median read depth obtained with homemade NGS and with AD4SEQ-HIVdb was comparable (2203 [IQR 1918–8328] reads vs. 4835 [3327–6512] reads, $p = 0.148$). With AD4SEQ-SmartVir, the lower coverage affected six B and six non-B subtypes, mainly at RT codons 14–49 and 260–319 and IN codons 1–75 and 201–288.

Table 4. Regions with a coverage depth of <100 reads per base according to the NGS system and the data processing method. There were no low-coverage regions within the protease coding regions.

Sample	NGS System and Data Processing Method	Region and Relative Amino Acids with Coverage < 100×
5826	AD4SEQ-SmartVir AD4SEQ-	RT 14–49
	HIVdb Homemade NGS-	RT 14–49
	HIVdb AD4SEQ-SmartVir	IN 1–25
5974	AD4SEQ-HIVdb	IN 201–284
	Homemade NGS-HIVdb	IN 201–288
5979	AD4SEQ-SmartVir AD4SEQ-	None
	HIVdb Homemade NGS-	RT 14–49, 223–235/IN 1–75, 201–284 RT
	HIVdb AD4SEQ-SmartVir	14–49, 223–235/IN 1–75, 201–288 None
6003	AD4SEQ-HIVdb	RT 260–275
	Homemade NGS-HIVdb	RT 260–319
		None

Table 4. Cont.

Sample	NGS System and Data Processing Method	Region and Relative Amino Acids with Coverage < 100×
6084	AD4SEQ-SmartVir AD4SEQ-	None IN
	HIVdb Homemade NGS-	201–209
	HIVdb AD4SEQ-SmartVir	None
6107	AD4SEQ-HIVdb	IN 1–10, 66–75, 159–171 IN
	Homemade NGS-HIVdb	1–11, 66–75 None
	AD4SEQ-SmartVir AD4SEQ-	RT 260–319
6216	HIVdb Homemade NGS-	RT 260–319
	HIVdb AD4SEQ-SmartVir	IN 1–39 IN
	AD4SEQ-HIVdb	1–75 IN 1–
6222	Homemade NGS-HIVdb	75 None
	AD4SEQ-SmartVir AD4SEQ-	RT 260–275; IN 201–284 IN
	HIVdb Homemade NGS-	201–288 None
6363	HIVdb AD4SEQ-SmartVir	None
	AD4SEQ-HIVdb	IN 201–288
	Homemade NGS-HIVdb	None None
6408	AD4SEQ-SmartVir AD4SEQ-	RT 260–319, 359
	HIVdb Homemade NGS-	None
	HIVdb AD4SEQ-SmartVir	RT 260–319
6436	AD4SEQ-HIVdb	RT 260–319
	Homemade NGS-HIVdb	None
	AD4SEQ-SmartVir AD4SEQ-	RT 260–319
6471	HIVdb Homemade NGS-	RT 260–319
	HIVdb AD4SEQ-SmartVir	None
	AD4SEQ-HIVdb	IN 1–31, 66–75
6493	Homemade NGS-HIVdb	IN 1–75 None
	AD4SEQ-SmartVir AD4SEQ-	IN 74–75
	HIVdb Homemade NGS-	IN 73–75
6592	HIVdb AD4SEQ-SmartVir	None
	AD4SEQ-HIVdb	RT 14–49
	Homemade NGS-HIVdb	RT 14–49
6880	AD4SEQ-SmartVir AD4SEQ-	None
	HIVdb	None
	Homemade NGS-HIVdb	RT 35–49
7312		None
7347		

RT, reverse transcriptase; IN, integrase.

Disagreement between RAMs reported by SmartVir and HIVdb when processing AD4SEQ FastQ files was observed in 10 samples (37.0%; Table 5). HIVdb reported one additional PI RAM in one case. For NRTIs, 1 mutation was reported by SmartVir and not by HIVdb, while 8 mutations were reported by HIVdb and not by Smartvir, including S68G in 6/8 cases. For NNRTIs, two mutations at position V179 were reported by HIVdb but not by SmartVir.

Table 5. Discordant report of drug resistance mutations between SmartVir and HIVdb interpretation tools from FASTQ files generated by the AD4SEQ sequencing method. Mutations in bold are those reported by only one interpretation tool. The frequency of each mutation is shown in brackets. There were no discordant cases with integrase inhibitor resistance mutations.

Sample	Data Processing Method	PIs	NRTIs	NNRTIs
5974	SmartVir	None	None	K103N (99%), N348I (99%)
	HIVdb	None	S68G (98%)	K103N (99%), N348I (99%)
6003	SmartVir	None	M184V (98%)	K103N (95%), K238N (96%)
	HIVdb	None	S68G (91%), M184V (98%)	K103N (93%), K238N (96%)
6006	SmartVir	None	None	K103N (99%), N348I (99%)
	HIVdb	None	S68G (98%)	K103N (99%), N348I (99%)
6436	SmartVir	None	None	K103N (99%) K103N
	HIVdb	None	S68G (81%)	(99%)
6471	SmartVir	None	M41L (98%), D67N (19%), M184V (91%), L210W (98%), T215Y (92%), K219E (9%)	L100I (99%), K103N (97%), N348I (99%)
	HIVdb	None	M41L (99%), E44A (15%), D67N (19%), M184V (92%), L210W (97%), T215Y (95%), K219E (11%)	L100I (99%), K103N (97%), N348I (100%)
6493	SmartVir	None	D67G (98%), K70R (99%), M184V (92%), T215I (94%), K219E (87%)	K103N (98%), V108I (99%), Y181C (26%), K238T (97%), N348I (99%)
	HIVdb	None	D67G (97%), S68G (98%), K70R (99%), M184V (93%), T215I (96%), K219E (89%)	K103N (99%), V108I (98%), Y181C (25%), K238T (94%), N348I (100%)
6817	SmartVir	None	None	K103N (69%) K103N
	HIVdb	None	None	(69%), V179T (94%)
6835	SmartVir	None	M41L (19%), L210W (98%), T215DS (D: 25%, S: 72%)	None
	HIVdb	M46I (5%)	M41L (19%), L210W (99%), T215DS (D: 25%, S: 73%)	None
6880	SmartVir	None	None	E138G (97%) E138G
	HIVdb	None	None	(96%), V179T (6%)
7312	SmartVir	None	D67NE (N: 8%, E: 89%), T69NG (N: 6%, G: 89%), K219Q (96%)	A98G (97%), V106I (98%), Y181C (66%)
	HIVdb	None	D67ΔN (Δ: 8%, N: 51%), S68G (8%), T69NG (N: 6%, G:88%), K219Q (98%)	A98G (97%), V106I (98%), Y181C (68%)

PIs, protease inhibitors; NRTIs, nucleoside reverse transcriptase inhibitors; NNRTI, non-NRTI.

3.4. Prediction of Drug Susceptibility

Table 6 shows the impact of the RAMs not reported uniformly by the four methods (Sanger sequencing, homemade NGS, AD4SEQ-SmartVir and AD4SEQ-HIVdb) on the prediction of drug susceptibility. Globally, drug susceptibility predictions were fully

concordant in 20/27 (74.1%) samples for all the drugs considered, including PIs (Atazanavir, ATV; Lopinavir, LPV; and Darunavir, DRV), NRTIs (Abacavir, ABC; Tenofovir Alafenamide, TAF; and Lamivudine/Emtricitabine, 3TC/FTC), NNRTIs (Doravirine, DOR; Rilpivirine, RPV; Etravirine, ETR; Efavirenz, EFV; and Nevirapine, NVP) and INIs (Dolutegravir, DTG; Bictegravir, BIC; and Cabotegravir, CAB).

Table 6. Discordant cases of predicted drug susceptibility according to the sequencing system and to the data processing method.

Sample	Sequencing System and Data Processing Method	PIs			NRTIs			NNRTIs					INIs		
		ATV	LPV	DRV	ABC	TAF	3TC/FTC	DOR	RPV	ETR	EFV	NVP	DTG	BIC	CAB
	Sanger-HIVdb Homemade	R	I	LLR	I	I	S	PLLR	R	R	R	R	R	R	R
5979	NGS-HIVdb AD4SEQ-	R	I	LLR	I	I	S	PLLR	R	R	R	R	R	R	R
	SmartVir AD4SEQ-HIVdb	R	I	LLR	LLR	LLR R I	S	PLLR	R	R	R	R	R	R	R
	Sanger Sequencing		LLR	LLR	LLR S	S	S	PLLR	R	R	R	R	R	R	R
	Homemade NGS AD4SEQ-	S	R	R S	S	S	R	I	R	I R	R	S	S	S R	I
6471	SmartVir AD4SEQ-HIVdb	R	I					R	I R	R	S	S	S R	I	R
	Sanger Sequencing	S	S	S	R	R	I	R	R	S	S	S R	I	R	I
	Homemade NGS AD4SEQ-	S	S	S	R	R		R	R	S	S	S R	PLLR	S	S
	SmartVir AD4SEQ-HIVdb	S	S	S	I	LLR SS		R	R	S	S	S R	I	I	I R
6493	Sanger Sequencing		S	I	LLR S	S		R	S	S	S R	I I	I	R	R
	Homemade NGS AD4SEQ-		S	I	LLR S	S		S	S	S R	I	I	R	R	S
	SmartVir AD4SEQ-HIVdb		S	I	LLR S	S		S	S S	S	I PLLR	PLLR	PLLR	S	S
	Sanger Sequencing		S	S	S S	S		S S	LLR	R	LLR	LLR I	S	S	S
6592	Homemade NGS AD4SEQ-		S	S	S S	S	S	LLR	R	LLR	LLR	I S	S	S	S
	SmartVir AD4SEQ-HIVdb		S	S	S S	S		LLR	R	LLR	LLR	I S	S	S S	I
	Sanger Sequencing		S	S	S S	S		S	S	R	R	S	S	S S	I
	Homemade NGS AD4SEQ-		S	S	S S	S		S	S	R	R	S	S	S S	I
6669	SmartVir AD4SEQ-HIVdb		S	S	S S	S	I	I	R	R	S	S	S S	I	I
	Sanger Sequencing		S	S	S S	S	I	R	R	S	S	S S	S	S	S
	Homemade NGS AD4SEQ-		S	S	S S	S		S	S	S	S	S S	S	S	S
	SmartVir AD4SEQ-HIVdb		S	S	S S	S		S	S	S	S	S			
6835	Sanger Sequencing		S	LLR	LLR S	S	S	S	S	S	S	S	S	PLLR S	S S
	Homemade NGS AD4SEQ-		S	LLR	LLR						S	S S	S	S	PLLR
	SmartVir AD4SEQ-HIVdb	PLLR	PLLR	S	LLR	LLR S		LLR	LLR	LLR	LLR	LLR I	S	S I	I
			S	S	I	I S		R	I	I	R	S S S	I	R	I
7312			S	S	I	I S		I	R	S	S	S LLR I	R	I	R
			S	S	LLR	LLR S	S	S	S S	LLR	R	I I	R	S	S S
			S	S	I	I S		S	I	R	I	I R	S	S S	I
			S	S	S	S SS		R	I	I	R	S S	S S	I	R I
7347			S	S	S S	S S						I	R	S	S S
		S	S S	S	S	S									
		S													

PIs, protease inhibitors; NRTIs, nucleoside reverse transcriptase inhibitors; NNRTI, non-NRTI; INIs, integrase inhibitors; ATV, atazanavir; LPV, lopinavir; DRV, darunavir; ABC, abacavir; TAF, tenofovir alafenamide; 3TC, lamivudine; FTC, emtricitabine; DOR, doravirine; RPV, rilpivirine; ETR, etravirine; EFV, efavirenz; NVP, nevirap-ine; DTG, dolutegravir; BIC, bictegravir; CAB, cabotegravir; S, full susceptibility (green); PLLR, potential low-level resistance (yellow); LLR, low-level resistance (light orange); I, intermediate resistance (orange); R, high-level resistance (red).

Homemade NGS gave discordant results with respect to AD4SEQ-SmartVir in two samples for NRTIs (6471 and 7312) and in one sample each for NNRTIs (6669) and for INIs (6835). AD4SEQ-SmartVir and AD4SEQ-HIVdb gave discordant results in one sample each for PI (ATV and LPV for 6835) and for NRTIs (ABC, TAF and 3TC/FTC for 7312).

Considering Sanger sequencing as a reference, homemade NGS was in agreement with Sanger sequencing for susceptibility predictions against all INIs and PIs but gave discordant predictions in 4/81 (4.9%) cases for NRTIs (6471 and 7312 for one drug and 6835 for two drugs) and in 14/135 (10.4%) cases for NNRTIs (6592 and 7312 for five drugs, 6493 for three drugs and 7347 for one drug). AD4SEQ-SmartVir was discordant with Sanger sequencing in 3/81 (3.7%) cases for NRTIs (7312 for three drugs), in 16/135 (11.9%) cases for NNRTIs (6592 and 7312 for five drugs, 6493 for three drugs, 6669 for two drugs and 7347 for one drug) and in 1/81 (1.2%) cases for INIs (6835). AD4SEQ-HIVdb gave discordant susceptibility predictions in 1/81 (1.2%) cases for PIs and INIs (6835 in both cases), and in 16/135 (11.9%) samples for NNRTIs (6592 and 7312 for five drugs, 6493 for three drugs, 6669 for two drugs and 7347 for one drug). Notably, most of the discrepancies between either NGS method and Sanger sequencing were explained by a lack of detection of minority RAMs (<20%) by Sanger sequencing, namely, in 10 (37.0%), 7 (25.9%) and 9 (33.3%) out of 27 cases with homemade NGS, AD4SEQ-SmartVir and AD4SEQ-HIVdb, respectively.

4. Discussion

NGS has redefined genome sequencing techniques, and HIV-1 genotyping has been an early NGS application in the field of infectious diseases with the aim of identifying minority RAMs that cannot be detected by Sanger sequencing [12]. Since NGS is more diversified and complex than Sanger sequencing, standardisation plays a key role in the transition from Sanger sequencing to NGS in clinical settings. Indeed, recent progress in HIV-1 NGS has led to the CE-IVD certification of some commercial systems, including the Sentosa® SQ HIV Genotyping Assay developed by Vela Diagnostics, the AD4SEQ HIV-1 Solution v2 developed by Arrow Diagnostics and the DeepChek® Assay HIV-1 Full PR/RT/INT Drug Resistance developed by ABL Diagnostics.

Due to the limits of the Sentosa® SQ HIV kit—based on the Ion Torrent platform that is more error prone and expensive than the small footprint Illumina platforms [13]—and the slow introduction of the DeepChek® HIV Assay in Italy, the AD4SEQ HIV-1 Solution v2 is currently the most widely used system in Italy. However, to our knowledge, there are no published studies evaluating the AD4SEQ HIV-1 Solution v2 kit in comparison with other NGS-based HIV-1 genotyping techniques or with the reference Sanger sequencing. In this work, we compared Sanger sequencing, AD4SEQ and a homemade amplicon-based NGS protocol to analyse a panel of 27 plasma samples derived from routine analysis. For both NGS methods, we used an Illumina MiSeq platform. The NGS reads generated by the homemade and AD4SEQ systems were processed by the Stanford HIVdb online tool for sequence reads and by the SmartVir system bundled with AD4SEQ, respectively. In addition, AD4SEQ NGS reads were also processed by HIVdb to compare the output of HIVdb and SmartVir on the same raw data (AD4SEQ-HIVdb vs. AD4SEQ-SmartVir). For both the NGS systems and Sanger sequencing, the RAMs detected were interpreted by the HIVdb 9.6 algorithm.

Overall, the Sanger sequencing and NGS results were more concordant for PI and INI than for NRTI and NNRTI RAMs. A higher proportion of additional PI and NRTI RAMs was detected by homemade NGS compared with AD4SEQ-SmartVir. Notably, in 14.8% of the samples, AD4SEQ-SmartVir did not report resistance mutations against NRTIs, which were also detected by Sanger sequencing. Most of these discrepancies were due to the missing S68G in the RT coding region. This mutation was correctly reported when the AD4SEQ data were analysed with the Stanford HIVdb system, indicating that some settings in the SmartVir pipeline likely led to the exclusion of this polymorphic mutation in the final report. Indeed, inspection of the AD4SEQ raw data clarified that S68G was identified at a frequency comparable with that of the homemade NGS system in all cases. An inquiry with the AD4SEQ manufacturer clarified that S68G was deliberately not included in the report because it does not confer any resistance unless K65R is also present, which was not the case in any of the samples analysed. However, HIVdb reports S68G even when alone because polymorphisms involved in drug resistance may play a role and also because clinical use of HIV drug resistance is typically based on cumulative HIV genotype data obtained throughout patient history. The same considerations apply to the RT V179T mutation, which triggers a score for the NNRTI etravirine only in the presence of the Y181C RAM. SmartVir reported V179T in one case together with Y181C but not in the two other cases where it occurred without Y181C.

Most importantly, a lower coverage with respect to homemade NGS was observed for AD4SEQ (samples with a coverage < 100 reads were 2, 12 and 16 for homemade NGS, AD4SEQ-SmartVir and AD4SEQ-HIVdb, respectively). While we were not able to identify any factor associated with low coverage in our dataset, a recently published study based on a larger number of sequence data generated by the AD4SEQ kit showed that non-B subtype and low viremia are associated with low coverage [14]. It must be noted that the apparently lowest coverage with AD4SEQ-HIVdb may have derived from improper handling of the sequence data contributed by AD4SEQ primers, which are proprietary and unknown. Thus, AD4SEQ data processing through pipelines other than SmartVir may not be recommended.

Reassuringly, predictions of drug susceptibility were affected only for NRTIs and NNRTIs in a few cases and mostly derived from the comparison between Sanger sequencing and NGS, which is expected due to the different sensitivity of the methods. Overall, we did not observe any large shift in the prediction of drug susceptibility from a high score to a low score (i.e., from sensitive to resistant or vice versa).

Several published works [12,15–17] have evaluated the performance of homemade NGS systems with respect to Sanger sequencing and obtained results similar to those shown in this study, consistent with the inherently higher sensitivity of NGS in detect-ing minority RAMs. While participation in external quality assessment programs is a recognised approach for validating homemade NGS methodologies, CE-IVD-approved kits are essential for clinical use. To date, only the Sentosa® SQ HIV kit has been compared with the reference Sanger sequencing [17,18]. Thus, this is the first paper analysing the performance of AD4SEQ HIV-1 Solution v2 kit by Arrow Diagnostics. Although we had the possibility of selecting samples shown to harbour drug resistant viruses by Sanger sequencing, the number of samples was limited and did not allow a wide representation of HIV-1 subtypes. In addition, all samples had >1000 HIV-1 RNA copies/mL; thus, we could not test the threshold of sensitivity for the AD4SEQ amplification method, reported to be at least 500 HIV-1 RNA copies/mL by the manufacturer. For these reasons, further validation experiments on a larger and more heterogeneous sample panel are advisable for completing the assessment of the system. Notwithstanding such limitations, this study conveys relevant information on the performance and caveats of the AD4SEQ system in clinical settings.

Supplementary Materials: The following supporting information can be downloaded at https://www.mdpi.com/article/10.3390/v16091465/s1, Table S1. Drug resistance mutations considered for the prediction of drug susceptibility in each sample according to the sequencing system and to the data processing method. Mutations in bold are those identified by only one or two sequencing systems. The frequency of each mutation identified by NGS is shown in brackets. Table S2. Sequence coverage across the protease (PR), reverse transcriptase (RT) and integrase (IN) regions with the different NGS systems. For AD4SEQ-SmartVir, the maximum and minimum number of reads per base and the frequency of bases with coverage >100x are shown, as provided by the SmartVir software. Median read depth per base for the FASTQ files generated by AD4SEQ and by homemade NGS was determined through the Sequence reads (NGS) analysis of the HIVdb program.

Author Contributions: Conceptualisation, F.S.; methodology, I.V. (Ilaria Vicenti), C.B. and L.F.; validation, C.B., L.F. and N.B.; formal analysis, I.V. (Ilaria Vicenti) and M.Z.; investigation, C.B., L.F., I.V. (Ilenia Varasi), C.P. and N.B.; resources, M.Z., I.V. (Ilaria Vicenti); data curation, F.S.; writing—original draft preparation, I.V. (Ilaria Vicenti), C.B. and L.F.; writing—review and editing, F.S. and M.Z.; visualisation, F.S., I.V. (Ilaria Vicenti); supervision, I.V. (Ilaria Vicenti); funding acquisition, M.Z. All authors have read and agreed to the published version of the manuscript.

Funding: This work received funding from the Ministero dell'Università e della Ricerca in the context of national project (PRIN 2020), project code 202074AA2B, titled "Multidisciplinary Assessment of the blood and gut-associated HIV Reservoir and Immunity following Switch from 3-drug to 2-drug Antiretroviral regimens in virologically suppressed patients" (MARISA).

Institutional Review Board Statement: Access to residual anonymized plasma samples derived from clinical practice was initially obtained through patient informed consent as approved by the local Ethics Committee at the University Hospital of Siena, Area Vasta Toscana Sud Est, R72.13, 23 November 2015.

Informed Consent Statement: Access to residual anonymised plasma samples derived from clinical practice was initially obtained through patients' informed consent as approved by the local Ethics Committee at the University Hospital of Siena.

Data Availability Statement: Data are contained within this article and Supplementary Materials. All data not included are available on request from the corresponding author.

Conflicts of Interest: The authors declare that they have no known competing financial interests or personal relationships that could have appeared to influence the work reported in this paper.

References

1. Kantor, R.; Gupta, R.K.; Author, C. We Should Not Stop Considering HIV Drug Resistance Testing at Failure of First-Line Antiretroviral Therapy. Lancet HIV 2022, 10, e202–e208. [CrossRef] [PubMed]
2. Carr, A.; Mackie, N.E.; Paredes, R.; Ruxrungtham, K. HIV Drug Resistance in the Era of Contemporary Antiretroviral Therapy: A Clinical Perspective. Antivir. Ther. 2023, 28, 13596535231201162. [CrossRef] [PubMed]
3. Llibre, J.M.; Pulido, F.; García, F.; Deltoro, M.G.; Blanco, J.L.; Delgado, R. Genetic Barrier to Resistance for Dolutegravir. AIDS Rev. 2015, 17, 56–64. [PubMed]
4. Loosli, T.; Hossmann, S.; Ingle, S.M.; Okhai, H.; Kusejko, K.; Mouton, J.; Bellecave, P.; van Sighem, A.; Stecher, M.; John Gill, M.; et al. HIV-1 Drug Resistance in People on Dolutegravir-Based Antiretroviral Therapy: A Collaborative Cohort Analysis. Lancet HIV 2023, 10, e733–e741. [CrossRef] [PubMed]
5. Lapointe, H.R.; Dong, W.; Lee, G.Q.; Bangsberg, D.R.; Martin, J.N.; Mocello, A.R.; Boum, Y.; Karakas, A.; Kirkby, D.; Poon, A.F.Y.; et al. HIV Drug Resistance Testing by High-Multiplex "Wide" Sequencing on the MiSeq Instrument. Antimicrob. Agents Chemother. 2015, 59, 6824–6833. [CrossRef] [PubMed]
6. Li, Q.; Yu, F.; Song, C.; Zhao, H.; Xiao, Q.; Lao, X.; Yang, S.; Tang, Y.; Zhang, F. HIV-1 Genotypic Resistance Testing Using Sanger and Next-Generation Sequencing in Adults with Low-Level Viremia in China. Infect. Drug Resist. 2022, 15, 6711–6722. [CrossRef] [PubMed]
7. Fox, E.J.; Reid-Bayliss, K.S.; Emond, M.J.; Loeb, L.A. Accuracy of Next Generation Sequencing Platforms. Next Gener Seq. Appl. 2014, 1, 1000106. [CrossRef] [PubMed]
8. Qin, D. Next-Generation Sequencing and Its Clinical Application. Cancer Biol. Med. 2019, 16, 4–10. [CrossRef] [PubMed]
9. Ode, H.; Matsuda, M.; Matsuoka, K.; Hachiya, A.; Hattori, J.; Kito, Y.; Yokomaku, Y.; Iwatani, Y.; Sugiura, W. Quasispecies Analyses of the HIV-1 Near-Full-Length Genome with Illumina MiSeq. Front. Microbiol. 2015, 6, 1258. [CrossRef] [PubMed]
10. Brumme, C.J.; Poon, A.F.Y. Promises and Pitfalls of Illumina Sequencing for HIV Resistance Genotyping. Virus Res. 2017, 239, 97–105. [CrossRef] [PubMed]
11. Struck, D.; Lawyer, G.; Ternes, A.M.; Schmit, J.C.; Bercoff, D.P. COMET: Adaptive Context-Based Modeling for Ultrafast HIV-1 Subtype Identification. Nucleic Acids Res. 2014, 42, e44. [CrossRef] [PubMed]
12. Ávila-Ríos, S.; Parkin, N.; Swanstrom, R.; Paredes, R.; Shafer, R.; Ji, H.; Kantor, R. Next-Generation Sequencing for HIV Drug Resistance Testing: Laboratory, Clinical, and Implementation Considerations. Viruses 2020, 12, 617. [CrossRef]
13. Bonifacio, M.A.; Genchi, C.; Lagioia, A.; Talamo, V.; Volpe, A.; Mariggiò, M.A. Analytical Assessment of the Vela Diagnostics NGS Assay for HIV Genotyping and Resistance Testing: The Apulian Experience. Int. J. Mol. Sci. 2022, 23, 2727. [CrossRef]
14. Armenia, D.; Carioti, L.; Micheli, V.; Bon, I.; Allice, T.; Bonura, C.; Bruzzone, B.; Bracchitta, F.; Cerutti, F.; Giammanco, G.M.; et al. Comparison of Different HIV-1 Resistance Interpretation Tools for Next-Generation Sequencing in Italy. Viruses 2024, 16, 1422. [CrossRef]
15. Fogel, J.M.; Bonsall, D.; Cummings, V.; Bowden, R.; Golubchik, T.; De Cesare, M.; Wilson, E.A.; Gamble, T.; Del Rio, C.; Batey, D.S.; et al. Performance of a High-Throughput next-Generation Sequencing Method for Analysis of HIV Drug Resistance and Viral Load. J. Antimicrob. Chemother. 2020, 75, 3510–3516. [CrossRef] [PubMed]
16. Tekin, D.; Gokengin, D.; Onay, H.; Erensoy, S.; Sertoz, R. Investigation of Drug Resistance against Protease, Reverse Transcriptase, and Integrase Inhibitors by next-Generation Sequencing in HIV-Positive Patients. J. Med. Virol. 2021, 93, 3627–3633. [CrossRef] [PubMed]
17. Bonsall, D.; Golubchik, T.; De Cesare, M.; Limbada, M.; Kosloff, B.; Macintyre-Cockett, G.; Hall, M.; Wymant, C.; Azim Ansari, M.; Abeler-Dörner, L.; et al. A Comprehensive Genomics Solution for HIV Surveillance and Clinical Monitoring in Low-Income Settings. J. Clin. Microbiol. 2020, 58, e00382-20. [CrossRef] [PubMed]
18. Raymond, S.; Nicot, F.; Carcenac, R.; Lefebvre, C.; Jeanne, N.; Saune, K.; Delobel, P.; Izopet, J. HIV-1 Genotypic Resistance Testing Using the Vela Automated next-Generation Sequencing Platform. J. Antimicrob. Chemother. 2018, 73, 1152–1157. [CrossRef] [PubMed]

J PREV MED HYG 2024; 65: E11-E16 OPEN ACCESS

COVID-19

SARS-CoV-2 and influenza virus coinfections in the Tuscan population during the 2021/2022 influenza season

GIOVANNA MILANO[1], SERENA MARCHI[2], ILARIA VICENTI[3], CAMILLA BIBA[3], LIA FIASCHI[3], CLAUDIA MARIA TROMBETTA[2,4], GIACOMO LAZZERI[2,4], EMANUELE MONTOMOLI[2,4,5], ILARIA MANINI[2,4]
[1] Department of Life Science, University of Siena, Siena, Italy; [2] Department of Molecular and Developmental Medicine, University of Siena, Siena, Italy; [3] Department of Medical Biotechnologies, University of Siena, Siena, Italy; [4] Interuniversity Research Center on Influenza and other Transmissible Infections; [5] VisMederi S.r.l., Siena, Italy

Keywords

Coinfection • Population • Respiratory viruses

Summary

Introduction. The 2021/2022 influenza season was not characterised by a well-defined incidence peak. As reported by the Italian National Institute of Health, a high value of incidence of influenza cases was recorded in week 13, but it was still lower than in other influenza seasons. This abnormal circulation was probably due to relaxation of the COVID-19 pandemic restriction measures, such as social dis-tancing, smart-working, home leaning and the use of masks, which greatly reduced the circulation of respiratory-transmitted viruses, including human respiratory syncytial virus (HRSV). The symptoms of SARS-CoV-2 and influenza are quite similar, sharing the human-to-human transmission route via respiratory droplets.

Introduction

SARS-CoV-2 is a non-segmented, enveloped, positive- sense RNA virus that began its worldwide spread in December 2019 [1]. The World Health Organization (WHO) declared the COVID-19 pandemic on March 2020. The virus spread all year round, showing peaks in winter and when social containment measures were relaxed [2]. Influenza is caused by a segmented, negative- sense RNA virus that gives rise to epidemics, mostly in the winter months. Of the four types of influenza viruses, influenza A (IAV) and B (IBV) are mainly responsible for seasonal influenza. Currently, A/H1N1 and A/H3N2 are the most widespread IAV subtypes circulating in the human population [3]. Human respiratory syncytial virus (HRSV) is a seasonal negative-sense RNA virus and prominent cause of acute lower respiratory tract infections in young children [4].

In response to the COVID-19 health emergency and given the absence of specific pharmacological therapies or highly effective vaccines to curb the spread of SARS-CoV-2, many countries adopted non- pharmaceutical mitigation strategies. These strategies included the use of personal protective equipment, implementation of social distancing measures, temporary closure of educational institutions and airports, and mandatory reporting of cases of infection, followed by

Methods. The aim of this study was to estimate the rate of coin-fection with influenza viruses and/or HRSV in SARS-CoV-2-pos-itive subjects (N = 940) in a population of central Italy during the 2021/2022 season.
Results. A total of 54 cases of coinfection were detected during the study period, 51 cases (5.4%) of SARS-CoV-2 and influ-enza virus and three cases (0.3%) of SARS-CoV-2 and HRSV coinfection.
Conclusions. These results highlight the importance of continu-ous monitoring of the circulation of influenza virus and other res-piratory viruses in the context of the COVID-19 pandemic.

isolation of affected individuals. This approach passively influenced the seasonal transmission patterns of airborne viruses, including influenza viruses and HRSV [5, 6]. The 2020/2021 influenza season in Italy was characterized by an initial phase of co-circulation of SARS-CoV-2 and influenza viruses, followed by a rapid decline in influenza transmission due to implementation of non-pharmaceutical measures. However, during the 2021/2022 influenza surveillance season (from week 42 of 2021 to week 17 of 2022), an increase in the incidence of influenza was recorded [7]. The epidemiological curve of influenza-like illness (ILI) cases showed a bimodal trend, peaking at week 52 of 2021 and weeks 12-13 of 2022, when positive samples again rose above the epidemic threshold of 10% positivity [8] (Fig. 1). The first wave was characterized as supported mainly by HRSV circulation, while influenza viruses dominated in the second wave [19].

An increasing number of studies show that patients affected with COVID-19 may also be coinfected with other respiratory pathogens [9-11]. Indeed, the coexistence of SARS-CoV-2 and influenza viruses led to cases of coinfection having more severe symptoms than infections with either virus alone [12].

The present study, performed during the 2021/2022 influenza season, investigated the prevalence of influenza or HRSV coinfections in SARS-CoV-2-positive subjects

Fig. 1. Incidence of influenza-like illness in Italy by week during the 2021/2022 influenza season, according to the Italian National Institute of Health [8].

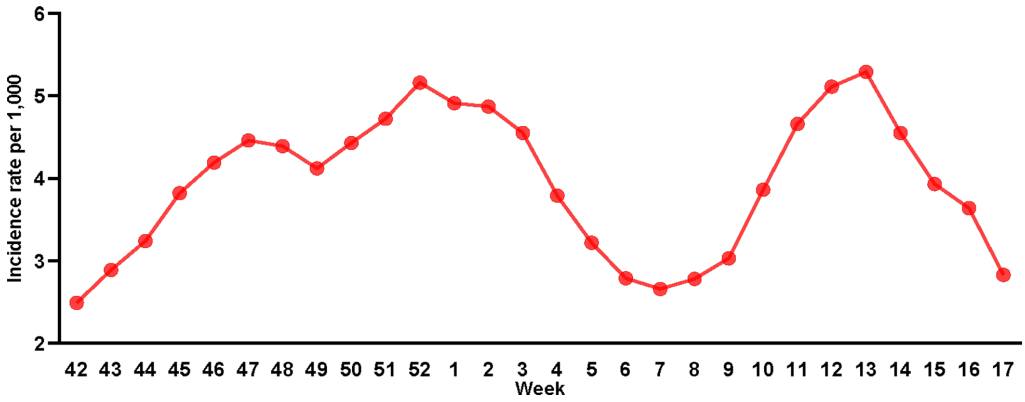

in Tuscany (Italy), with the aim of underlining the importance of continuing epidemiological surveillance of other respiratory viruses in addition to SARS-CoV-2.

Materials and methods

Study design

Oropharyngeal swabs were collected by general practitioners, during the 2021/2022 influenza surveillance season (from week 46 of 2021 to week 17 of 2022) in Siena, Tuscany (Italy), and stored at -80°C. A total of 940 swabs were selected as having previously tested positive for SARS-CoV-2: 742 collected during the first influenza wave (week 46 of 2021 to week 4 of 2022) and 198 during the second (week 5 to week 17 of 2022). Information on the age and sex of the subject was available for 860 swabs. The median age of subjects was 30 years (range 1-65 years), 422 were male and 438 were female. Swabs were divided by age group as follows: 1-10 years (N = 52), 11-20 years (N = 146), 21-30 years (N = 260), 31-40 years (N = 147), 41-50 years (N = 125), and 51-65 years (N = 130). No information on COVID-19 or influenza vaccination status was available. Informed consent was submitted and signed by all patients who voluntarily underwent swabbing

Laboratory analysis

Total RNA was extracted from specimens by QIAamp Viral RNA Mini kit (Qiagen, Hilden, Germany). Real- time reverse transcriptase–polymerase chain reaction tests (RT-PCR) were performed for IAV, IBV and HRSV with Flu/HRSV kit (Siemens) on nasopharyngeal swabs of subjects who had already tested positive for SARS-CoV-2 by COVID-19 HT Screen (Clonit, Abbiategrasso, Italy). At the same time, one-step real- time RT-PCR was performed in a final volume of 25 µL (SuperScript III Platinum One-Step qRT-PCR Kit, Thermo Fisher Scientific, Waltham, MA, USA) to subtype for pandemic influenza virus A/H1N1 (Flu A/ pH1N1) and seasonal influenza virus A/H3N2 (Flu A/ H3N2) on samples positive for IAV. H3-For Primer: AAGCATTCCYAATGACAAACC, H3-Rev Primer: ATT GCR CCR AAT ATG CCT CTA GT, H3-Probe: Fam – 5' CAG GAT CAC A"T"A TGG GSC CTG TCC CAG – 3' SPACER – BHQ-1 and H1pdm-For Primer: GTG CTA TAA ACA CCA GYC TCC CAT T,H1pdm- Rev Primer: AGA YGG GAC ATT CCT CAA TCC TG, H1pdm-Probe: Fam – 5' TGG CCA GYC "T" CA ATT TTG TGC TTT TTA CAT A - 3' SPACER – BHQ-1, were used.

Statistical analysis

The median ages of the total and influenza-positive populations were calculated. The number of SARS-CoV-2/influenza or HRSV coinfection cases by period of collection (first and second influenza waves) and age group (above or below median age, i.e. 30 years) was compared by the Yates corrected chi-square test. Statistical significance was set at $p < 0.05$ (two- tailed test). All statistical analysis was performed using GraphPad Prism 6 software.

Results

A total of 54 cases (5.7%) of coinfection were detected during the study period: 51 cases (5.4%) of SARS-CoV-2 and influenza viruses (43 for IAV and 8 for IBV) and three cases (0.3%) of SARS-CoV-2 and HRSV. Of the influenza cases, 34 cases of IAV were A/H3N2 subtype while the remaining 9 cases were not attributed to a subtype. The 8 cases of IBV were not subtyped.

As reported in Figure 2, most coinfections were detected during the first influenza wave (36/43 cases of IAV, 6/8 cases of IBV and 2/3 cases of HRSV), albeit showing no statistically significant difference with respect to the second wave.

For 860 samples, including all those in which an influenza virus or HRSV coinfection was detected, information on the sex and age of the subjects was available.

Fig. 2. Cases of coinfection with SARS-CoV-2 and human respiratory syncytial (HRSV), influenza A (IAV) or B (IBV) viruses from November 2021 to May 2022. Dashed vertical line separates first (left) and second (right) wave of influenza.

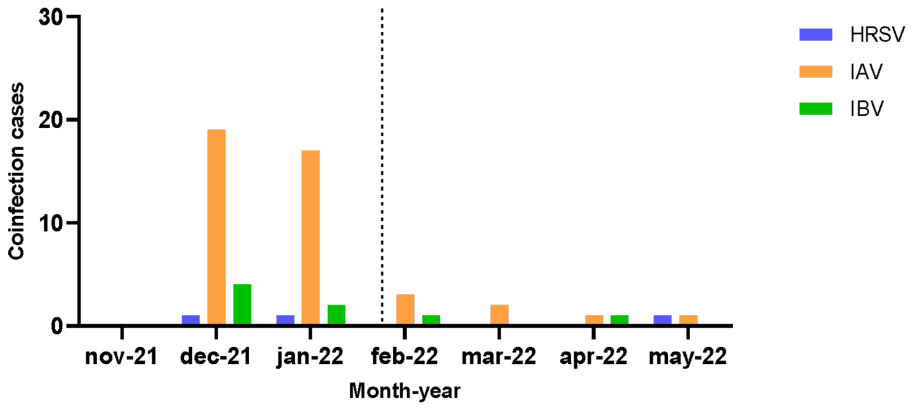

Fig. 3. Cases of coinfection with SARS-CoV-2 and human respiratory syncytial (HRSV), influenza A (IAV) or B (IBV) viruses by age group. Dashed vertical line indicates the median age of the study population (30 years).

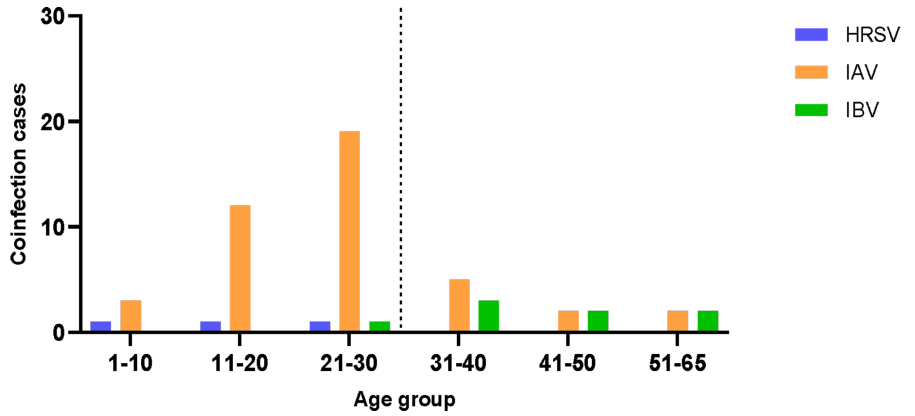

No significant difference in the distribution of cases by sex was found, while Figure 3 shows the distribution of coinfection cases by age.

SARS-CoV-2 coinfections with HRSV were only detected in subjects under 30 years of age (median age of positive subjects 14 years), although the difference was not significant. Coinfections with IAV were detected in all age groups, but the prevalence was higher in subjects of 30 years and under (median age of positive subjects 23 years, $p = 0.0009$), while IBV was detected mainly in subjects of 30 years and over (median age of positive subjects 43 years, $p = 0.0494$). Some PCR results regarding Flu/HRSV kit (Siemens) are shown in Figure 4.

Discussion

In December 2019, identification of a new coronavirus in Wuhan, China, demanded a prompt response and global cooperation by health authorities [6]. The pandemic influenced the seasonal transmission patterns of airborne viruses. SARS-CoV-2 shares transmission through direct contact and airborne contagion as well as symptoms, including fever, cough, sore throat, fatigue, nasal congestion and respiratory distress, with the influenza virus, complicating differentiation of the two infections [5, 6]. Cases of coinfection with SARS-CoV-2 and influenza proved to have symptoms that were more severe [12]. After 2019/2020, the incidence of ILI in Italy declined due to non-pharmaceutical actions imposed for SARS-CoV-2. In the 2021/2022 season, an increase in the incidence of infections caused by influenza viruses was observed, with an overall positivity rate of 14.4% [19] although significantly lower than that observed before the COVID-19 pandemic. Indeed, the season was characterized by low circulation of influenza, the first cases being reported in week 52 of 2021. Circulation increased from week 8 of 2022, reaching a maximum in week 12 of the same year, when COVID-19 restrictions were relaxed [13].

In this study, we found a total of three cases of coinfection of SARS-CoV-2 and HRSV and 51 cases of coinfection of SARS-CoV-2 and influenza viruses: 43 cases of IAV and 8 cases of IBV. Ignoring influenza virus type, influenza coinfection cases were detected in 5.4% of the SARS-CoV-2-positive subjects tested in this study, a coinfection rate in line with those reported in other countries [14-16].

E13

Fig. 4. Representative results of PCR. Green fluorescence for Influenza A positive samples, blue fluorescence for HRSV positive sample.

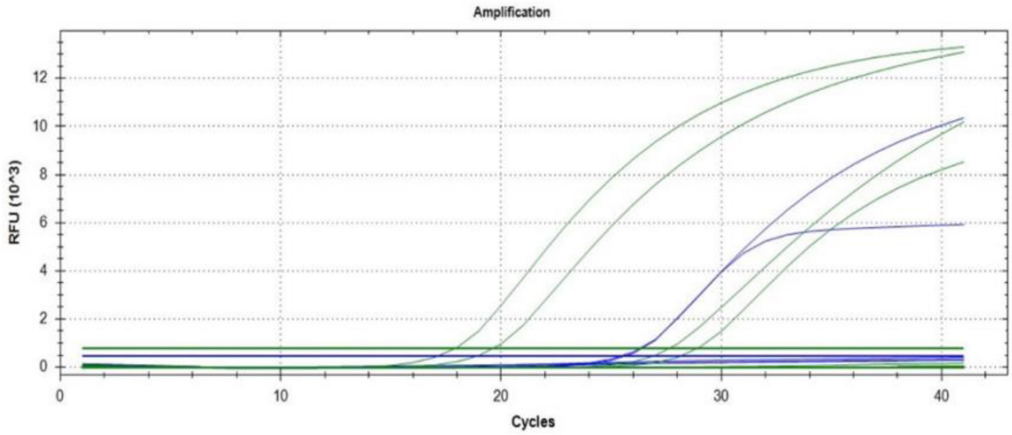

Among IAV cases, 34 were caused by A/H3N2 subtype, in line with Italian and European data reporting it to be the predominant influenza subtype during the 2021/2022 season [17, 18].

The majority of SARS-CoV-2 and influenza coinfections were found during the first wave of the influenza season. A similar distribution was observed in a study conducted in children and adolescents hospitalized in the US, where influenza-associated hospitalizations characterized by influenza and SARS-CoV-2 coinfections were higher in December and January months [20]. IAV and SARS-CoV-2 coinfections were higher in the first months of the season also in a US study conducted in individuals from University of Missouri Health Care [21], suggesting that coinfection with SARS-CoV-2 Omicron variant may have been reduced compared to coinfections with Delta variant, due to different viral antagonism to IAVs. In a surveillance study conducted on hospitalized subjects in Tuscany during the same season, three cases of SARS-CoV-2 and influenza coinfection were found in March in the second half of the influenza season [17]. The same study reported two cases of HRSV infection, one of which involved coinfection with SARS-CoV-2. Both cases occurred in subjects aged 30 years or under, in line with the results of our study. In contrast to our results, a report by Cong et al in a population older than 18 years, the median age of co-infected persons was older than the fifth year [25]. As reported in few studies, in patients with COVID-19-Influenza co-infection, the need for intervention with mechanical ventilation and hospital stay increase compared with patients infected with only one of the two respiratory viruses, suggesting an aggravation of the disease picture [23, 24]. Although it appears that the copresence of the two viruses does not result in increased mortality [25]

Our study has some limitations. Information on clinical features, medication use and outcomes, as well as vaccination status for COVID-19 and/or influenza was not available and sequencing of SARS-CoV-2- and influenza-positive samples was not performed. In addition, since in Italy administration of live attenuated influenza vaccines (LAIV) are authorised for use in persons aged between 2 and 18 years [22], we cannot exclude detection of influenza antigen from vaccinal strains in younger age groups swabs. Moreover, other respiratory viruses potentially coinfecting with SARS-CoV-2, such as parainfluenza viruses, were not included.

Few studies on respiratory virus epidemiology and coinfections have been conducted in Italy in the 2021/2022 season. The 2021/2022 influenza season was peculiar as it saw the partial resurgence of respiratory viruses after the advent of COVID-19, therefore the characterization of as much as possible the epidemiology of respiratory viruses and coinfections with SARS-CoV-2 is of outmost importance to understand the post-pandemic epidemiology of respiratory viruses.

Given the overlapping symptoms and epidemiology of the influenza virus and SARS-CoV-2, it remains of primary importance to conduct differential diagnosis of these major airborne-transmitted viruses to avert complications related to infection. The use of multiplex RT-PCR tests, as in our study, ensures a timely diagnosis and consequently an appropriate clinical approach to each patient. Despite its limitations, our study underscores the significance of continuous monitoring of the circulation of influenza viruses.

Funding

This work received funding from the Italian Ministry of Education, University and Research (PRIN 202022GZEHE_01); EU funding within the NextGenerationEU-MUR PNRR Extended Partnership initiative on Emerging Infectious Diseases (Project no. PE00000007, INF-ACT) and by the EuCARE Project funded by the European Union's Horizon Europe Research and Innovation Program, Grant Agreement No. 101046016.

Informed consent statement

Informed consent was obtained from all subjects involved in the study.

Data availability statement

The data presented in this study are available on request from the corresponding author.

Conflict of interest statement

The authors declare no conflict of interest. The funders had no role in the design of the study; in the collection, analyses, or interpretation of data; in the writing of the manuscript; or in the decision to publish the results.

Authors' contributions

IM, GM: conceptualization. IM: methodology. IM: validation. SM: formal analysis. GM, IV, LF, C.B: investigation. CMT, IM, IV, EM: resources. SM: data curation. GM: writing-original draft preparation. SM: writing-review and editing. SM: visualization. IM: supervision. IM: project administration. All authors have read and agreed to the published version of the manuscript.

References

[1] Zhu N, Zhang D, Wang W, Li X, Yang B, Song J, Zhao X, Huang B, Shi W, Lu R, Niu P, Zhan F, Ma X, Wang D, Xu W, Wu G, Gao GF, Tan W; China Novel Coronavirus Investigat- ing and Research Team. A novel coronavirus from patients with pneumonia in China, 2019. N Engl J Med 2020;382:727-33. https://doi.org/10.1056/NEJMoa2001017.

[2] Civil Protection Department. Available at: https://www.protezi- onecivile.gov.it/en/ (Accessed on: 26/05/2022).

[3] Krammer F, Smith GJD, Fouchier RAM, Peiris M, Kedzierska K, Doherty PC, Palese P, Shaw ML, Treanor J, Webster RG, García-Sastre A. Influenza. Nat Rev Dis Primers 2018;4:3. htt- ps://doi.org/10.1038/s41572-018-0002-y.

[4] Halabi KC, Wang H, Leber AL, Sánchez PJ, Ramilo O, Mejias A. Respiratory syncytial virus and SARS-CoV-2 coinfections in children. Pediatr Pulmonol 2022;57:3158-60. https://doi. org/10.1002/ppul.26127.

[5] Flerlage T, Boyd DF, Meliopoulos V, Thomas PG, Schultz- Cherry S. Influenza virus and SARS-CoV-2: pathogenesis and host responses in the respiratory tract. Nat Rev Microbiol 2021;19:425-41. https://doi.org/10.1038/s41579-021-00542-7.

[6] Ozaras R, Cirpin R, Duran A, Duman H, Arslan O, Bakcan Y, Kaya M, Mutlu H, Isayeva L, Kebanlı F, Deger BA, Bekeshev E, Kaya F, Bilir S. Influenza and COVID-19 coinfection: report of six cases and review of the literature. J Med Virol 2020;92:2657- 65. https://doi.org/10.1002/jmv.26125.

[8] Istituto Superiore della Sanità, Epicentro. Available at: https:// www.epicentro.iss.it/influenza/flunews21-22#epi (Accessed on: 25/10/2023).

[9] Bai L, Zhao Y, Dong J, Liang S, Guo M, Liu X, Wang X, Huang Z, Sun X, Zhang Z, Dong L, Liu Q, Zheng Y, Niu D, Xiang M, Song K, Ye J, Zheng W, Tang Z, Tang M, Zhou Y, Shen C, Dai M, Zhou L, Chen Y, Yan H, Lan K, Xu K. Coinfection with influenza A virus enhances SARS-CoV-2 infectivity. Cell Res 2021;31:395-403. https://doi.org/10.1038/s41422-021-00473- 1.

[10] Burrel S, Hausfater P, Dres M, Pourcher V, Luyt CE, Teyssou E, Soulié C, Calvez V, Marcelin AG, Boutolleau D. Co-infection of SARS-CoV-2 with other respiratory viruses and performance of lower respiratory tract samples for the diagnosis of COV- ID-19. Int J Infect Dis 2021;102:10-3. https://doi.org/10.1016/j. ijid.2020.10.040.

[11] Xiaojuan Z, Yiyue G, Tao W, Kangchen Z, Yin C, Bin W, Feng- cai Z, Baoli Z, Lunbiao C. Co-infection with respiratory patho- gens among COVID-2019 cases. Virus Res 2020;285:198005. https://doi.org/10.1016/j.virusres.2020.198005.

[12] Uyeki TM, Hui DS, Zambon M, Wentworth DE, Monto AS. Influenza. Lancet 2022;400:693-706. https://doi.org/10.1016/ S0140-6736(22)00982-5.

[13] Rapporto Influnet. Available at: https://www.iss.it/site/rmi/in- flunet/pagine/rapportoinflunet.aspx (Accessed on: 09/02/2023).

[14] Steponavičienė A, Burokienė S, Ivaškevičienė I, Stacevičienė I, Vaičiūnienė D, Jankauskienė A. Influenza and respiratory syncytial virus infections in pediatric patients during the COV- ID-19 pandemic: a single-center experience. Children (Basel) 2023;10:126. https://doi.org/10.3390/children10010126.

[15] Trifonova I, Christova I, Madzharova I, Angelova S, Voleva S, Yordanova R, Tcherveniakova T, Krumova S, Korsun N. Clinical significance and role of coinfections with respiratory pathogens among individuals with confirmed severe acute res- piratory syndrome coronavirus-2 infection. Front Public Health 2022;10:959319. https://doi.org/10.3389/fpubh.2022.959319. Saeedeh. E.; Mojtaba. K.; Barat. B.; Nayeb. F.D.; Zahra. N.; Tahereh. N.; Faezeh. S. The circulation of common respiratory viruses and their co-infection with severe respiratory syndrome coronavirus 2 before and after coronavirus disease of 2019 vac- cination. Jundishapur J Microbiol 2022;15:e133326. Https:// doi.org/10.5812/jjm-133326.

[16] Milano G, Capitani E, Camarri A, Bova G, Capecchi PL, Lazzeri G, Lipari D, Montomoli E, Manini I. Surveillance of influenza and other airborne transmission viruses during the 2021/2022 season in hospitalized subjects in Tuscany, Italy. Vaccines (Ba- sel) 2023;11:776. https://doi.org/10.3390/vaccines11040776.

[17] Istituto Superiore della Sanità, Epicentro. Available at: https:// www.epicentro.iss.it/influenza/flunews#vir (Accessed on: 26/05/2022).

[18] Istituto Superiore della Sanità, Epicentro. Available at: https:// www.epicentro.iss.it/ben/2022/4/virus-influenzali-vaccinazi o- ni-influnet-2021-2022 (Accessed on: 19/12/2023).

[19] Adams K, Tastad KJ, Huang S, Ujamaa D, Kniss K, Cum- mings C, Reingold A, Roland J, Austin E, Kawasaki B, Meek J, Yousey-Hindes K, Anderson EJ, Openo KP, Reeg L, Leegwater L, McMahon M, Bye E, Poblete M, Landis Z, Spina NL, En- gesser K, Bennett NM, Gaitan MA, Shiltz E, Moran N, Sutton M, Abdullah N, Schaffner W, Talbot HK, Olsen K, Staten H, Taylor CA, Havers FP, Reed C, Budd A, Garg S, O'Halloran A, Brammer L. Prevalence of SARS-CoV-2 and influenza coinfec- tion and clinical characteristics among children and adolescents aged < 18 years who were hospitalized or died with influenza – United States, 2021-22 influenza season. MMWR Morb Mortal Wkly Rep 2022;71:1589-96. https://doi.org/10.15585/mmwr. mm7150a4.

[7] Istituto Superiore della Sanità, Epicentro. Available at: https://www.epicentro.iss.it/influenza/stagione-in-corso (Accessed on: 01/07/2022).

[20] Tang C, Boftsi M, Staudt L., Jane A. McElroy e, Tao Li f, Duong S, Adrienne Ohler g, Detlef Ritter h, Richard Hammer d,h, Jun Hang f, XiuFeng Wan. SARS-CoV-2 and influenza co-

infection: a cross-sectional study in central Missouri during the 2021-2022 influenza season. Virology 2022:576:105-10.https://doi.org/10.1016/j.virol.2022.09.009.

[21] Ministero della Salute, Available at: https://www.salute.gov.it/portale/p5_1_2.jsp?id=103&lingua=italiano#:~:text =%C3%88%20indicato%20dai%2018%20anni%20di%20et%C3%A0.&text=Il%20vaccino%20vivo%20attenuato%20%C3%A8,tra%202%20e%2018%20anni (Accessed on 19/12/2023).

[22] Garg I, Gangu K, Shuja H, Agahi A, Sharma H, Bobba A, Nas- rullah A, Chourasia P, Pal S, Sheikh AB, Shekhar R. COVID-19 and influenza coinfection outcomes among hospitalized pa- tients in the United States: a propensity matched analysis of national inpatient sample. Vaccines (Basel) 2022;10:2159. https:// doi.org/10.3390/vaccines10122159.

[23] Swets MC, Russell CD, Harrison EM, Docherty AB, Lone N, Girvan M, Hardwick HE; ISARIC4C Investigators; Visser LG, Openshaw PJM, Groeneveld GH, Semple MG, Baillie JK. SARS-CoV-2 co-infection with influenza viruses, respiratory syncytial virus, or adenoviruses. Lancet 2022;399:1463-4. htt- ps://doi.org/10.1016/S0140-6736(22)00383-X.

[24] Cong B, Deng S, Wang X, Li Y. The role of respiratory co-infec- tion with influenza or respiratory syncytial virus in the clinical severity of COVID-19 patients: a systematic review and meta- analysis. J Glob Health 2022;12:05040. https://doi.org/10.7189/ jogh.12.05040.

Received on January 16, 2024. Accepted on March 13, 2024.

Correspondence: Ilaria Manini, Department of Molecular and Developmental Medicine, University of Siena, via Aldo Moro 2, 53100, Siena. E-mail: ilaria.manini@unisi.it

How to cite this article: Milano G, Marchi S, Vicenti I, Biba C, Fiaschi L, Trombetta CM, Lazzeri G, Montomoli E, Manini I. SARS-CoV-2 and influenza virus coinfections in the Tuscan population during the 2021/2022 influenza season. J Prev Med Hyg 2024;65:E11-E16. https://doi.org/10.15167/2421-4248/jpmh2024.65.1.3179

viruses

MDPI

Article

In Vitro Combinatorial Activity of Direct Acting Antivirals and Monoclonal Antibodies against the Ancestral B.1 and BQ.1.1 SARS-CoV-2 Viral Variants

Lia Fiaschi †, Camilla Biba †, Ilenia Varasi, Niccolò Bartolini, Chiara Paletti, Federica Giammarino, Francesco Saladini, Maurizio Zazzi and Ilaria Vicenti *

Department of Medical Biotechnologies, University of Siena, 53100 Siena, Italy; lia.fiaschi@unisi.it (L.F.); camilla.biba@student.unisi.it (C.B.); ilenia.varasi@student.unisi.it (I.V.); niccolo.bartolini@student.unisi.it (N.B.); c.paletti@student.unisi.it (C.P.); federica.giammari@gmail.com (F.G.); saladini6@unisi.it (F.S.); maurizio.zazzi@unisi.it (M.Z.)

* Correspondence: vicenti@unisi.it

† These authors contributed equally to this work.

Abstract: Combination antiviral therapy may be helpful in the treatment of SARS-CoV-2 infection; however, no clinical trial data are available, and combined use of direct-acting antivirals (DAA) and monoclonal antibodies (mAb) has been reported only anecdotally. To assess the cooperative effects of dual drug combinations in vitro, we used a VERO E6 cell-based in vitro system with the ancestral B.1 or the highly divergent BQ.1.1 virus to test pairwise combinations of the licensed DAA, including nirmatrelvir (NRM), remdesivir (RDV) and the active metabolite of molnupiravir (EIDD-1931) as well the combination of RDV with four licensed mAbs (sotrovimab, bebtelovimab, cilgavimab, tixagevimab; tested only with the susceptible B.1 virus). According to SynergyFinder 3.0 summary and weighted scores, all the combinations had an additive effect. Within DAA/DAA combinations, paired scores with the B.1 and BQ.1.1 variants were comparable. In the post hoc analysis weighting synergy by concentrations, several cases of highly synergistic scores were detected at specific drug concentrations, both for DAA/DAA and for RDV/mAb combinations. This was supported by in vitro confirmation experiments showing a more than a linear shift of a drug-effective concentration (IC_{50}) at increasing concentrations of the companion drug, although the effect was prominent with DAA/DAA combinations and minimal or null with RDV/mAb combinations. These results support the cooperative effects of dual drug combinations in vitro, which should be further investigated in animal models before introduction into the clinic.

Keywords: SARS-CoV-2; mAb; DAA; combination antiviral therapy; in vitro synergism; Omicron variant

Citation: Fiaschi, L.; Biba, C.; Varasi, I.; Bartolini, N.; Paletti, C.; Giammarino, F.; Saladini, F.; Zazzi, M.; Vicenti, I. In Vitro Combinatorial Activity of Direct Acting Antivirals and Monoclonal Antibodies against the Ancestral B.1 and BQ.1.1 SARS-CoV-2 Viral Variants. Viruses 2024, 16, 168. https://doi.org/10.3390/v16020168

Academic Editor: Luis Martinez-Sobrido

Received: 4 January 2024
Revised: 19 January 2024
Accepted: 20 January 2024
Published: 23 January 2024

1. Introduction

Severe Acute Respiratory Syndrome Coronavirus 2 (SARS-CoV-2), which causes coro-navirus disease 2019 (COVID-19), has expanded worldwide since its emergence in China in December 2019, resulting in a global pandemic with more than 700 million confirmed cases and about 7 million deaths documented as of September 2023 (https://COVID19.who.int/ accessed on 20 September 2023). Massive vaccination and natural SARS-CoV-2 infections and reinfections have progressively expanded immunity to SARS-CoV-2, drastically re-ducing the incidence of COVID-19 and its severe outcomes in the immunocompetent population. As a result, the end to COVID-19 as a global health emergency was declared in May 2023 by the World Health Organization (https://www.who.int/europe/emergencies/ situations/COVID-19 accessed on 20 September 2023). However, SARS-CoV-2 continues to circulate endemically in the global population, causing serious illness in the most fragile categories, such as elderly people comorbid and immunocompromised patients [1,2]. The

persistent circulation of SARS-CoV-2 in the human population has been driven by the ability to evade the host immune response, particularly since the emergence of the Omicron variant and the plethora of its sublineages, which continue to evolve rapidly and challenge population immunity [3]. In addition, waning immunity combines with decreased vac-cine acceptance to pave the way to novel epidemic waves [4]. Thus, early treatment of symptomatic patients with available antiviral medications remains crucial to protect fragile individuals and limit virus spread and evolution.

Currently, available anti-SARS-CoV-2 agents include the direct-acting antivirals (DAA) remdesivir (RDV), molnupiravir (MNP), and ritonavir-boosted nirmatrelvir (NRM) as well as anti-spike monoclonal antibodies (mAb) [5]. Unfortunately, continued virus evolution has progressively decreased or abolished mAb neutralization activity, with few cases of restored activity against the currently dominating virus lineages [6]. On the other hand, DAA has maintained their activity across multiple variants due to the high conservation of the targeted viral enzymes [7]. However, current DAA may be unable to fully prevent severe disease progression, and their use is limited by a number of drug–drug interactions (NRM), inconvenient administration (RDV), or mutagenicity concerns (MNP) [8]. Indeed, the development of novel drugs or different therapeutic approaches remains a key priority [9]. While waiting for novel agents, one option recently gaining interest is to combine available drugs into a drug cocktail based on the long-standing success of combination therapy in HIV and HCV infection [10]. The key advantage of this approach is that each drug used in the combination can act at a different step in the virus replication cycle, increasing the effectiveness of the treatment while reducing the emergence of drug-resistant viral variants. Interestingly, if the drugs interact synergistically, the active dose can be reduced with respect to monotherapy, potentially lowering toxicity. Although no combination therapy is approved for the treatment of COVID-19, some studies have recently evaluated the combined effect of licensed or candidate anti-SARS-CoV-2 compounds in vitro [11–14] and in animal models [15,16] and anecdotal cases of combined administration of two anti-SARS-CoV-2 treatments in clinical practice have been reported [17–20].

In this work, we evaluated the in vitro interactions between approved anti-SARS-CoV-2 compounds in a live virus cell-based assay using the prototype SARS-CoV-2 B.1 virus and a more recent omicron lineage (BQ.1.1). We included all the three DAA (RDV, MNP, NRM) plus the four mAb which maintained activity during the initial evolution of the Omicron lineage.

2. Materials and Methods

2.1. Cells and Viral Stocks

The VERO E6 monkey cell line (ATCC® CRL-1586) was used to propagate and titrate the viral stocks and to determine the antiviral activity of the antiviral compounds, alone or in combination. VERO E6 cells were propagated in DMEM High Glucose medium (Euroclone, Pero, Italy) supplemented with 10% Fetal Bovine Serum (FBS) and 1% Streptomycin/Penicillin (PS) (Euroclone, Pero, Italy) in a humidified incubator at 37 °C with 5% CO_2. The same medium with a lower FBS concentration (1%) was used for viral infection experiments. For all DAA activity experiments, VERO E6 cells were pre-treated with 0.5 µM CP-100356 hydrochloride inhibitor to reduce the efflux activity of P-glycoprotein, which is overexpressed by this cell line [21,22].

The SARS-CoV-2 stocks used for the experiments included the wild type B.1 (GI-SAID code EPI_ISL_2472896) and the Omicron BQ.1.1 (EPI_ISL_17257516) variant, kindly provided by the Department of Biomedical and Clinical Sciences Luigi Sacco, University of Milan, Italy. Viral stocks were expanded in VERO E6 cells and titrated as previously described [23].

2.2. Drugs and Cytotoxicity Assay

The P-glycoprotein inhibitor CP-100356 (cat. HY-108347) and the DAA, including RDV (cat. HY-104077), NRM (cat. HY-138687) and EIDD-1931 (the active metabolite of MNP;

cat. HY-125033), were supplied by MedChemExpress (Monmouth Junction, NJ, USA) as powder and dissolved in 100% dimethyl sulfoxide (DMSO). Biosimilar mAb, including bebtelovimab (BEB; ref. PXTA1750-100), sotrovimab (SOT; ref. PXTA1637-100), tixagevimab (TIX; ref. PXTA1032-100) and cilgavimab (CIL; ref. PXTA1033-100) were supplied by ProteoGenix SAS (Schiltigheim, France) as powder and dissolved in phosphate-buffered saline (PBS).

The cytotoxicity of all investigated compounds was assayed in VERO E6 cells as previously described [22]. Briefly, cell viability was calculated using the CellTiter Glo 2.0 Luminescent Cell Viability Assay (Promega, Madison, WI, USA), and luminescence values were measured using the GloMax® Discover Multimode Microplate Reader (Promega, Madison, WI, USA) and elaborated with the GraphPad PRISM software version 9.0 (La Jolla, CA, USA). The half-maximal cytotoxic concentration (CC_{50}) and the compound con-centration allowing 90% cell viability (CC_{10}) were calculated using a non-linear regression analysis of the dose–response curves and the ECanything GraphPad function. The CC_{10} was used for each compound as the starting concentration in the antiviral activity assay.

2.3. Antiviral Activity Assay

To determine the antiviral activity of each compound against the B.1 and BQ.1.1 SARS-CoV-2 variants, a direct yield reduction assay, based on the infection of cells in the presence of serial drug dilutions, was performed as previously described [22]. The day before the infection, 6000 VERO E6 cells per well were pre-seeded on 96-well adhesion plates to ensure 70% confluence on the day of infection. Cells were treated with 4-fold decreasing concentrations of each antiviral and after 1 h incubation at 37 °C with 5% CO_2, the cells were infected at 0.005 multiplicity of infection (MOI). To test mAb activity, the viral stocks were pre-incubated at MOI 0.005 with mAb dilutions for 1 h at 37 °C and then the virus/mAb mixture was transferred onto semiconfluent pre-seeded VERO E6 cells. In both cases, after an additional 72 h incubation, cell viability was measured with CellTiter Glo 2.0. The half-maximal inhibitory concentration (IC_{50}) was calculated using a non-linear regression analysis of the dose–response curves generated with GraphPad PRISM. Infected and uninfected cells without drugs were used to calculate the 0% and 100% cell viability, respectively, and used to normalize the results.

The different DAA combinations (NRM/EIDD-1931, NRM/RDV, RDV/EIDD-1931) were evaluated against the B.1 and BQ.1.1 variants. In addition, RDV only was tested in combination with the four mAb (RDV/SOT, RDV/BEB, RDV/CIL, RDV/TIX) based on convenience in the perspectives of clinical use since both RDV and mAb must be admin-istered parenterally. These combinations could only be tested against the B.1 prototype virus because none of the mAb considered was active against the BQ.1.1 variant. The protocol previously described to determine the antiviral activity of individual compounds was adapted to the dual compound combinations. To generate the dual combinations, six 4-fold serial dilutions of the first compound were mixed with six 4-fold serial dilutions of the second compound in 96-well plates to obtain 36 different combos in a two-dimensional matrix. Briefly, for the DAA combos, the drug combination matrix was incubated for 1 h at 37 °C on pre-seeded semiconfluent VERO E6 cells, and the cultures were then infected with B.1 and BQ.1.1 viral stock at 0.005 MOI. For the mAb/antiviral combos, the B.1 viral stock was pre-incubated for 1 h at 37 °C with mAb dilutions, and then the virus/mAb mixture was transferred at 0.005 MOI onto VERO-E6 cells pretreated with serial DAA dilutions. For both conditions, infected cells were incubated for an additional 72 h at 37 °C with 5% CO_2, and cell viability was calculated with the Cell Titer-Glo 2.0 protocol as described above. Each plate also included the dose–response curves for each individual compound, a mock infection control, and an infection control without antivirals to normalize the results. Two independent experiments were performed for each combination.

2.4. Dose-Effect Relationships with Compound Combinations

Antiviral activity data derived from compound combinations were analyzed using the online SynergyFinder 3.0 tool (https://synergyfinder.fimm.fi/ accessed on 12 October 2023). This version of the software was recently implemented with post-analysis options enabling better exploration and interpretation of the dose-effect relationships between antiviral agents at any tested concentration [24]. The default Zero interaction potency (ZIP) model was used to determine the type of drug–drug interaction by comparing the change in the potency of the dose–response curves between individual drugs and their combinations. The ZIP model combines the advantages of both the Loewe additivity and the Bliss independence models, aiming at a systematic assessment of various types of drug interaction patterns that may arise in a high-throughput drug combination screening [25]. Briefly, the Loewe additivity model quantifies the excess over the expected response as if the two drugs were the same drug, while the Bliss model computes the drug–drug interaction effect with respect to a multiplicative effect between two drugs acting independently from each other. For each dual compound combination, the results were expressed as a single summary Synergy Score (SS), which is averaged over all the dose combination measurements and is interpreted as the percent change in response due to drug interactions with respect to the effect of the individual drugs (e.g., a synergy score of 20 indicates 20% increased activity beyond expectation). The interaction is visualized using 2D and 3D synergy maps that highlight the synergistic and antagonistic dose areas in red and green, respectively. As per the indications of the system, an antagonistic, additive, and synergistic effect of the drug combination is defined by a summary SS value below or equal to −10, from −10 to 10, and above 10, respectively [24]. In addition, SynergyFinder 3.0 implements a "Weighting synergy by concentrations" post hoc analysis, returning a weighted SS metric as a measure of synergy at lower drug dose windows where toxicity is less likely and clinical application is favored [24].

To confirm the results obtained by SynergyFinder 3.0, we selected drug concentrations that were repeatedly detected as synergistic (SS > 10) in the drug–drug matrix and directly measured the IC_{50} shift of the drug combination in experiments where Compound 1 at three fixed concentrations (IC_{50} plus two 2-fold dilutions) was mixed with six 4-fold decreasing concentrations of Compound 2. The three Compound 2 IC_{50} values obtained in the presence of the fixed concentrations of Compound 1 were compared with the IC_{50} of Compound 2 alone, and three corresponding fold shift values in Compound 2 IC_{50} were calculated as IC_{50} [Compound 2 alone]/IC_{50} [Compound 1 + Compound 2].

2.5. Statistical Analysis

SynergyFinder 3.0 does not perform any statistical comparison among summary or weighted SS values obtained with different compound combinations. Since the summary SS is the average of all the individual SS obtained with all the concentration pairs tested, the overall combinatorial effects of the three DAA pairs, as well as those of the three RDV/mAb groups, were compared using the Kruskal–Wallis test, followed by Mann–Whitney pairwise comparisons between groups. SS values obtained with the same DAA/DAA concentrations against the B.1 and BQ.1.1 viral variants were compared using the Wilcoxon signed rank test. Analyses were performed using IBM SPSS Statistics, version 20 (IBM Corp., Armonk, NY, USA), and all p-values were 2-sided.

3. Results

The IC_{50} of EIDD-1931, RDV and NRM, when tested alone, were 2.40 ± 0.40/ 1.59 ± 0.44, 0.06 ± 0.03/0.03 ± 0.01 and 0.10 ± 0.03/0.10 ± 0.01 µM against B.1/BQ.1.1, respectively. The mAb tested, namely CIL, TIX, BEB, and SOT were active only against the wild type B.1 SARS-CoV-2 variant (IC_{50} values: 0.20 ± 0.13, 0.07 ± 0.04, 0.03 ± 0.01, 0.81 ± 0.32 µg/mL, respectively). All the IC_{50}, CC_{50}, and CC_{10} values are reported in Table 1.

Table 1. Cytotoxicity and anti-SARS-CoV-2 activity of nirmatrelvir (NRM), EIDD-1931 (the active form of molnupiravir), remdesivir (RDV), sotrovimab (SOT), bebtelovimab (BEB), cilgavimab (CIL) and tixagevimab (TIX) in VERO-E6 cells. The antivirals were tested against the Wild Type B.1 strain and the BQ.1.1 Omicron variant. CC_{50}: half-maximal toxic drug concentration; CC_{10}: drug concentration causing 10% cells cytotoxicity; IC_{50}: half-maximal inhibitor drug concentration; IC_{90}: drug concentration inhibiting 90% of viral replication; SD: Standard Deviation; NA: Not Active.

	CC_{50} µM Mean ± SD	CC_{10} µM Mean ± SD	IC_{50} µM vs. B.1 Mean ± SD	IC_{90} µM vs. B.1 Mean ± SD	IC_{50} µM vs. BQ.1.1 Mean ± SD	IC_{90} µM vs. BQ.1.1 Mean ± SD
NRM	40.7 ± 4.0	2.9 ± 0.2	0.1 ± 0.03	0.2 ± 0.1	0.1 ± 0.01	0.2 ± 0.01
EIDD-1931	43.3 ± 6.0	3.1 ± 0.4	2.4 ± 0.4	2.5 ± 0.1	1.6 ± 0.4	1.8 ± 0.7
RDV	17.2 ± 0.2	4.2 ± 0.6	0.06 ± 0.03	0.2 ± 0.05	0.03 ± 0.01	0.1 ± 0.01
	CC_{50} ng/mL Mean ± SD	CC_{10} ng/mL Mean ± SD	IC_{50} ng/mL vs. B.1 Mean ± SD	IC_{90} ng/mL vs. B.1 Mean ± SD	IC_{50} µM vs. BQ.1.1 Mean ± SD	IC_{90} µM vs. BQ.1.1 Mean ± SD
SOT	>2400	>2400	813 ± 324	1718 ± 594	NA	NA
BEB	>60	>60	33 ± 7 204	89 ± 9 1385	NA	NA
CIL	>360	>360	±1354	± 862	NA	NA
TIX	>360	>360	68 ± 41	305 ± 71	NA	NA

The DAA combos tested against the wild type B.1 and BQ.1.1 strains were NRM/EIDD-1931, NRM/RDV, and RDV/EIDD-1931 while all mAb were tested only against the wild type B.1 strain in combination with RDV, the only injectable DAA (RDV/SOT, RDV/BEB, RDV/CIL, RDV/TIX). To evaluate DAA/DAA or RDV/mAb interactions, we analyzed the data generated from combination experiments using the SynergyFinder 3.0 software and applying the ZIP multiple synergy algorithm that combines Bliss and Loewe reference models and returns summary SS and weighted SS metrics averaging the results over all the dose combination measurements and at clinically relevant lower drug dose windows, respectively. An example of the output generated by analyzing the 36-cell matrix obtained with the NRM/RDV combo against the B.1 SARS-CoV-2 strain is shown in Figure 1. The weighted SS for all the DAA combinations indicated additivity against B.1 (2.1 ± 0.4 for NRM/EIDD-1931, 1.9 ± 1.4 for NRM/RDV and 0.9 ± 0.7 for RDV/EIDD-1931) and BQ.1.1 (0.0 ± 0.7 for NRM/EIDD-1931, 2.1 ± 2.1 for NRM/RDV and 1.7 ± 2.5 for RDV/EIDD-1931). Additivity was also observed for all RDV/mAb combos against B.1 (6.1 ± 2.9 for RDV/SOT, 4.2 ± 3.3 for RDV/BEB, 0.8 ± 0.1 for RDV/CIL and 2.6 ± 2.7 for RDV/TIX). The more comprehensive summary score metric confirmed additivity for all the combinations tested. Summary and weighted SS are indicated in Table 2, while the 2-D Synergy plots generated by each experiment are shown in Supplementary Figure S1.

Despite the overall additive effect shown by summary and weighted SS for all the combinations, there were specific drug combo concentrations below to the IC_{90} of the indi-vidual drugs, showing synergy. Table 3 shows these cases, stratified by their SS (10–29.9, 30–50, and above 50). The highest SS were obtained for several RDV/mAb concentrations, particularly with SOT, BEB, and TIX, which was also reflected by the highest overall sum-mary and weighted SS (Table 2). Among DAA combinations, only NRM/RDV reached the highest SS stratum, but only at one concentration, while hits at lower synergistic strata were detected for NRM/EIDD-1931, RDV/EIDD-1931, and again NRM/RDV. The number of hits showing synergy for NRM/EIDD-1931, NRM/RDV, and RDV/EIDD-1931 was 5, 6, and 2, respectively. When comparing SS values obtained with all the DAA/DAA and DAA/mAb combinations and the B.1 virus, the Kruskal–Wallis test revealed signifi-cant differences ($p < 0.001$), and post hoc pairwise analysis detected significantly higher synergy for RDV/SOT compared with the other RDV/mAb combinations (RDV/BEB, $p = 0.006$; RDV/CIL, $p < 0.001$; RDV/TIX, $p = 0.006$) and with two DAA/DAA combina-tions (NRM/EIDD-1931, $p < 0.001$; NRM/RDV, $p = 0.010$; RDV/EIDD-1931, $p = 0.004$). However, weighted SS values indicating synergistic effects often were outliers in the overall distribution of data points for most dual combinations (Supplementary Figure S2). SS

values remained significantly higher for the RDV/SOT combo when comparing only the four DAA/mAb combinations ($p < 0.001$ compared with RDV/CIL and $p = 0.002$ compared with RDV/BEB and RDV/TIX). Within the DAA/DAA combination subset, a comparable number of cases showing synergy was detected with the B.1 and BQ.1.1 viruses (8 each), and there was no statistically significant difference in the SS values when comparing B.1 to BQ.1.1 at paired DAA/DAA concentrations ($p = 0.153$).

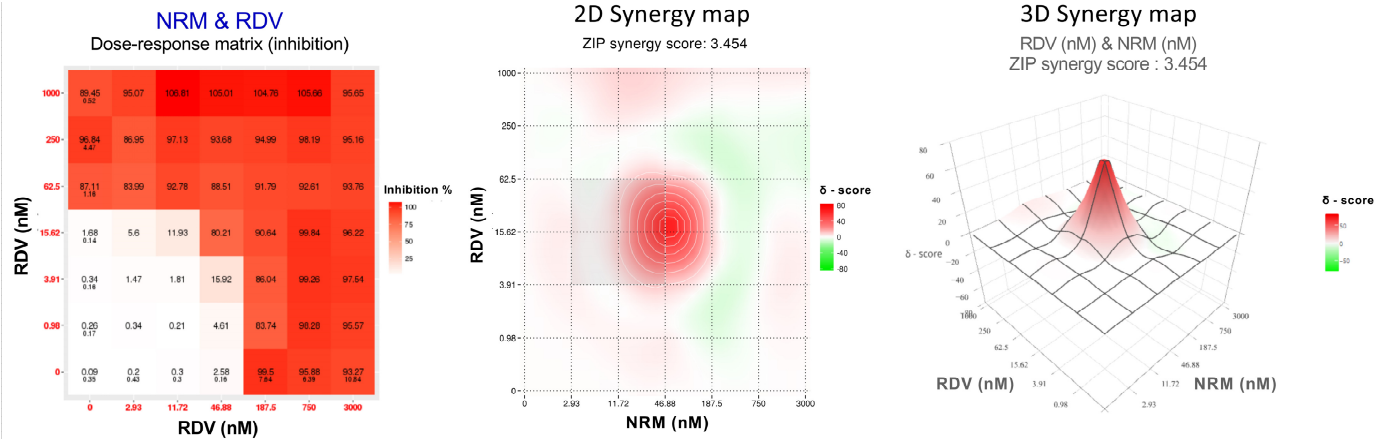

Figure 1. Dose–response matrix, two-dimensional (2D) and three-dimensional (3D) synergy maps gen-erated using SynergyFinder 3.0 by applying the ZIP model on the Nirmatrelvir (NRM)/Remdesivir (RDV) combination tested against the ancestral B.1 SARS-CoV-2 strain.

Table 2. Summary synergy scores (SS) and weighted SS of all the tested antiviral combinations generated using the Synergy Finder 3.0 online software (https://synergyfinder.fimm.fi/ accessed on 12 October 2023). The antiviral pairwise combinations of nirmatrelvir (NRM), EIDD-1931 (the active form of molnupiravir), and remdesivir (RDV) were tested against the ancestral B.1 and the Omicron BQ.1.1 SARS-CoV-2 variant. The combinations of RDV with each of the four monoclonal antibodies (mAb), including sotrovimab (SOT), bebtelovimab (BEB), cilgavimab (CIL), and tixagevimab (TIX), were tested only against the ancestral B.1 SARS-CoV-2 variant. NP: Not performed.

	Summary SS vs. B.1 Mean ± SD	Weighted SS vs. B.1 Mean ± SD	Summary SS vs. BQ.1.1 Mean ± SD	Weighted SS vs. BQ.1.1 Mean ± SD
NRM/EIDD-1931	−3.1 ± 3.1	2.1 ± 0.4	−2.7 ± 1.3	0.0 ± 0.7
RDV/EIDD-1931	0.4 ± 6.2 2.0	0.9 ± 0.7	2.6 ± 6.5	1.7 ± 2.5
NRM/RDV	± 2.0 8.8 ±	1.9 ± 1.4	−0.2 ± 3.7	2.1 ± 2.1
RDV/SOT RDV/BEB	10.3 5.7 ±	6.1 ± 2.9	NP NP	NP NP
RDV/TIX	2.6 0.6 ± 6.4	4.2 ± 3.3	NP	NP
RDV/CIL	−2.0 ± 0.5	2.6 ± 2.7	NP	NP
		0.8 ± 0.1		

As a proof of concept, the IC_{50} synergistic potency shift was measured in infected cells treated with three fixed drug concentrations of the first compound plus scalar concentra-tions of the second compound. As a fixed drug, we selected NRM and RDV because they repeatedly showed synergy at specific concentrations (0.05 and 0.02 µM, respectively) close to their IC_{50} (Table 3). As shown in Figure 2 and in Supplementary Table S1, the IC_{50} of NRM with the addition of RDV 0.06 µM and 0.03 µM was reduced by 33- and 8-fold against B.1 and by >140- and 14-fold against BQ.1.1, respectively. A synergistic potency shift in EIDD-1931 IC_{50} was also induced by the addition of NRM at 0.1 µM and 0.05 µM against B.1 (88- and 11-fold, respectively) and against BQ.1.1 (28- and 7-fold, respectively) and by the addition of RDV at 0.06 µM and 0.03 µM against B.1 (>26- and 26-fold, respectively) and against BQ.1.1 (>30- and 30-fold, respectively). As shown in Figure 2 and in Supplementary

Table S1, lower synergistic potency shifts were observed when fixed RDV concentrations were tested in combination with mAb. Indeed, the addition of RDV 0.06 µM reduced SOT, BEB, and TIX IC_{50} by 4-, 2- and 3-fold, respectively, while the addition of RDV 0.03 µM re-duced SOT and TIX IC_{50} by 2-fold and did not affect BEB IC_{50}. At the lowest concentration tested (0.015 µM), RDV induced a 2-fold reduction only in SOT IC_{50}. In conclusion, the results obtained in the proof-of-concept experiments suggested a synergistic interaction with the DAA/DAA combinations; however, a cooperative effect between RDV and mAb was measurable only for RDV/SOT.

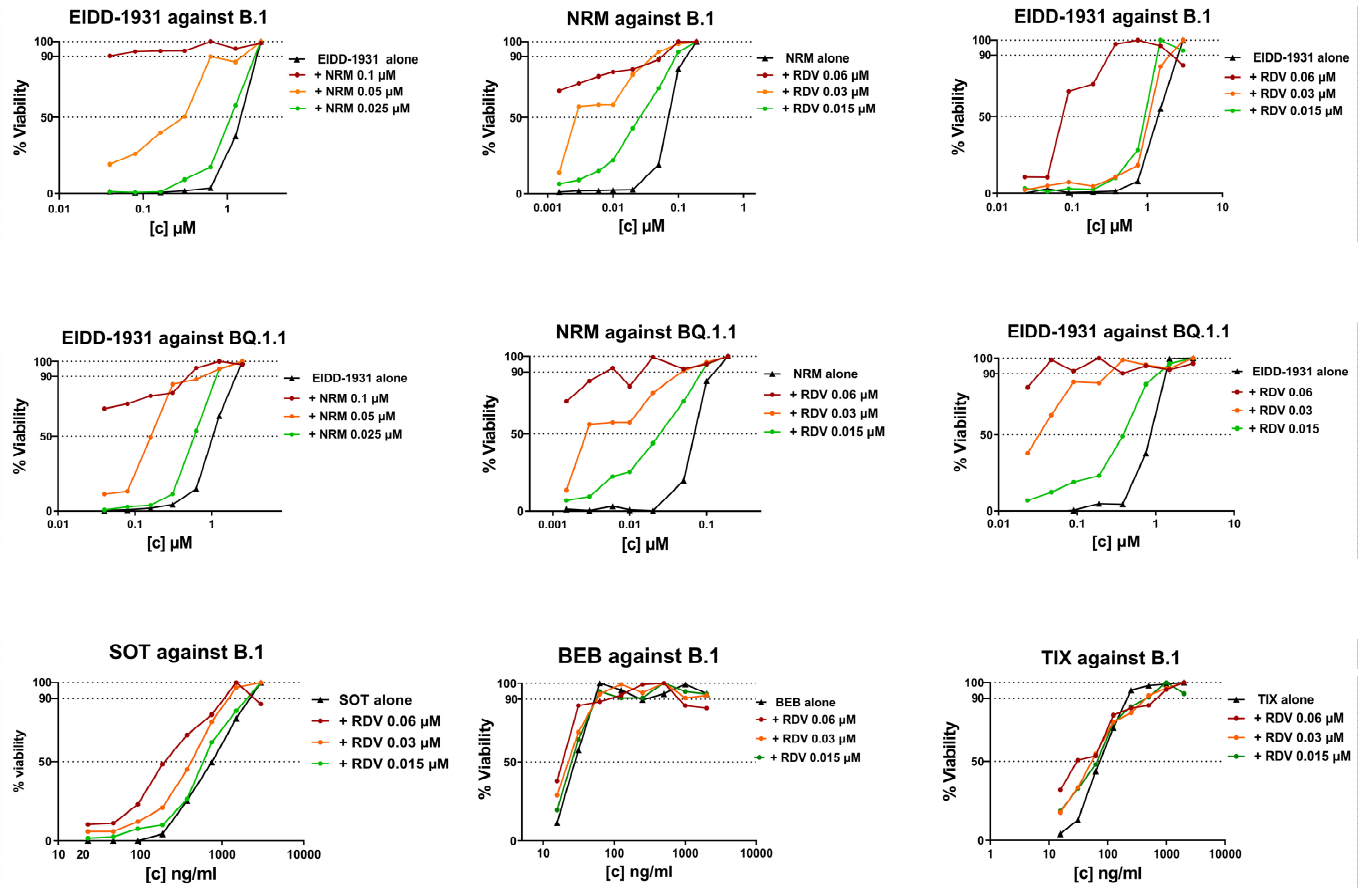

Figure 2. IC_{50} synergistic potency shift experiments in B.1 or BQ.1.1 virus infected VERO E6 cells treated with three fixed drug concentrations of Compound 1 (as indicated in the graph title) plus scalar concentrations of Compound 2 (as indicated in the legend). The three concentrations of Compound 1 were chosen as the IC_{50} of Compound 1 alone, plus two 2-fold dilutions. The scalar concentration of Compound 2 is the same as that used in the SynergyFinder 3.0 matrix. The concentration of Compound 2 on the x-axis is expressed as micromolar for DAA and as ng/mL for mAb, while the y-axis shows the percentage of cell viability. DAA/DAA combinations were tested against the ancestral B.1 SARS-CoV-2 strain and the BQ.1.1 Omicron variant, while RDV/mAb combinations were tested only against the ancestral B.1 SARS-CoV-2 strain. Graphs were generated using GraphPad PRISM software version 9 (La Jolla, CA, USA).

Table 3. Concentrations of pairwise drug combinations below each drug IC_{90} and showing synergism in the SynergyFinder 3.0 matrix, stratified by synergy score values (10–29.9, 30–50, and above 50).

Synergy Score Stratum	Drug Combination	Concentrations [a]	Viral Variant
>50	RDV/NRM	0.02/0.05 0.04/8.8	B.1 and BQ1.1
	RDV/SOT	0.04/35.2 0.04/140.6 0.04/0.6 0.04/2.2	B.1
	RDV/BEB	0.04/8.9 0.04/2.2 0.04/8.8 0.05/0.75 0.05/1.50	B.1
	RDV/TIX	0.01/562.5 0.04/562.5 0.04/35	B.1
30–50	NRM/EIDD-1931	0.003/0.07 0.01/0.08	B.1 B.1 and BQ.1.1
	RDV/SOT	0.05/0.09 0.02/1.5 0.03/0.75	B.1 B.1 B.1 B.1
	RDV/TIX	0.02/0.05	B.1 B.1
10–29.9	NRM/EIDD-1931	0.004/0.05 0.006/0.05 0.02/0.03	B.1 and BQ.1.1 BQ.1.1 B.1 B.1 and BQ.1.1
	RDV/EIDD-1931	0.02/0.01 0.01/8.9 0.01/35	BQ.1.1 BQ.1.1 BQ.1.1 B.1
	RDV/NRM		B.1
	RDV/BEB		
	RDV/TIX		

[a] Concentrations are expressed as µM for DAA and ng/mL for mAb.

4. Discussion

While antiviral combination therapy has met with extraordinary success in the treat-ment of chronic infections, including HIV and HCV, expanding the concept to acute infections such as influenza and COVID-19 has just started to be considered [26,27]. A strong argument for combining drugs with different mechanisms of action is the need to limit the emergence of drug resistance, which is clearly a major issue with persistent viruses. However, there have been reports of rapid selection of drug resistance also with exposure of SARS-CoV-2 to mAb or DAA, particularly in immunocompromised subjects requiring prolonged treatment [28–31]. Combination therapy with SARS-CoV-2 has been so far lim-ited to mAb cocktails, including casirivimab/imdevimab, bamlanivimab/etesevimab, and CIL/TIX. However, these combinations target the same virus replication step.

Although combined administration of two anti-SARS-CoV-2 treatments in the clinical setting has been anecdotally reported [17–20], it is currently unlikely that clinical trials comparing drug combinations to single-drug anti-SARS-CoV-2 therapy are designed. Thus, in vitro assessment of the potential for cooperative effects with multiple drugs plays a key role at this time. Of note, privileging in vitro over difficult-to-obtain in vivo data is not novel in the SARS-CoV-2 treatment arena, where authorization of mAb has been often revoked based on in vitro inefficacy data, rather than on clinical trials, with newly emerging viral variants [32]. Assessment of the dose-effect relationship with drug combinations involves measuring inhibition of viral replication in a standardized virus-cell system where different concentrations of the drugs of interest are combined. Synergistic interactions

are formally defined by activity scores, which are higher than the sum of the activities of the individual drugs. Several tools are available online which are based on different mathematical models to define combinatorial effects as synergy, additivity, or antagonism (e.g., MacSynergy II™, CompuSyn, Combenefit, SynergyFinder) [33]. The available tools range from simple spreadsheet-based systems to software packages assisted by a graphical user interface and based on machine learning algorithms [34]. Since there is no consensus on how to define synergy [35], it is important to include post hoc analysis and discover the specific drug concentrations resulting in unequivocal synergy. Indeed, by using the latest release of the popular SynergyFinder, we detected highly scored synergistic potency shifts at specific concentrations of the drug combinations tested, although summary weighted SS indicated additive effects only, and, notably, we could largely support this indication using confirmatory laboratory tests.

Our results can be compared with a few published data of this kind. The NRM/EIDD-1931 combo was scored as synergistic in two previous studies, one using SynergyFinder 2.0 with the HSA algorithm to process data from a VERO E6 cell line-based system with the B.1 virus [11], the other using SynergyFinder 3.0 with the Bliss algorithm, Calu-3 cells and the Delta virus [13]. In addition, NRM and MNP were shown to increase the survival rate by >2-fold in the K18-hACE2 transgenic mouse model compared with either drug alone [16]. Another study reported an additive effect of the RDV/EIDD-1931 combination by applying the original SynergyFinder version with the ZIP algorithm in A549-ACE2-TMPRSS2 cells infected with the Omicron BA.5 virus [15]. Thus, previous reports and our study consistently show a cooperative interaction with combinations of licensed DAA. The difference between additive and synergistic effects is not straightforward to define due to the diversity of methods employed and the absence of a gold standard assay. We used the most updated version of SynergyFinder, which, in addition to the summary SS metric, also returns a weighted SS computed at lower drug concentrations and allows post hoc analysis at specific drug concentrations. Such analysis indeed revealed highly synergistic interactions, which may have driven an overall synergistic result with earlier SynergyFinder versions [11]. Synergistic hits were scored for all the three DAA/DAA combinations and for RDV with three of the four mAb considered. Indeed, our work is the first to comprehensively test all three licensed DAA and perform a first-time analysis of RDV plus mAb. Other strengths of our experimental design include the use of the CP-100356 hydrochloride drug efflux inhibitor to better mimic in vivo DAA activity and the assessment of the DAA combinatorial effects against two highly divergent viruses such as the ancestral B.1 and the later emerging Omicron BQ.1.1 variant. Comparable effects were shown with the two viral strains, as expected from the known variant-independent activity of SARS-CoV-2 polymerase and protease inhibitors [7]. A further step in this work should be updating the viral variants with those currently circulating as well as testing whether the synergistic effects measured translate into a different barrier to in vitro resistance selection.

Finally, we corroborated SynergyFinder 3.0 data with in vitro experiments to measure the IC_{50} shift for representative drug combinations where three 2-fold dilutions of one compound, downward from its IC_{50}, were used together with a complete dilution series of a second compound. By selecting cases with repeated synergistic scores at concentrations close to the IC_{50}, we showed that a 2-fold increase in the concentration of the first compound decreased the IC_{50} of the second compound by much more than 2-fold, supporting the synergistic effect indicated using SynergyFinder 3.0. Of note, while this was evident with DAA combinations, the effect was smaller or null with RDV/mAb combinations, advising for further studies to better define the interaction between these drugs acting at extracellular and intracellular levels. This highlights the need to support data obtained from SynergyFinder or similar tools with in vitro confirmation experiments, particularly in light of the multiplicity and frequent updates of the algorithms. In principle, any algorithm estimating combinatorial effects among drugs should be used as a starting point for further analysis and not be conclusive on its own. When a clinical trial is not feasible, advanced in vitro systems should be used, including suitable 3D lung tissue systems [36]. Most

importantly, in vivo experiments should be designed in a suitable animal model before moving forward to a wide introduction of combination therapy into the clinic. SARS-CoV-2 animal models have been progressively improved [37] and should now be an integral part of the lessons learned from the COVID-19 pandemic [9].

Supplementary Materials: The following supporting information can be downloaded at: https://www.mdpi.com/article/10.3390/v16020168/s1, Table S1: IC_{50} synergistic potency shift measured in infected VERO E6 cells; Figure S1: Bi-dimensional (2D) synergy plots of antivirals against the two SARS-CoV-2 strains tested, generated using Synergy Finder 3.0 (https://synergyfinder.fimm.fi/ accessed on 12 October 2023); Figure S2: Overall combinatorial effects of the three DAA pairs as well as those of the three RDV/mAb groups compared by the Kruskal–Wallis test followed by Mann–Whitney pairwise comparisons between groups.

Author Contributions: Conceptualization, I.V. (Ilaria Vicenti); methodology, I.V. (Ilaria Vicenti), L.F. and C.B.; validation, L.F., C.B. and N.B.; formal analysis, F.S. and M.Z.; investigation, L.F., C.B., I.V. (Ilenia Varasi), C.P. and N.B.; resources, M.Z. and I.V. (Ilaria Vicenti); data curation, I.V. (Ilenia Varasi); writing—original draft preparation, I.V. (Ilaria Vicenti), C.B. and L.F.; writing—review and editing, F.S and M.Z.; visualization, F.G.; supervision, I.V. (Ilaria Vicenti); project administration, I.V. (Ilaria Vicenti); funding acquisition, I.V. (Ilaria Vicenti) and M.Z. All authors have read and agreed to the published version of the manuscript.

Funding: This work received funding from the Ministero dell'Università e della Ricerca (PRIN 202022GZEHE_01); EU funding within the NextGenerationEU-MUR PNRR Extended Partnership initiative on Emerging Infectious Diseases (Project no. PE00000007, INF-ACT) and by the EuCARE Project funded by the European Union's Horizon Europe Research and Innovation Program, Grant Agreement No. 101046016.

Institutional Review Board Statement: Not applicable.

Informed Consent Statement: Not applicable.

Data Availability Statement: Data are contained within the article and Supplementary Materials. All data not included are available on request from the corresponding author.

Conflicts of Interest: The authors declare that they have no known competing financial interests or personal relationships that could have appeared to influence the work reported in this paper.

References

1. Semenzato, L.; Botton, J.; Drouin, J.; Baricault, B.; Bertrand, M.; Jabagi, M.-J.; Cuenot, F.; Le Vu, S.; Dray-Spira, R.; Weill, A.; et al. Characteristics Associated with the Residual Risk of Severe COVID-19 after a Complete Vaccination Schedule: A Cohort Study of 28 Million People in France. Lancet Reg. Health. Eur. 2022, 19, 100441. [CrossRef] [PubMed]
2. Turtle, L.; Thorpe, M.; Drake, T.M.; Swets, M.; Palmieri, C.; Russell, C.D.; Ho, A.; Aston, S.; Wootton, D.G.; Richter, A.; et al. Outcome of COVID-19 in Hospitalised Immunocompromised Patients: An Analysis of the WHO ISARIC CCP-UK Prospective Cohort Study. PLoS Med. 2023, 20, e1004086. [CrossRef] [PubMed]
3. Qu, P.; Faraone, J.N.; Evans, J.P.; Zheng, Y.-M.; Carlin, C.; Anghelina, M.; Stevens, P.; Fernandez, S.; Jones, D.; Panchal, A.R.; et al. Enhanced Evasion of Neutralizing Antibody Response by Omicron XBB.1.5, CH.1.1, and CA.3.1 Variants. Cell Rep. 2023, 42, 112443. [CrossRef] [PubMed]
4. Menegale, F.; Manica, M.; Zardini, A.; Guzzetta, G.; Marziano, V.; d'Andrea, V.; Trentini, F.; Ajelli, M.; Poletti, P.; Merler, S. Evaluation of Waning of SARS-CoV-2 Vaccine-Induced Immunity: A Systematic Review and Meta-Analysis. JAMA Netw. Open 2023, 6, e2310650. [CrossRef] [PubMed]
5. Mustafa, S.S.; Stern, R.A.; Patel, P.C.; Chu, D.K. COVID-19 Treatments: Then and Now. J. Allergy Clin. Immunol. Pract. 2023, 11, 3321–3333. [CrossRef] [PubMed]
6. Touret, F.; Giraud, E.; Bourret, J.; Donati, F.; Tran-Rajau, J.; Chiaravalli, J.; Lemoine, F.; Agou, F.; Simon-Lorière, E.; van der Werf, S.; et al. Enhanced Neutralization Escape to Therapeutic Monoclonal Antibodies by SARS-CoV-2 Omicron Sub-Lineages. iScience 2023, 26, 106413. [CrossRef]
7. Cho, J.; Shin, Y.; Yang, J.-S.; Kim, J.W.; Kim, K.-C.; Lee, J.-Y. Evaluation of Antiviral Drugs against Newly Emerged SARS-CoV-2 Omicron Subvariants. Antivir. Res. 2023, 214, 105609. [CrossRef]
8. Del Borgo, C.; Garattini, S.; Bortignon, C.; Carraro, A.; Di Trento, D.; Gasperin, A.; Grimaldi, A.; De Maria, S.G.; Corazza, S.; Tieghi, T.; et al. Effectiveness, Tolerability and Prescribing Choice of Antiviral Molecules Molnupiravir, Remdesivir and Nirmatrelvir/r: A Real-World Comparison in the First Ten Months of Use. Viruses 2023, 15, 1025. [CrossRef]

9. Li, G.; Hilgenfeld, R.; Whitley, R.; De Clercq, E. Therapeutic Strategies for COVID-19: Progress and Lessons Learned. Nat. Rev. Drug Discov. 2023, 22, 449–475. [CrossRef]
10. Shyr, Z.A.; Cheng, Y.-S.; Lo, D.C.; Zheng, W. Drug Combination Therapy for Emerging Viral Diseases. Drug Discov. Today 2021, 26, 2367–2376. [CrossRef]
11. Gidari, A.; Sabbatini, S.; Schiaroli, E.; Bastianelli, S.; Pierucci, S.; Busti, C.; Comez, L.; Libera, V.; Macchiarulo, A.; Paciaroni, A.; et al. The Combination of Molnupiravir with Nirmatrelvir or GC376 Has a Synergic Role in the Inhibition of SARS-CoV-2 Replication In Vitro. Microorganisms 2022, 10, 1475. [CrossRef] [PubMed]
12. Nguyenla, X.; Wehri, E.; Van Dis, E.; Biering, S.B.; Yamashiro, L.H.; Zhu, C.; Stroumza, J.; Dugast-Darzacq, C.; Graham, T.G.W.; Wang, X.; et al. Discovery of SARS-CoV-2 Antiviral Synergy between Remdesivir and Approved Drugs in Human Lung Cells. Sci. Rep. 2022, 12, 18506. [CrossRef] [PubMed]
13. Wagoner, J.; Herring, S.; Hsiang, T.-Y.; Ianevski, A.; Biering, S.B.; Xu, S.; Hoffmann, M.; Pöhlmann, S.; Gale, M.; Aittokallio, T.; et al. Combinations of Host- and Virus-Targeting Antiviral Drugs Confer Synergistic Suppression of SARS-CoV-2. Microbiol. Spectr. 2022, 10, e0333122. [CrossRef] [PubMed]
14. Wang, X.; Sacramento, C.Q.; Jockusch, S.; Chaves, O.A.; Tao, C.; Fintelman-Rodrigues, N.; Chien, M.; Temerozo, J.R.; Li, X.; Kumar, S.; et al. Combination of Antiviral Drugs Inhibits SARS-CoV-2 Polymerase and Exonuclease and Demonstrates COVID-19 Therapeutic Potential in Viral Cell Culture. Commun. Biol. 2022, 5, 154. [CrossRef] [PubMed]
15. Abdelnabi, R.; Maes, P.; de Jonghe, S.; Weynand, B.; Neyts, J. Combination of the Parent Analogue of Remdesivir (GS-441524) and Molnupiravir Results in a Markedly Potent Antiviral Effect in SARS-CoV-2 Infected Syrian Hamsters. Front. Pharmacol. 2022, 13, 1072202. [CrossRef] [PubMed]
16. Jeong, J.H.; Chokkakula, S.; Min, S.C.; Kim, B.K.; Choi, W.-S.; Oh, S.; Yun, Y.S.; Kang, D.H.; Lee, O.-J.; Kim, E.-G.; et al. Combination Therapy with Nirmatrelvir and Molnupiravir Improves the Survival of SARS-CoV-2 Infected Mice. Antivir. Res. 2022, 208, 105430. [CrossRef] [PubMed]
17. Gidari, A.; Sabbatini, S.; Schiaroli, E.; Bastianelli, S.; Pierucci, S.; Busti, C.; Saraca, L.M.; Capogrossi, L.; Pasticci, M.B.; Francisci, D. Synergistic Activity of Remdesivir-Nirmatrelvir Combination on a SARS-CoV-2 In Vitro Model and a Case Report. Viruses 2023, 15, 1577. [CrossRef] [PubMed]
18. Lanzafame, M.; Gottardi, M.; Guella, L.; Collini, L.; Costa, G.; Guella, A.; Vento, S. Successful Treatment of Persistent SARS-CoV-2 Infection with Nirmatrelvir/Ritonavir plus Sotrovimab in Four Immunocompromised Patients. J. Chemother. 2023, 35, 623–626. [CrossRef]
19. Marangoni, D.; Antonello, R.M.; Coppi, M.; Palazzo, M.; Nassi, L.; Streva, N.; Povolo, L.; Malentacchi, F.; Zammarchi, L.; Rossolini, G.M.; et al. Combination Regimen of Nirmatrelvir/Ritonavir and Molnupiravir for the Treatment of Persistent SARS-CoV-2 Infection: A Case Report and a Scoping Review of the Literature. Int. J. Infect. Dis. 2023, 133, 53–56. [CrossRef]
20. Mikulska, M.; Sepulcri, C.; Dentone, C.; Magne, F.; Balletto, E.; Baldi, F.; Labate, L.; Russo, C.; Mirabella, M.; Magnasco, L.; et al. Triple Combination Therapy with 2 Antivirals and Monoclonal Antibodies for Persistent or Relapsed Severe Acute Respiratory Syndrome Coronavirus 2 Infection in Immunocompromised Patients. Clin. Infect. Dis. 2023, 77, 280–286. [CrossRef]
21. Zhu, Y.; Binder, J.; Yurgelonis, I.; Rai, D.K.; Lazarro, S.; Costales, C.; Kobylarz, K.; McMonagle, P.; Steppan, C.M.; Aschenbrenner, L.; et al. Generation of a VeroE6 Pgp Gene Knock out Cell Line and Its Use in SARS-CoV-2 Antiviral Study. Antivir. Res. 2022, 208, 105429. [CrossRef] [PubMed]
22. Fiaschi, L.; Dragoni, F.; Schiaroli, E.; Bergna, A.; Rossetti, B.; Giammarino, F.; Biba, C.; Gidari, A.; Lai, A.; Nencioni, C.; et al. Efficacy of Licensed Monoclonal Antibodies and Antiviral Agents against the SARS-CoV-2 Omicron Sublineages BA.1 and BA.2. Viruses 2022, 14, 1374. [CrossRef] [PubMed]
23. Vicenti, I.; Martina, M.G.; Boccuto, A.; De Angelis, M.; Giavarini, G.; Dragoni, F.; Marchi, S.; Trombetta, C.M.; Crespan, E.; Maga, G.; et al. System-Oriented Optimization of Multi-Target 2,6-Diaminopurine Derivatives: Easily Accessible Broad-Spectrum Antivirals Active against Flaviviruses, Influenza Virus and SARS-CoV-2. Eur. J. Med. Chem. 2021, 224, 113683. [CrossRef] [PubMed]
24. Ianevski, A.; Giri, A.K.; Aittokallio, T. SynergyFinder 3.0: An Interactive Analysis and Consensus Interpretation of Multi-Drug Synergies across Multiple Samples. Nucleic Acids Res. 2022, 50, W739–W743. [CrossRef] [PubMed]
25. Yadav, B.; Wennerberg, K.; Aittokallio, T.; Tang, J. Searching for Drug Synergy in Complex Dose-Response Landscapes Using an Interaction Potency Model. Comput. Struct. Biotechnol. J. 2015, 13, 504–513. [CrossRef] [PubMed]
26. Koszalka, P.; Subbarao, K.; Baz, M. Preclinical and Clinical Developments for Combination Treatment of Influenza. PLoS Pathog. 2022, 18, e1010481. [CrossRef]
27. Yan, D.; Yan, B. Viral Target and Metabolism-Based Rationale for Combined Use of Recently Authorized Small Molecule COVID-19 Medicines: Molnupiravir, Nirmatrelvir, and Remdesivir. Fundam. Clin. Pharmacol. 2023, 37, 726–738. [CrossRef]
28. Ahmadi, A.S.; Zadheidar, S.; Sadeghi, K.; Nejati, A.; Salimi, V.; Hajiabdolbaghi, M.; Mokhtari-Azad, T.; Yavarian, J. SARS-CoV-2 Intrahost Evolution in Immunocompromised Patients in Comparison with Immunocompetent Populations after Treatment. J. Med. Virol. 2023, 95, e28877. [CrossRef]
29. Hogan, J.I.; Duerr, R.; Dimartino, D.; Marier, C.; Hochman, S.E.; Mehta, S.; Wang, G.; Heguy, A. Remdesivir Resistance in Transplant Recipients with Persistent Coronavirus Disease 2019. Clin. Infect. Dis. 2023, 76, 342–345. [CrossRef]

30. Yang, S.; Multani, A.; Garrigues, J.M.; Oh, M.S.; Hemarajata, P.; Burleson, T.; Green, N.M.; Oliai, C.; Gaynor, P.T.; Beaird, O.E.; et al. Transient SARS-CoV-2 RNA-Dependent RNA Polymerase Mutations after Remdesivir Treatment for Chronic COVID-19 in Two Transplant Recipients: Case Report and Intra-Host Viral Genomic Investigation. Microorganisms 2023, 11, 2096. [CrossRef]
31. Zuckerman, N.S.; Bucris, E.; Keidar-Friedman, D.; Amsalem, M.; Brosh-Nissimov, T. Nirmatrelvir Resistance-de Novo E166V/L50V Mutations in an Immunocompromised Patient Treated with Prolonged Nirmatrelvir/Ritonavir Monotherapy Leading to Clinical and Virological Treatment Failure—A Case Report. Clin. Infect. Dis. 2023, ciad494. [CrossRef] [PubMed]
32. Wu, M.Y.; Carr, E.J.; Harvey, R.; Mears, H.V.; Kjaer, S.; Townsley, H.; Hobbs, A.; Ragno, M.; Herman, L.S.; Adams, L.; et al. WHO's Therapeutics and COVID-19 Living Guideline on MAbs Needs to Be Reassessed. Lancet 2022, 400, 2193–2196. [CrossRef] [PubMed]
33. Foucquier, J.; Guedj, M. Analysis of Drug Combinations: Current Methodological Landscape. Pharmacol. Res. Perspect. 2015, 3, e00149. [CrossRef] [PubMed]
34. Fuentealba-Manosalva, O.; Mansilla, M.; Buelvas, N.; Martin-Martin, A.; Torres, C.G.; López-Muñoz, R.A. Mind the Curve: Dose-Response Fitting Biases the Synergy Scores across Software Used for Chemotherapy Combination Studies. Int. J. Mol. Sci. 2023, 24, 9705. [CrossRef]
35. Wooten, D.J.; Meyer, C.T.; Lubbock, A.L.R.; Quaranta, V.; Lopez, C.F. MuSyC Is a Consensus Framework That Unifies Multi-Drug Synergy Metrics for Combinatorial Drug Discovery. Nat. Commun. 2021, 12, 4607. [CrossRef]
36. Plebani, R.; Bai, H.; Si, L.; Li, J.; Zhang, C.; Romano, M. 3D Lung Tissue Models for Studies on SARS-CoV-2 Pathophysiology and Therapeutics. Int. J. Mol. Sci. 2022, 23, 10071. [CrossRef]
37. Lin, Q.; Lu, C.; Hong, Y.; Li, R.; Chen, J.; Chen, W.; Chen, J. Animal models for studying coronavirus infections and developing antiviral agents and vaccines. Antivir. Res. 2022, 203, 105345. [CrossRef]

Journal of Infection 87 (2023) 270–272

Contents lists available at ScienceDirect

Journal of Infection

journal homepage: www.elsevier.com/locate/jinf

Letter to the Editor

Neutralizing antibodies response to novel SARS-CoV-2 omicron sublineages in long-term care facility residents after the fourth dose of monovalent BNT162b2 COVID-19 vaccination

Severe Acute Respiratory Syndrome Coronavirus 2 (SARS-CoV-2), the etiologic agent of the Coronavirus Disease 19 (COVID-19), has been progressively adapting to the human host since the beginning of the epidemic.[1] The Omicron variant, first identified in South Africa in November 2021, is the best adapted variant of concern (VOC), combining highly efficient binding to the ACE-2 cell receptor and immune escape. Since its emergence, Omicron has evolved into a plethora of descendant sublineages, including BA.1, BA.2, BA.3, BA.4, and BA.5. While BA.3 was rapidly outcompeted and lost in viral evolution, the other sublineages were expanded following a me-chanism of convergent spike evolution. During late 2022 or early 2023, BA.1, BA.2 and BA.5 were completely replaced by their des-cendants including BQ.1.1, derived by BA.5, and BA.2.75.2, XBB.1 and CH.1.1, derived by BA.2 (https://cov-spectrum.org/explore/World/). All these variants have been shown to escape natural and vaccine induced immunity elicited by pre-omicron antigens, however hybrid immunity resulting from a combination of natural infection and vaccination may still confer some degree of protection.[2] A key point is whether uninfected but highly vulnerable individuals undergoing multiple vaccination with the ancestral antigen preparation have any residual protection from SARS-CoV-2 infection and disease.

We quantified the magnitude and durability of neutralizing antibodies (NtAb) to the currently predominant sublineages BA.2.75.2, BQ.1.1, XBB.1 and CH.1.1 in a fragile population of long-term care facility (LTCF) residents who were naïve to SARS-COV-2 infection and vaccinated with four doses of the monovalent BNT162b2 COVID- 19 mRNA vaccine. Plasma samples were collected from 40 residents at Pio Albergo Trivulzio, the largest Italian LTCF, 71 [68–75] and 89 [80–91] median [IQR] days after the third (T3) and fourth (T4) BNT162b2 vaccine dose, respectively. Live virus NtAb titers were measured and reported as the serum dilution yielding 50% protec-tion of cells from in vitro viral infection (ID_{50}).[3] The Elecsys Anti- SARS-CoV-2 S system (Roche, Basel, Swiss) was used to quantify the anti-spike protein binding antibody units (BAU) at T3 and T4 as well as at the earlier time points T2a and T2b corresponding to 64 [62–64] and 203 [202–204] median days after the second dose vaccination, respectively. The study group had a median age of 91 [84–94] years, included 35 females and 5 males and no subject with positive anti-nucleocapsid serology at first vaccine dose. Weekly screening for incident SARS-CoV-2 infection by swab analysis re-mained negative in all subjects during the study period (ending in July 2022). Most residents (87.2%) presented at least one co-morbidity, mostly dementia (59.0%), diabetes mellitus (30.8%), his-tory of ictus (25.6%) or ischemic heart disease (23.1%). Thirteen patients (32.5%) had at least three comorbidities and polypharmacy was common (Table 1).

All but one patient had measurable anti-spike antibody titers after the second BNT162b2 vaccine dose (2953 [31–6546] BAU). PAT35 remained negative for anti-spike Ab and NtAbs at all time points analyzed. NtAb titers to the wild type B.1 variant significantly increased at T4 (1094 [612–3252] ID_{50}) with respect to T3 (518 [60–1515] ID_{50}) ($p < 0.001$). A significant increase was also observed when comparing the median anti-spike BAU at T3 and T4 (9939 [4168–12,500] vs. 12,500 [6413–12,500]; $p = 0.008$). NtAb titers against B.1 and anti-spike BAU correlated well at T3 (Spearman rho 0.697, $p < 0.001$) and T4 (rho 0.479, $p = 0.002$; Supplementary Fig. 1). At T4, median NtAb titers to B.1 correlated with those to each omicron variant ($p < 0.001$ for all comparisons; Supplementary Table 1) but absolute values were significantly higher with respect to BA.5 (287 [38–533], 4-fold), BA.2.75.2 (30 [15–67], 37-fold), BQ.1.1 (22 [11–58], 49-fold), XBB.1 (13 [5–24], 84-fold] and CH.1.1 (13 [5–19], 84-fold) ($p < 0.001$ for all comparisons) (Fig. 1). In the ranking of NtAb titers (B.1 > BA.5 > BA.2.75.2 > BQ.1.1 > XBB.1 = CH.1.1), each variant was significantly better neutralized than the following variants, with the exception of XBB.1 vs. CH.1.1 ($p = 0.031$ for BQ.1.1 vs. BA.2.75.2; $p < 0.001$ for all other comparisons). Of note, in addition to PAT35 who never mounted any neutralizing response for the whole vaccination cycle, 4 patients did not neutralize BA.5 and BA.2.75.2, and 8, 12 and 14 patients did not neutralize BQ.1.1, CH.1.1 and XBB.1, respectively.

Aging and high levels of comorbidity pose a major risk of COVID- 19 progression in LTCF residents.[4] Indeed, this population was prioritized for vaccination and regularly monitored to detect incident SARS-CoV-2 infections and timely start available treatments. By September 2022, over 98% of LTCF residents in Italy had com-pleted the primary vaccination cycle and 93% had received one or more booster doses (https://www.epicentro.iss.it/en/coronavirus/pdf/REPORT_STRUTTURE_dic2020_sett2022_english.pdf). To our knowledge, this is the first work to analyze the NtAb response against multiple, recently predominant Omicron sublineages in a fragile population of SARS-CoV-2-naïve LTCF residents vaccinated with four doses of monovalent BNT162b2 COVID-19 mRNA vaccine.

Increased NtAb response following the fourth dose of COVID-19 mRNA vaccine, mostly BNT162b2, was recently documented in an-other Italian study of immunocompromised patients.[5] Comparing absolute NtAb titers across studies is challenging due to differences in the reference virus, methods, and procedures. However, the NtAb response measured in our study is comparable to that reported after

https://doi.org/10.1016/j.jinf.2023.06.019

Table 1
Study population, comorbidities and therapy. COPD: Chronic Obstructive Pulmonary Disease; SCC: Squamous Cell Carcinoma; Dementia: from moderate to severe; Anemia: HB values below 10 g/dl; Malnutrition: MUST score = 2 or BMI < 18.5.

ID	Gender	Age (years)	Comorbidities	Treatment
PAT03	F	100	Previous cerebral stroke, dementia	-
PAT04	F	89	Diabetes mellitus, previous cerebral stroke, dementia	-
PAT05	M	95	Ischemic heart disease, dementia, active tumor	-
PAT07	F	84	Ischemic heart disease, COPD, asthma-emphysema, dementia COPD,	-
PAT09	F	75	malnutrition	-
PAT13	F	94	Previous cerebral stroke, dementia	-
PAT18	F	76	Dementia	-
PAT20	M	83	Ischemic heart disease, diabetes mellitus, COPD, asthma-emphysema	-
PAT22	M	84	Ischemic heart disease, chronic renal failure, dementia, COPD, asthma-emphysema, SCC Ischemic	Steroid
PAT27	F	95	heart disease, anemia	Anticoagulant
PAT28	M	79	Diabetes mellitus, active tumor, hepatic cirrhosis	Anticoagulant
PAT29	F	91	Diabetes mellitus, previous cerebral stroke, dementia	Steroid, anticoagulant
PAT35	F	82	Diabetes mellitus, dementia, anemia	-
PAT38	F	97	Dementia	-
PAT42	F	92	Diabetes mellitus, dementia, anemia	Anticoagulant
PAT43	F	77	COPD, dementia	-
PAT46	F	79	Diabetes mellitus	-
PAT47	F	97	Diabetes mellitus, dementia, previous cerebral stroke	-
PAT48	F	92	Active tumor pathology	-
PAT50	F	91	Dementia	-
PAT52	F	94	Dementia	-
PAT55	F	86	COPD, asthma-emphysema, dementia	-
PAT58	F	94	Ischemic heart disease, dementia	-
PAT65	F	94	Dementia	-
PAT66	F	99	Ischemic heart disease	-
PAT67	F	87	Diabetes mellitus, dementia, autoimmune pathology	Steroid
PAT69	F	88	Diabetes mellitus, previous cerebral stroke, active tumor, malnutrition	-
PAT70	F	95	Diabetes mellitus, dementia	-
PAT73	F	102	Previous cerebral stroke	-
PAT75	F	95	Diabetes mellitus, dementia	-
PAT80	M	84	Previous cerebral stroke, dementia	-
PAT84	F	88	Previous cerebral stroke	-
PAT87	F	92	Ischemic heart disease, dementia	-
PAT88	F	91	Ischemic heart disease, previous cerebral stroke	-

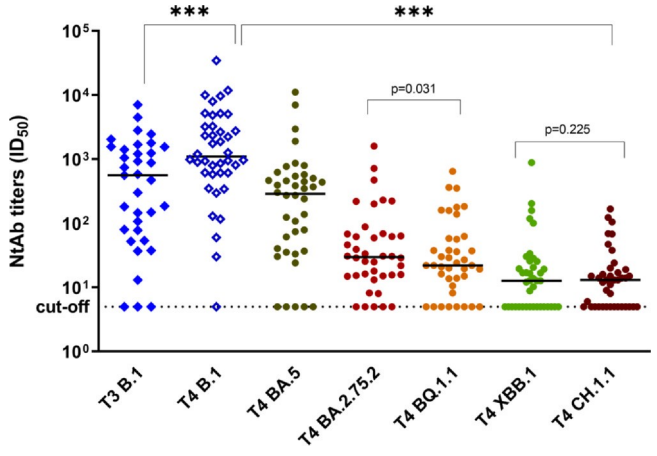

VIRUS	T3	T4
B.1	518 (78-1515)	1093 (612-3252)
BA.5	NP	287 (38-533)
BA.2.75.2	NP	30 (15-67)
BQ.1.1	NP	22 (11-58)
XBB.1	NP	13 (5-24)
CH.1.1	NP	13 (5-19)

NP: Not performed

Fig. 1. Neutralizing antibodies (NtAbs) titers to SARS-CoV-2 variants B.1, BA.5, BA.2.75.2, BQ.1.1, XBB.1 and CH.1.1 in 40 fragile long-term care residents after the third (T3) and fourth (T4) BNT162b2 COVID-19 mRNA monovalent vaccine dose. Antibodies with ID_{50} titers < 10 were defined as negative and scored as 5 for statistical analysis.
Asterisks indicate significance levels: *** correspond to p < 0.001.

the fourth BNT162b2 in healthcare workers in Israel.[6] These data highlight that the fourth booster is of value in maintaining humoral immunity to SARS-CoV-2 and reassures that valid titers can be achieved in late adulthood with multiple immunizations. Indeed, our patient population remained free of incident SARS-CoV-2 in-fection during the whole observation period considered. However, our LTCF residents have been living in a highly protected environ-ment and the study covered up to July 2022 only, thus exposure to the latest Omicron variants escaping vaccine immunity was mar-ginally included. Another limitation of our study is the lack of ana-lysis of the T cell response, which is an integral component of immunity, although more prominent in protection from disease ra-ther than from infection.[7] Nevertheless, our data corroborate the concept that regular boosting can be effective in preventing infection and disease in very late adulthood. Further development in vaccine research is awaited to make SARS-CoV-2 vaccination more con-venient and effective and protect the most vulnerable categories.

Funding

This work received funding from the European Union's Horizon Europe Research and Innovation Actions under grant no. 101046041; from the Ministero dell'Università e della Ricerca (PRIN 202022GZEHE_01); EU funding within the NextGenerationEU-MUR PNRR Extended Partnership initiative on Emerging Infectious Diseases (Project no. PE00000007, INF-ACT) and by the EuCARE Project funded by the European Union's Horizon Europe Research and Innovation Program, Grant Agreement No. 101046016.

Institutional review board statement

The retrospective study was conducted in accordance with the Declaration of Helsinki and approved by the Ethics Committee, "INMI L. Spallanzani" (protocol code 66-2022, approved on 23 November 2022). Informed consent was obtained from all subjects involved in the study.

CRediT authorship contribution statement

Ilaria Vicenti, Maurizio Zazzi, Alessia Lai, Claudia Balotta: Conceptualization, Supervision. Gianguglielmo Zehender, Maurizio Zazzi: Funding. Ilenia Varasi, Lia Fiaschi, Camilla Biba, Annalisa Bergna: Experimental work. Ilaria Vicenti, Ilenia Varasi, Annalisa Bergna, Carla Della Ventura, Agostino Riva, Antonella Gatti, Barbara Caimi: Data generation and curation. Alessia Lai, Annalisa Bergna, Carla Della Ventura: Strain collection. Alessia Lai, Ilaria Vicenti, Ilenia Varasi: Sequencing and bioinformatics. Ilenia Varasi, Ilaria Vicenti, Maurizio Zazzi: Statistical analysis. Antonella Gatti, Barbara Caimi, Claudia Balotta, Agostino Riva: Clinical data col-lection. Ilenia Varasi, Ilaria Vicenti, Alessia Lai, Camilla Biba, Gianguglielmo Zehender: Writing. All authors: Review and agree-ment with the final version of the manuscript.

Declaration of Competing Interest

The authors declare that they have no known competing fi-nancial interests or personal relationships that could have appeared to influence the work reported in this paper.

Appendix A. Supplementary material

Supplementary data associated with this article can be found in the online version at doi:10.1016/j.jinf.2023.06.019.

References

1. Markov PV, Ghafari M, Beer M, Lythgoe K, Simmonds P, Stilianakis NI, et al. The evolution of SARS-CoV-2. Nat Rev Microbiol 2023;21(6):361–79. https://doi.org/10. 1038/s41579-023-00878-2
2. Bobrovitz N, Ware H, Ma X, Li Z, Hosseini R, Cao C, et al. Protective effectiveness of previous SARS-CoV-2 infection and hybrid immunity against the omicron variant and severe disease: a systematic review and meta-regression. Lancet Infect Dis 2023;23(5):556–67. https://doi.org/10.1016/S1473-3099(22)00801-5
3. Dragoni F, Schiaroli E, Micheli V, Fiaschi L, Lai A, Zehender G, et al. Impact of SARS- CoV-2 omicron BA.1 and delta AY.4.2 variants on the neutralization by sera of patients treated with different authorized monoclonal antibodies. Clin Microbiol Infect 2022;28:1037–9. https://doi.org/10.1016/j.cmi.2022.03.005
4. Caimi B, Franzetti M, Velleca R, Lai A, Gatti A, Rossi PL, et al. Sero-survey on long- term care facility residents reveals increased risk of sub-optimal antibody response to BNT162b2: implications for breakthrough prevention. BMC Geriatr 2022;22:191. https://doi.org/10.1186/s12877-022-02884-0
5. Rescigno M, Agrati C, Salvarani C, Giannarelli D, Costantini M, Mantovani A, et al. Neutralizing antibodies to Omicron after the fourth SARS-CoV-2 mRNA vaccine dose in immunocompromised patients highlight the need of additional boosters. Front Immunol 2023;14:1104124. https://doi.org/10.3389/fimmu.2023
6. Regev-Yochay G, Gonen T, Gilboa M, Mandelboim M, Indenbaum V, Amit S, et al. Efficacy of a fourth dose of Covid-19 mRNA vaccine against omicron. N Engl J Med 2022;386:1377–80. https://doi.org/10.1056/NEJMc2202542
7. Sette A, Sidney J, Crotty ST. Cell responses to SARS-CoV-2. Annu Rev Immunol 2023;41:343–73. https://doi.org/10.1146/annurev-immunol-101721-061120

Ilenia Varasi
Department of Medical Biotechnologies, University of Siena, Siena, Italy

Alessia Lai
Department of Biomedical and Clinical Sciences, University of Milan, Milan, Italy
EpiSoMi CRC-Centro di Ricerca Coordinato, University of Milan, Milan, Italy

Lia Fiaschi
Department of Medical Biotechnologies, University of Siena, Siena, Italy

Annalisa Bergna
Department of Biomedical and Clinical Sciences, University of Milan, Milan, Italy
EpiSoMi CRC-Centro di Ricerca Coordinato, University of Milan, Milan, Italy

Antonella Gatti, Barbara Caimi
Azienda di Servizi alla Persona, Istituto Milanese Martinit e Stelline e Pio Albergo Trivulzio, Milan, Italy

Camilla Biba
Department of Medical Biotechnologies, University of Siena, Siena, Italy

Carla Della Ventura
Department of Biomedical and Clinical Sciences, University of Milan, Milan, Italy
EpiSoMi CRC-Centro di Ricerca Coordinato, University of Milan, Milan, Italy

Claudia Balotta
Azienda di Servizi alla Persona, Istituto Milanese Martinit e Stelline e Pio Albergo Trivulzio, Milan, Italy

Agostino Riva
Department of Biomedical and Clinical Sciences, University of Milan, Milan, Italy

Gianguglielmo Zehender
Department of Biomedical and Clinical Sciences, University of Milan, Milan, Italy
EpiSoMi CRC-Centro di Ricerca Coordinato, University of Milan, Milan, Italy

Maurizio Zazzi, Ilaria Vicenti *
Department of Medical Biotechnologies, University of Siena, Siena, Italy

*Corresponding author.
E-mail addresses: ilenia.varasi@student.unisi.it (I. Varasi), alessia.lai@unimi.it (A. Lai), lia.fiaschi@unisi.it (L. Fiaschi), annalisa.bergna@unimi.it (A. Bergna), antonella.gatti@pioalbergotrivulzio.it (A. Gatti), barbara.caimi@pioalbergotrivulzio.it (B. Caimi), camilla.biba@student.unisi.it (C. Biba), carla.dellaventura@gmail.com, carla.dellaventura@unimi.it (C. Della Ventura), claudia.balotta@unimi.it (C. Balotta), agostino.riva@unimi.it (A. Riva), gianguglielmo.zehender@unimi.it (G. Zehender), maurizio.zazzi@unisi.it (M. Zazzi), vicenti@unisi.it (I. Vicenti).

vaccines

MDPI

Brief Report

SARS-CoV-2 Neutralizing Antibodies to B.1 and to BA.5 Variant after Booster Dose of BNT162b2 Vaccine in HIV Patients COVID-Naïve and on Successful Antiretroviral Therapy

Ilaria Vicenti [1,†], Monica Basso [2,†], Nicole Pirola [2], Beatrice Bragato [2], Maria Cristina Rossi [3], Mario Giobbia [3], Susanna Pascoli [4], Antonio Vinci [5], Sara Caputo [2], Ilenia Varasi [1], Camilla Biba [1], Lia Fiaschi [1], Maurizio Zazzi [1,‡] and Saverio Giuseppe Parisi [2,*,‡]

[1] Department of Medical Biotechnologies, University of Siena, 53100 Siena, Italy; vicenti@unisi.it (I.V.); ilenia.varasi@gmail.com (I.V.); camilla.biba@student.unisi.it (C.B.); lia300790@gmail.com (L.F.); maurizio.zazzi@unisi.it (M.Z.)

[2] Department of Molecular Medicine, University of Padova, 35100 Padova, Italy; monica.basso@unipd.it (M.B.); nicole.pirola@studenti.unipd.it (N.P.); beatrice.bragato@studenti.unipd.it (B.B.); sara.caputo@studenti.unipd.it (S.C.)

[3] Infectious Diseases Unit, Treviso Hospital, 31100 Treviso, Italy; mariacristina.rossi@aulss2.veneto.it (M.C.R.); mario.giobbia@aulss2.veneto.it (M.G.)

[4] Microbiology Unit, Department of Specialist and Laboratory Medicine, Ca' Foncello University Hospital, 31100 Treviso, Italy; susanna.pascoli@aulss2.veneto.it

[5] Hospital Health Management Area, Local Health Authority "Roma 1", Borgo Santo Spirito 3, 00193 Rome, Italy; antonio.vinci.at@hotmail.it

* Correspondence: saverio.parisi@unipd.it; Tel.: +39-04-9827-2344 †

These authors contributed equally to this work.

‡ These authors also contributed equally to this work.

check for updates

Citation: Vicenti, I.; Basso, M.; Pirola, N.; Bragato, B.; Rossi, M.C.; Giobbia, M.; Pascoli, S.; Vinci, A.; Caputo, S.; Varasi, I.; et al. SARS-CoV-2 Neutralizing Antibodies to B.1 and to BA.5 Variant after Booster Dose of BNT162b2 Vaccine in HIV Patients COVID-Naïve and on Successful Antiretroviral Therapy. Vaccines 2023, 11, 871. https://doi.org/10.3390/vaccines11040871

Academic Editor: Zhi Yang

Received: 23 March 2023
Revised: 14 April 2023
Accepted: 17 April 2023
Published: 20 April 2023

Abstract: Live virus neutralization is the gold standard to investigate immunity. This prospective observational study aimed to determine the magnitude of response against the original B.1 lineage and against the BA.5 lineage six months after the third BNT162b2 mRNA vaccine dose in patients with HIV infection on successful antiretroviral treatment and no previous SARS-CoV-2 infection. A total of 100 subjects (M/F 83/17, median age 54 years) were included in the analysis: 95 had plasma HIV RNA <40 copies/mL, the median CD4+ T cell count at the administration of the third dose was 580 cells/mm^3, and the median nadir CD4+ T cell count was 258 cells/mm^3. Neutralizing antibodies (NtAb) against B.1 were detectable in all the subjects, but those to BA.5 were only detected in 88 ($p < 0.001$). The median NtAb titer to B.1 was significantly higher than that to BA.5 (393 vs. 60, $p < 0.0001$), and there was a strong positive correlation between the paired measurements ($p < 0.0001$). Linear regression on a subset of 87 patients excluding outlier NtAb titers showed that 48% of the changes in NtAb titers to BA.5 are related to the changes in value titers to B.1. SARS-CoV-2 variants evolve rapidly, challenging the efficacy of vaccines, and data on comparative NtAb responses may help in tailoring intervals between vaccine doses and in predicting vaccine efficacy.

Keywords: BNT162b2 mRNA vaccine; third dose; HIV; SARS-CoV-2; B.1 lineage; BA.5 lineage; neutralizing antibodies

1. Introduction

The continuous evolution of the SARS-CoV-2 virus has been a major challenge over the three years of the pandemic. The Omicron variant (B.1.1.529), first identified in South Africa in November 2021, rapidly replaced the previously dominant variants, becoming the fifth variant of concern (VOC) as declared by the WHO on 26 November 2021. Since its emergence, the Omicron variant (B.1.1.529) has evolved into a plethora of descendant sublineages, including BA.1, BA.2, BA.3, BA.4, and BA.5. The BA.5 sublineage has been

dominant in Italy for several months, with an estimated prevalence higher than 90% up to October 2022 [1]. This subvariant is characterized by 30 mutations in the spike protein and about 20 in other sites of the genome with respect to the initial version of SARS-CoV-2 [2]. As a consequence, BA.5 can significantly escape neutralizing antibodies induced both by infection with previous VOCs and by vaccination, and a substantial proportion of the general population is not protected from BA.4/5-related hospitalization at less than 6 months after the third vaccine dose. Hachmann et al. [3] demonstrated that the neutralizing antibody titer against BA.5 was lower by a factor of 21 with respect to the titer against WA1/2020 and lower by a factor of 3.3 with respect to the titer against BA.1, and Tartof et al. [4] described adjusted effectiveness of 73% (95% CI 25–91) against hospitalisation and of 43% (95% CI 10–63) against emergency department admission. Two key mutations are involved in the immune escape shown by BA.5: F486V and L452R, present in the receptor binding domain (RBD) of the spike protein and able to reduce serum neutralization with respect to BA.1 and BA.2 in patients vaccinated with three doses. The first mutation, F486V, is an amino acid substitution not identified in other Omicron subvariants, and the second mutation, L452R, is different from L452Q identified in BA.2.12.1 because Q is an amino acid with no charge while L is an amino acid that has a hydrophobic side chain (probably more interferent with antibody binding) [5–7].

The CD4+ memory response to the BNT162b2 vaccine is a complex phenomenon: unlike the neutralizing response, the combination BNT162b2/BNT162b2 elicits a more efficient cellular response with respect to a combination adenovirus vector-based vaccine, AZD122/BNT162b2 [8]. A low decline of CD4+ T cell memory occurs throughout the months, but there is a total recovery after the third BNT162b2 vaccine dose [9]. Taken together, these data showed a successful memory response lasting many months in healthy subjects. In HIV-positive patients, the influence of viroimmunological parameters had to be taken into account: most subjects on successful ART with a high CD4+ cell count at inclusion and receiving two doses of the BNT162b2 vaccine had a cellular response after six months, and a high number of CD4+ cell count is a predicting factor [10]. A comparable T cell response after six months from the third dose of the BNT162b2 vaccine was described in patients with either less or more than 200 cells/mm^3, but with virological suppression (median HIV RNA 40 copies/mL) [11]. These results suggest that a standard vaccine schedule could be applied to HIV patients with ongoing successful ART, but untreated or failed subjects may need a tailored vaccine administration.

Anti-SARS-CoV-2 vaccines are safe, and they were shown to reduce morbidity and mortality: real-word data confirmed the data reported in registration studies [12–14]. The third dose and its timing have a peculiar role: HIV-positive patients who received 2 vaccine doses are at higher risk of breakthrough infections with respect to HIV-negative subjects, but the third BNT162b2 dose has a protective role [15], and a higher neutralizing antibody seronversion rate was described in HIV-positive patients receiving the third dose of the inactivated COVID-19 vaccine after 5 months with respect to the 3-month interval, especially in subjects with a CD4 count <200 cells/mm^3 [16].

Patients with HIV infection boosted with either heterologous or homologous COVID-19 vaccines showed a strong antibody response as evaluated with IgG ELISA against SARS CoV-2 spike (i.e., from a median of 2644 AU/mL 182 days after the first vaccine dose to a median of 143,088 AU/mL about a month post-third dose [17] and from a median of 107 AU/mL at pre-booster study time to a median of 1580 AU/mL four weeks after the third dose [18]), but a few data were reported on authentic virus neutralization response against the BA.5 variant after the third vaccine dose in patients receiving an mRNA vaccine. Previous studies described a neutralizing response following booster vaccination in subjects receiving an mRNA vaccine, but the targets were wild-type (Wuhan A), Delta (B.1.617.2; AY.2), and Omicron (B.1.1.529; BA.1) [19–21].

Therefore, the aim of this study was to determine the magnitude of SARS-CoV-2 neutralizing antibodies (NtAb) against the original B.1 lineage and against the BA.5 lineage

six months after the third BNT162b2 mRNA vaccine dose in patients with HIV infection on antiretroviral treatment (ART).

2. Materials and Methods

2.1. Study Design and Population

The study was a prospective, observational, single cohort study approved by the "Comitato per la Sperimentazione Clinica di Treviso e Belluno" (protocol code 812/2020), and written informed consent was obtained from each participant.

The patient cohort included 100 subjects with HIV infection, aged more than 18 years, who completed a three-dose regimen of the BNT162b2 vaccine. Previous or present SARS-CoV-2 infection was excluded based on the clinical history and the lack of positive results on nasopharyngeal swabs analyzed for clinical needs (including contact tracing).

Patients were enrolled at the Infectious Diseases Unit of the Treviso Hospital, Treviso, Italy. There was no loss on follow-up.

The study was reported according to the Strengthening the Reporting of Observational Studies in Epidemiology (STROBE) Statement [22].

2.2. Variables and Assessment Methods

Plasma HIV viremia, CD4+ T cell count at the time of the third vaccine dose, CD4+ T cell count at nadir, and main clinical and demographic characteristics of the patients were collected. A successful HIV-1 suppression was defined when HIV RNA viremia was below 40 copies/mL.

Six months after the third BNT162b2 vaccine dose, NtAb titers were determined in a live virus microneutralization assay against the BA.5 omicron sublineage (EPI _ISL_14513768) (BA.5.1) and the B.1 wild-type SARS-CoV-2 strain (EPI_ISL_2472896) as previously de-scribed [23,24]. Briefly, two-fold serial dilutions of sera were incubated with 100 $TCID_{50}$ of the corresponding SARS-CoV-2 strain and then added to pre-seeded Vero E6 cells and incubated for 72 h at 37 C with 5% CO_2. The virus cytopathic effect was quantified by measuring cell viability with the Cell-titer Glo 2.0 system in a GloMax Discover luciferase plate reader (Promega, Madison, WI, USA). The NtAb titer (ID_{50}) was defined as the re-ciprocal value of the sample dilution that showed 50% protection from the virus-induced cytopathic effect. Each serum was tested in duplicate, and each run included an uninfected control, an infected control, and the virus back-titration to confirm the virus inoculum. The initial validation of the assay was performed with the First WHO International Standard anti-SARS-CoV-2 immunoglobulin (Version 3.0, Dated 17 December 2020; code 20/268 NIBSC, Ridge, UK) [25]. Sera with ID_{50} below 10 were defined as negative and scored as 5 for statistical analysis.

2.3. Statistical Analysis

Statistical analysis was carried out using MedCalc® Statistical Software version 20.116 (MedCalc Software Ltd., Ostend, Belgium) and Stata v. 17.0. (StataCorp. College Station, TX, USA). Data were summarized using absolute and relative frequencies for categorical variables and median and IQR for numerical variables. Mann–Whitney U test, chi-squared test, and Fisher's exact test were employed as appropriate. A spearman rank correlation was applied for the comparison of NtAb titers to B.1 and BA.5 lineages and for comparison with other continuous variables. The statistical significance level was set at = 0.05 for all analyses.

2.4. Bias and Sensitivity Analysis

The main source of bias lies in the inadvertent inclusion of patients who had contracted an asymptomatic, undiagnosed SARS-CoV-2 infection. This would translate into erroneously including subjects with hybrid immunity (infection plus vaccination), which has been shown to be of higher magnitude and broader compared with the response to vaccine alone [14].

To reduce this potential source of bias, a sensitivity analysis was performed by ex-cluding patients with NtAb titers exceedingly high within the cohort. The Grubbs test was applied to identify such outliers of NtAb titers to either B.1 or BA.5, independently [26]. Pearson's correlation and linear regression analyses were then used on this subset.

3. Results

A total of 100 subjects (Male/Female 83/17, median age 54 years, IQR 49–60 years) were included in the analysis. All of them were on ART, most (68%) on triple drug regimens, and with suppressed HIV viremia (95%). The median CD4+ T cell count at the administration of the third dose was 580 cells/mm^3 (IQR 411–786 cells/mm^3), and the median nadir CD4+ T cell count was 258 cells/mm^3 (IQR 117–360 cells/mm^3). The characteristics of the study population are reported in Table 1.

Table 1. Main characteristics of the study population (n = 100).

Male, n (%)	83 (83)
Caucasians, n (%)	88 (88) 36
Age at HIV diagnosis (years), median (IQR) Age at study enrollment (years), median (IQR)	(28–48) 54 (49–60)
Absolute number of CD4+ T cell count at nadir (cells/mm^3), median (IQR)	258 (117–360)
Patients with <200 CD4+ T cell count at nadir, n (%)	36 (36) 580
Current CD4+ T cell count (cells/mm^3), median (IQR)	(411–786)
Patients with suppressed undetectable plasma HIV RNA, n (%) HIV	95 (95)
RNA value in patients with detectable HIV viremia (copies/mL), median (IQR)	58 (49–72)

The main results of our study were the stronger neutralizing response to B.1 with respect to BA.5, the positive correlation between the two titers, and the lack of correlation with CD4+ cell count.

NtAb against B.1 was detectable in all the subjects; conversely, 12 patients were negative for BA.5 ($p < 0.001$). Overall, the median NtAb titer to B.1 was significantly higher than that to BA.5 (393, IQR 128–866 vs. 60, IQR 28–143, $p < 0.0001$); however, there was a strong positive correlation between the paired measurements ($r = 0.854$, 95% CI 0.79–0.9, $p < 0.0001$) (Figure 1). The difference in NtAb titers between the two strains remained significant when subjects only scored positive for both lineages were analyzed (459 [IQR 162–907] to B.1 vs. 72 [36–204] to BA.5, $p < 0.0001$). Only one subject, an African male, showed NtAbs titers to BA.5 higher than to B.1 (2961 vs. 1378). In this case, the BA.5, but not the B.1, was recognized as an outlier.

Neither NtAb titers to B.1 nor to BA.5 showed any correlation with current CD4+ T cell counts ($r = 0.0752$, $p = 0.5680$; and $r = 0.00461$, $p = 0.9721$; respectively) or with CD4+ T cell counts at nadir ($r = 0.0380$, $p = 0.7148$; and $r = 0.0426$, $p = 0.6819$; respectively). NtAb titers to BA.5, but not to B.1, had a positive correlation with age at diagnosis ($r = 0.276$, 95% CI 0.08–0.450, $p = 0.0063$) and at enrollment ($r = 0.227$, 95% CI 0.0309–0.406, $p = 0.0239$).

Sensitivity Analysis

Thirteen patients were excluded in a sensitivity analysis excluding outlier NtAb titers (2 to B.1, 5 to BA.5, and 6 to both strains; see Supplementary Table S1). The correlation between NtAb titers to B.1 and BA.5 was confirmed in the resulting subset of 87 patients ($r = 0.69$, $p < 0.0001$). The significantly higher NtAb titer to B.1 was confirmed in this subgroup of 87 patients (268, IQR 114–593 vs. 50, IQR 25–105, $p < 0.0001$). Linear regression showed that 48% of the changes in NtAb titers to BA.5 are related to the changes in value titers to B.1 (Figure 2).

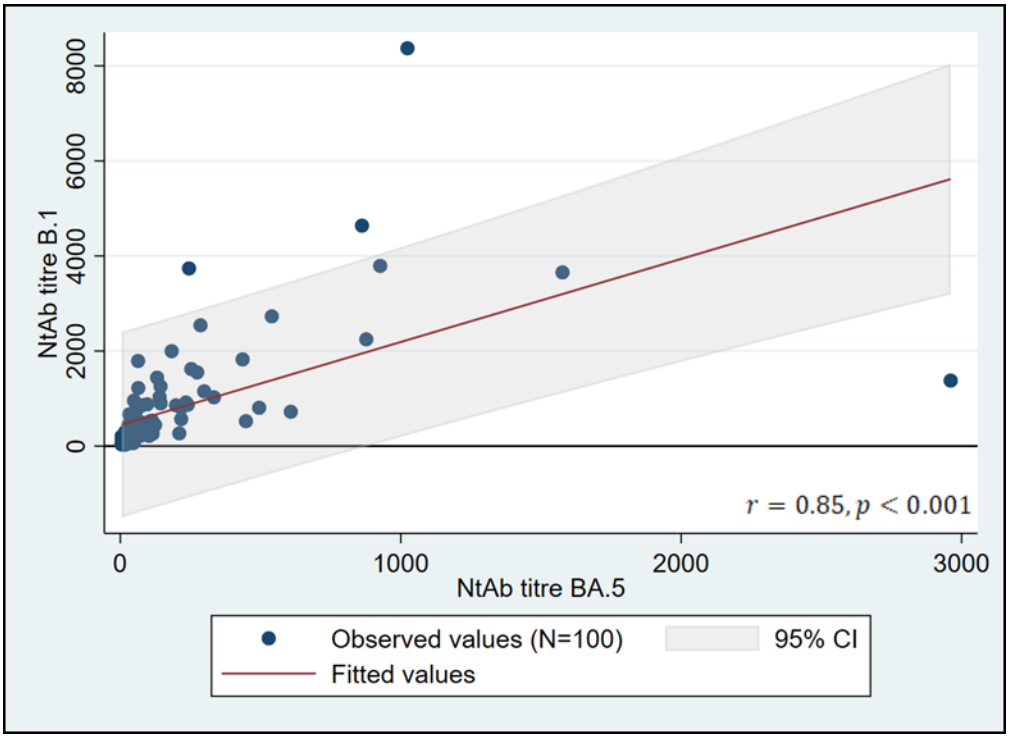

Figure 1. Linear regression between B.1 titers and BA.5 titers in HIV patients 6 months after the third BNT162b2 vaccine dose (entire cohort). NtAb titers are expressed as ID_{50}, which is the reciprocal value of the sera dilution and shows 50% protection from the virus-induced cytopathic effect.

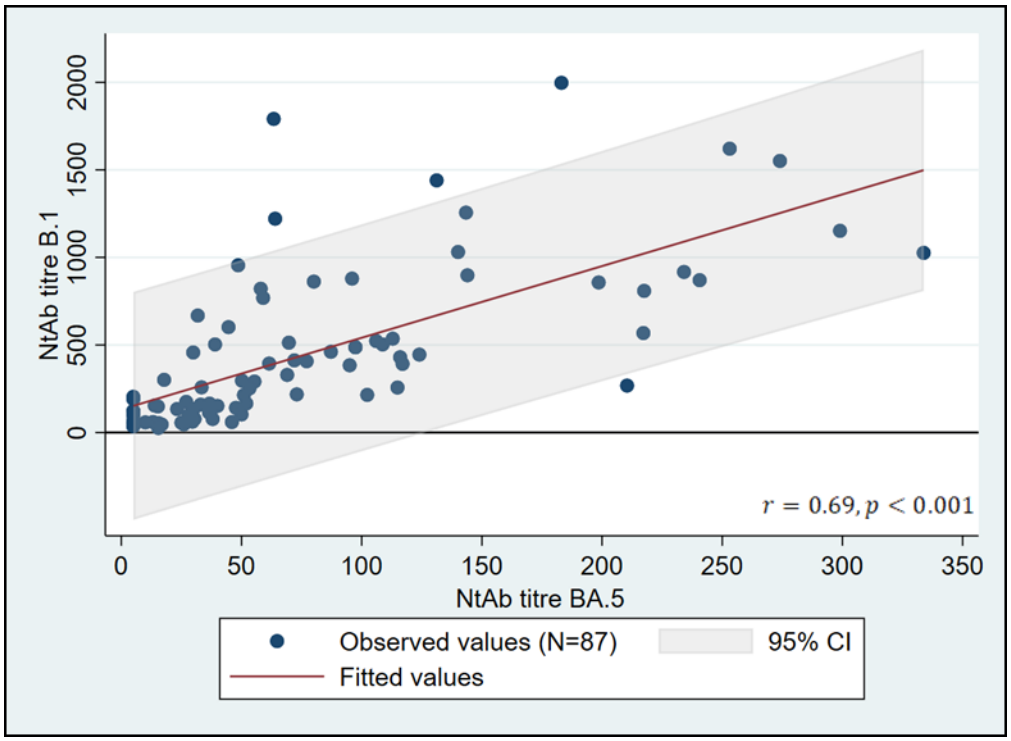

Figure 2. Linear regression between B.1 and BA.5 titers in HIV patients 6 months after the third BNT162b2 vaccine dose (outliers excluded from cohort). NtAb titers are expressed as ID_{50}, which is the reciprocal value of the sera dilution and shows 50% protection from the virus-induced cytopathic effect.

A detailed comparison between the main results and the sensitivity analysis was reported in Supplementary Table S2.

4. Discussion

Here we describe the correlation between NtAb titers against B.1 and against BA.5 six months after the third dose of the BNT162b2 vaccine in a cohort of 100 HIV-positive subjects on successful ART and COVID-naïve.

NtAb titers to BA.5 were significantly lower with respect to titers to B.1 six months after the third dose of the BNT162b2 vaccine in a cohort of HIV-positive subjects, mostly on suc-cessful ART. This result is in agreement with previously reported data in patients receiving three vaccine doses and having NtAb tested about one month [5,27] and eight months [28] after the third dose. The subjects enrolled in the first study [27] were HIV-positive patients on ART with a median CD4+ T cell count > 500 cells/mm^3, while subjects included in the studies by Cheng et al. [5] and by Anichini et al. [28] were likely HIV-uninfected (no information was reported). Taken together, all these results suggest that the striking diver-gence of Omicron BA.5 is the major driver for vaccine escape and that the NtAb response in immune restored HIV-positive subjects is similar to that occurring in HIV-negative patients [27,29]. The independence of the neutralizing activity to BA.5 from immunocom-petence is in accord with the data reported in the study by Corma-Gomez et al. [30], who described a lower neutralizing activity to BA.5 with respect to B.1 from 4 to 8 weeks after the booster vaccine dose both in patients with CD4 counts < 200 cells/mm^3 and in those with CD4 counts 200 cells/mm^3.

Despite a significantly lower response to BA.5, there was a clear correlation between NtAb titers to B.1 and to BA.5, both in the overall study population and in the subset excluding subjects with outliers to either viral strain. Despite an overall low response, NtAb titers to BA.5 varied over three orders of magnitude. This might reflect the inclusion of subjects with an undiagnosed prior SARS-CoV-2 infection and/or higher cross-reactivity due to prior exposure to seasonal human coronaviruses [31]. The latter could explain the positive correlation between BA.5 NtAb titers and patient age detected in our case file, but this is a hypothesis that needs to be confirmed on a larger number of patients.

There is an increasing interest in the clinical role of a model able to predict the humoral response to SARS-CoV-2 vaccine in specific populations: Voutouri et al. [32] elaborated a mechanistic model to simulate the efficacy of a vaccine booster in immunosuppressed patients, and Parisi et al. [24] described the kinetics of the response to the ancestral virus in a cohort of healthcare workers infected during the first SARS-CoV-2 wave and monitored to the completion of their triple vaccination cycle.

Real-life investigations focused on the disease severity of the SARS-CoV-2 infection caused by the BA.5 strain sublineage reported quite different results. During the BA.1 and BA.4/BA.5 waves, the risk of admission to an intensive care unit, mechanical ventilation, or steroid prescription/death within 21 days from diagnosis was lower with respect to the ancestral, Beta, and Delta waves. In addition, vaccination had a protective role [33], and a considerable risk reduction of death outcome associated with a booster vaccine dose was observed either for BA.5 or BA.2 related infections [34]. Conversely, a Danish nationwide population-based study described a higher hospitalization rate in subjects with BA.5 infection with respect to subjects with BA.2 infection (1.9% vs. 1.4%) [35]: BA.5 infection was also associated with an 18% increased rate of hospitalization and a longer duration of symptoms compared to BA.1 [36,37].

The main limitations of the study are the lack of patients with a previous SARS-CoV-2 infection, the lack of patients vaccinated with the new bivalent mRNA formulations expressing BA.5, and the lack of a control group. Furthermore, it has to be underlined the unavailability of a longitudinal evaluation of neutralizing response and cellular analysis of T-cell memory response: we did not include these data in our study because of the difficulty of obtaining a large amount of blood from patients who are already regularly monitored and because of the elevated costs of such studies, which make it necessary to work in a

biosafety level 3 laboratory. We identified COVID-19-naïve subjects based on self-reported data, as currently accepted [18,38]: antibody titers against the N antigen protein waned with time [39,40], and they could not be detectable after SARS-CoV-2 infection [41,42].

On the other hand, this study included 100 HIV-positive subjects, all vaccinated with the same mRNA vaccine and regularly followed, who are an ideal cohort for prolonged monitoring of humoral responses and for assessing an overtime titer threshold for immuno-logical protection from BA.5 infection [43]. Of note, in our study, the interval between booster vaccine dose and neutralizing activity testing is six months, so that giving updated information on the humoral response to the wild-type virus and to BA.5 is at a time corre-sponding to the administration of the fourth vaccine dose [44]. Future evaluations of the cohort enrolled in this study will be aimed at studying neutralizing response durability in persistently COVID-naïve patients and modification over time of the titer in breakthrough cases. The availability of studies on the humoral response in HIV patients receiving the same vaccine schedule but with different viroimmunological characteristics (i.e., failed sub-jects) or with comorbidities modifying the immune response (i.e., cancer on chemotherapy) could help to individualize the risk of severe disease in these frail subjects and to prescribe the more appropriate treatment in the case of SARS-CoV-2 infection.

5. Conclusions

SARS-CoV-2 variants evolve rapidly, challenging the efficacy of vaccines and data on comparative NtAb response may help in tailoring intervals between vaccine doses and in predicting vaccine efficacy. NtAb titers are the best correlate of protection from severe COVID-19 [45] and live virus neutralization, despite the time consuming and requiring biosafety level 3 containment, remains the gold standard to investigate immunity in specific cohorts. In the HIV-positive population, further studies are needed to define the role of the fourth vaccine dose and what immunovirological parameters may impact the success of vaccination [38].

Supplementary Materials: The following supporting information can be downloaded at: https://www.mdpi.com/article/10.3390/vaccines11040871/s1, Table S1: Neutralizing antibody titers to B.1 and to BA.5 classified as outliers (n = 19). Data are expressed as ID_{50}: reciprocal value of the sample dilution that showed a 50% protection from the virus-induced cytopathic effect; Table S2: Raw data and comparison after outlier (n = 13) removal.

Author Contributions: Conceptualization, S.G.P.; methodology, M.Z., I.V. (Ilaria Vicenti), L.F., S.P., C.B., I.V. (Ilenia Varasi) and N.P.; validation, I.V. (Ilaria Vicenti), S.G.P. and M.Z.; formal analysis, A.V., M.Z. and I.V. (Ilaria Vicenti); resources, M.C.R., N.P., B.B., M.G. and S.C.; data curation, S.G.P.; writing—original draft preparation, M.B., M.Z. and S.G.P.; writing—review and editing, A.V., M.B., M.Z. and S.G.P.; visualization, I.V. (Ilaria Vicenti) and B.B.; supervision, S.G.P.; project administration, M.B.; funding acquisition, S.G.P. and M.Z. All authors have read and agreed to the published version of the manuscript.

Funding: This research was funded by the University of Padua, grant numbers DOR-2021 and DOR-2022 to S.G.P. and M.B., and by the EuCARE Project funded by the European Union's Horizon Europe Research and Innovation Programme, Grant Agreement No. 101046016 to M.Z. and I.V. (Ilaria Vicenti).

Institutional Review Board Statement: The study was conducted in accordance with the Declaration of Helsinki and approved by the Ethics Committee, "Comitato per la Sperimentazione Clinica di Treviso e Belluno" (protocol code 812/2020, approved on 12 November 2020).

Informed Consent Statement: Informed consent was obtained from all subjects involved in the study.

Data Availability Statement: The raw data on demographics and clinical status of participants are protected and not available due to data privacy laws. The processed data are available from the corresponding author upon reasonable request.

Acknowledgments: We would like to thank Alessia Lai for making the SARS-CoV-2 lineage B strain available for this study.

Conflicts of Interest: The authors declare no conflict of interest. The funders had no role in the design of the study; in the collection, analysis, or interpretation of data; in the writing of the manuscript; or in the decision to publish the results.

References

1. Available online: https://www.iss.it/web/guest/-/bollettino-varianti-del-28-ottobre-2022 (accessed on 7 November 2022). 2. Caputo, E.; Mandrich, L. SARS-CoV-2: Searching for the Missing Variants. Viruses 2022, 14, 2364. [CrossRef] [PubMed]
3. Hachmann, N.P.; Miller, J.; Collier, A.Y.; Ventura, J.D.; Yu, J.; Rowe, M.; Bondzie, E.A.; Powers, O.; Surve, N.; Hall, K.; et al. Neutralization Escape by SARS-CoV-2 Omicron Subvariants BA.2.12.1, BA.4, and BA.5. N. Engl. J. Med. 2022, 387, 86–88. [CrossRef] [PubMed]
4. Tartof, S.Y.; Slezak, J.M.; Puzniak, L.; Hong, V.; Frankland, T.B.; Ackerson, B.K.; Takhar, H.; Ogun, O.A.; Simmons, S.; Zamparo, J.M.; et al. BNT162b2 vaccine effectiveness against SARS-CoV-2 omicron BA.4 and BA.5. Lancet Infect. Dis. 2022, 22, 1663–1665. [CrossRef] [PubMed]
5. Cheng, S.S.; Mok, C.K.; Li, J.K.; Ng, S.S.; Lam, B.H.; Jeevan, T.; Kandeil, A.; Pekosz, A.; Chan, K.C.; Tsang, L.C.; et al. Plaque-neutralizing antibody to BA.2.12.1, BA.4 and BA.5 in individuals with three doses of BioNTech or CoronaVac vaccines, natural infection and breakthrough infection. J. Clin. Virol. 2022, 156, 105273. [CrossRef] [PubMed]
6. Quadir, N.; Singh, J.; Alam, A.; Malik, A.A.; Rahman, S.A.; Hira, S.; Ehtesham, N.Z.; Sundar, D.; Hasnain, S.E. Evolution of SARS-CoV-2: BA.4/BA.5 Variants Continues to Pose New Challenges. Viruses 2022, 14, 2610. [CrossRef] [PubMed]
7. Tuekprakhon, A.; Nutalai, R.; Dijokaite-Guraliuc, A.; Zhou, D.; Ginn, H.M.; Selvaraj, M.; Liu, C.; Mentzer, A.J.; Supasa, P.; Duyvesteyn, H.M.E.; et al. Antibody escape of SARS-CoV-2 Omicron BA.4 and BA.5 from vaccine and BA.1 serum. Cell 2022, 185, 2422–2433. [CrossRef]
8. Baek, Y.J.; Kim, W.J.; Ko, J.H.; Lee, Y.J.; Ahn, J.Y.; Kim, J.H.; Jang, H.C.; Jeong, H.W.; Kim, Y.C.; Park, Y.S.; et al. A heterologous AZD1222 priming and BNT162b2 boosting regimen more efficiently elicits neutralizing antibodies, but not memory T cells, than the homologous BNT162b2 regimen. Vaccine 2023, 41, 1694–1702. [CrossRef]
9. Mise-Omata, S.; Ikeda, M.; Takeshita, M.; Uwamino, Y.; Wakui, M.; Arai, T.; Yoshifuji, A.; Murano, K.; Siomi, H.; Nakagawara, K.; et al. Memory B Cells and Memory T Cells Induced by SARS-CoV-2 Booster Vaccination or Infection Show Different Dynamics and Responsiveness to the Omicron Variant. J. Immunol. 2022, 209, 2104–2113. [CrossRef]
10. Manni, S.; Ruetsch, C.; Fabre, R.; Ticchioni, M.; Graça, D.; Pradier, C.; Seitz-Polski, B.; Lotte, L.; Brglez, V.; Vassallo, M. Immune response to BNT162b2 SARS-CoV-2 vaccine in patients living with HIV: The COVIH-DAPT study. Front. Immunol. 2023, 14, 1136723. [CrossRef]
11. Tortellini, E.; Zingaropoli, M.A.; Mancarella, G.; Marocco, R.; Carraro, A.; Jamhour, M.; Barbato, C.; Guardiani, M.; Dominelli, F.; Pasculli, P.; et al. Quality of T-Cell Response to SARS-CoV-2 mRNA Vaccine in ART-Treated PLWH. Int. J. Mol. Sci. 2022, 23, 14988. [CrossRef]
12. Levy, I.; Rahav, G. The effect of HIV on COVID-19 vaccine responses. Curr. Opin. HIV AIDS, 2023; preprint version. [CrossRef] 13. Bieńkowski, C.; Skrzat-Klapaczyńska, A.; Firląg-Burkacka, E.; Horban, A.; Kowalska, J.D. The Clinical Effectiveness and Safety of Vaccinations against COVID-19 in HIV-Positive Patients: Data from Observational Study in Poland. Vaccines 2023, 11, 514. [CrossRef]
14. Polack, F.P.; Thomas, S.J.; Kitchin, N.; Absalon, J.; Gurtman, A.; Lockhart, S.; Perez, J.L.; Pérez, M.G.; Moreira, E.D.; Zerbini, C.; et al. Safety and Efficacy of the BNT162b2 mRNA Covid-19 Vaccine. N. Engl. J. Med. 2020, 383, 2603–2615. [CrossRef]
15. Coburn, S.B.; Humes, E.; Lang, R.; Stewart, C.; Hogan, B.C.; Gebo, K.A.; Napravnik, S.; Edwards, J.K.; Browne, L.E.; Park, L.S.; et al. Analysis of Postvaccination Breakthrough COVID-19 Infections Among Adults With HIV in the United States. JAMA Netw. Open 2022, 5, e2215934. [CrossRef]
16. Wang, Y.; Li, J.; Zhang, W.; Liu, S.; Miao, L.; Li, Z.; Fu, A.; Bao, J.; Huang, L.; Zheng, L.; et al. Extending the dosing interval of COVID-19 vaccination leads to higher rates of seroconversion in people living with HIV. Front. Immunol. 2023, 14, 1152695. [CrossRef]
17. Fidler, S.; Fox, J.; Tipoe, T.; Longet, S.; Tipton, T.; Abeywickrema, M.; Adele, S.; Alagaratnam, J.; Ali, M.; Aley, P.K.; et al. Booster vaccination against SARS-CoV-2 induces potent immune responses in people with HIV. Clin. Infect. Dis. 2023, 76, 201–209. [CrossRef]
18. Gianserra, L.; Donà, M.G.; Giuliani, E.; Stingone, C.; Pontone, M.; Buonomini, A.R.; Giuliani, M.; Pimpinelli, F.; Morrone, A.; Latini, A. Immunogenicity and Safety of BNT162b2 Homologous Booster Vaccination in People Living with HIV under Effective cART. Vaccines 2022, 10, 1243. [CrossRef]
19. Kling, K.D.; Janulis, P.; Demonbreun, A.R.; Sancilio, A.; Berzins, B.; Krueger, K.; Achenbach, C.; Price, R.; Sullivan, M.; Caputo, M.; et al. No difference in anti-spike antibody and surrogate viral neutralization following SARS-CoV-2 booster vaccination in persons with HIV compared to controls (CO-HIV Study). Front. Immunol. 2023, 13, 1048776. [CrossRef]
20. Park, J.H.; Chung, H.; Kim, M.C.; Choi, S.H.; Chung, J.W. Immune Responses against the Omicron Variant of SARS-CoV-2 after a Third Dose of COVID-19 Vaccine in Patients Living with Human Immunodeficiency Virus (PLWH): Comparison with Healthcare Workers. Vaccines 2022, 10, 2129. [CrossRef]

21. Moussaoui, M.E.; Desmecht, S.; Tashkeev, A.; Lambert, N.; Maes, N.; Braghini, J.; Marechal, N.; Quintana, C.; Briquet, K.; Gofflot, S.; et al. Reduced T-cell response following a third dose of SARS-CoV-2 vaccine in infection-naïve people living with HIV. J. Infect. 2022, 85, 702–769. [CrossRef]
22. von Elm, E.; Altman, D.G.; Egger, M.; Pocock, S.J.; Gotzsche, P.C.; Vandenbroucke, J.P. The Strengthening the Reporting of Observational Studies in Epidemiology (STROBE) Statement: Guidelines for reporting observational studies. Lancet 2007, 370, 1453–1457. [CrossRef]
23. Vicenti, I.; Basso, M.; Gatti, F.; Scaggiante, R.; Boccuto, A.; Zago, D.; Modolo, E.; Dragoni, F.; Parisi, S.G.; Zazzi, M. Faster decay of neutralizing antibodies in never infected than previously infected healthcare workers three months after the second BNT162b2 mRNA COVID-19 vaccine dose. Int. J. Infect. Dis. 2021, 112, 40–44. [CrossRef] [PubMed]
24. Parisi, S.G.; Mengoli, C.; Basso, M.; Vicenti, I.; Gatti, F.; Scaggiante, R.; Fiaschi, L.; Giammarino, F.; Iannetta, M.; Malagnino, V.; et al. Long-Term Longitudinal Analysis of Neutralizing Antibody Response to Three Vaccine Doses in a Real-Life Setting of Previously SARS-CoV-2 Infected Healthcare Workers: A Model for Predicting Response to Further Vaccine Doses. Vaccines 2022, 10, 1237. [CrossRef] [PubMed]
25. Kristiansen, P.A.; Page, M.; Bernasconi, V.; Mattiuzzo, G.; Dull, P.; Makar, K.; Plotkin, S.; Knezevic, I. WHO International Standard for anti-SARS-CoV-2 immunoglobulin. Lancet 2021, 397, 1347–1348. [CrossRef] [PubMed]
26. Grubbs, F.E. Sample criteria for testing outlying observations. Ann. Math. Stat. 1950, 21, 27–58. [CrossRef]
27. Lapointe, H.R.; Mwimanzi, F.; Cheung, P.K.; Sang, Y.; Yaseen, F.; Speckmaier, S.; Barad, E.; Moran-Garcia, N.; Datwani, S.; Duncan, M.C.; et al. Antibody response durability following three-dose COVID-19 vaccination in people with HIV receiving suppressive ART. AIDS 2022, 37, 709–721. [CrossRef]
28. Anichini, G.; Terrosi, C.; Gori Savellini, G.; Gandolfo, C.; Barbagli, F.; Carta, G.A.; Fabrizi, S.; Miceli, G.B.; Cusi, M.G. Antibody Response against Circulating Omicron Variants 8 Months after the Third Dose of mRNA Vaccine. Vaccines 2022, 10, 1512. [CrossRef]
29. Antinori, A.; Cicalini, S.; Meschi, S.; Bordoni, V.; Lorenzini, P.; Vergori, A.; Lanini, S.; De Pascale, L.; Matusali, G.; Mariotti, D.; et al. Humoral and Cellular Immune Response Elicited by mRNA Vaccination Against Severe Acute Respiratory Syndrome Coronavirus 2 (SARS-CoV-2) in People Living With Human Immunodeficiency Virus Receiving Antiretroviral Therapy Based on Current CD4 T-Lymphocyte Count. Clin. Infect. Dis. 2022, 75, e552–e563.
30. Corma-Gómez, A.; Fernández-Fuertes, M.; Viñuela, L.; Domínguez, C.; Santos, M.; Fuentes-López, A.; Rojas, A.; Fernández-Pérez, N.; Martín-Carmona, J.; Serrano-Conde, E.; et al. Reduced neutralizing antibody response to SARS-CoV-2 vaccine booster dose in people living with HIV with severe immunosuppression. J. Med. Virol. 2023, 95, e28602. [CrossRef]
31. Hu, C.; Wang, Z.; Ren, L.; Hao, Y.; Zhu, M.; Jiang, H.; Wang, S.; Li, D.; Shao, Y. Pre-existing anti-HCoV-OC43 immunity influences the durability and cross-reactivity of humoral response to SARS-CoV-2 vaccination. Front. Cell. Infect. Microbiol. 2022, 12, 978440. [CrossRef]
32. Voutouri, C.; Hardin, C.C.; Naranbhai, V.; Nikmaneshi, M.R.; Khandekar, M.J.; Gainor, J.F.; Stylianopoulos, T.; Munn, L.L.; Jain, R.K. Mechanistic model for booster doses effectiveness in healthy, cancer, and immunosuppressed patients infected with SARS-CoV-2. Proc. Natl. Acad. Sci. USA 2023, 120, e2211132120. [CrossRef]
33. Davies, M.A.; Morden, E.; Rousseau, P.; Arendse, J.; Bam, J.L.; Boloko, L.; Cloete, K.; Cohen, C.; Chetty, N.; Dane, P.; et al. Outcomes of laboratory-confirmed SARS-CoV-2 infection during resurgence driven by Omicron lineages BA.4 and BA.5 compared with previous waves in the Western Cape Province, South Africa. Int. J. Infect. Dis. 2023, 127, 63–68. [CrossRef] [PubMed]
34. Kislaya, I.; Casaca, P.; Borges, V.; Sousa, C.; Ferreira, B.I.; Fonte, A.; Fernandes, E.; Dias, C.M.; Duarte, S.; Almeida, J.P.; et al. Comparative Effectiveness of COVID-19 Vaccines in Preventing Infections and Disease Progression from SARS-CoV-2 Omicron BA.5 and BA.2, Portugal. Emerg. Infect. Dis. 2023, 29, 569–575. [CrossRef] [PubMed]
35. Hansen, C.H.; Friis, N.U.; Bager, P.; Stegger, M.; Fonager, J.; Fomsgaard, A.; Gram, M.A.; Christiansen, L.E.; Ethelberg, S.; Legarth, R.; et al. Risk of reinfection, vaccine protection, and severity of infection with the BA.5 omicron subvariant: A nation-wide population-based study in Denmark. Lancet Infect. Dis. 2023, 23, 167–176. [CrossRef] [PubMed]
36. Russell, S.L.; Klaver, B.R.A.; Harrigan, S.P.; Kamelian, K.; Tyson, J.; Hoang, L.; Taylor, M.; Sander, B.; Mishra, S.; Prystajecky, N.; et al. Clinical severity of Omicron subvariants BA.1, BA.2, and BA.5 in a population-based cohort study in British Columbia, Canada. J. Med. Virol. 2023, 95, e28423. [CrossRef] [PubMed]
37. Kouamen, A.C.; Da Cruz, H.; Hamidouche, M.; Lamy, A.; Lloyd, A.; Castro Alvarez, J.; Roussel, M.; Josset, L.; Enouf, V.; Felici, C.; et al. Regional COVID-19 Investigation Group; Laboratory Group. Rapid investigation of BA.4/BA.5 cases in France. Front. Public Health 2022, 10, 1006631. [CrossRef]
38. Basso, M.; Pirola, N.; Pascoli, S.; Bragato, B.; Vinci, A.; Iannetta, M.; Colombo, F.; Geremia, N.; Martignago, L.; Rossi, M.C.; et al. Humoral Response after Two Doses of BNT162b2 mRNA Vaccine Has a Role in Predicting Response after Three Doses That Is Related to Plasma HIV Viremia and Nadir CD4+ Cell Count in HIV-Positive Patients. Vaccines 2022, 11, 82. [CrossRef]
39. Paul, G.; Strnad, P.; Wienand, O.; Krause, U.; Plecko, T.; Effenberger-Klein, A.; Giel, K.E.; Junne, F.; Galante-Gottschalk, A.; Ehehalt, S.; et al. Jürgensen JS. The humoral immune response more than one year after SARS-CoV-2 infection: Low detection rate of anti-nucleocapsid antibodies via Euroimmun ELISA. Infection 2023, 51, 83–90. [CrossRef]
40. Lea, C.S.; Simeonsson, K.; Kipp, A.M.; McNeill, C.; Wilcox, L.; Irish, W.; Morris, H.; Diaz, O.M.; Fallon, J.T.; Roper, R.L. Waning of SARS-CoV-2 Seropositivity among Healthy Young Adults over Seven Months. Vaccines 2022, 10, 1532. [CrossRef]

41. Van Elslande, J.; Oyaert, M.; Lorent, N.; Vande Weygaerde, Y.; Van Pottelbergh, G.; Godderis, L.; Van Ranst, M.; André, E.; Padalko, E.; Lagrou, K.; et al. Lower persistence of anti-nucleocapsid compared to anti-spike antibodies up to one year after SARS-CoV-2 infection. Diagn. Microbiol. Infect. Dis. 2022, 103, 115659. [CrossRef]
42. Krutikov, M.; Palmer, T.; Tut, G.; Fuller, C.; Azmi, B.; Giddings, R.; Shrotri, M.; Kaur, N.; Sylla, P.; Lancaster, T.; et al. Prevalence and duration of detectable SARS-CoV-2 nucleocapsid antibodies in staff and residents of long-term care facilities over the first year of the pandemic (VIVALDI study): Prospective cohort study in England. Lancet Healthy Longev. 2022, 3, e13–e21. [CrossRef]
43. Regev-Yochay, G.; Lustig, Y.; Joseph, G.; Gilboa, M.; Barda, N.; Gens, I.; Indenbaum, V.; Halpern, O.; Katz-Likvornik, S.; Levin, T.; et al. Correlates of protection against COVID-19 infection and intensity of symptomatic disease in vaccinated individuals exposed to SARS-CoV-2 in households in Israel (ICoFS): A prospective cohort study. Lancet Microbe, 2023; preprint version. [CrossRef]
44. World Health Organization (WHO). Coronavirus Disease (COVID-19) and People Living with HIV. Updated 29 July 2022. Available online: https://www.who.int/news-room/questions-and-answers/item/coronavirus-disease-(covid-19)-covid-19 and-people-living-with-hiv (accessed on 30 November 2022).
45. Khoury, D.S.; Schlub, T.E.; Cromer, D.; Steain, M.; Fong, Y.; Gilbert, P.B.; Subbarao, K.; Triccas, J.A.; Kent, S.J.; Davenport, M.P. Correlates of Protection, Thresholds of Protection, and Immunobridging among Persons with SARS-CoV-2 Infection. Emerg. Infect. Dis. 2023, 29, 381–388. [CrossRef]

viruses

MDPI

Article

Efficacy of Licensed Monoclonal Antibodies and Antiviral Agents against the SARS-CoV-2 Omicron Sublineages BA.1 and BA.2

Lia Fiaschi [1], Filippo Dragoni [1], Elisabetta Schiaroli [2], Annalisa Bergna [3], Barbara Rossetti [4], Federica Giammarino [1], Camilla Biba [1], Anna Gidari [2], Alessia Lai [3], Cesira Nencioni [4], Daniela Francisci [2], Maurizio Zazzi [1] and Ilaria Vicenti [1,*]

[1] Department of Medical Biotechnologies, University of Siena, 53100 Siena, Italy; lia300790@gmail.com (L.F.); dragoni16@student.unisi.it (F.D.); federica.giammari@gmail.com (F.G.); camilla.biba@student.unisi.it (C.B.); maurizio.zazzi@unisi.it (M.Z.)

[2] Department of Medicine and Surgery, Clinic of Infectious Diseases, University of Perugia, 06129 Perugia, Italy; elisabetta.schiaroli@unipg.it (E.S.); annagidari91@gmail.com (A.G.); daniela.francisci@unipg.it (D.F.)

[3] Department of Biomedical and Clinical Sciences L. Sacco, University of Milan, 20157 Milan, Italy; annalisa.bergna@unimi.it (A.B.); alessia.lai@unimi.it (A.L.)

[4] Infectious Disease Department, USL SUDEST, Toscana, Misericordia Hospital, 58100 Grosseto, Italy; brossetti1982@gmail.com (B.R.); cesira.nencioni@uslsudest.toscana.it (C.N.)

* Correspondence: vicenti@unisi.it; Tel.: +39-057-7233-855

Abstract: Newly emerging SARS-CoV-2 variants may escape monoclonal antibodies (mAbs) and antiviral drugs. By using live virus assays, we assessed the ex vivo inhibition of the B.1 wild-type (WT), delta and omicron BA.1 and BA.2 lineages by post-infusion sera from 40 individuals treated with bamlanivimab/etesevimab (BAM/ETE), casirivimab/imdevimab (CAS/IMD), and sotrovimab (SOT) as well as the activity of remdesivir, nirmatrelvir and molnupiravir. mAbs and drug activity were defined as the serum dilution (ID_{50}) and drug concentration (IC_{50}), respectively, showing 50% protection of virus-induced cytopathic effect. All pre-infusion sera were negative for SARS-CoV-2 neutralizing activity. BAM/ETE, CAS/IMD, and SOT showed activity against the WT (ID_{50} 6295 (4355–8075) for BAM/ETE; 18,214 (16,248–21,365) for CAS/IMD; and 456 (265–592) for SOT) and the delta (14,780 (ID_{50} 10,905–21,020) for BAM/ETE; 63,937 (47,211–79,971) for CAS/IMD; and 1103 (843–1334) for SOT). Notably, only SOT was active against BA.1 (ID_{50} 200 (37–233)), whereas BA.2 was neutralized by CAS/IMD (ID_{50} 174 (134–209) ID_{50}) and SOT (ID_{50} 20 (9–31) ID_{50}), but not by BAM/ETE. No significant inter-variant IC_{50} differences were observed for molnupiravir (1.5 0.1/1.5 0.7/1.0 0.5/0.8 0.01 M for WT/delta/BA.1/BA.2, respectively), nirmatrelvir (0.05 0.02/0.06 0.01/0.04 0.02/0.04 0.01 M) or remdesivir (0.08 0.04/0.11 0.08/ 0.05 0.04/0.08 0.01 M). Continued evolution of SARS-CoV-2 requires updating the mAbs arsenal, although antivirals have so far remained unaffected.

Keywords: SARS-CoV-2; mAbs; nirmatrelvir; remdesivir; molnupiravir; microneutralization assay; cell-based assay; omicron sublineages

check for updates

Citation: Fiaschi, L.; Dragoni, F.; Schiaroli, E.; Bergna, A.; Rossetti, B.; Giammarino, F.; Biba, C.; Gidari, A.; Lai, A.; Nencioni, C.; et al. Efficacy of Licensed Monoclonal Antibodies and Antiviral Agents against the SARS-CoV-2 Omicron Sublineages BA.1 and BA.2. Viruses 2022, 14, 1374. https://doi.org/10.3390/v14071374

Academic Editor: Eloise Mastrangelo

Received: 26 May 2022
Accepted: 22 June 2022
Published: 23 June 2022

1. Introduction

While worldwide vaccination has played a key role in the global control of COVID-19, both natural and vaccine-induced immunity have been shown to wane rapidly and be subject to escape by divergent virus variants [1,2]. In addition, a proportion of individ-uals could not be vaccinated due to specific underlying morbidity or personal choice. Thus, development of therapeutics for treatment and prevention of COVID-19 has been set as a public health priority, delivering at fast pace a number of monoclonal antibodies (mAbs) targeting the virus spike protein as well as three small molecule antivirals interfer-

ing with SARS-CoV-2 RNA synthesis (remdesivir, molnupiravir) or polyprotein cleavage (nirmatrelvir).

The viral enzymes have a high degree of conservation across SARS-CoV-2 lineages, thus antiviral activity is expected to be unaffected by viral variants, as preliminarily shown by limited in vitro data [3,4]. By contrast, the recent spread of the highly divergent SARS-CoV-2 omicron lineages has changed the landscape of mAbs activity with respect to previ-ous virus variants. Namely, the BA.1 lineage lost susceptibility to the first developed bam-lanivimab/etesevimab (BAM/ETE) and casirivimab/imdevimab (CAS/IMD) therapeutic mAbs combos as well as to the prophylactic cilgavimab/tixagevimab (CIL/TIX) combo while remaining partly sensitive to sotrovimab (SOT). However, SOT further decreased ac-tivity against the subsequent BA.2 variant which appears to have restored susceptibility to CIL and partly to IMD. Data about mAbs susceptibility for the minor BA.3 and the recently detected BA.4 and BA.5 lineages are scanty, with preliminary evidence for SOT activity against BA.3 [5] and partial or limited CIL activity against BA.4 and BA.5 [6,7]. According to the latest COVID-19 treatment guidelines (https://files.covid19treatmentguidelines.nih.gov/guidelines/covid19treatmentguidelines.pdf; updated 17 June 2022), the administra-tion of BAM/ETE, CAS/IMD, and SOT mAbs is not recommended, due to the expected lack of activity against the dominating omicron lineages. Bebtelovimab, which retains activity against all SARS-CoV-2 variants, remains the only mAbs approved by the FDA and submitted for approval to the EMA for emergency use for treatment of COVID-19. In addition, CIL/TIX can be administered as pre-exposure prophylaxis.

It must be noted that due to the pressure to deliver effective treatments, mAbs activity on contemporary SARS-CoV-2 lineages is inferred exclusively from in vitro data, while pivotal clinical trials were conducted during epidemic waves dominated by virus variants which have later disappeared. In addition, in vitro data have been generated by different methods including a variety of live virus or pseudovirus neutralization assays and surrogate tests such as SARS-CoV-2 spike binding measured by enzyme immunoassay or surface plasmon resonance. This has generated some data inconsistency across studies. In this study, we expanded our previous work [8] based on an ex vivo approach to test the licensed therapeutic mAbs BAM/ETE, CAS/IMD, and SOT against the omicron BA.1 and BA.2 lineages as well as against the ancestral B.1 strain and the previously dominating delta variant. By examining mAbs activity in post-infusion sera from treated patients in an authentic in vitro neutralization assay, we provide the best surrogate data for in vivo activity. Moreover, we tested on the same SARS-CoV-2 variants the three licensed antivirals, both with and without the P-glycoprotein (P-gp) inhibitor CP-100356, to further define their resilience to virus variability and current therapeutic potential.

2. Materials and Methods

2.1. Patients and Sera

The study was approved by the local Ethics Committee and written informed consent was obtained from all the patients enrolled (Neutro-COVID observational study, protocol number 4069/21). The study was conducted in accordance with the Declaration of Helsinki. Patients undergoing mAbs treatment were enrolled consecutively and selected based on undetectable NtAb before therapy, independently from their vaccination status. A pair of patient sera was collected, one before (baseline to comply with the negative NtAb selection criterion) and another one-hour post mAbs infusion (to test mAbs activity against the different virus variants). Thirty sera from a previous study [8] were included with their original NtAb values, although a random selection of 15 sera were retested against the wild-type virus to ensure consistency across the two studies, yielding comparable results.

2.2. Cells and Viral Stocks

VERO E6 (CRL 1586TM ATCC®, Gaithersburg, MA, USA), an adherent cell line de-rived from African green monkey kidney, was used to propagate and titrate the viral stocks as previously described [9]. The same cell line was used in the live virus microneutral-

ization and drug susceptibility assays. VERO E6 cells were propagated in DMEM High Glucose (Euroclone, Pero, Italy) supplemented with 10% Fetal Bovine Serum (FBS, Eu-roclone, Pero, Italy) and 1% of Streptomycin/Penicillin (PS) (Euroclone, Pero, Italy) in a humified incubator at 37 C with 5% of CO_2. The same medium, containing 1% of FBS instead of 10% (infection medium), was used in all viral infection experiments. Uninfected cell cultures were handled in a Biosafety Level 2 (BSL2) laboratory, whereas all the infec-tion experiments were performed in a BSL3 containment. The SARS-CoV-2 B.1 (D614G) wild-type, delta and omicron BA.1 and BA.2 stocks, used to challenge the mAbs sera in neutralization experiments and to determine the antiviral activity of drug compounds in drug susceptibility assays, are detailed in Supplementary Table S1. Before performing the neutralization and phenotypic experiments, six replicates of 5-fold serial dilution of each viral stock were titrated in VERO E6 cells to determine the Tissue Culture Infectious Dose per milliliter ($TCID_{50}/_{mL}$), which is defined as the amount of virus required to infect 50% of replicate cell cultures as previously described [9]. The cytopathic effect and consequently the $TCID_{50}/_{mL}$ was determined by luminescence as described below. In addition, each viral stock was initially quantified by plaque assay as previously published [9].

2.3. Live Virus Microneutralization Assay

Microneutralization experiments were performed as previously described [8]. Briefly, after inactivation at 56 C for 30 min, the patient serum was prediluted 1:5 and two-fold serial dilutions were prepared in 96-well format. One hundred 50% $TCID_{50}$ of each SARS-CoV-2 viral stock were added to the sera and incubated at 37 C with 5% CO_2 for 1 h. Then, serum-virus mixtures were added to 5000 pre-seeded VERO E6 cells in 96-well plates and incubated at 37 C with 5% CO_2. After 72 h, the ability of sera to neutralize the virus was determined measuring the cell viability by the CellTiter-Glo 2.0 Luminescent Cell Viability Assay (Promega, Madison, WI, USA) with the GloMax® Discover Multimode Microplate Reader (Promega, Madison, WI, USA) and the mAbs neutralization titer was expressed as the serum dilution corresponding to half-maximal inhibition of virus-induced cell death (ID_{50}). Sera below 5 ID_{50} were scored as not neutralizing and given a 2.5 value for statistical analysis.

Each serum was tested in technical duplicates in two independent experiments. Each plate included: (i) a mock infection control (uninfected cells); (ii) a virus control (infected cells without patient serum); (iii) a known SARS-CoV-2 neutralizing serum (positive con-trol), yielding a median titer of 69 (59.3–69.9) in five independent runs. In addition, the virus test dose was confirmed by back titration, consisting of two-fold serial dilutions of each viral stock (100, 50, 25, 12.5, and 6.25 $TCID_{50}$). The virus test dose was considered acceptable if the back-titration results were positive in at least 3 subsequent virus dilutions. For a run to be valid, the coefficient of variation for the technical duplicates and for the two independent experiments had to be both below 30%. The initial validation of the assay was performed with the First WHO International Standard [10] anti-SARS-CoV-2 immunoglobulin (Version 3.0, Dated 17 December 2020; code 20/268 NIBSC, Ridge, UK).

2.4. Drug Susceptibility Assay

The P-gp inhibitor CP-100356 hydrochloride (MCE® cat. HY-108347 distributed by DBA, Milan, Italy), Remdesivir (MCE® cat. HY-104077 distributed by DBA, Milan, Italy), Nirmatrelvir (MCE® cat. HY-138687 distributed by DBA, Milan, Italy) and EIDD-1931 (MCE® cat. HY-125033 distributed by DBA, Milan, Italy), the active form of molnupiravir, were supplied as powder and dissolved in 100% dimethyl sulfoxide (DMSO). The VERO E6 cytotoxicity of CP-100356 hydrochloride alone and of the three antiviral drugs both with and without the addition of 0.5 M CP-100356 was determined by the Cell Titer-Glo 2.0 Luminescent Cell Viability Assay (Promega) according to the manufacturer's protocol. The luminescence values obtained from cells treated with the antiviral compounds or DMSO were measured through the GloMax® Discover Multimode Microplate Reader (Promega), normalized with luminescence emitted by untreated cells, and elaborated

with the GraphPad PRISM software version 6.01 (La Jolla, CA, USA) to calculate the half-maximal cytotoxic concentration (CC_{50}). Based on the CC_{50}, a non-toxic dose corresponding to 90–100% cell viability was used for each compound as the maximum concentration in the antiviral assays.

To determine the antiviral activity of the drugs, 4-fold decreasing concentrations of remdesivir, nirmatrelvir and EIDD-1931 were added to 5000 pre-seeded VERO E6 cells as described [11] and viral isolates were used at MOI 0.005 (corresponding to 100 $TCID_{50}$) to infect the cultures after one hour. After 72 h incubation, antiviral drug activity was deter-mined by measuring cell viability with the Cell Titer-Glo protocol as described above and expressed as half-maximal inhibitory drug concentration (IC_{50}). Infected and uninfected cells without drugs were used to calculate the 100% and 0% of viral replication, respectively. Drugs were tested in technical duplicates in at least two independent experiments. The experiments were performed in the absence and in the presence of the P-gp inhibitor to evaluate the impact of the efflux system on the different compounds. The P-gp inhibitor concentration was set at 0.5 M based on cytotoxicity data (Supplementary Figure S1) and previous literature [11,12].

2.5. Statistical Analysis

Data were expressed as median followed by interquartile range [IQR] as appropriate for the distribution of data based on the Shapiro–Wilk test for normality. The Kruskal–Wallis test followed by Mann–Whitney test post hoc analysis was used to compare independent groups, whereas the Friedman test followed by Wilcoxon Rank Sum test post hoc analysis was used to compare multiple paired data.

3. Results

3.1. mAb Treated Patients

Of 50 subjects screened, 40 were enrolled (19 males, 59.8 17.7 years) including 6 who were previously vaccinated but lacked NtAb at baseline. Of these, 5 had haemato-oncologic disease and the remaining one was a 69-year-old male with underlying hypertension, chronic ischemic cardiomyopathy, dyslipidemia. Only one of the enrolled patients was asymptomatic whereas the others had mild symptoms of SARS-CoV-2 infection including fever (67.5%, n = 27), cough (65.0%, n = 26), headache (37.5%, n = 15), arthomyalgia (30.0%, n = 12), dysgeusia (17.5%, n = 7), gastrointestinal disorders (12.5%, n = 5), and dyspnea (5.0%, n = 2). Comorbidities and detailed information about enrolled individuals are indicated in Supplementary Table S2. Patients were treated with BAM/ETE (n = 12), CAS/IMD (n = 14), or SOT (n = 14) starting 3.7 1.6 days from diagnosis.

Two patients were hospitalized (one in BAM/ETE and one in the CAS/IMD group), the others resolved SARS-CoV-2 infection without clinical complications. The time from mAb infusion to SARS-CoV-2 RNA negativization was available only in 22 individuals treated with BAM/ETE (n = 11) or CAS/IMD (n = 11) and was not significantly different with the two cocktails (15 vs. 13 days for BAM/ETE and CAS/IMD, respectively).

3.2. Neutralizing Activity of mAbs against Different Viral Variants

In post-infusion sera, BAM/ETE, CAS/IMD, and SOT showed activity against the wild type (6295 (4355–8075) ID_{50} for BAM/ETE; 18,214 (16,248–21,365) ID_{50} for CAS/IMD; and 456 (265–592) ID_{50} for SOT) and the delta (14,780 (10,905–21,020) ID_{50} for BAM/ETE, 63,937 (47,211–79,971) ID_{50} for CAS/IMD, and 1103 (843–1334) ID_{50} for SOT). However, BA.1 was neutralized only by SOT (200 (37–233) ID_{50}) whereas BA.2 was neutralized by CAS/IMD (174 (134–209) ID_{50}) and SOT (20 (9–31) ID_{50}), but not by BAM/ETE (Figure 1).

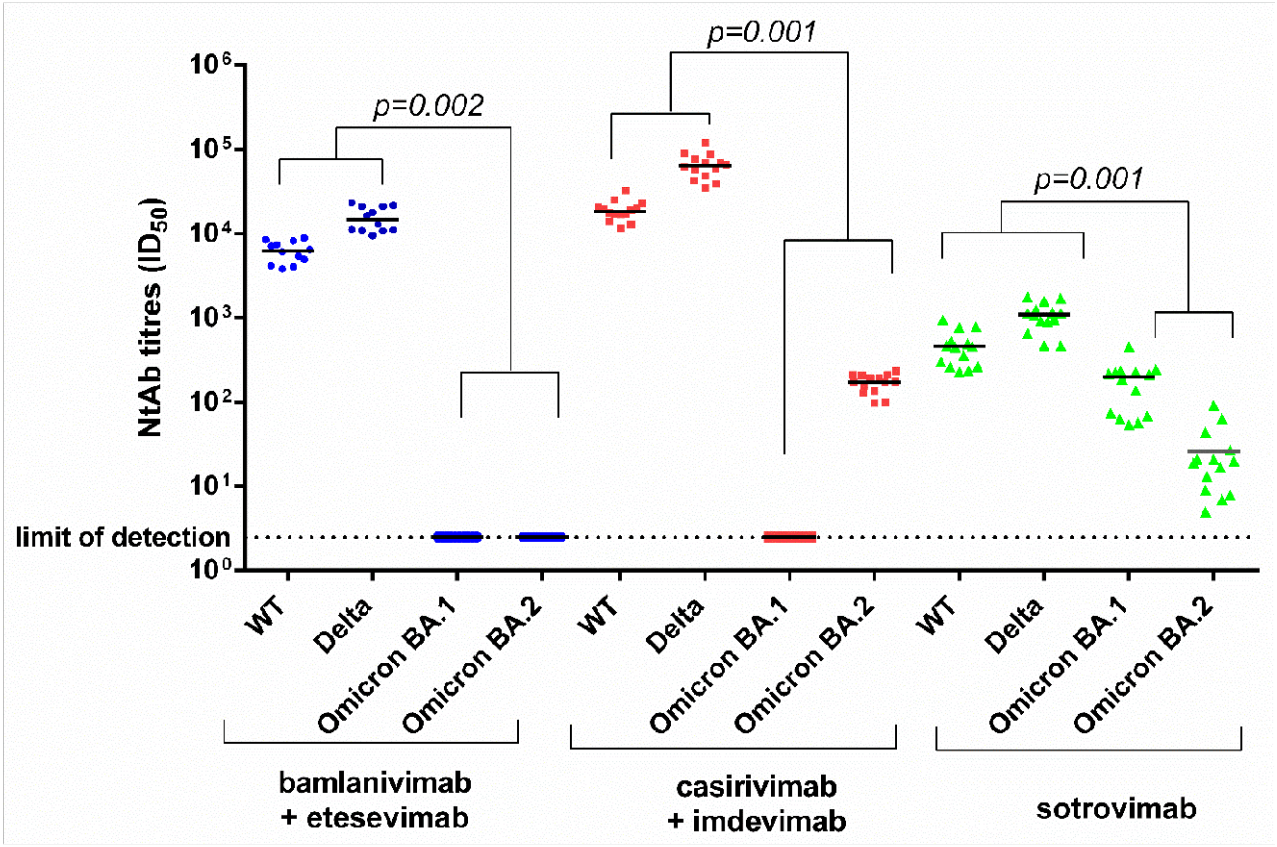

Figure 1. Ex vivo anti-SARS-CoV-2 wild type, delta, omicron (BA.1 and BA.2) neutralizing anti-body titers measured in sera from 40 patients following infusion of bamlanivimab/etesevimab, casirivimab/imdevimab, or sotrovimab monoclonal antibodies. Blue dots, red squares and green triangles represents patients treated with bamlanivimab + etesevimab, casirivimab + indevimab and sotrovimab, respectively. Paired data were analyzed by the non-parametric Wilcoxon Signed Rank Sum test. NtAb titers before infusion were negative against each variant tested (not shown in figure). NtAb: neutralizing antibody; ID_{50}: the reciprocal value of the sera dilution showing the 50% protection of virus-induced cytopathic effect; WT: wild type.

When NtAb titers were analyzed as fold-change (FC) with respect to the wild-type strain, BAM/ETE, CAS/IMD and SOT neutralized the delta variant with 2.5 (1.8–3.6), 3.5 (2.4–5.1) and 2.1 (1.6–3.4) FC increase, respectively (all $p < 0.001$). With respect to wild type, SOT neutralizing activity decreased more with BA.2 (23.9 (14.2–43.5) FC) than with BA.1 (2.8 (1.1–4.1) FC) ($p < 0.001$). The partially regained activity of CAS/IMD against BA.2 was 99.3 (91.8–138.5) fold lower than that against the wild-type virus, a larger FC decrease compared with SOT ($p < 0.001$), although the absolute NtAb titer of CAS/IMD remained higher than that of SOT, due to the lower dosage and/or intrinsic activity of the latter. Indeed, NtAb titers were significantly higher for CAS/IMD vs. BAM/ETE and for both CAS/IMD and BAM/ETE vs. SOT against the wild-type and delta virus, as well as for CAS/IMD vs. SOT against BA.2 ($p < 0.001$ for all comparisons).

3.3. Antiviral Activity of Nirmatrelvir, Molnupiravir and Remdesivir in VERO E6

Table 1 shows the cytotoxicity and the antiviral activity data for EIDD-1931, nirmatrelvir and remdesivir. No significant differences were observed for any drug IC_{50} across the viral variants considered. The impact of the P-gp inhibitor, as measured with the wild-type virus, was negligible with EIDD-1931 but highly relevant with remdesivir and nirmatrelvir, resulting in increased antiviral activity by 88- and 126-fold, respectively (Figure 2).

Table 1. Anti-SARS-CoV-2 activity of EIDD-1931 (the active form of molnupiravir), remdesivir and nirmatrelvir in VERO E6 cells. Compounds were tested in absence of P-gp inhibitor (CP-100356 hydrochloride) against wild-type strain and in presence of 0.5 M P-gp inhibitor against Wild Type (WT), Delta, BA.1, and BA.2 variants. CC_{50}: half-maximal toxic drug concentration; IC_{50}: half-maximal inhibitor drug concentration; SD: Standard Deviation.

Compound	CC_{50} (M)	IC_{50} WT (M) Mean SD	IC_{50} Delta (M) Mean SD	IC_{50} BA.1 (M) Mean SD	IC_{50} BA.2 (M) Mean SD
EIDD-1931	40.6 3.7	1.10 0.10			
EIDD-1931 plus P-gp inhibitor	43.3 6.0	1.50 0.10	1.50 0.70	1.00 0.50	0.80 0.01
Nirmatrelvir	69.6 1.0	5.80 0.80			
Nirmatrelvir plus P-gp inhibitor	40.7 4.4	0.05 0.02	0.06 0.01	0.04 0.02	0.04 0.01
Remdesivir	205.0 35.4	6.90 2.30			
Remdesivir plus P-gp inhibitor	17.2 0.2	0.08 0.04	0.11 0.08	0.05 0.04	0.08 0.01

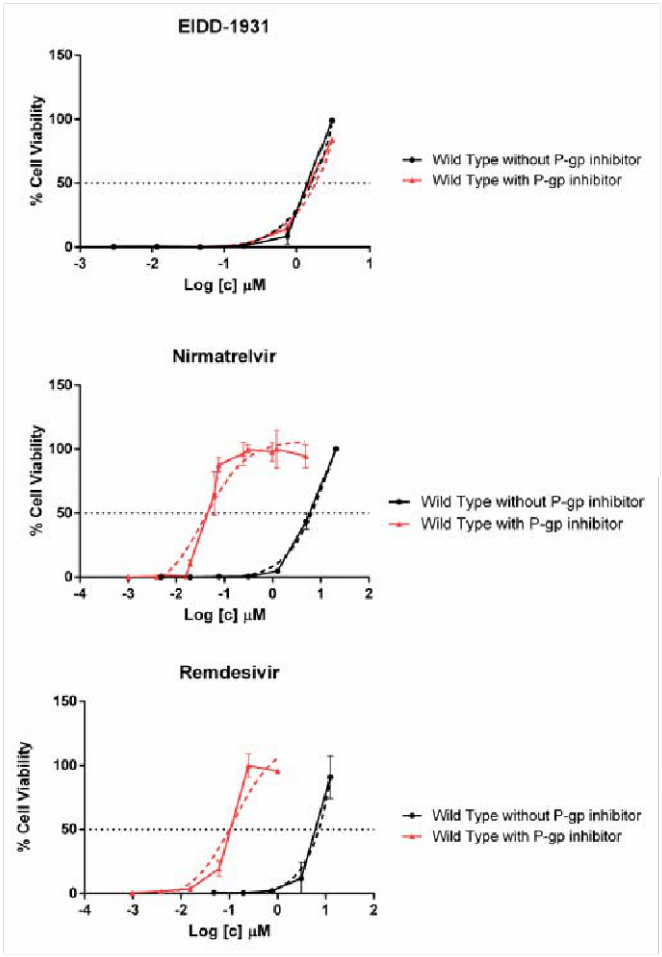

Figure 2. Comparison between antiviral activity of EIDD-1931, Nirmatrelvir and Remdesivir against wild-type SARS-CoV-2 virus with (0.5 M) or without the addition of P-gp inhibitor. On the x-axis is indicated the micromolar drug concentration in logarithmic scale. The horizontal dashed line indicates the drug IC_{50} corresponding to 50% cell viability whereas the dashed curves indicate the dose response fitting curve generated by GraphPad PRISM software version 6.01 (La Jolla, CA, USA).

4. Discussion

Despite a limited evolutionary rate, continuous massive worldwide replication of SARS-CoV-2 has generated an array of mutants, with new variants typically outpacing past

lineages and quickly becoming dominant [13]. Not surprisingly, most mutations in evolutionarily successful variants have occurred in the spike glycoprotein resulting in improved virus entry and increased transmissibility [14]. First detected in late 2021, the omicron variant led a major shift in SARS-CoV-2 evolution [15], driven by an unprecedented number of spike mutations and further evolving into a constellation of related lineages including BA.1, BA.1.1, BA.2 and later BA.3, BA.4 and BA.5, with some sublineages spreading faster than others in specific countries such BA.2.12.1 in the US [6]. A major consequence of omicron divergence from past lineages is the markedly reduced neutralization by sera from individuals recovering from natural infection with previously dominating variants and/or immunized with vaccines derived from the ancestral virus strain [16]. Likewise, several mAbs based on virus variants dominating the first epidemic waves have lost activity against omicron lineages [17].

Unlike the other licensed mAbs, SOT was derived from the antibody repertoire of an individual recovered from SARS-CoV in 2003 and shown to be cross-reactive to SARS-CoV-2, thus targeting a highly conserved domain [18]. Indeed, when compared with BAM/ETE and CAS/IMD, SOT had the smallest-fold decrease in activity against omicron BA.1 and BA.2 with respect to the ancestral reference virus, both in previous in vitro studies [19,20] and in this ex vivo study. However, we observed higher absolute NtAb titers to BA.2 with CAS/IMD compared to SOT in our ex vivo assay. This apparently contradictory result likely derived from the combination of three factors. First, IMD may have residual activity against BA.2, despite a fold decrease with respect to the ancestral virus ranging from 20 to 500 [4,19–21]. Second, the in vivo dosage of CAS/IMD is higher than that of SOT (1200 plus 1200 mg vs. 500 mg). Third, the intrinsic in vitro neutralizing activity of SOT is one order of magnitude lower than that of CAS or IMD, as indicated by EC_{50} values with the susceptible wild-type virus [3,22,23].

At present, it is unclear how this expected activity, for both SOT and CAS/IMD, can translate into clinical benefit with BA.2 infection. It must be emphasized that in vitro neutralization assays can capture just one component of the mAbs activity. Indeed, unlike other mAbs, neither SOT nor CAS/IMD have been engineered to remove effector functions such as engagement of Fc receptors, and SOT was recently shown to trigger antibody-dependent cytotoxicity and phagocytosis [5,24]. Of note, both SOT and CAS/IMD, as well as CIL/TIX, have been recently reported to curb experimental disease progression in the BA.2 infected hamster model, as shown by decreased infectious virus titer in the lungs by a factor which was comparable with the D614G infected control animals [25].

As opposed to mAbs variant-dependent activity, it was reassuring to confirm that the three licensed antivirals retain their full potency in vitro against the BA.1 and BA.2 omicron lineages. Of note, there has been only one report documenting this activity against the currently dominating BA.2 variant in vitro [4]. While VERO cells were used both in the previous and in our study, we extended the analysis by testing drug activity both in the presence and in the absence of the CP-100356 hydrochloride P-gp inhibitor. This is important because VERO cells overexpress P-gp, a condition which should not occur in human SARS-CoV-2 cell targets in vivo. In addition, nirmatrelvir is administered in vivo together with ritonavir which inhibits the P450 cytochrome CYP3A4 isoenzyme as well as P-gp [26]. Our results without the P-gp inhibitor closely matched the activity shown in the previous in vitro work under the same experimental conditions but we also showed that under P-gp inhibitor treatment the activity is enhanced around 100-fold for nirmatrelvir and for remdesivir. In addition, we comprehensively tested the cytotoxicity of the P-gp inhibitor in the same cell line, both alone and in combination with the different drugs, thus analyzing drug/P-gp inhibitor interactions. Indeed, the P-gp inhibitor decreased cell viability by 20% at 2 M, a concentration which has been used in some of the previous studies evaluating the antivirals against past virus lineages [27,28]. This data helps to define how to measure antiviral activity of current and future antivirals.

Thus, our work strengthens the concept of resilience to SARS-CoV-2 variability with antivirals as opposed to the continuous challenge with mAbs. However, both antivirals

and mAbs should be retested with any new virus variant. We believe our work contributes to the need to set technical aspects and procedures to comprehensively define the potential of the antiviral armamentarium, including mAbs and small molecules, and keep pace with virus variability during the ongoing pandemic.

Supplementary Materials: The following are available online at https://www.mdpi.com/article/10.3390/v14071374/s1, Table S1: Lineage classification of strains included in the study, accession number and spike identified mutations. Table S2: Clinical features of enrolled individuals. Figure S1: Cytotoxicity of the P-gp inhibitor CP-100356 in VERO E6 cells.

Author Contributions: I.V., M.Z. and D.F. Conceptualization; I.V. and F.D. Methodology; L.F., A.B., E.S. and C.B. performed the experiments; L.F., F.G. and I.V. performed data analysis; A.G., C.N., B.R., A.L. and E.S. collected the samples and provided the virus lineages for this work; I.V. and L.F. Writing—original draft preparation; I.V. and M.Z. Writing—review and editing; C.B. and L.F. Visualization; I.V. and F.D. Supervision; C.N., M.Z. and D.F. Project administration. All authors have read and agreed to the published version of the manuscript.

Funding: This work was partly funded by the European Commission under HORIZON-HLTH-2021-CORONA-01, Project EuCARE, grant agreement N. 101046016.

Institutional Review Board Statement: The study was conducted according to the guidelines of the Declaration of Helsinki, and approved by the local Ethics Committee of Perugia Hospital (Neutro-COVID observational study, protocol number 4069/21 accepted 21 January 2021).

Informed Consent Statement: Informed consent was obtained from all subjects involved in the study.

Data Availability Statement: Not applicable.

Acknowledgments: We would like to thank Alessandro Lanari for his clinical support in this study.

Conflicts of Interest: M.Z. reports consultancy for ViiV Healthcare, Gilead Sciences, GlaxoSmithKline, Janssen-Cilag, Theratechnologies, Merck Sharp and Dohme, and grants for his institution from ViiV Healthcare, Theratechnologies and Gilead Sciences outside the submitted work. B.R. received support for travel to meetings from Abbvie, Gilead Sciences, Janssen-Cilag, MSD, ViiV Healthcare, and Bristol Myers Squibb, and fees for attending advisory boards and speaker's honoraria from Abbvie, Gilead Sciences, Janssen-Cilag, MSD, ViiV Healthcare, and Bristol-Myers Squibb. All other authors: no conflicts to declare.

References

1. Markov, P.V.; Katzourakis, A.; Stilianakis, N.I. Antigenic Evolution Will Lead to New SARS-CoV-2 Variants with Unpredictable Severity. Nat. Rev. Microbiol. 2022, 20, 251–252. [CrossRef] [PubMed]
2. Tao, K.; Tzou, P.L.; Nouhin, J.; Gupta, R.K.; de Oliveira, T.; Kosakovsky Pond, S.L.; Fera, D.; Shafer, R.W. The Biological and Clinical Significance of Emerging SARS-CoV-2 Variants. Nat. Rev. Genet. 2021, 22, 757–773. [CrossRef] [PubMed]
3. Takashita, E.; Kinoshita, N.; Yamayoshi, S.; Sakai-Tagawa, Y.; Fujisaki, S.; Ito, M.; Iwatsuki-Horimoto, K.; Chiba, S.; Halfmann, P.; Nagai, H.; et al. Efficacy of Antibodies and Antiviral Drugs against COVID-19 Omicron Variant. N. Engl. J. Med. 2022, 386, 995–998. [CrossRef]
4. Takashita, E.; Kinoshita, N.; Yamayoshi, S.; Sakai-Tagawa, Y.; Fujisaki, S.; Ito, M.; Iwatsuki-Horimoto, K.; Halfmann, P.; Watanabe, S.; Maeda, K.; et al. Efficacy of Antiviral Agents against the SARS-CoV-2 Omicron Subvariant BA.2. N. Engl. J. Med. 2022, 386, 1475–1477. [CrossRef] [PubMed]
5. Cathcart, A.L.; Havenar-Daughton, C.; Lempp, F.A.; Ma, D.; Schmid, M.A.; Agostini, M.L.; Guarino, B.; di iulio, J.; Rosen, L.E.; Tucker, H.; et al. The Dual Function Monoclonal Antibodies VIR-7831 and VIR-7832 Demonstrate Potent in Vitro and in Vivo Activity against SARS-CoV-2. bioRxiv 2022, 2021.03.09.434607. [CrossRef]
6. Cao, Y.; Yisimayi, A.; Jian, F.; Song, W.; Xiao, T.; Wang, L.; Du, S.; Wang, J.; Li, Q.; Chen, X.; et al. BA.2.12.1, BA.4 and BA.5 Escape Antibodies Elicited by Omicron Infection. bioRxiv 2022, 2022.04.30.489997. [CrossRef]
7. Yamasoba, D.; Kosugi, Y.; Kimura, I.; Fujita, S.; Uriu, K.; Ito, J.; Sato, K.; The Genotype to Phenotype Japan (G2P-Japan) Consortium. Sensitivity of Novel SARS-CoV-2 Omicron Subvariants, BA.2.11, BA.2.12.1, BA.4 and BA.5 to Therapeutic Monoclonal Antibodies. bioRxiv 2022, 2022.05.03.490409. [CrossRef]
8. Dragoni, F.; Schiaroli, E.; Micheli, V.; Fiaschi, L.; Lai, A.; Zehender, G.; Rossetti, B.; Gismondo, M.R.; Francisci, D.; Zazzi, M.; et al. Impact of SARS-CoV-2 Omicron BA.1 and Delta AY.4.2 Variants on the Neutralization by Sera of Patients Treated with Different Authorized Monoclonal Antibodies. Clin. Microbiol. Infect. 2022, 28, 1037–1039. [CrossRef]

9. Vicenti, I.; Martina, M.G.; Boccuto, A.; de Angelis, M.; Giavarini, G.; Dragoni, F.; Marchi, S.; Trombetta, C.M.; Crespan, E.; Maga, G.; et al. System-Oriented Optimization of Multi-Target 2,6-Diaminopurine Derivatives: Easily Accessible Broad-Spectrum Antivirals Active against Flaviviruses, Influenza Virus and SARS-CoV-2. Eur. J. Med. Chem. 2021, 224, 113683. [CrossRef]
10. Kristiansen, P.A.; Page, M.; Bernasconi, V.; Mattiuzzo, G.; Dull, P.; Makar, K.; Plotkin, S.; Knezevic, I. WHO International Standard for Anti-SARS-CoV-2 Immunoglobulin. Lancet 2021, 397, 1347–1348. [CrossRef]
11. Vangeel, L.; Chiu, W.; de Jonghe, S.; Maes, P.; Slechten, B.; Raymenants, J.; André, E.; Leyssen, P.; Neyts, J.; Jochmans, D. Remdesivir, Molnupiravir and Nirmatrelvir Remain Active against SARS-CoV-2 Omicron and Other Variants of Concern. Antiviral Res. 2022, 198, 105252. [CrossRef]
12. Hoffman, R.L.; Kania, R.S.; Brothers, M.A.; Davies, J.F.; Ferre, R.A.; Gajiwala, K.S.; He, M.; Hogan, R.J.; Kozminski, K.; Li, L.Y.; et al. Discovery of Ketone-Based Covalent Inhibitors of Coronavirus 3CL Proteases for the Potential Therapeutic Treatment of COVID-19. J. Med. Chem. 2020, 63, 12725–12747. [CrossRef]
13. Flores-Vega, V.R.; Monroy-Molina, J.V.; Jiménez-Hernández, L.E.; Torres, A.G.; Santos-Preciado, J.I.; Rosales-Reyes, R. SARS-CoV-2: Evolution and Emergence of New Viral Variants. Viruses 2022, 14, 653. [CrossRef] [PubMed]
14. de Souza, A.S.; de Freitas Amorim, V.M.; Guardia, G.D.A.; dos Santos, F.F.; Ulrich, H.; Galante, P.A.F.; de Souza, R.F.; Guzzo, C.R. Severe Acute Respiratory Syndrome Coronavirus 2 Variants of Concern: A Perspective for Emerging More Transmissible and Vaccine-Resistant Strains. Viruses 2022, 14, 827. [CrossRef] [PubMed]
15. Guo, Y.; Han, J.; Zhang, Y.; He, J.; Yu, W.; Zhang, X.; Wu, J.; Zhang, S.; Kong, Y.; Guo, Y.; et al. SARS-CoV-2 Omicron Variant: Epidemiological Features, Biological Characteristics, and Clinical Significance. Front. Immunol. 2022, 13, 877101. [CrossRef] [PubMed]
16. Evans, J.P.; Zeng, C.; Qu, P.; Faraone, J.; Zheng, Y.-M.; Carlin, C.; Bednash, J.S.; Zhou, T.; Lozanski, G.; Mallampalli, R.; et al. Neutralization of SARS-CoV-2 Omicron Sub-Lineages BA.1, BA.1.1, and BA.2. Cell Host Microbe 2022, S1931-3128(22)00220-7. [CrossRef] [PubMed]
17. Ai, J.; Wang, X.; He, X.; Zhao, X.; Zhang, Y.; Jiang, Y.; Li, M.; Cui, Y.; Chen, Y.; Qiao, R.; et al. Antibody Evasion of SARS-CoV-2 Omicron BA.1, BA.1.1, BA.2, and BA.3 Sub-Lineages. Cell Host Microbe 2022, S1931-3128(22)00243-8. [CrossRef]
18. Pinto, D.; Park, Y.J.; Beltramello, M.; Walls, A.C.; Tortorici, M.A.; Bianchi, S.; Jaconi, S.; Culap, K.; Zatta, F.; de Marco, A.; et al. Cross-Neutralization of SARS-CoV-2 by a Human Monoclonal SARS-CoV Antibody. Nature 2020, 583, 290–295. [CrossRef]
19. Bruel, T.; Hadjadj, J.; Maes, P.; Planas, D.; Seve, A.; Staropoli, I.; Guivel-Benhassine, F.; Porrot, F.; Bolland, W.-H.; Nguyen, Y.; et al. Serum Neutralization of SARS-CoV-2 Omicron Sublineages BA.1 and BA.2 in Patients Receiving Monoclonal Antibodies. Nat. Med. 2022, 6, 1297–1302. [CrossRef]
20. Arora, P.; Zhang, L.; Krüger, N.; Rocha, C.; Sidarovich, A.; Schulz, S.; Kempf, A.; Graichen, L.; Moldenhauer, A.-S.; Cossmann, A.; et al. SARS-CoV-2 Omicron Sublineages Show Comparable Cell Entry but Differential Neutralization by Therapeutic Antibodies. Cell Host Microbe 2022, S1931-3128(22)00223-2. [CrossRef]
21. Iketani, S.; Liu, L.; Guo, Y.; Liu, L.; Chan, J.F.-W.; Huang, Y.; Wang, M.; Luo, Y.; Yu, J.; Chu, H.; et al. Antibody Evasion Properties of SARS-CoV-2 Omicron Sublineages. Nature 2022, 604, 553–556. [CrossRef] [PubMed]
22. Touret, F.; Baronti, C.; Bouzidi, H.S.; de Lamballerie, X. In Vitro Evaluation of Therapeutic Antibodies against a SARS-CoV-2 Omicron B.1.1.529 Isolate. Sci. Rep. 2022, 12, 4683. [CrossRef] [PubMed]
23. VanBlargan, L.A.; Errico, J.M.; Halfmann, P.J.; Zost, S.J.; Crowe, J.E.; Purcell, L.A.; Kawaoka, Y.; Corti, D.; Fremont, D.H.; Diamond, M.S. An Infectious SARS-CoV-2 B.1.1.529 Omicron Virus Escapes Neutralization by Therapeutic Monoclonal Antibodies. Nat. Med. 2022, 28, 490–495. [CrossRef]
24. Case, J.B.; Mackin, S.; Errico, J.; Chong, Z.; Madden, E.A.; Guarino, B.; Schmid, M.A.; Rosenthal, K.; Ren, K.; Jung, A.; et al. Resilience of S309 and AZD7442 Monoclonal Antibody Treatments against Infection by SARS-CoV-2 Omicron Lineage Strains. bioRxiv 2022, 2022.03.17.484787. [CrossRef]
25. Uraki, R.; Kiso, M.; Iida, S.; Imai, M.; Takashita, E.; Kuroda, M.; Halfmann, P.J.; Loeber, S.; Maemura, T.; Yamayoshi, S.; et al. Characterization and Antiviral Susceptibility of SARS-CoV-2 Omicron/BA.2. Nature 2022. [CrossRef]
26. Marzolini, C.; Kuritzkes, D.R.; Marra, F.; Boyle, A.; Gibbons, S.; Flexner, C.; Pozniak, A.; Boffito, M.; Waters, L.; Burger, D.; et al. Prescribing Nirmatrelvir-Ritonavir: How to Recognize and Manage Drug-Drug Interactions. Ann. Intern. Med. 2022, 175, 744–746. [CrossRef]
27. Owen, D.R.; Allerton, C.M.N.; Anderson, A.S.; Aschenbrenner, L.; Avery, M.; Berritt, S.; Boras, B.; Cardin, R.D.; Carlo, A.; Coffman, K.J.; et al. An Oral SARS-CoV-2 M pro Inhibitor Clinical Candidate for the Treatment of COVID-19. Science 2021, 374, 1586–1593. [CrossRef] [PubMed]
28. Rosales, R.; McGovern, B.L.; Rodriguez, M.L.; Rai, D.K.; Cardin, R.D.; Anderson, A.S.; P.S.P. study group; Sordillo, E.M.; van Bakel, H.; Simon, V.; et al. Nirmatrelvir, Molnupiravir, and Remdesivir maintain potent in vitro activity against the SARS-CoV-2 Omicron variant. bioRxiv 2022, 2022.01.17.476685. [CrossRef]